Analyse spatio-temporelle de la morphologie des rivières en tresses par LiDAR aéroporté

Sandrine Tacon

CNRS, UMR-5600 EVS
IRSTEA, ETGR
Ecole doctorale Sciences Sociales (ED 483)
Université Lyon 2

Analyse spatio-temporelle de la morphologie des rivières en tresses par LiDAR aéroporté

Thèse de doctorat de géographie, aménagement et urbanisme

présentée et soutenue publiquement le 11 septembre 2015 par

Sandrine LALLIAS-TACON

sous la direction d'Hervé PIEGAY et Frédéric LIEBAULT

MEMBRES DU JURY

Laurent Astrade, Maître de Conférences, CNRS UMR 5204, Université de Savoie	(Examinateur)
Frédéric Liébault, Chargé de recherche, Irstea Grenoble, ETGR,	(Encadrant)
Jean-Luc Peiry, Professeur, CNRS UMR 6042 GEOLAB, Université de Clermont 2	(Rapporteur)
Hervé Piégay, Directeur de Recherche, CNRS UMR 5600 EVS, Université de Lyon	(Directeur)
Massimo Rinaldi, Professeur-associé, Université de Florence, Italie	(Rapporteur)
Benoît Terrier, Agence de l'Eau Rhône-Méditerranée-Corse	(Examinateur)

REMERCIEMENTS

Ce manuscrit clôt une fabuleuse aventure débutée quelques années plus tôt par mon entrée dans le monde de la recherche et des rivières en tresses par la petite porte d'un CDD à Irstea qui s'est prolongé par cette thèse. Je remercie, tout d'abord, Frédéric Liébault, mon encadrant de thèse, pour m'avoir fait confiance pour le CDD et ensuite pour la thèse et ce jusqu'à la fin qui a été un peu plus longue que prévue. Sa rigueur pour le traitement des données et la rédaction des articles scientifiques a été pour moi très formateur. Je le remercie aussi de m'avoir fait découvert ce magnifique sujet d'étude, que sont les rivières en tresses des Alpes françaises, longuement parcourues sur le terrain et observées de longues heures au travers de MNT ou de photographies aériennes. Mes chaleureux remerciements vont aussi à Hervé Piégay, mon directeur de thèse, pour m'avoir apporté une approche nouvelle des traitements de données SIG et des statistiques, ses connaissances sur les rivières en tresses, mais aussi pour sa bienveillance dans les moments difficiles. Votre vision complémentaire m'a permis d'aller au fond de mes questionnements scientifiques, du traitement des données et de la discussion des résultats. Je me rappellerai encore longtemps de mon chapitre 3 qui nous en aura fait voir de toutes les couleurs…

Je tiens à remercier les deux rapporteurs de mon manuscrit Jean-Luc Peiry et Massimo Rinaldi pour avoir accepté d'évaluer mon travail, ainsi que Laurent Astrade et Benoît Terrier pour leur participation au jury de thèse.

Durant cette thèse, j'ai bénéficié d'un comité de suivi, que je remercie pour leurs visions extérieures à la thèse : Alain Recking, Yann Le Coarer, Michal Tal, John Pitlick. Je remercie plus particulièrement Yann Le Coarer pour m'avoir montré ses travaux et ses codes sur le traitement des données LiDAR et pour le prêt du dGPS d'Irstea-Aix-en-Provence.

J'adresse mes remerciements à IRSTEA Grenoble et en particulier l'unité ETNA, qui m'a accueillie et m'a permis de réaliser cette thèse dans de bonnes conditions, ainsi qu'au CNRS UMR 5600, mon deuxième laboratoire d'accueil.

Cette thèse a bénéficié des financements du projet ANR Risknat (GESTRANS ANR-09-RISK-004/GESTRANS), du CNRS-INSU (EC2CO-CYTRIX programme), de l'ORE Draix-Bléone et de la ZABR.

Je remercie les personnes qui m'on apporté leur aide: Lise Vaudor pour ses supers codes en R, Hervé Bellot pour ses connaissances en traitement du signal, Marie-Laure Trémélo pour le prêt de dGPS et le traitement des données, Laurent Albrecht pour le pré-traitement des données dGPS,

Walter Bertoldi sur ces travaux, et les nombreux collègues qui m'ont aidée sur le terrain (Pauline, Mathieu, Véronique, Eric, Coraline).

Mes remerciements vont aux équipes du projet tresses et Gestrans. Les séminaires Gestrans ont été riches en échanges et le dernier qui rassembla tous les chercheurs internationaux dans le domaine des rivières en tresses au Cloître de Sainte-Croix restera pour moi un très bon souvenir.

J'ai une grande pensée à mes collègues de "galère" : Pauline, Mathieu, Philomène, Adeline, Joshua, Paolo, Nejib, Nicolas, qui ont débarqué au fil des années et je remercie les nouveaux doctorants pour m'avoir apporté la fraîcheur des débuts de thèse: Pascal, Lingran, Coraline, Guillaume, Gaëtan, Raphaël, Hoan,… Je remercie aussi Christian et Fred pour leurs nombreux goûters au labo méca et les viennoiseries du matin de Christian.

J'ai une petite pensée aux nombreuses personnes qui ont partagé mes nombreux bureaux, de façon plus au moins longue, Pauline ma collègue des tresses, et les derniers qui m'ont accueillie de façon "clandestine": Pascal, Firmin, Hoan, Coraline et Guillaume.

Enfin, je remercie les doctorants, anciens doctorants, post-doctorants, permanents de l'UMR 5600 qui m'ont accueillie chaleureusement lors de mes visites: Mélanie, Barbara, Fanny, Vincent, Véronique, Jérémie, Emeline, Elsa, Marie-Laure, Kristell, Bianca.... Les missions drône resteront aussi pour moi un très bon souvenir.

Mon dernier grand merci va à Jérôme, qui a su croire en moi jusqu'à la fin…

SOMMAIRE

RESUME

Les rivières en tresses sont caractérisées par un réseau complexe de chenaux multiples très mobiles dans l'espace et dans le temps, séparés par des bancs sédimentaires pas ou peu végétalisés, qui sont émergés en période de basses et moyennes eaux. A long terme, en fonction du régime sédimentaire et hydrologique, ces rivières construisent des plaines alluviales complexes constituées d'une mosaïque d'unités correspondant à des échelles spatio-temporelles différentes. Jusqu'au début des années 2000, l'étude *in situ* de ces rivières était fondée sur des levés topographiques très discontinus dans l'espace, ce qui limitait le champ d'investigation de la complexité morphologique des lits en tresses. Le développement récent du LiDAR (Ligth Detection And Ranging) aérien permet une acquisition rapide de la morphologie 3D des mosaïques fluviales à de fines résolutions spatiales et sur de grandes étendues. Les données LiDAR permettent aussi de mesurer la topographie sous la végétation et de fournir des indicateurs de cette végétation. L'objectif de cette thèse a été d'utiliser ces nouvelles données pour améliorer la connaissance des réponses morphologiques des lits en tresses à différentes échelles spatio-temporelles.

Dans un premier temps, 2 levés LiDAR séquentiels ont permis de détecter les changements morphologiques d'une tresse de 7 km survenus suite à une crue de période de retour 14 ans (Chapitre 2). Ces travaux ont été réalisés sur le site du Bès, un affluent de la Bléone. Les résultats ont mis en évidence l'importance des différentes étapes de traitement de l'information dans le calcul du bilan sédimentaire. Il apparaît que le réalignement des nuages de points séquentiels et que l'évaluation sommaire de la bathymétrie à partir d'une hauteur d'eau moyenne sont des étapes primordiales pour le calcul du bilan. La prise en compte de la variabilité spatiale de l'incertitude altimétrique en fonction des états de surface a permis d'établir des seuils critiques de détection du changements spatialement distribués dans la plaine d'inondation. Cette dernière étape a permis d'optimiser le calcul du bilan sédimentaire et de produire une cartographie robuste des déformations morphologiques (érosion et dépôt). L'exploitation des résultats a montré que le réseau des chenaux tressés a été profondément remanié pendant la crue, du fait de l'occurrence de nombreuses avulsions. L'estimation du taux de renouvellement des formes a permis de mettre en évidence qu'au moins 54% de la bande active a participé au transport solide pendant la crue.

Dans un deuxième temps, les données LiDAR ont été utilisées pour caractériser la signature morphologique des lits en tresses à l'échelle plurikilométrique (Chapitre 3). L'extraction systématique de profils en travers de la bande de tressage a permis d'étudier les variations longitudinales de plusieurs métriques morphologiques (largeur de bande active, Bed Relief Index, nombre de chenaux) et d'établir des longueurs d'onde caractéristiques de ces signaux. L'analyse a

porté sur un linéaire de plus de 25 km réparti sur 9 sites, dans les bassins versants de la Drôme, du Drac et de la Bléone. Le site du Bès a été levé deux fois pour étudier l'impact de la crue du période de retour 14 ans sur la signature morphologique. Premièrement, ces données mettent clairement en évidence l'effet du confinement de la tresse sur ses propriétés morphologiques avec entre autres un élargissement de la bande active à l'amont de ces zones. Deuxièmement, deux périodes caractéristiques ont été mises en évidence : autour de 3-4 et de 9-10 fois la largeur de la bande active. La période à 3-4 serait liée à la dynamique des macroformes (bancs élémentaires). La période à 10 pourrait être liée à la dynamique de transfert à long terme des sédiments et pourrait correspondre aux successions longitudinales des mégaformes sédimentaires.

Finalement, les données de LIDAR aérien ont été couplées à une étude diachronique de photographies aériennes pour reconstruire l'historique de formation des différentes unités spatiales composant la plaine d'inondation et relier cette structure avec les caractéristiques des unités de végétation (Chapitre 4). 3 rivières en tresses ont été étudiées dans les Alpes françaises avec un degré croissant d'activité : le Bouinenc, la Drôme et le Bès. Cette méthodologie a permis de reconstruire les différentes phases d'incision du lit avec deux périodes majeurs : avant 1948 et seconde partie du 20ème siècle. Il a été montré que l'intensité des crues contrôle le caractère brutal des phases d'incision avec une incision forte pour les crues de période de retour 50 ans et que, d'autre part, les crues induisent des élargissements plus faibles de la bande active en cas d'apport sédimentaire déficitaire. Ces changements à long terme jouent un rôle significatif pour expliquer la mosaïque de la végétation de la plaine d'inondation avec une végétation bien développée et composée majoritairement d'unité matures dans le cas d'une rétraction et d'une incision sur le long terme. Les rivières plus actives présentent une diversité d'unité de végétation plus équilibrée. Enfin, la présence de lande arbustive semble être un bon indicateur des périodes d'incision.

ABSTRACT

Braided rivers are characterised by a complex network of several low-flow channels, highly mobiles in time and space, interspersed with gravel bars with or without sparse vegetation. Long term changes of braided rivers form complex floodplains composed of sedimentary deposits mosaics, which differ in term of spatial and time scales, in function of hydrologic forcing and sediment supply. Until the beginning of 2000s, the topographic monitoring of braided channels was restricted to irregularly spaced surveys limiting the morphologic investigation of braided river complexity. The recent development of airborne LiDAR (Ligth Detection And Ranging) allows rapid acquisition of 3D morphology of fluvial mosaic with high resolution and high precision over large areas. With LiDAR data, it is also possible to measure understorey topography and vegetation characteristics. The goal of this thesis is to use these new data to improve our understanding of braided channel morphological responses at different spatial and time scales.

In a first time, two sequential airborne LiDAR surveys were used to reconstruct morphological changes of a 7-km-long braided river channel following a 14-year return period flood (Chapter 2). This was done on the Bès River, a tributary of the Bléone River in southeastern France. Results highlighted the importance of different data processing steps in sediment budget computation. This showed that surface matching and summary assessment of bathymetry from mean depth have both a considerable effect on the net sediment budget. Spatially distributed propagation of uncertainty based on surface conditions of the channel allows us to compute levels of detection of elevation changes for improving sediment budget and to product a comprehensive map of channel deformations. Analysis of these data shows that the braided channel pattern was highly disturbed by the flood owing to the occurrence of several channel avulsions. 54% of the pre-flood active channel was reworked by the flood.

In a second time, LiDAR data were used to look at longitudinal signatures of cross-sectional morphology at the scale of several kilometers (Chapter 3). Airborne LiDAR surveys were disaggregated into 10 m-regularly space cross-sections to study longitudinal variation of different morphologic indicators (active channel width, Bed Relief index, number of channel). This study was done on 9 study reaches distributed on five braided rivers in Drôme, Drac and Bléone catchments (French Alps). One study reach was survey twice to look at the temporal change of cross-sectional morphology due to a 14-yr return period flood. First, these data highlighted the effect of braided river confinement/obstruction on morphologic signature with upstream widening pattern. Secondly, two characteristic wavelengths have been identified from these signals: 3-4 and

10 times the active channel width. The first could be link to the dynamics of macroforms. The second could be associated to the dynamics of megaforms and long term sediment transfer.

Finally, airborne LiDAR data were associated with archived aerial photos to reconstruct floodplain formation and relate this geomorphic organisation with vegetation patch characters. This is achieved on 3 different braided rivers in French Alps with an increasing degree of activity: the Bouinenc Torrent, the Drôme River and the Bès River. This methodology allowed us to establish the timing of channel incision with the identification of two major periods: before 1948 and second part of 20th century. We highlighted that flood intensity controlled smoothed or brutal channel incision with high incision for Q_{50} flood and that large and medium floods induced lower channel widening in sediment supply limited conditions. These long term changes are playing a significant role to explain vegetation mosaics with a well-developed vegetated floodplain mainly composed of mature units following long term narrowing and incision. Rivers with higher activity show an equi-diversity of floodplain vegetation units. Finally, presence of shrubland patches seems to be good indicator of incision periods.

CHAPITRE 1

ETAT DE LA QUESTION ET PROBLEMATIQUE SCIENTIFIQUE

A. Cadre scientifique

1. Les rivières en tresses

1.1. Définition

Les rivières en tresses sont caractérisées par un réseau complexe de chenaux multiples très mobiles dans l'espace et dans le temps, séparés par des bancs sédimentaires pas ou peu végétalisés, qui sont émergés en période de basses et moyennes eaux. Les rivières en tresses sont présentes dans des contextes géographique et climatique très variés. On les trouve aussi bien en zone de montagne qu'en plaine et sous des climats arides, méditerranéens ou encore tropicaux. Cette forte variabilité se traduit par une large gamme d'altitudes, de pentes, de tailles de bassin versant, de régimes hydrologiques et de granulométries (charge sableuse ou graveleuse) (Fig. 1).

Le style en tresses a été identifié dès les premiers travaux de classification des styles fluviaux (Leopold and Wolman, 1957), le différenciant des styles à lit unique, rectiligne et méandriforme. Schumm (1985) a suggéré une distinction entre le style en tresses et le style anastomosé, caractérisé par la présence d'îles souvent très densément végétalisées et plutôt par une faible dynamique. Plus récemment, Nanson et Knighton (1996) ont introduit le style en anabranches qui correspond à la diffluence de différents chenaux autonomes, ces chenaux pouvant être de type rectiligne, méandriforme ou en tresses (Fig. 2). Le style divaguant (« wandering ») est souvent défini comme un style de transition entre le style en tresses et le style à méandre (Ferguson and Werrity, 1983). Ce style se caractérise par un chenal principal très sinueux à travers une bande active rectiligne et largement occupée par des bancs de galets. Le nombre de chenaux est cependant faible et la bande active plus étroite que celle des tronçons en tresses.

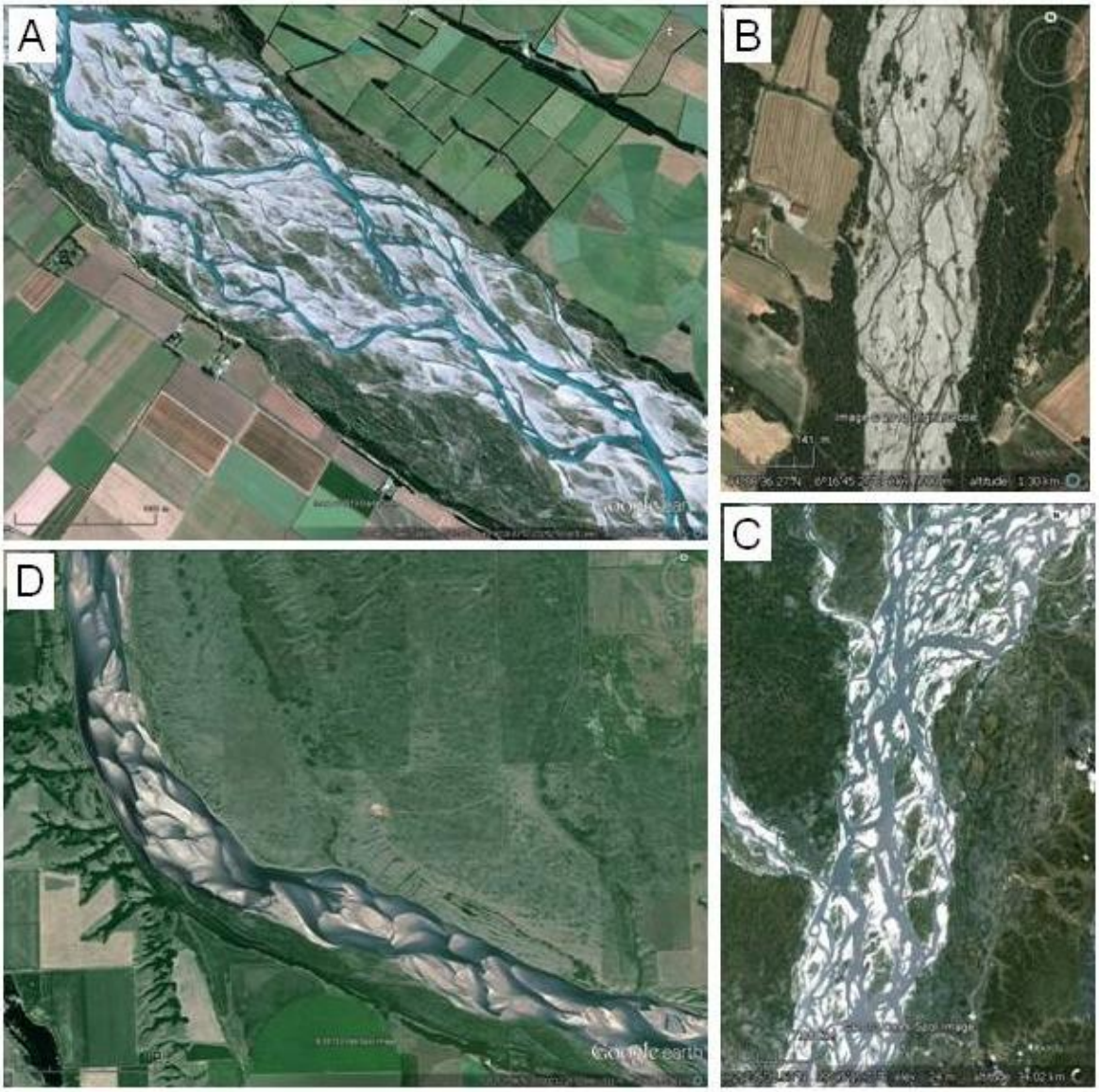

Fig. 1. Exemples de rivières en tresses dans le monde; rivières à granulométrie grossière (A, B, C) et à granulométrie fine (D) de largeur de bande active allant de plus de 15 km (C) à 200 m (B) ; A) Rakaia River, Nouvelle Zélande ; B) la Bléone, France ; C) Brahmaputra River, Asie ; (D) South Saskatchewan River, Canada ; Source : Google earth.

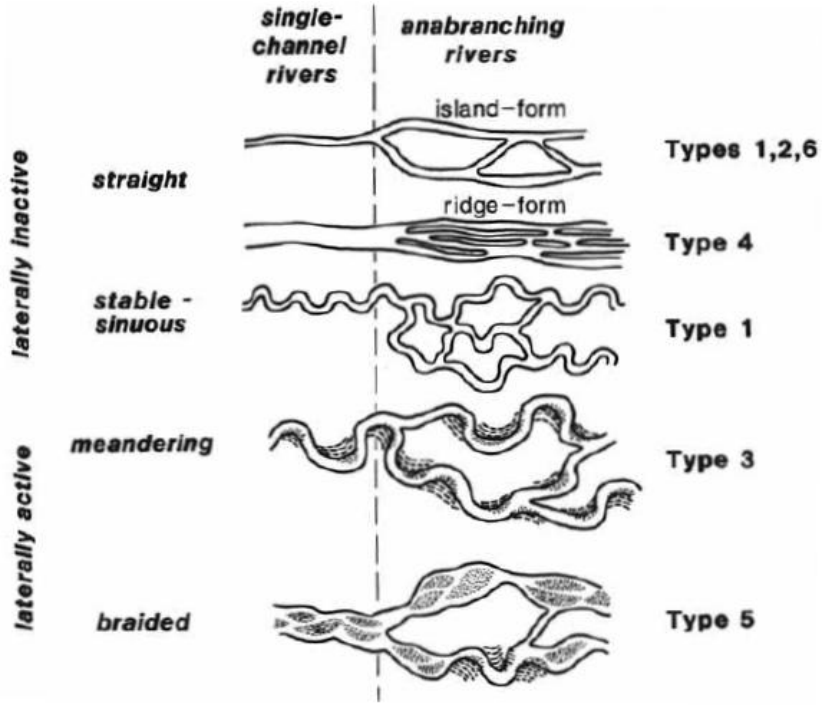

Fig. 2. Classification des styles fluviaux, d'après Nanson et Knighton, 1996.

Brice (1978) a réalisé une classification du style en tresses en fonction de la densité des îles végétalisées et par la suite, Schumm (1985) a différencié les styles « *bar-braided* » et « *island-braided* », sur la base de la fréquence d'îles végétalisées stables. Cette typologie a été reprise dans les travaux sur le Tagliamento en Italie, le définissant comme "island-braided" (e.g.Gurnell and Petts, 2002, Fig.3). Le style "island-braided" est considéré par certains auteurs comme un autre style de rivière en tresses bien différencié du style "bar-braided". Il serait lié à des conditions spécifiques de bassins versants et de conditions locales (Edwards et al., 1999; Gurnell et al., 2001; Gurnell et al., 2005). D'autres auteurs voient ces deux styles comme des stades d'évolution différents des rivières en tresses liés à l'histoire des crues et à l'abondance des apports sédimentaires (Belletti et al., 2013b).

Fig. 3. Vue oblique du Tagliamento (Copyright Diego Cruciat. Licensed under the Creative Commons 3.0 license).

1.2. Les conditions du tressage

Différents facteurs d'occurrence des lits en tresses ont été mis en évidence : l'abondance de la charge de fond, des berges relativement peu cohésives et érodables, permettant la mobilité latérale, et une puissance fluviale relativement forte (pente et débit) (Leopold and Wolman, 1957; Ferguson, 1987; Knighton, 1998). La faible végétalisation du lit et des berges favoriserait l'occurrence des tresses en réduisant la cohésion des bancs et le dépôt de fines, et permettant au chenal de s'élargir et de migrer latéralement. Cette absence ou faible densité de végétation peut être liée aux conditions climatiques ou à la fréquence de remobilisation du lit par les crues par rapport au taux de croissance de la végétation (Paola, 2001; Hicks et al., 2008). Paola (2001) a défini cette temporalité par T^*, un indice sans dimension défini par $T^* = T_{veg}E/B$, où T_{veg} est le temps nécessaire à la colonisation et à la croissance de la végétation vers un stade mature résistant à l'érosion, E est le taux annuel moyen d'érosion latérale du lit actif et B est la largeur du lit actif. $T^* < 1$ indique un taux de croissance élevé par rapport à la migration du chenal, $T^* > 1$ indique une migration rapide du chenal par rapport à la croissance de la végétation. Des travaux conduits en canal expérimental ont aussi clairement montré que l'extension de la végétation au sein d'un lit en tresses favorise une métamorphose fluviale, le style en tresses cédant place à un lit à chenal unique (Tal et al., 2004; Tal and Paola, 2010).

1.3. Etat des rivières en tresses en France

Dans le bassin du Rhône, le style en tresses a connu une phase d'extension à partir du 14ème siècle jusqu'à la fin du 18ème siècle (Bravard, 1989, 2000). Durant cette période, le tressage est favorisé par la dégradation anthropique du couvert végétal amplifiant la production sédimentaire au cours des 17ème et 18ème siècles dans un contexte climatique favorable (Petit Âge Glaciaire).

A partir du début du 20ème siècle, ce style fluvial enregistre un recul dans les Alpes françaises. Un recensement des rivières en tresses dans ce secteur a mis en évidence une disparition de 53 % du linéaire des tronçons tressés (i.e. 559 km) au cours du dernier siècle (Piégay et al., 2009). Les rivières les plus affectées sont les grandes rivières (Isère, Rhône, Durance, Arve, Verdon et Var) et celles localisées dans les Alpes du Nord (Fig. 4). L'endiguement, les aménagements hydro-électriques et les extractions de graviers sont considérés comme étant les principales causes de ces évolutions.

L'étude de la dynamique latérale d'une cinquantaine de tronçons en tresses du bassin du Rhône (Belletti et al., 2013b) et de la trajectoire géomorphologique de trente d'entre eux (Liébault et al., 2013a) a mis en évidence un rétrécissement et une incision de la bande active pour respectivement 80 et 56% des tronçons au cours du 20ème siècle. L'incision est associée à la présence de sites d'extraction de graviers alors que les sections en exhaussement présentent une recharge sédimentaire plus importante en provenance des berges et de torrents actifs. Un gradient Alpes du Nord/Alpes du Sud a été observé avec une incision généralisée et un rétrécissement plus important pour les Alpes du Nord. Dans les Alpes du Sud, un gradient est/ouest est observé avec les tronçons les plus actifs et en exhaussement à l'est.

Ces études régionales font suite à de nombreuses études de cas montrant cette incision et cette rétraction des rivières en tresses françaises depuis le 19ème siècle : sur l'Eygues (Kondolf et al., 2007), sur des rivières du bassin de la Drôme, du Roubion et de l'Eygues (Liébault and Piégay, 2002) ou encore sur les grandes rivières (Isère, Rhône, Durance, Arve, Drôme et Var) (Bravard and Peiry, 1993).

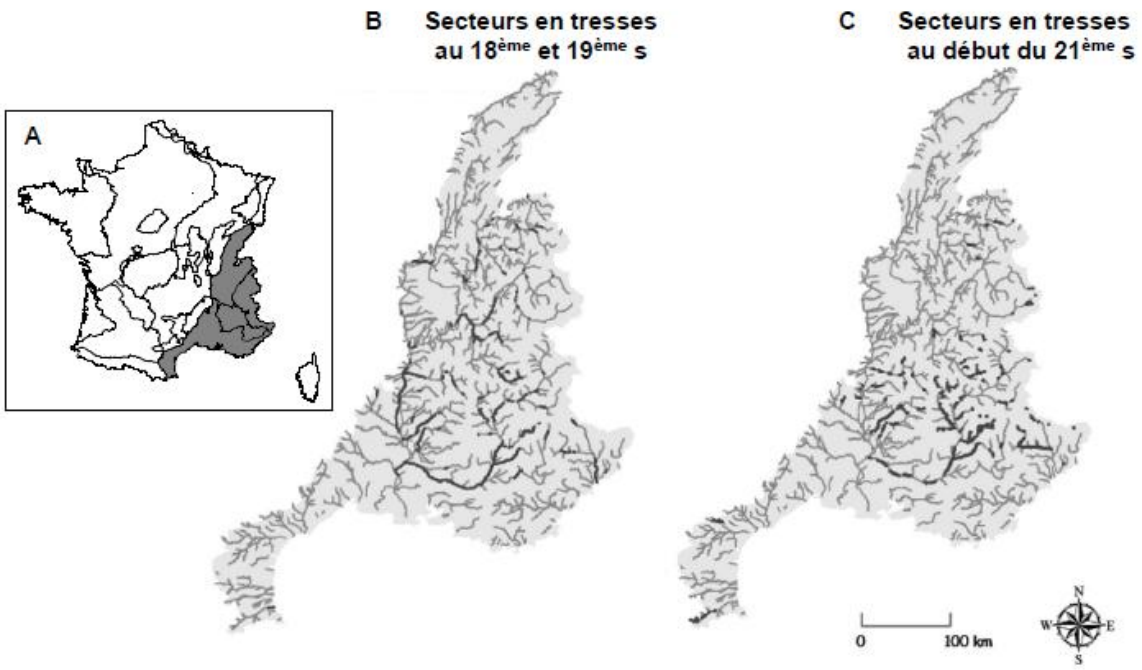

Fig. 4. A) Localisation du district Rhône-Méditerranée en France (excepté les parties basses et ouest du bassin de la Saône) ; Recensement des rivières en tresse en noir du district Rhône-Méditerranée au 18ème et milieu du 19ème siècle (B) et au début du 21ème siècle (C) (modifié d'après Piégay et al., 2009).

Cette tendance à la disparition du tressage a aussi été largement observée dans les Alpes italiennes (Surian and Rinaldi, 2003). Des études récentes ont cependant montré une tendance à l'élargissement de certaines rivières en tresses italiennes depuis la fin des années 1990 (Surian and Rinaldi, 2003; Surian, 2009; Surian et al., 2009b; Comiti et al., 2011; Ziliani and Surian, 2012, Fig. 5). Cette tendance récente est attribuée à l'interruption des extractions de graviers depuis la fin des années 1970. Cet élargissement a aussi été localement observé sur les rivières en tresses françaises (Piégay et al., 2009; Belletti et al., 2013b). Belleti et al. (2013b) ont montré que ce phénomène était lié à des crues récentes dans un contexte régional favorable en termes d'apport sédimentaire.

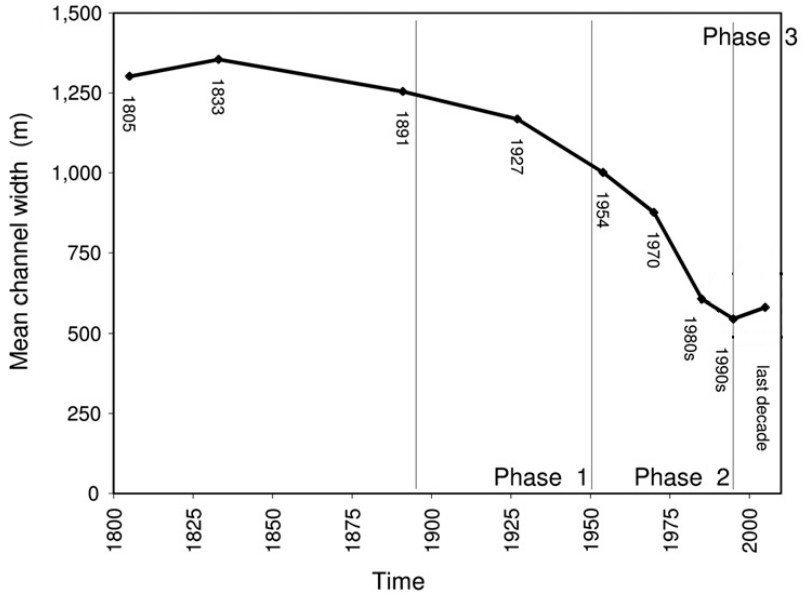

Fig. 5. Evolution de la largeur de la bande active du Tagliamento (Italie) durant les deux derniers siècles; la phase 1 correspond à 33% de rétrécissement de la bande active, la phase 2 à 56% avec un taux de 6-18 m/an et la phase 3 à un processus modéré d'élargissement (4 m/an) (modifié d'après Ziliani and Surian, 2012).

2. Morphologie des rivières en tresses

2.1. Morphologie générale des rivières en tresses

Le paysage d'une rivière en tresses se compose de différentes unités morphologiques, remaniées à des échelles de temps différentes par des crues d'intensité variable. Ces unités se distinguent par le taux de recouvrement et le stade de développement du couvert végétal, la granulométrie, la fréquence d'inondation et la stabilité de la surface (Reinfelds and Nanson, 1993; Haschenburger and Cowie, 2009).

La bande active correspond aux chenaux en eau et aux bancs de graviers non végétalisés (Fig. 6A). Ces surfaces sont généralement remaniées par des crues annuelles ou biannuelles. Récemment, des expériences en laboratoire ont montré que le transport solide ne s'effectuait pas dans tous les chenaux en eau, différenciant les chenaux actifs des chenaux inactifs (Bertoldi et al., 2009b; Ashmore et al., 2011). La bande fluviale inclut la bande active et les îles végétalisées, c'est-à-dire les patchs de végétation entourés par des bancs de graviers ou des chenaux en eau. Le corridor naturel intègre la bande fluviale et les peuplements spontanés riverains (Piégay et al., 2009). Le corridor naturel se compose de niveaux topographiques variés et de peuplements végétaux ayant atteint des stades de développement différents (végétation pionnière à mature).

Le profil en travers des rivières en tresses est caractérisé par un ratio largeur sur profondeur élevé, typiquement supérieur à 20 (Fig. 6B). Pour un tronçon donné, les chenaux en eau observés au sein de la bande active diffèrent en termes de pente, de profondeur d'eau et d'altitude relative.

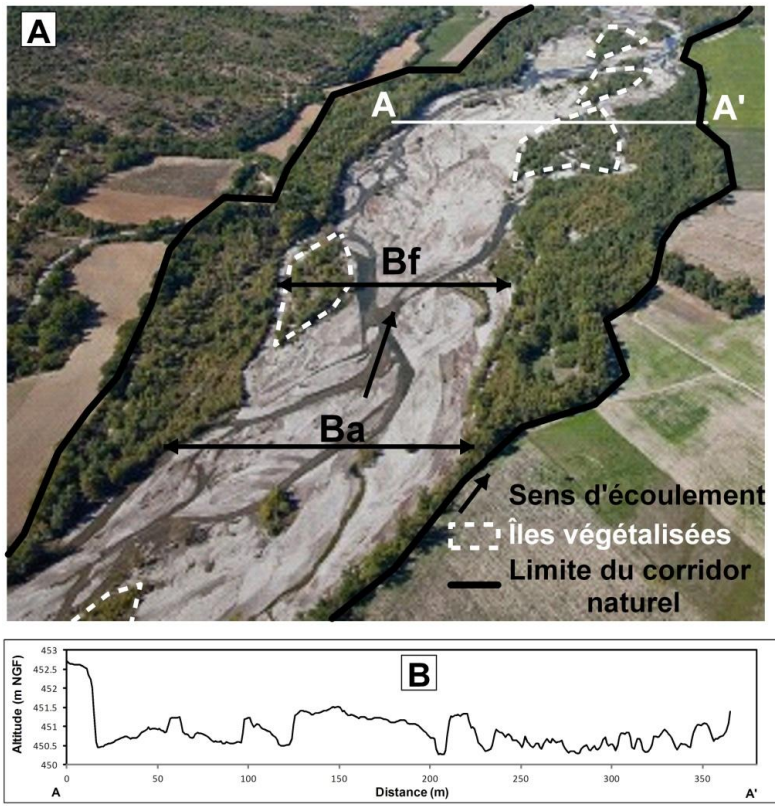

Fig. 6. Photographie illustrant les unités morphologiques caractéristiques d'une rivière en tresses (A) ; Ba : bande active ; Bf : bande fluviale ; AA' situation de la section en travers correspondant au profil en travers de la figure 6B (exemple de la Bléone, Source : www.photographeAerien.com pour Agence de l'eau Rhône Méditerranée et Corse).

2.2. Les bancs alluviaux

Les premiers travaux sur la morphologie des rivières en tresses définissent les bancs comme les formes sédimentaires élémentaires des rivières en tresses (Krigström, 1962; Smith, 1974; Church and Jones, 1982). Plusieurs auteurs ont mis en évidence l'existence de nappes de charriage ("gravel sheet" ; Whiting et al., 1988; Ashmore, 1991b), qui correspondent à une zone de dépôt alluvionnaire résultant d'un événement hydrologique. Elles sont composées de graviers ou de sables, d'une épaisseur de quelques diamètres de grain, les limites peuvent être définies par une rupture de pente nette et des changements visibles de granulométrie ou par un front diffus superposé à la couche sous-jacente ("diffuse gravel sheet" ; Whiting et al., 1988). Les bancs unitaires (Fig. 7), qui sont composés d'une ou plusieurs nappes de charriage peuvent être médians, longitudinaux, transversaux, diagonaux ou latéraux (« point-bars ») en fonction principalement de

leur forme et de leur localisation dans le chenal (Church and Jones, 1982; Fig. 8). Ces formes de bancs simples peuvent coexister côte à côte dans des bancs complexes, pouvant avoir un noyau végétalisé. Ces bancs composites reflètent la complexité des processus sédimentaires (érosion et dépôt) qui sont à l'origine du motif de tressage. Cette classification hiérarchique des bancs a aussi récemment été mise en évidence dans des études in situ sur la formation et l'évolution des bancs de rivières au style divaguant (Rice et al., 2009; Ham and Church, 2012).

Fig. 7. Exemple de bancs unitaires sur la rivière du Bès (Alpes de Haute-Provence, France).

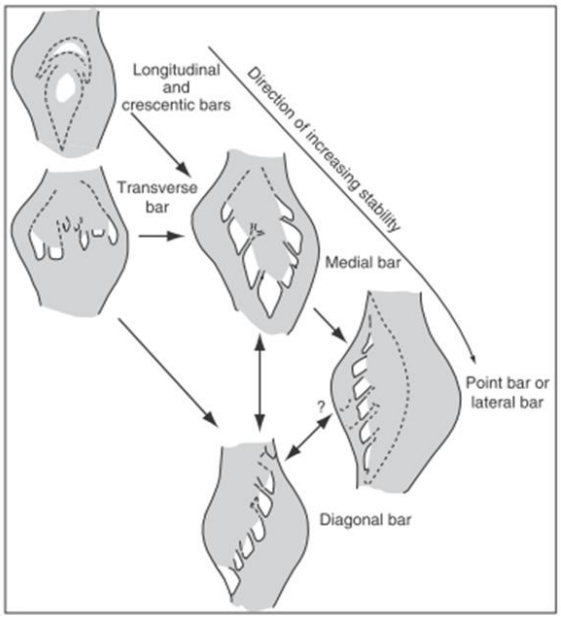

Fig. 8. Schéma illustrant la typologie des bancs d'une rivière en tresses et leurs principales évolutions, d'après Church et Jones (1982) modifié par Buffington et Montgomery (2013).

2.3. Unité confluence – bifurcation

L'unité confluence-banc/bifurcation est aussi définie comme un élément morphologique élémentaire des rivières en tresses. La zone de confluence contrôle la direction et l'abondance du flux sédimentaire dans le réseau de chenaux en aval et *in fine* le processus de sédimentation des bancs. Les confluences sont des zones de transfert entre les sites d'érosion amont et les sites de dépôt aval. Certaines études ont montré une analogie entre l'unité confluence-banc/bifurcation et l'unité seuil-mouille des rivières à chenal unique. Un lien statistique a été établi entre la longueur d'onde de l'unité seuil-mouille et la longueur d'onde de l'unité confluence/bifurcation (Ashmore, 2001; Bertoldi and Tubino, 2007; Hundey and Ashmore, 2009). La longueur de l'unité confluence-bifurcation est approximativement 4-5 fois la largeur du chenal actif (Ashworth, 1996; Hundey and Ashmore, 2009).

2.4. Le réseau de tressage

Certains auteurs ont proposé des classifications hiérarchiques simples fondées sur l'ordination des chenaux et bancs (Williams and Rust, 1969; Jackson, 1975; Bristow, 1987; Bridge, 1993 ; Figure 9A à C).Williams and Rust (1969, Fig. 9A) différencient trois niveaux de chenaux et de bancs, avec un premier niveau qui correspond aux principaux chenaux qui s'écoulent autour des bancs d'ordre 1. Les deuxième et troisième niveaux correspondent à la dissection du banc d'ordre 1. Pour Bristow (1987, Fig. 9B), l'ordre des bancs se réfère à l'ordre des chenaux qui les entourent. Bridge (1993, Fig. 9C) simplifie cette hiérarchisation en définissant les bancs principaux et les chenaux adjacents par l'ordre 1 et les chenaux incisant ces bancs par l'ordre 2. Church et Jones (1982) proposent une hiérarchisation fondée sur le comptage des jonctions de chenaux et des bancs pour un nombre de chenaux fondamentaux définis par une longueur d'onde donnée (Fig. 9D). Ces classifications ont été critiquées car elles sont dépendantes du débit (Jackson, 1978; Smith, 1978; Bridge, 1993 in Ham and Church, 2012).

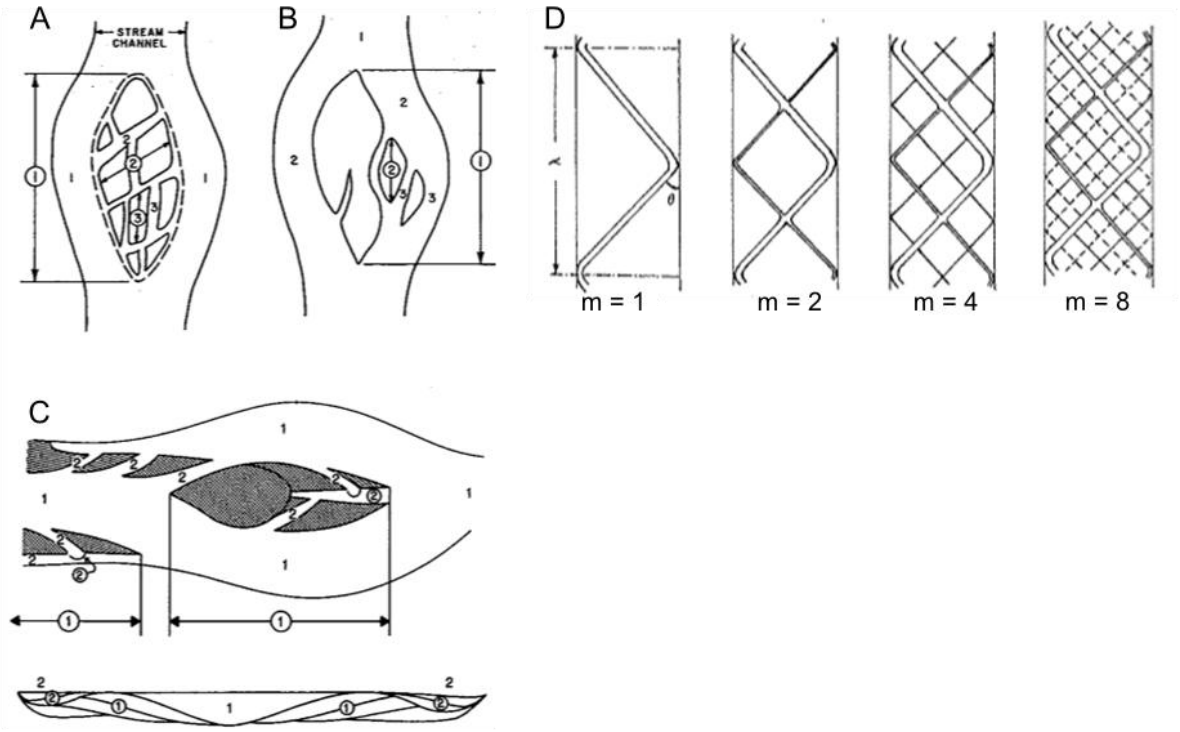

Fig. 9. Classification hiérarchique des bancs selon A) Williams et Rust (1969), B) Bristow (1987) et C) Bridge (1993) d'après Bridge (1993) ; D) Classification hiérarchique des subdivisions d'une rivière en tresses, m représente le nombre de chenaux fondamentaux de longueur d'onde λ, d'après Church and Jones(1982).

2.5. Indicateurs morphologiques

2.5.1. Indicateurs de la morphologie en plan

Le degré de tressage est reconnu comme une propriété morphologique de base des rivières en tresses et son calcul a fait l'objet de nombreux indices. Egozi et Ashmore (2008) ont recensé l'ensemble de ces indices et effectué une étude comparative. Ces indices peuvent se différencier en 3 catégories selon l'objet pris en compte et le mode de calcul : les indices fondés sur la dimension et la fréquence des bancs (Brice, 1964; Germanoski and Schumm, 1993), sur la longueur totale des chenaux pour une longueur de rivière donnée, équivalent à des indices de sinuosité totale (Hong and Davies, 1979; Mosley, 1981) ou encore sur le nombre de chenaux (Howard et al., 1970). La comparaison de ces indices en canal expérimental a montré que ceux fondés sur la dimension et la fréquence des bancs et ceux mesurant la sinuosité totale sont corrélés mais indépendants des indices dénombrant les chenaux. L'ensemble de ces indices est sensible aux valeurs de débit pendant la mesure avec une sensibilité plus faible pour les indices fondés sur le comptage des chenaux. Ces indices doivent être mesurés sur une longueur équivalente à 10 fois

la largeur du lit mouillé à débit morphogène (~ 2/3 fois la longueur caractéristique du tressage définie par Ashmore, 2001, cf. § 2.3) et considérer au moins 10 sections en travers espacées au minimum d'une largeur de lit mouillé à débit morphogène pour les indices dénombrant le nombre de chenaux. Egozi et Ashmore (2008) conseillent d'utiliser les indices dénombrant les chenaux car ils sont facilement mesurables et moins sensibles à la sinuosité, à l'orientation du chenal et aux débits.

D'autres indicateurs plus généraux sont intéressants pour l'étude de la morphologie en plan des rivières en tresses comme la largeur de la bande active ou de la bande fluviale, et le ratio entre les deux, qui mesure le taux de végétalisation du lit en tresses. Une relation entre la largeur de la bande active et la taille du bassin versant a été mise en évidence sur différents échantillons de rivières en tresses des Alpes françaises (Equation 1, Piégay et al., 2009). Ainsi la normalisation de largeur active par la taille du bassin versant permet une comparaison inter-site. La bande active normalisée (W^*, équation 2) est un bon indicateur de la contribution sédimentaire du bassin à la rivière (Belletti et al., 2013b; Liébault et al., 2013a).

$$W = 8.05\ CA^{0.44} \quad (1)$$

$$W^* = W\ CA^{0.44} \quad (2)$$

avec W, la largeur de la bande active, CA, la superficie du bassin versant et W^*, la bande active normalisée; selon Piégay et al. (2009) sur un échantillon de 49 tronçons en tresses des Alpes françaises.

Plus récemment, des auteurs se sont intéressés à la mesure de la largeur des chenaux actifs, c'est-à-dire ceux où le transport solide s'effectue, comme indicateur de la dynamique de la rivière en tresses (Ashmore et al., 2011). En effet, un lien a été mis en évidence entre la largeur des chenaux actifs et le taux de tressage.

Des indices sur le nombre de nœuds par unité de surface (Bertoldi et al., 2009b) ou leur espacement (Ashworth, 1996; Bertoldi and Tubino, 2005; Hundey and Ashmore, 2009) ont récemment été proposés. Bertoldi et al (2009b) ont mis en évidence un lien entre le nombre de nœuds par unité de surface et la largeur de la bande active.

2.5.2. Indicateurs morphologiques s'appuyant sur le profil en travers

Si la planimétrie a permis de proposer différents indices, les mesures effectuées sur une section en travers ont été peu exploitées. Un indice de variabilité altimétrique du profil en travers (Bed Relief Index, *BRI*) a été développé en 1970 par Smith pour mettre en évidence la différence de relief entre les sections dominées par les bancs longitudinaux, *BRI* plus fort, de celles dominées par les bancs transversaux, *BRI* plus faible. Il exprime la somme des changements altitudinaux le long du profil en travers rapportée à sa longueur (Equation 3). Cet indice a été repris par Germanoski and Schumm (1993) pour comparer la micro-morphologie des profils en travers d'une rivière en tresses en canal expérimental soumis à un excès ou un déficit de sédiment.

$$BRI\,(Smith) = \frac{2[(Z_1 + \ldots Z_n) - (z_1 + \ldots z_n)] \pm z_{e1}, z_{e2}}{L} 100 \qquad 3$$

avec (Z_1+…Z_n), la somme des altitudes des points hauts du transect, (z_1+…z_n), la somme des altitudes des points bas du transect, L, la longueur du transect et z_{e1} et z_{e2}, l'altitude des 2 points d'extrémité du transect.

Un second *BRI* a été développé par Hoey and Sutherland (1991) pour explorer le lien entre le régime sédimentaire et le relief des profils en travers des rivières en tresses en canal expérimental. Cet indice est une mesure dimensionnelle de l'écart-type des altitudes du profil en travers (Equation 4).

$$BRI(Hoey) = \left(\sum_{i=1}^{n-1} \left[(z_i^2 + z_{i+1}^2)/2 \right]^{0.5} \left[x_{i+1} - x_i \right] \right) \Big/ (x_n - x_1) \qquad 4$$

avec n, le nombre de point du transect, z_i, la différence entre l'altitude du point i et l'altitude moyenne du transect et x_i, la distance du point i.

Plus récemment, Liébault et al (2013a) ont proposé un *BRI* adimensionnel (*BRI**) basé sur la formule du *BRI* développée par Hoey and Sutherland (1991). Cet indice correspond à l'écart-type des altitudes du profil en travers par rapport à l'altitude moyenne divisé par la longueur du profil en travers mesurée entre les pieds de berge de la bande active :

$$BRI^* = \left(\frac{1}{n}\sum_{i=1}^{n} (z_i - Z)^2\right)^{0.5} / (x_n - x_i) \qquad 5$$

avec *n*, le nombre de point du transect, z_i, l'altitude du point *i*, *Z*, l'altitude moyenne du transect et x_i, la distance du point *i*.

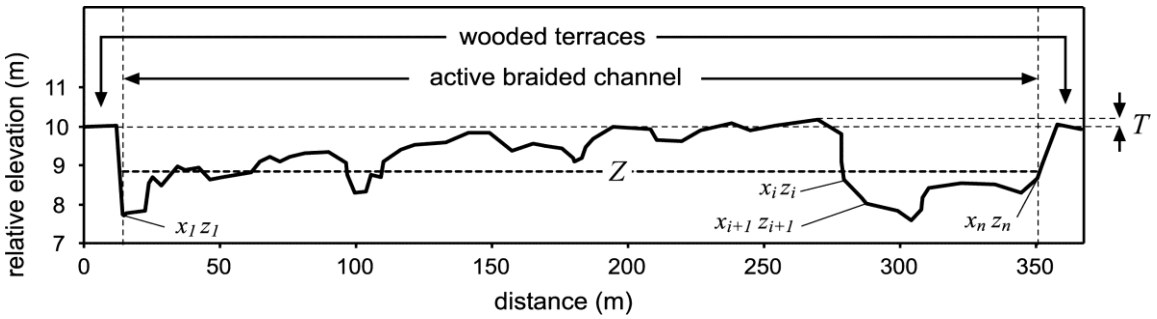

Fig. 10. Schéma d'un profil en travers montrant le calcul du *BRI** (Liébault et al., 2013a).

2.6. Facteurs externes influençant le tressage

In situ, Belletti et al. (2013b) ont montré un lien très complexe entre l'indice de tressage, la périodicité des crues, le régime sédimentaire et la nappe phréatique. L'indice de tressage notamment ne dépend pas uniquement du débit solide et/ou du débit liquide mais aussi de la relation qu'il y a entre la nappe et les eaux superficielles. Même en conditions d'étiage, une rivière peut ainsi avoir un taux de tressage marqué.

2.6.1. Le régime hydrologique

L'impact du régime hydrologique sur la morphologie des rivières en tresses a été observé in situ par les nombreuses études sur les changements morphologiques à long terme des rivières en tresses françaises ou italiennes, où par exemple la diminution du débit à l'aval d'un barrage est un des facteurs mis en évidence dans la disparition du style en tresses par une forte rétraction de la bande active (Piégay et al., 2006; Piégay et al., 2009). La réduction des pics de crues facilite l'établissement de la végétation sur les bancs. Par exemple, une diminution de 66% de la bande active de la Durance a été observée en 1986, soit 30 ans après la construction du barrage de Serre-Ponçon (Piégay et al., 2009). Les changements morphologiques observés suite à la modification du régime hydrologique liée à l'implantation de barrage sont aussi lié à l'interruption du transit sédimentaire par celui-ci.

Plusieurs travaux ont aussi mis en évidence un lien entre la largeur de la bande active et l'occurrence de la dernière crue de période de retour 10 ans (Comiti et al., 2011; Belletti et al., 2013b, 2014). Les crues de période de retour de 10 ans provoquent une érosion des berges et des

îles et par conséquence une augmentation de la bande active. La revégétalisation post-crue de ces surfaces est complexe et dépend de l'occurrence de période optimale pour la germination (Hervouet et al., 2011).

2.6.2.Le régime sédimentaire

L'impact du régime sédimentaire sur la morphologie en plan des rivières en tresses a été étudié par de nombreux auteurs en canal expérimental en faisant varier l'apport solide en entrée (Ashmore, 1991a; Hoey and Sutherland, 1991; Germanoski and Schumm, 1993). Ces études ont globalement mis en évidence une augmentation du nombre de bancs, de l'indice de tressage et de la largeur de la bande active en régime sédimentaire excédentaire et des tendances inverses en régime déficitaire. Les rivières en exhaussement montrent aussi des largeurs normalisées (W^*) plus fortes que les rivières en incision (Liébault et al., 2013a). Les rivières en surlargeur (valeur de W^* forte) indiquent plutôt des conditions limitées en capacité de transport (transport-limited conditions), alors que les rivières en souslargeur (W^* faible) indiquent plutôt des conditions limitées en fourniture sédimentaire (supply-limited conditions).

Concernant l'impact du régime sédimentaire sur la morphologie en travers, les conclusions des expérimentations de laboratoire divergent. Hoey et Sutherland (1991) ont observé des valeurs de *BRI* faibles pour le régime en excès et des valeurs plus élevés pour le régime en déficit, en raison de l'incision du chenal principal dans les bancs. Germanoski et Schumm (1993) ont observé des valeurs de *BRI* élevées pour le régime en excès sédimentaire, lié selon eux à la multiplication du nombre de bancs et donc à l'augmentation de la rugosité. Cette divergence d'observation peut être liée à la différence dans la façon de calculer le *BRI*, qui pour Hoey et Sutherland se base sur l'écart-type des altitudes par rapport à la moyenne alors que pour Germanoski et Schumm (1993), le calcul se base sur la somme des altitudes des points hauts et des points bas. Ainsi quand le nombre de bancs augmente, le nombre de points hauts et de points bas augmente aussi en conséquence et conduit à une valeur élevée du *BRI*. Récemment, toujours en canal expérimental, les résultats de Leduc (2013) rejoignent ceux de Hoey et Sutherland (1991). L'impact du régime sédimentaire sur la morphologie en travers des rivières en tresses a également été analysé in situ à partir d'un échantillon de rivières en tresses (Liébault et al., 2013a). Ces auteurs ont observé comme Hoey et Sutherland (1991) des valeurs élevées de *BRI* pour les rivières en incision et des valeurs plus faibles pour les rivières en exhaussement.

3. Dynamique des rivières en tresses

3.1. Genèse

Les mécanismes à l'origine de la formation d'un patron de tressage ont été largement étudiés en canal expérimental (Leopold and Wolman, 1957; Ashmore, 1991b; Ashworth, 1996) et plus sporadiquement sur le terrain (Leopold and Wolman, 1957; Wheaton et al., 2013) en raison de la difficulté de suivi in situ des processus de tressage. Ces processus ont récemment été synthétisés par Kleinhans et al. (2013).

L'initiation du tressage est causée par une accumulation locale de sédiment résultant souvent de l'immobilisation d'une nappe de charriage et de la perte d'énergie de l'écoulement (Ashmore, 1991b). Le tressage se réalise ensuite soit par diffluence de l'écoulement autour des bancs soit par érosion de ces bancs. Les principaux mécanismes observés sont recensés dans le tableau 1 et illustrés par la Fig. 11. Les 4 principaux sont le dépôt d'un banc central, la conversion d'un banc transversal, la coupure d'un banc ponctuel et la dissection multiple d'un banc. Le maintien du tressage s'effectue par la répétition d'un ou plusieurs de ces mécanismes (Ashmore, 1991b) ou par « l'anastomose secondaire » (Church, 1972), c'est-à-dire la réoccupation de chenaux qui ont été abandonnés (Krigström, 1962; Ferguson and Werrity, 1983; Carson, 1984b, a).

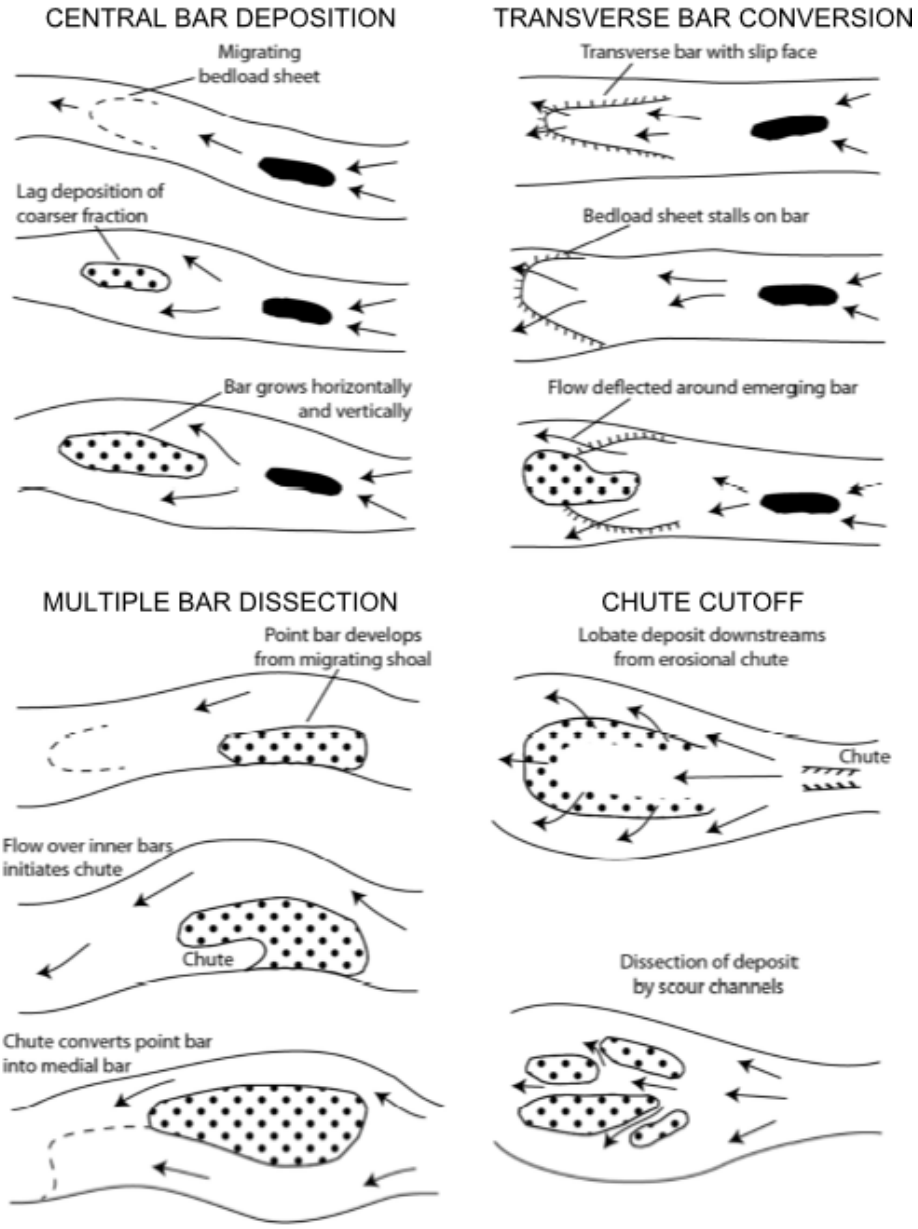

Fig. 11. Les 4 principaux mécanismes de développement du tressage (Leopold et Wolman, 1957 ; Ashmore, 1991a ; Ferguson, 1993). Schéma d'après Belletti (2012).

Table 1. Principaux mécanismes de formation du tressage.

Processus	Mécanismes	Références
Dépôt	**Dépôt d'un banc central** (Central bar deposition) Dépôt successif de nappes de charriage au milieu du chenal construisant un banc central par accrétion latérale et régressive. A partir d'une certaine hauteur de banc, les écoulements sont déviés de part et d'autre, provoquant des érosions de berge. Contrainte de cisaillement proche du seuil de mise en mouvement.	Leopold and Wolman (1957); Ashmore (1991a)
	Conversion d'un banc transversal (transverse bar conversion/lobe deposition) Création d'un banc transversal à l'aval d'une zone d'affouillement de confluence. Banc avec une face pentue d'avalanche. Des nappes de charriage sont stoppées sur ce banc et contribuent à l'accrétion verticale. Les écoulements sont déviés de part et d'autre d'un lobe central élevé, formant des zones d'affouillement. Contrainte de cisaillement très supérieure au seuil de mise en mouvement. La forme du banc a plus de relief en comparaison avec le mécanisme de barre centrale.	Leopold and Wolman (1957); Krigström (1962) ; Church and Jones (1982) ; Ashmore (1991a) ; Goff and Ashmore (1994) ; Ashworth (1996)
Erosion	**Coupure d'un banc ponctuel** (chute cut-off) Processus alternatif le plus communément décrit en rivière à gravier et en laboratoire sur fonds sableux. Erosion régressive à travers un banc alterné ou ponctuel pour suivre une route plus directe, capturant progressivement une part d'écoulement plus importante. Le banc se transforme en banc médian. Souvent généré par une diminution locale de la profondeur du à l'arrivée d'une nappe de charriage.	Ashmore (1991a); [Friedkin, 1945 ; Kinoshita, 1957 ; Krigström (1962); Hickin (1969); Ikeda (1973); Hong and Davies (1979) Ashmore, 1982; Fergusson and Werrity (1983); Bridge 1985; Lewin 1976; Carson 1986] in Ashmore (1991a); Rundle (1985b); Germanoski and Schumm (1993)
	Dissection multiple d'un banc (multiple dissection/lobe dissection) Rapport largeur / profondeur élevé Ecoulement concentré dans de multiples chutes qui forment un banc lobé à leur aval : déviation de l'écoulement Mécanisme caractéristique dans les rivières de Nouvelle Zélande.	Rundle (1985a, b); Ashmore (1991a)
	Dissection des bancs pendant la décrue (deux phases de débits)	Rundle (1985a, b)

3.2. A l’échelle d’une crue

Le nombre de chenaux augmente avec l'augmentation du débit jusqu'à ce que l'eau recouvre les bancs émergés réduisant le nombre de chenaux (Luchi et al., 2007; Bertoldi et al., 2009a; Welber et al., 2012). Les changements morphologiques sont corrélés positivement à la hauteur d'eau (Bertoldi et al., 2009a; Bertoldi et al., 2010, Fig. 12). Une corrélation positive a aussi été montrée entre la largeur totale des chenaux actifs et le débit (Bertoldi et al., 2010; Ashmore et al., 2011). Des changements morphologiques ont été observés pour des débits très faibles, inférieurs au débit de plein bord (Bertoldi et al., 2009a; Surian et al., 2009a; Bertoldi et al., 2010). Sur le Tagliamento (Italie), une différence majeure a été mise en évidence par Bertoldi et al. (2010) pour les débits inférieurs au débit de plein bord, définis comme "flow pulse" par Tockner et al. (2000) et les débits supérieurs au débit de plein bord ("flood pulse", Junk et al., 1989). Pour les débits inférieurs au débit de plein bord ("flow pulse"), les changements morphologiques sont limités aux chenaux principaux et correspondent à des changements mineurs résultant de l’érosion de berge à l'apex des sinuosités et pouvant être associés à l'évolution d'un chenal unique de type méandriforme. Ces changements à l'échelle des chenaux actifs sont généralement observés à court terme (Ashmore et al., 2011). Pour les débits supérieurs au débit de plein bord ("flood pulse"), un réarrangement du réseau de tressage est observé avec une évolution des bifurcations causant des changements brusques de la position des chenaux, appelées avulsions. Les unités morphologiques (nœuds, bancs, chenaux) ne sont plus reconnaissables après ce type d'événement (Bertoldi et al., 2010).

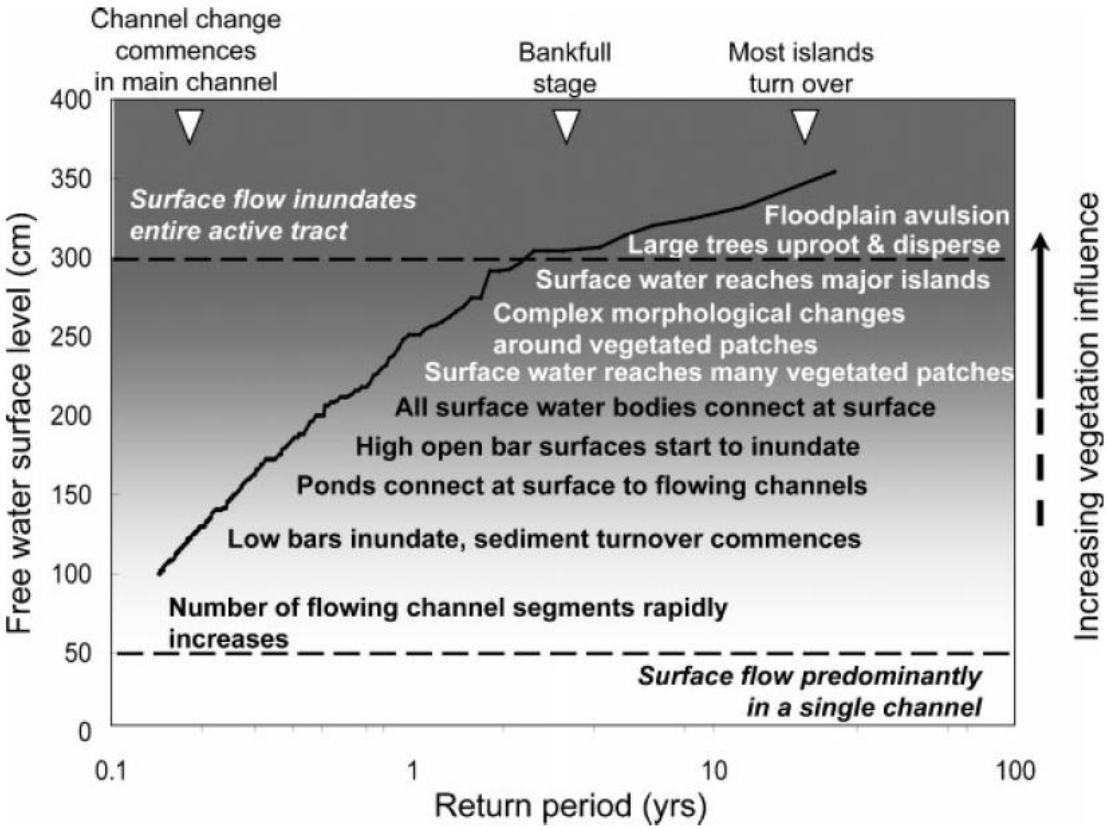

Fig. 12. Relation entre les crues, la hauteur d'eau et les changements morphologiques observés sur la rivière Tagliamento (Italie) (Bertoldi et al., 2009a).

Différents processus morphologiques ont été mis en évidence à partir d'observations lors de crues (Goff and Ashmore, 1994; Milan et al., 2007; Hicks et al., 2008; Wheaton et al., 2013). Sur la rivière Waimakariri (Nouvelle-Zélande), les auteurs observent une migration latérale des chenaux, une croissance des bancs, un creusement des confluences, des avulsions (nouveau réseau de chenaux et remplissage des chenaux pré-avulsion), un développement et une migration de nappes de charriage et de bancs, une incision locale de chenaux et un recoupement de bancs pendant la décrue (Hicks et al., 2008). Sur la rivière Feshie (Royaume Uni), Wheaton et al. (2013) ont mis en évidence que les 4 principaux mécanismes de formation du tressage (Cf. §3.1 et Fig. 11) représentent 61% des changements volumétriques totaux et que l'érosion de berge est un mécanisme secondaire important (17% des changements totaux). Sur la rivière pro-glaciaire Sunwapta (Canada), Goff et Ashmore (1994) ont observé que la destruction des bancs s'effectuait par redirection de l'écoulement ou par la progression aval des zones de confluence et la reconstruction des bancs s'effectuait par l'accrétion de bancs unitaires sur la tête, les côtés et la queue d'un banc et dans un cas par la dissection d'un large banc lobé unitaire.

3.3. A long terme

Les principaux changements enregistrés à long terme par les rivières en tresses à la suite d'une modification durable des facteurs de contrôle sont typiquement :

1) La rétraction et l'incision de la bande active avec une baisse systématique de l'intensité de tressage, le plus souvent sous l'effet d'une réduction de la charge sédimentaire (Liébault and Piégay, 2002; Rinaldi, 2003; Surian and Rinaldi, 2003, 2004; Surian and Cisotto, 2007; Gurnell et al., 2009; Piégay et al., 2009; Surian et al., 2009b; Comiti et al., 2011; Ziliani and Surian, 2012; Bollati et al., 2014). L'incision du chenal principal entraîne la formation de bancs perchés, ce qui favorise le développement de la végétation dans la plaine alluviale et augmente la résistance de ces surfaces à l'érosion. Les surfaces les moins actives sont en effet communément colonisées par la végétation, pouvant faire évoluer le style en tresses vers un style à chenal unique de type divagant ou à méandres (Fig. 13A) (Cf. table 2 de Gurnell et al. 2009 recensant différents exemples européens).

2) L'élargissement et l'exhaussement de la bande active avec une augmentation de l'intensité de tressage et une forte tendance à l'avulsion liés à des apports sédimentaires excédentaires (Ashworth et al., 2004). Des cas d'apparition du tressage ont été décrits suite à une augmentation des apports sédimentaires due à une exploitation minière (Pickup and Higgins, 1979), ou suite à une éruption volcanique (Gran and Montgomery, 2005; Pierson et al., 2009).

Des modèles conceptuels d'évolution à long terme des rivières en tresses ont été développés à partir de l'observation de l'évolution des rivières en tresses italiennes (Surian and Rinaldi, 2003, 2004; Bollati et al., 2014, Fig. 13A-B) et françaises (Liébault et al., 2013a; Fig. 13C). Liébault et al. (2013a) décrivent le cycle de dégradation/restauration des rivières en tresses en fonction du *BRI** et la différence d'altitude entre les terrasses arborées et la bande active (*T*, cf. Fig. 10). Une rivière en tresses exhaussée présente un faible *BRI** avec une bande active qui se situe altimétriquement au même niveau que la terrasse. Lorsque la dégradation commence, le *BRI** augmente et la bande active s'enfonce en dessous du niveau des terrasses (flèche 1 de la Fig. 13C). Ce processus est ensuite accentué (flèche 2). Le cycle de restauration commence par la diminution du *BRI** mais la bande active est toujours fortement encaissée dans les terrasses (flèche 3). L'exhaussement de la bande active se manifeste ensuite avec une diminution de l'encaissement (flèches 4 et 5). Bollati et al. (2014) mettent en évidence sur la rivière Trebbia une plus légère incision après une première phase d'incision et de rétraction de la bande active, qui est alors associée à un début d'élargissement de la bande active (Etat III de la Fig. 13B). La phase suivante se caractérise alors par l'exhaussement et l'élargissement de la bande active (Etat IV).

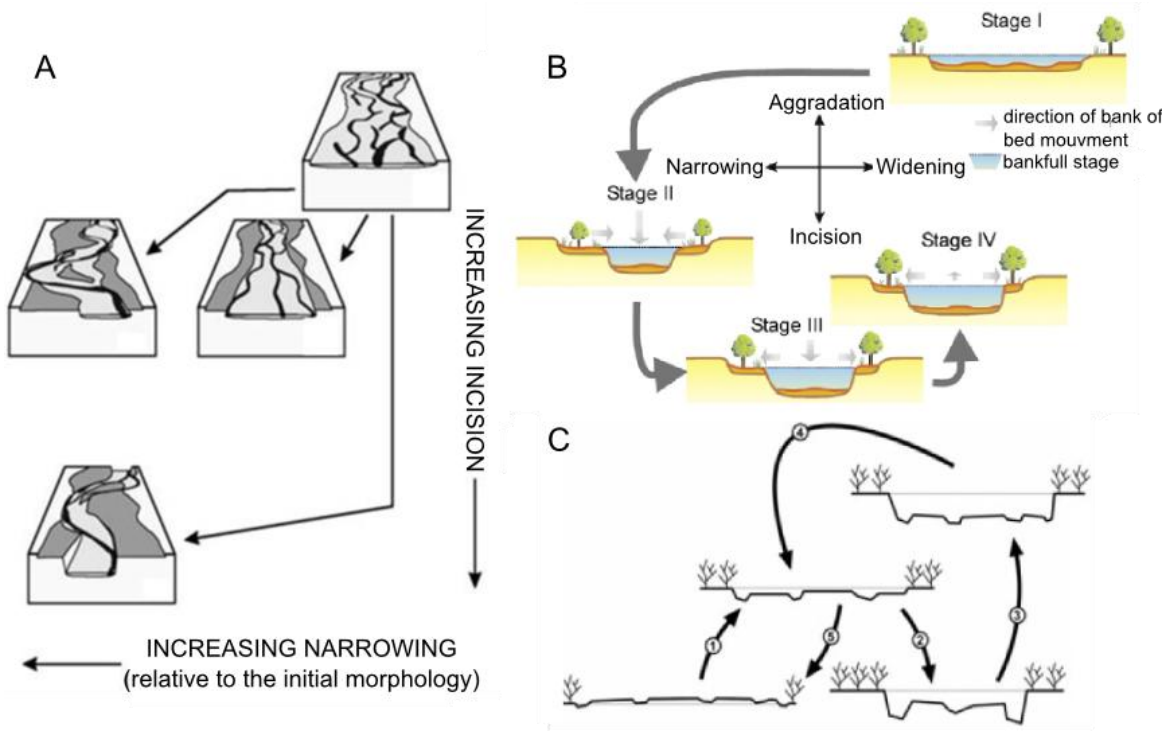

Fig. 13. Modèle conceptuel d'évolution des rivières en tresses : A) Rivières italiennes (modifié d'après Surian and Rinaldi, 2003); B) Lower Trebbia (Bollati et al., 2014); C) Rivières des Alpes françaises (Liébault et al., 2013a)

A long terme, il en découle une mosaïque complexe d'unités morphologiques correspondant à des stades de développements différents. Reinfelds and Nanson (1993) et Haschenburger and Cowie (2009) ont décrit précisément les différents stades des unités morphologiques pour les rivières Waimakariri et Ngarururoro, deux rivières en tresses de Nouvelle Zélande (Fig. 14). Ces stades diffèrent en termes de fréquence d'inondation, d'extension, d'épaisseur de dépôts de sédiments fins, de couvert végétal (strate dominante et taux de recouvrement), et de temps de stabilité (de 5 à plus de 60 ans).

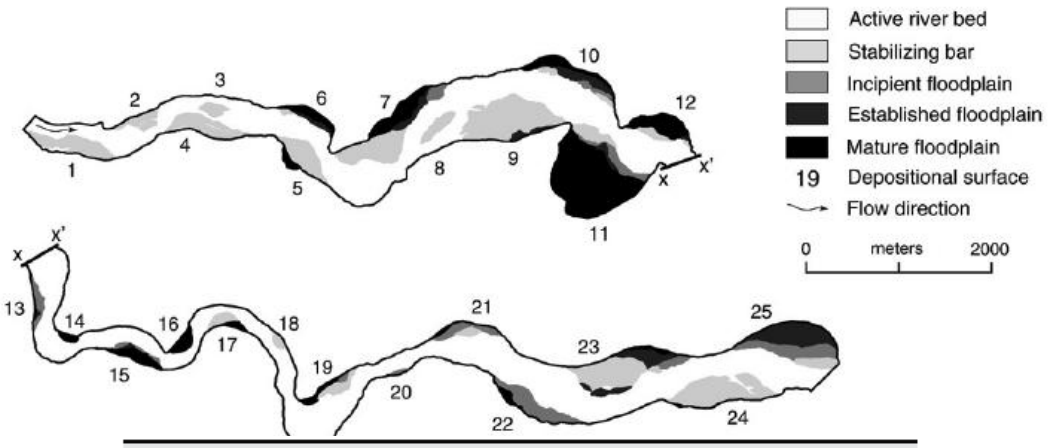

Stage	Inundating discharge[a]	Extent (E) and depth (d) of accreted fines	Vegetation and coverage (C)	Surface stability (t)
Active river bed	<0.3	$E \Rightarrow 0\%$ $d<2$ cm	Herbaceous plants; $C<15\%$	$t<5$ years
Stabilizing bar	0.3	$10<E<85\%$; Infill by fines but gravels and cobbles still exposed; $1<d<30$ cm	Herbaceous with some woody plants; $10<C<90\%$	$3<t<10$ years
Incipient floodplain	0.5	$E \Rightarrow 100\%$; no large clasts exposed; $10<d<40$ cm	Balanced mix between herbaceous and woody plants; $C \sim 100\%$	$10<t<35$ years
Established floodplain	0.9	$E \sim 100\%$ $35<d<110$ cm	Increased extent, age, and diversity of woody plants; $C \sim 100\%$	$20<t<60$[b] years
Mature floodplain	1.2	$E \sim 100\%$ $15<d<160$[c] cm	Increased extent, age, and diversity of woody plants; $C \sim 100\%$	$t>60$[b] years

[a] Discharge needed to first inundate given stage on mean basis divided by mean annual flood.
[b] Estimated using aerial photography record so underestimated.
[c] An underestimate. This stage contains a number of observations where the basal gravel layer was not reached but further digging was not possible.

Fig. 14. Différents stades de la plaine d'inondation de la rivière Ngaruroro (Nouvelle-Zélande) ; A) Cartographie ; B) Critères de description (Stade, débit d'inondation, extension et hauteur des accumulations de sédiments fins, type de végétation et taux de recouvrement, temps de stabilité) (d'après Haschenburger and Cowie, 2009).

4. Caractérisation de la morphologie des rivières en tresses

Les premiers travaux relatifs à la caractérisation de la morphologie des rivières en tresses étaient fondés sur l'analyse de photographies aériennes ou sur le suivi de profils en travers (Ashworth and Ferguson, 1986; Carson and Griffiths, 1989; Ferguson and Ashworth, 1992; Goff and Ashmore, 1994).

A partir du milieu des années 1990, le développement de nouvelles technologies de mesures topographiques, fondées sur des instruments terrestres (station totale, dGPS, LiDAR terrestre: Ligth Detection And Ranging), aéroportés (LiDAR aérien), bathymétriques ou encore sur des techniques de télédétection (photogrammétrie) a permis l'acquisition rapide de données topographiques à des résolutions spatiales de plus en plus fines et sur de grandes étendues géographiques (Fig. 15). Ces données permettent de réaliser facilement des Modèles Numériques de Terrain (MNT) de haute résolution. Les premiers MNT de rivières en tresses ont été produits à partir de photogrammétrie terrestre (Lane et al., 1994; Lane et al., 1995) ou aérienne (Westaway et al., 2000) couplées avec des mesures au tachéomètre pour les surfaces immergées, ou par dGPS (Brasington et al., 2000a). A la suite de ces premières études, un nombre considérable de travaux a été fondé sur des techniques variées comme la photogrammétrie à partir de photographies obliques (Chandler et al., 2002), les acquisitions par LiDAR aérien infrarouge (Charlton et al., 2003; Lane et al., 2003; Hicks et al., 2008; Höfle et al., 2009; Bertoldi et al., 2011; Legleiter, 2012; Moretto et al., 2012a), terrestre (Milan et al., 2007; Williams et al., 2011; Brasington et al., 2012), ou bathymétrique dont la longueur d'onde bleu-verte permet de pénétrer les surfaces en eau et de mesurer la bathymétrie (Kinzel et al., 2007; Bailly et al., 2010) et récemment la photogrammétrie par corrélation dense (SfM, Structure From Motion, Javernick et al., 2014).

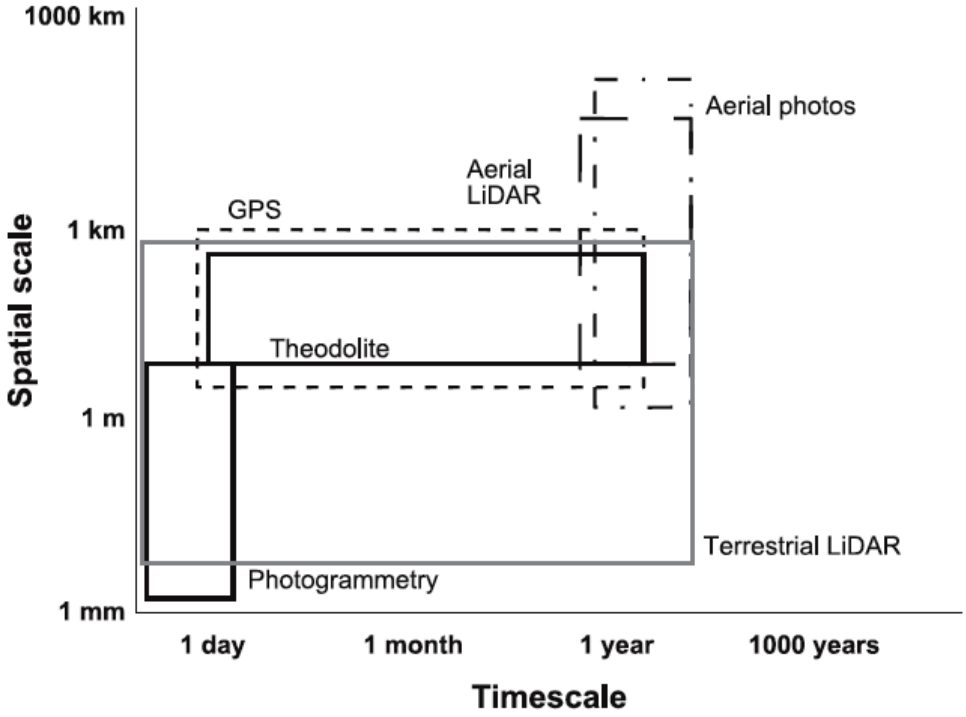

Fig. 15. Limite d'application temporelle et spatiale des technologies de levé (d'après Heritage and Hetherington, 2007).

De récentes études ont montré que les données de LiDAR aérien infrarouge présentaient de nombreux avantages par rapport aux autres technologies pour l'étude de la morphologie des tresses à l'échelle de 1 à plusieurs dizaines de km (Hicks et al., 2008). Le LiDAR permet notamment de mesurer la topographie sous la végétation et de fournir des informations sur l'occupation du sol (premier et dernier retour d'onde, et intensité du signal rétrodiffusé). Par rapport à la photogrammétrie, les levés LiDAR ne sont pas dépendants des conditions d'éclairement, nécessitent des points de contrôle limités et le coût au m² est plus faible (Hicks et al., 2008). Une des limites récurrentes du LiDAR infrarouge est l'incapacité de mesurer la topographie sous l'eau, comme le montre la synthèse d'Hicks et al. (2012).

Dans le cadre de l'étude des rivières en tresses, le LiDAR a majoritairement été utilisé pour l'étude des changements morphologiques. Une attention particulière a été dédiée à l'estimation de l'incertitude des données LiDAR (Lane et al., 2003; Hicks et al., 2008; Moretto et al., 2012a; Moretto et al., 2012b). La topographie des surfaces immergées est acquise à partir de la délimitation automatique des surfaces en eau (Höfle et al., 2009) et de la mesure des hauteurs d'eau à partir de la radiométrie de l'eau sur des photographies aériennes (Legleiter, 2012; Moretto et al., 2012a; Moretto et al., 2012b). Charlton et al. (2003) ont contrôlé la qualité des données LiDAR en les comparant à des levés topographiques au théodolite sur des profils en travers. D'autres études ont utilisé les données LiDAR pour estimer les érosions de berge (Surian and Cisotto, 2007), quantifier le taux d'incision du lit à partir des terrasses (Turitto et al., 2010), ou encore l'évolution altitudinale de profils en travers (Comiti et al., 2011).

Des études récentes explorent les données de LiDAR aérien pour caractériser la ripisylve (Hall et al., 2009; Johansen et al., 2010; Michez et al., 2013; Picco et al., 2014). Ces études extraient des caractéristiques des patchs de végétation à partir du modèle numérique de canopée (CHM) comme leur limite, leur continuité longitudinale, la hauteur des arbres, la densité de la végétation ou encore la surface de végétation surplombante les chenaux en eau. Le niveau de l'eau par rapport à l'altitude des patchs de végétation est déterminé en fonction de l'altitude des chenaux en eau calculé à partir du MNT. L'utilisation du LiDAR aérien pour étudier la structure de la végétation en lien avec la morphologie du lit sous-jacent est cependant récente. Sur la rivière Tagliamento, Bertoldi et al. (2011, 2013) utilisent des données combinées de LiDAR aérien, de photographies aériennes et de mesures de terrain pour (1) étudier la colonisation de la bande active par la végétation et son impact sur la topographie (Bertoldi et al., 2011); (2) étudier l'origine du bois mort et sa dynamique de dépôt (Bertoldi et al., 2013).

B. Problématique et démarche scientifique

Un recensement récent des rivières en tresses du bassin Rhône-Méditerranée en France a montré qu'elles représentent un linéaire de 650 km (Piégay et al., 2009). Ce linéaire s'est fortement réduit au cours du XX^{ème} siècle sous l'effet des extractions de graviers, des endiguements, des aménagements hydro-électriques et de la reconquête forestière des montagnes. Il s'agit d'une évolution d'autant plus préoccupante que ces rivières sont reconnues comme support d'écosystèmes remarquables, à très forte valeur patrimoniale à l'échelle de la France, mais aussi à celle de l'Europe. Depuis ce constat et dans un contexte européen où l'atteinte d'un bon état écologique des rivières est un objectif fort (Directive Cadre sur l'Eau), il est devenu nécessaire de promouvoir une gestion adaptée de ces milieux, fondée sur une meilleure connaissance de leur fonctionnement morphodynamique et sédimentaire. Il apparaît aussi que l'instabilité morphologique de ces rivières, associée à l'intensité forte du transport solide, peut être une source importante de risque pour les populations qui vivent à proximité de ces rivières. Les pressions locales en faveur de l'aménagement et du curage des lits en tresses sont donc souvent très fortes, et les gestionnaires doivent aujourd'hui définir des politiques qui permettent de concilier ces attentes divergentes. C'est dans ce contexte qu'ont été construits deux projets de recherche interdisciplinaires dans lesquels s'inscrit cette thèse : le projet ANR Risknat GESTRANS (GEStion des risques liés aux crues par une meilleure prise en compte du TRANsit Sédimentaire) et le projet Rivières en Tresses de la ZABR (Zone Atelier Bassin du Rhône), soutenu par l'Agence de l'Eau Rhône-Méditerranée-Corse.

L'objectif principal de la thèse a été d'extraire et d'analyser les structures et les dynamiques morphologiques et sédimentaires des lits en tresses à partir de l'utilisation de données acquises par LiDAR aéroporté. Ces données topographiques permettent depuis peu d'accéder à un niveau d'information très élevé en termes de densité spatiale et de précision, et elles peuvent être produites sur de grandes emprises spatiales. Elles sont donc très adaptées à l'étude des systèmes morphologiques complexes comme les lits en tresses, où l'imbrication d'unités morphologiques de tailles très différentes est omniprésente. Les relevés par LiDAR aéroporté se sont d'autre part généralisés ces dernières années dans les plans de gestion des rivières alpines. Ils remplacent progressivement les levés topographiques terrestres traditionnels, qui deviennent de moins en moins attractifs en termes de coûts et de rendus. Ce contexte a permis de collecter de nombreuses données LiDAR en contexte de lits en tresses réalisés ces dernières années dans les bassins

versants de la Bléone, de la Drôme et du Drac. L'analyse exploratoire de ces données a permis d'identifier trois grands axes de travail qui structurent la thèse (Fig. 16) : (i) la détection des changements morphologiques à l'échelle d'une crue, (ii) l'analyse des signatures morphologiques longitudinales, et (iii) l'analyse de changement morphologique pluri-décennal en lien avec les unités végétales de la mosaïque fluviale.

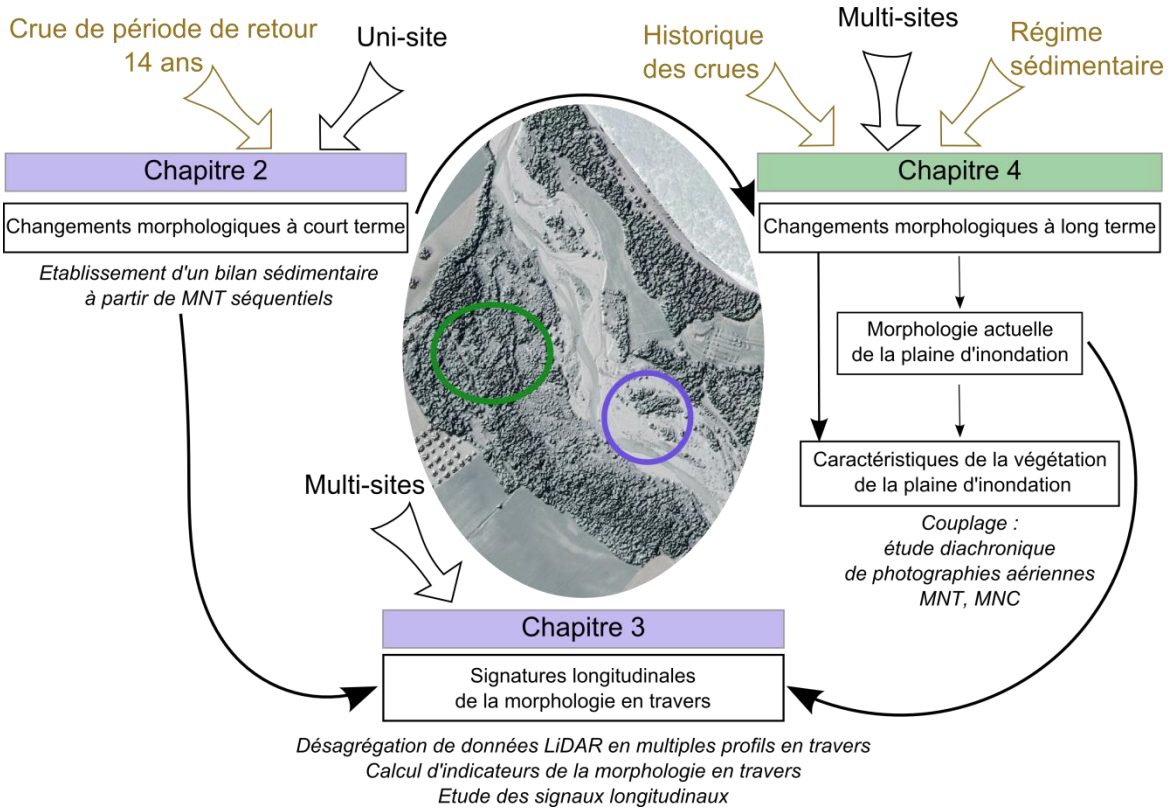

Fig. 16. Schéma synthétique de l'organisation du manuscrit, principaux questionnements abordés dans les différents chapitres et méthodologies associées.

Différentes approches ont été combinées afin de répondre aux questions suivantes :

Axe 1 : détection des changements morphologiques à l'échelle d'une crue (Chapitre 2)

Ce premier axe présente une portée essentiellement méthodologique. Il s'agit de proposer une méthodologie robuste de traitement de deux nuages de point LiDAR séquentiel afin d'établir un bilan sédimentaire et détecter les changements morphologiques. L'influence des différentes étapes de traitement dans le calcul du bilan sédimentaire ont été mesurée. Il s'appuie sur 2 levés LiDAR séquentiels d'une tresse de 7 km de long mesurée avant et après une crue de période de retour de 14 ans. Plusieurs questions ont fait l'objet de développements spécifiques. Quelle est l'importance de l'erreur systématique d'alignement des scènes LiDAR et comment cette erreur est-elle distribuée spatialement ? Quel est l'effet de sa propagation sur le calcul du bilan sédimentaire ?

Comment prendre en compte l'effet des surfaces en eau sur le bilan sédimentaire lorsque la bathymétrie optique ne peut être utilisée ? Cet effet, déjà démontré pour les petites crues où les changements morphologiques sont concentrés dans les chenaux (Lane et al., 2003), est-il encore significatif pour une crue décennale ? Comment l'erreur aléatoire est-elle influencée par les états de surface des lits en tresses ? Comment sa prise en compte influence t-elle le calcul du bilan sédimentaire ? Quelle a été la réponse du motif de tressage à la crue et quelle a été l'importance des surfaces contributives au transport solide au sein de la bande active ?

Axe 2 : signatures morphologiques longitudinales des tresses (Chapitre 3)

Cet axe s'appuie principalement sur l'analyse de la variabilité spatiale des signatures morphologiques des tresses à partir d'un linéaire de 25 km réparti sur 9 sites dans les bassins versants de la Drôme, du Drac et de la Bléone, pour lequel nous disposons de données LiDAR aéroportées. Plusieurs métriques morphologiques ont été extraites automatiquement sur des transects positionnés à intervalles réguliers, de manière à analyser les oscillations morphologiques longitudinales des tresses. Ces données ont permis de traiter plusieurs questions. Est-il possible de détecter des ruptures longitudinales dans les signatures morphologiques et comment ces ruptures peuvent-elles être interprétées ? Peut-on détecter une périodicité dans les signatures longitudinales et quelles sont les longueurs caractéristiques de ces périodes ? Ces signatures sont-elles associées aux effets de la dernière crue ou au contraire sont-elles plutôt intégratrices du fonctionnement morphosédimentaire à plus long terme de la tresse ? Est-il possible d'établir un lien entre ces périodes et les grandeurs caractéristiques des formes sédimentaires imbriquées de la bande de tressage ?

Axe 3 : analyse du changement morphologique pluri-décennal en lien avec les unités végétales de la mosaïque fluviale (Chapitre 4)

Le dernier axe exploite un autre point fort des acquisitions par LiDAR aéroporté, celui de fournir en tout point de la plaine, y compris dans la forêt riveraine, une série de valeurs altimétriques de la topographie et du toit de la canopée. Ces données très difficiles à collecter in situ permettent ainsi d'explorer la variabilité altimétrique du lit majeur et le lien qu'il peut exister avec les caractéristiques de végétation. Une approche combinant une acquisition par LiDAR aéroporté et une étude diachronique de photographies aériennes anciennes permet-elle ainsi de reconstruire l'historique de formation des différentes unités spatiales composant la plaine d'inondation ? Les différentes phases d'incision observées pour les rivières en tresses françaises sont-t-elles à l'origine de niveaux topographiques imbriqués ? Peut-on mettre en évidence un impact des crues sur les changements morphologiques pluri-décennaux ? Dans un second temps,

cette approche permet-elle de caractériser les différentes unités de végétation et de lier ces caractéristiques à l'historique de formation de la plaine d'inondation et à sa morphologie actuelle ?

C. Organisation du manuscrit

Ce premier chapitre a permis de présenter le cadre scientifique et méthodologique sur lequel se base ce travail de thèse, avec dans un premier temps une synthèse bibliographique des recherches relatives à la morphologie des rivières en tresses, et à leurs dynamiques à court et long terme, et dans un second temps un recensement des méthodes de mesures mises en œuvre pour caractériser la morphologie des rivières en tresses en axant plus particulièrement sur les données LiDAR aéroporté.

Les questions scientifiques explorées (Cf. chapitre 1-B) sont alors détaillées dans les chapitres qui suivent. Chacun d'eux correspond à un article scientifique et présente un état de l'art plus spécifique de la problématique, une présentation du ou des sites d'études, une méthodologie propre, des résultats, et une discussion. Le chapitre 2 a été publié dans *Geomorphology* (Lallias-Tacon et al., 2014) et le chapitre 4 a été soumis à Catena.

CHAPITRE 2

CALCUL DU BILAN SEDIMENTAIRE D'UNE RIVIERE EN TRESSES AVEC DES DONNEES MULTI-TEMPORELLES ACQUISES PAR LIDAR AEROPORTE : ESTIMATION DES ERREURS ETAPE PAR ETAPE

A. Résumé

Des levés LiDAR (Ligth Detection And Ranging) aéroportés multi-temporels ont été utilisés pour calculer le bilan sédimentaire d'un tronçon en tresses de 7 km de long. Ces levés ont été acquis sur la rivière du Bès, affluent de rive droite de la Bléone dans les Préalpes du Sud (France). Les deux levés LiDAR étudiés encadrent une crue enregistrée en décembre 2009 et dont la période de retour est de 14 ans. Le traitement des données comprend (i) le réalignement des deux nuages de points bruts, (ii) la propagation des incertitudes spatialement distribuées en fonction des conditions de surface (bancs faiblement ou densément végétalisés, surfaces immergées, forêts alluviales), calculées à partir de mesures topographiques et (iii) la soustraction d'une hauteur d'eau moyenne à la valeur du pixel des modèles numériques de terrain pour les surfaces immergées, calculée à partir de mesures de hauteur d'eau. L'influence de chaque étape de traitement sur le calcul du bilan sédimentaire a été étudiée. Les résultats montrent que le réalignement des nuages de points et la soustraction des hauteurs d'eau ont un effet considérable sur le calcul du bilan sédimentaire. La prise en compte des incertitudes a un plus faible effet sur le bilan sédimentaire mais cette étape est cruciale pour produire des cartes compréhensives des changements morphologiques. La qualité des données LiDAR a été contrôlée avec de nombreux points de référence acquis lors de campagnes de terrain. Les résultats ont montré que des levés LiDAR ayant une forte densité de points (7-9 points/m²) permettent une détection des changements d'altitudes avec un intervalle de confiance de 95% compris entre 19 et 30 cm. L'étude des changements morphologiques a montré que 54% de la bande active avant la crue a enregistré des changements morphologiques et la forme du tressage a été complètement modifiée par la crue par de nombreuses avulsions de chenaux.

Ce travail a fait l'objet d'une publication dans la revue *Geomorphology* qui est présentée dans les pages suivantes.

Mots clés : LiDAR aérien multi-temporel ; rivière en tresses ; bilan sédimentaire ; propagation d'incertitudes.

B. Step by step error assessment in braided river sediment budget using airborne LiDAR data

Lallias-Tacon, S., Liébault, F., Piégay, H., 2014. Step by step error assessment in braided river sediment budget using airborne LiDAR data. Geomorphology 214, 307-323. http://dx.doi.org/10.1016/j.geomorph.2014.02.014.

Abstract

Sequential airborne LiDAR surveys were used to reconstruct the sediment budget of a 7-km-long braided river channel in southeastern France following a 14-year return period flood and to improve its accuracy step by step. Data processing involved (i) surface matching of the sequential point clouds, (ii) spatially distributed propagation of uncertainty based on surface conditions of the channel, and (iii) water depth subtraction from the digital elevation models based on water depths measured in the field. The respective influence of each processing step on sediment budget computation was systematically documented. This showed that surface matching and water depth subtraction both have a considerable effect on the net sediment budget. Although DEM of difference thresholding based on uncertainty analysis on absolute elevation values had a smaller effect on the sediment budget, this step is crucial for the production of a comprehensive map of channel deformations. A large independent data set of RTK-GPS checkpoints was used to control the quality of the LiDAR altimetry. The results showed that high density (7-9 points/m²) airborne LiDAR surveys can provide a very high level of detection of elevation changes on the exposed surfaces of the channel, with a 95% confidence interval level of detection between 19 and 30 cm. Change detection from LiDAR data revealed that 54% of the pre-flood active channel was reworked by the flood. The braided channel pattern was highly disturbed by the flood owing to the occurrence of several channel avulsions.

Keywords: sequential airborne LiDAR; braided river; sediment budget; uncertainty propagation analysis.

1. Introduction

Braided gravel-bed rivers have long been recognized as very active geomorphic systems, but until recently, the lack of techniques to fully reconstruct the complex morphology of multithread river corridors have hindered our understanding of their dynamics. Until the mid-1990s, the topographic monitoring of braided channels was restricted to regularly spaced and fixed cross sections revisited after significant flow events (Ashworth and Ferguson, 1986; Carson and Griffiths, 1989; Ferguson and Ashworth, 1992). The main problem was the insufficient spatial resolution in the longitudinal direction, which fails to provide a clear picture of the complex assemblage of macroforms constituting these channels. Another issue was the high level of uncertainty for the computation of erosion and deposition volumes used in sediment budgets. These problems were partially solved with the application of techniques delivering spatially distributed topographic data that can be used to construct a digital elevation model (DEM) of the channel. The first DEMs of braided channels were produced by ground-based analytical (Lane et al., 1994, 1995) or airborne digital (Westaway et al., 2000) photogrammetry coupled with tacheometry for the survey of submerged areas and with real-time kinematic global positioning systems (RTK-GPS) (Brasington et al., 2000b). These pioneering studies were followed by a considerable number of works using a wide variety of techniques: oblique digital photogrammetry (Chandler et al., 2002), airborne light detection and ranging (LiDAR) (Charlton et al., 2003; Lane et al., 2003; Hicks et al., 2008; Höfle et al., 2009; Bertoldi et al., 2011; Legleiter, 2012; Moretto et al., 2012a), short-wavelength green LiDAR, capable of penetrating through the water column for mapping bathymetry (Kinzel et al., 2007; Bailly et al., 2010), and terrestrial laser scanning (TLS) (Milan et al., 2007; Williams et al., 2011; Brasington et al., 2012). Each of these techniques presents specific advantages explaining why they continue to be widely used in the braided river research community. However, airborne LiDAR seems more attractive given its prevalence in recent studies.

The popularity of airborne LiDAR is explained by its ability to cover large areas with high resolution and high precision DEMs, including ground surfaces covered by vegetation (Wehr and Lohr, 1999). Sequential airborne LiDAR surveys have been successfully deployed in large gravel-bed braided rivers to produce detailed maps of erosion and deposition. The first published study concerns the Waimakariri River in New Zealand, where a LiDAR-derived DEM of a 3.3-km reach was compared with a DEM obtained with airborne digital photogrammetry (Lane et al., 2003). The level of detection (LoD) of significant elevation change (68% confidence interval) was between 16 and 33 cm, depending on the wet or dry conditions of the channel during both surveys. However, braided channel responses exclusively derived from sequential airborne LiDAR data are still rare. Hicks et al. (2008) reported the case of the Waimakariri River, where

two 1-m resolution LiDAR DEMs in 2000 and 2003 were compared, with a spatially averaged LoD of about 20 cm. A more recent study on the Brenta River in Italy showed similar results, with a LoD between 22 and 29 cm using two LiDAR DEMs of a 4.5-km-long braided channel (Moretto et al., 2012a). Other studies based on airborne LiDAR in braided environments include: (i) quality control of the LiDAR altimetry with ground-based topographic surveys (Charlton et al., 2003); (ii) estimation of bank erosion (Surian and Cisotto, 2007); (iii) development of procedures for the automatic extraction of water surfaces from LiDAR point clouds (Höfle et al., 2009), which can be coupled with spectrally-based bathymetry (Legleiter, 2012); (iv) quantification of long-term incision rates from terraces (Turitto et al., 2010); and (v) analysis of the topographic signature of vegetation establishment in braided channels (Bertoldi et al., 2011).

Uncertainty assessment in DEMs of difference (DoD) and sediment budget computation is a key issue for geomorphic interpretation of topographic changes. In fact, it is crucial to distinguish real morphological changes from noise. Uncertainty in DoD application has already received considerable attention (Brasington et al., 2000b; Lane et al., 2003; Wheaton et al., 2010; Milan et al., 2011). Recent studies with conventional terrestrial survey techniques (RTK-GPS, total station) highlighted the spatial variability of uncertainty. Greater uncertainty is found in areas of high topographic variability (high grain and/or form roughness) and low point density (Heritage et al., 2009; Wheaton et al., 2010; Milan et al., 2011). The precision of altimetric data is also recognized to decrease significantly with the density of the vegetation cover and the slope steepness (Bowen and Waltermire, 2002; Hodgson and Bresnahan, 2004). These findings have not yet been incorporated in airborne LiDAR data processing for river environments, as the only factor of uncertainty that has been taken into account in the sediment budget computation is the wet or dry condition of the channel (Lane et al., 2003; Hicks et al., 2008; Erwin et al., 2012; Moretto et al., 2012a). Recently, Carley et al. (2012) tested different DoD uncertainty procedures and showed that LoD subtraction from the raw DoD was the correct method to achieve a physically sound sediment budget compared to LoD exclusion (discarding DoD cells with values below the LoD).

A persistent problem with LiDAR data is that classically used near-infrared laser pulses (NIR, 1064 nm) are strongly absorbed by water and fail to provide the relief of submerged areas (Reusser and Bierman, 2007; Notebaert et al., 2009), even if for very shallow water conditions (typically < 5 cm), some bed detection can be obtained from NIR laser (Milan et al., 2007). A common way to solve this problem is to derive the flow depth from multispectral (RGB) imagery acquired simultaneously with laser scans (Lane et al., 2003; Bertoldi et al., 2011; Legleiter, 2012; Moretto et al., 2012a). The DEM of the submerged relief is obtained by subtracting optically derived water depths from the water surface, which can be automatically extracted from LiDAR point density and/or LiDAR intensity images (Höfle et al., 2009; Legleiter, 2012). This method

requires calibrating a rating curve between water depth and a spectral predictor using data collected in the field concomitantly with the LiDAR survey. The performance of this procedure is contingent to the hydraulic and substrate properties of the channel during the survey. The best conditions for obtaining an accurate bathymetry are shallow clear water with highly reflective substrate (Legleiter, 2012). However, even under optimal conditions, the optical-bathymetric approach fails to capture deep water depths (> 50 cm in the case study reported by Legleiter, 2012). This can be solved using green LiDAR systems (532 nm), which are more suitable for deep water and which do not give realistic data for water depths < 30–40 cm (Kinzel et al., 2007; Bailly et al., 2010).

Although airborne LiDAR data is still expensive and not adapted for submerged channel conditions, these data are becoming increasingly available, notably in the context of regional and local water resources management plans (Cavalli and Tarolli, 2011). During the last 5 years in France, most of the large alpine rivers have been surveyed for the implementation of sustainable management of channel morphology and sediment transport, with the financial support of the French Water Agency. Therefore, requests from river managers are increasing concerning the potential of LiDAR data for the monitoring of channel changes. This is particularly true for braided rivers, which are recognized as endangered aquatic ecosystems highly sensitive to the preservation of active morphodynamics (Piégay et al., 2009). Given the constraints associated with the use of optical bathymetric mapping of the submerged part of river channels (availability of orthorectified multispectral imagery simultaneously acquired with the LiDAR survey, data acquisition of water depth in the field during the survey), there is a need to evaluate what can be achieved in terms of morphological change reconstitution and sediment budgeting when only LiDAR data are available (without aerial imagery), a situation which is very frequent in the operational context.

This paper addresses the issue of assessing errors in the quantification of morphological changes of a braided channel after the occurrence of a 14-year return-period flood in 2009, using exclusively airborne LiDAR data acquired in 2008 and 2010. A method for estimating geomorphic changes in the aquatic zones is proposed in a context where no airborne images are available, as frequently seen in operational studies. A complementary objective was to produce spatially distributed uncertainty from data collected in the field for different surface conditions. This data set gave insights into the quality of LiDAR altimetry for typical channel conditions of gravel-bed braided channels. Finally, data are used to characterize the flood effect on the braided channel pattern, by identification of the most active morphological processes and by quantification of the braidplain turnover.

2. Study site

2.1. The Bès River

The Bès River is a gravel-bed braided river located near Digne-les-Bains in the Southern French Prealps, with a 234-km² drainage area. It is the main tributary to the Bléone River in the Durance River basin (Fig. 17A). The geology of the catchment consists of sedimentary rocks, mainly limestone, marls, and marly limestone. Elevations range from 640 to 2700 m asl. The catchment is 70% covered by forest, 25% by grassland, and 5% by agricultural land. The climate is Mediterranean and mountainous, with snow in winter and high intensity rainfall in summer and autumn. The mean annual precipitation is 930 mm. The analysis of the historical long-profile of the Bès revealed an aggradation trend (+ 1.11 m between 1911 and 2009) during the twentieth century, which can be linked to the high sediment supply from active torrents in the catchment (Liébault et al., 2013a).

The study reach covers the last 7 km of the Bès River (midpoint at 44°09’32.89’’ N., 6°14’36.49’’ E.; Fig. 17B). Here, the Bès is braided with a channel slope of 0.014, a surface median grain size (D_{50}) of 40–50 mm (derived from gravel surface photographs processed with Digital Gravelometer software), and a mean active channel width of 130 m (Fig. 17C). ‘Active channel’ refers here as the unvegetated gravel bars and low-flow channels. The braided channel is composed of a complex mosaic of gravel bars with some vegetated islands encroached by pioneer trees and shrubs. The braided channel occupies almost the entire valley floor (about 71%), the remaining corresponding to riparian forests or agricultural lands on terraces. Braided channel expansion is limited by steep hillsides. Along this reach, the main tributary is the Galabre Torrent (20 km²) on the right bank that supplies a great deal of sediment to the Bès, as attested by the formation of an alluvial fan at the confluence (Fig. 17B). Many small tributary gullies are also present in the right and left sides of the valley.

The flow record has been available since 1965 at the Pérouré gauging station approximately 1.5 km upstream of the study reach. The hydrological regime is characterized by spring snowmelt high flows, summer low flows, and rainfall autumn high flows. The mean annual discharge is 2.78 $m^3 s^{-1}$. The 2-, 5- and 10-year return-period instantaneous peak discharges are 57, 99, and 130 $m^3 s^{-1}$, respectively.

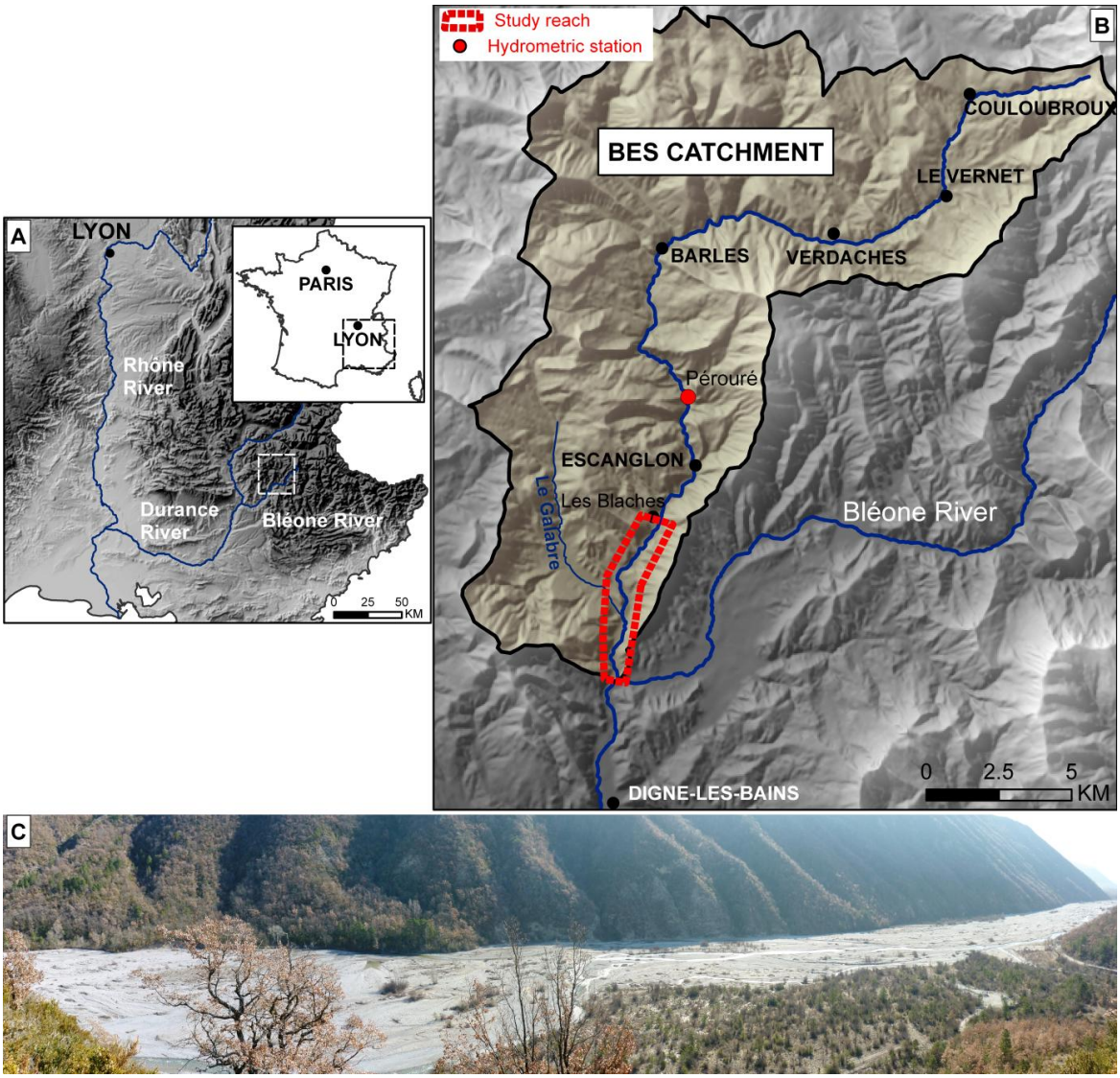

Fig. 17. The study site: (A) location in SE France; (B) general map of the Bès River catchment with the position of the 7-km study reach; (C) general view of the lower braided Bès River, the flow direction is from left to right.

2.2. The December 2009 flood

The main flood that occurred between the two LiDAR surveys was characterized by two successive peaks that occurred between 22 and 24 December 2009, with a return period of 10 and 14 years, respectively (Fig. 18). The instantaneous peak discharge was estimated at 171 m^3 s^{-1}. This multipeak flood was generated by a rapid air temperature warming associated with a wet Mediterranean southwestern depression, when the catchment was covered by a substantial snow layer (Navratil et al., 2012). For the rest of the period between the two LiDAR surveys, discharges were low with high spring flows of moderate intensity so that morphological changes can be mainly attributed to the December 2009 flood.

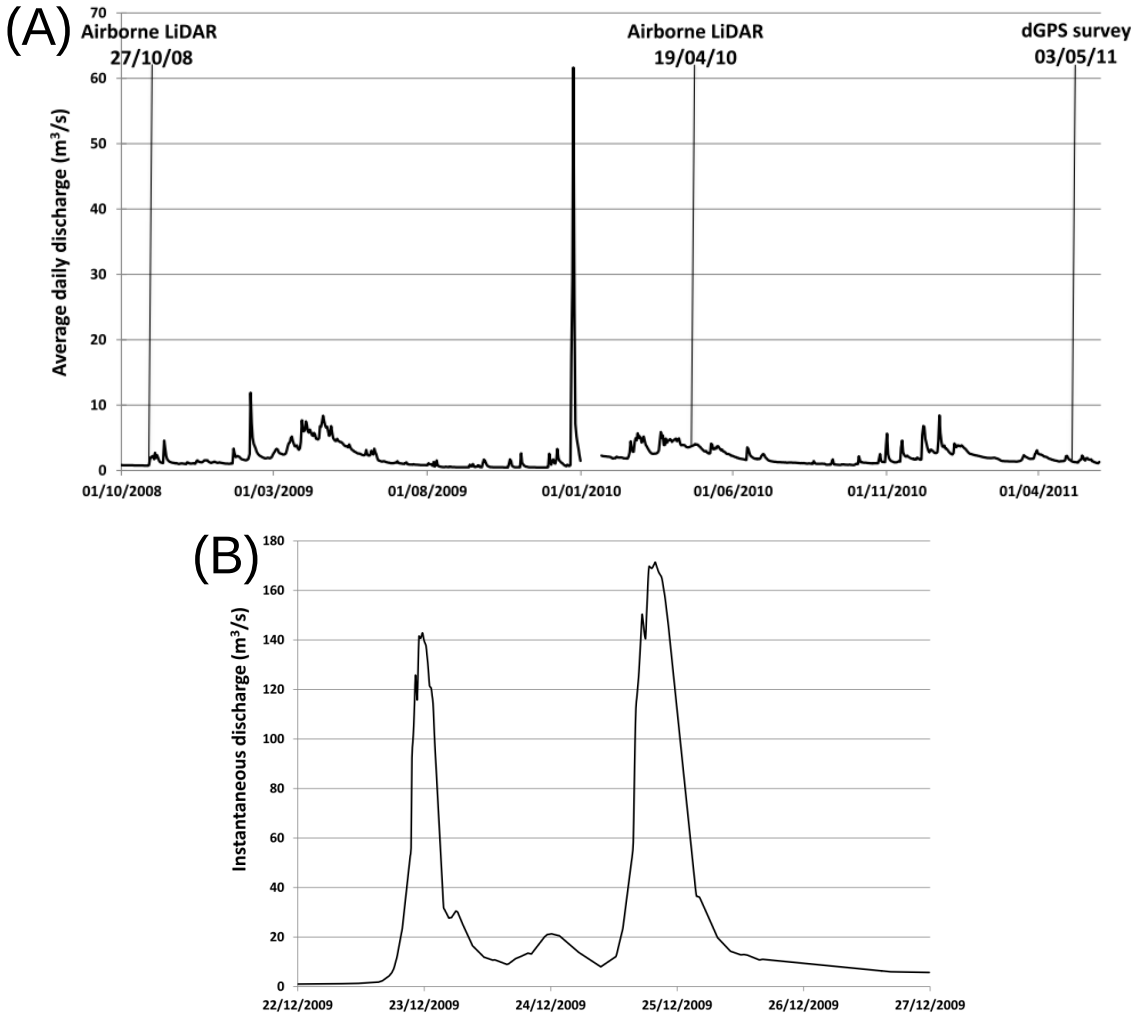

Fig. 18. (A) Average daily discharge series of the Bès River between 1 October 2008 and 1 June 2011 showing a single important flood between the two airborne LiDAR surveys; (B) instantaneous discharge of the December 2009 multipeak flood; data from the Pérouré gauging station (DREAL PACA).

3. Methodology

Morphological changes of the study reach were studied with two airborne LiDAR surveys: the first was done on 27 October 2008 and the second on 19 April 2010.

3.1. LiDAR data acquisition and pre-processing

Sequential airborne LiDAR data of the study reach were collected by the same private company, Sintegra. Technical specifications of the airborne LiDAR platforms (LiDAR sensors, RTK-GPS, and inertial measurement units) and flight conditions in 2008 and 2010 are presented in Table 2. The overall performance of the two surveys is slightly different, with a higher altimetric precision in 2010 (5 cm, versus 10 cm in 2008) and equal planimetric precision (15 cm). These values were obtained from comparison with ground RTK-GPS checkpoints measured on exposed flat surfaces by Sintegra. The higher altimetric precision of the 2010 survey is explained by the deployment of higher performance laser and inertial measurement unit (IMU) sensors (Table 2). Although the flying height of the 2010 survey was higher, this does not affect the planimetric precision because the beam divergence of the LiDAR sensor (and so the laser footprint) was lower in 2010. The ground point density was slightly higher in 2008. Compared to most of the previous infrared LiDAR applications in fluvial environments (see table 22.2 in Milan and Heritage, 2012), these two LiDAR surveys show a much higher point density. LiDAR surveys were composed of overlapping flight lines that were merged together by Sintegra (seven lines in 2008 and six in 2010) using the alignment algorithm of the TerraScan software. LiDAR point clouds were automatically classified by Sintegra into ground and no-ground points with the Axelsson filter (Axelsson, 2000) of the TerraScan software. This first automatic classification was completed by manual editing based on orthophoto interpretation. The average point density after vegetation filtering was 8.6 points m^{-2} in 2008 and 7.0 points m^{-2} in 2010. Raw data were delivered as ASCII files of *xyz* point clouds of unclassified echoes and ground echoes. The two data sets were georeferenced using the same local coordinate system (*Lambert 2 Etendu* for planimetric datum, and *IGN 69* for elevation datum). The DEMs were constructed with ArcGIS using a simple workflow in which ground points were used to derive a triangular irregular network (TIN) using Delaunay triangulation, which was then linearly resampled into a 0.5-m grid. In fact, Heritage et al. (2009) demonstrated that linear interpolation from TIN and kriging provide the best interpolation methods for river channel morphology. The DEMs were cut with a mask corresponding to the area of potential morphological changes owing to the flood to focus the analysis on relevant surfaces. This mask was based on an expert interpretation of the DoD. A first raw DoD was calculated by subtracting the 2008 elevations from those of 2010 on a cell-by-cell

basis. Net volumetric changes were calculated by multiplying the elevation change by the surface area of each cell. These volumes were summed into erosional and depositional categories to produce a net volumetric budget.

Table 2. Technical specifications of 2008 and 2010 airborne LiDAR surveys; the altimetric and planimetric errors were provided by Sintegra from RTK-GPS ground control points locally measured on a road (60 points in 2008 and 50 points in 2010); SDE: standard deviation of error.

Specification	2008 survey	2010 survey
Date	27/10/2008	19/04/2010
Aircraft type	Partenavia P68C	
RTK-GPS	Topcon Legacy-H, dual-frequency (L1, L2)	
Inertial measurement unit (IMU)	iTraceR-F200	NUS5
Gyroscope drift (°/h)	0.75	0.1
Laser scan	Riegl LMS Q560	Leica ALS60
Scanning mechanism	Rotating polygon mirror	Oscillating mirror
Pulse repetition rate (kHz)	200	116
Laser beam wavelength (nm)	1550	1064
Type of echo	Full waveform	
Flight height (m)	460	700
Flight speed (knots)	100	110
Angle of scan (°)	0-30	0-30
Laser beam divergence (mrad)	0.5	0.22
Footprint diameter on flat terrain (m)	0.23-0.25	0.15-0.17
Number of flight lines	7	6
Elevation precision of laser points (SDE in cm)	10	5
Planimetric precision of laser points (SDE in cm)	15	15
Ground point density (points m^{-2})	8.6	7.0
Ground point spacing (m)	0.55	0.60
Mean daily discharges of the Bès River (m^3 s^{-1})	0.75	3.64

3.2. Multitemporal LiDAR point cloud alignment

To control the quality of superposition between the two ground point clouds in stable terrains, the elevation of 2008 ground points (Z_{08}) situated along a road on the right bank of the river were compared with the 2010 elevation (Z_{10}) of the closest ground point, using a 10-cm maximum distance between points. The data set is composed of 132,268 couples of points. The difference in elevation ($\Delta_{Zr} = Z_{08} - Z_{10}$) was calculated to characterize the quality of the superposition. This operation revealed an offset between the two data sets, nonuniformly distributed in the longitudinal direction. It was then necessary to match the two sequential point clouds. An alignment operation performed on 1x1-km tiles with the automatic iterative closest point algorithm from the Polyworks software was done by selecting stable surfaces. This method is often used for alignment of adjacent scans of terrestrial LiDAR and sometimes for fusion of the airborne and terrestrial LiDAR point cloud (Iavarone and Vagners, 2003; Rabatel et al., 2008; Theule et al., 2012). A new sediment budget was computed using the merged DEMs to look at the effect of alignment on erosion and deposition volumes.

3.3. Spatial distribution of errors based on channel surface conditions

3.3.1. Dry surfaces

Spatially distributed error in the DoD was accounted by separating errors induced by LiDAR survey and errors induced by interpolation method used to produce DEM. Surveying errors were estimated with RTK-GPS field measurements by sampling different types of terrains, i.e., road, fine-grained (D_{50}~20–30 mm) and coarse-grained (D_{50}~50–60 mm) unvegetated exposed gravel bars, exposed gravel bars with sparse and dense pioneer shrub vegetation, alluvial forest, and channel banks. A total of 1186 points were measured in May 2011 with a Leica 1200 differential GPS in RTK mode, which provides centimetric accuracy (1 cm in *xy*, and 2 cm in *z*). The RTK-GPS is 3 times more accurate in *z* than LiDAR, and it provides a relevant independent means to control the quality of the LiDAR altimetry, even if the two instruments do not measure exactly the same object. LiDAR provides elevation averaging over the footprint size of the laser beam, whereas GPS provides the elevation at the scale of the rod tip, which is typically a few centimetres in diameter. This can partly explain differences between the two measures.

During the period between the 2010 LiDAR survey and the 2011 GPS survey, the Bès River underwent low discharges with an instantaneous maximum discharge of 11.80 $m^3\ s^{-1}$, which

corresponds to a return period lower than 1 year (Fig. 18A). We assumed that these flow conditions were not high enough to generate substantial channel deformations between the two surveys. However, the submerged topography has probably been slightly modified, but not the exposed surfaces.

Elevation of the GPS checkpoint (Z_{gps}) was compared to the elevation of the nearest 2010 LiDAR point (Z_{lidar}) to calculate the altimetric error ($\Delta_{Zgps} = Z_{gps} - Z_{lidar}$). Systematic error was corrected by subtracting the mean value of Δ_{Zgps} calculated from points measured on the road and fine-grained exposed gravel bars before characterizing the random error of the laser altimetry (Kinzel et al., 2007; Notebaert et al., 2009; Legleiter, 2012). These two types of terrain correspond to the most reliable conditions for characterizing the systematic error of the laser altimetry (flat and unvegetated terrains with a low surface roughness). The standard deviation of error (SDE) for each type of terrain was used for characterizing the random error of the LiDAR survey. The May 2011 ground survey can only be used to evaluate the precision of the 2010 LiDAR survey. For the 2008 survey, the only information available is the GPS control from Sintegra, which was done on the road. This control revealed altimetric precision twice as low for 2008 as for 2010. Therefore, the SDE for different terrain conditions obtained in 2010 were multiplied by a factor of 2 to assess the precision of the 2008 LiDAR survey.

The different types of surface were digitized on GIS for each LiDAR survey from the DSM (digital surface model), which includes vegetation echoes (Fig. 19A). Three classes were differentiated by expert photointerpretation. The first class corresponds to unvegetated or sparsely vegetated exposed gravel bars (vegetation cover < 60% of the total surface area, type 1). The second corresponds to exposed gravel bars with dense pioneer vegetation (vegetation cover > 60% of the total surface area, type 2), and the last corresponds to alluvial forests (type 3). Fig. 19B-C shows vegetation characteristics of each type of surface in terms of vegetation cover and vegetation height, calculated from the DCM (digital canopy model), which corresponds to the difference between DSM and DEM and shows vegetation height. The vegetation was defined by DCM pixel higher than 0.5 m.

Interpolation errors were accounted following the methodology proposed by Heritage et al. (2009) and Milan et al. (2011), which quantified the effect of local topographic roughness on interpolation error. For each survey, a linear regression equation is established between the standard deviation of elevation error, i.e., difference between LiDAR points and DEM pixel elevations, and topographic roughness, i.e., standard deviation of LiDAR point elevation in a 1-m radius moving window. Interpolation error is deducted from the linear regression equation for each pixel as a function of the topographic roughness value.

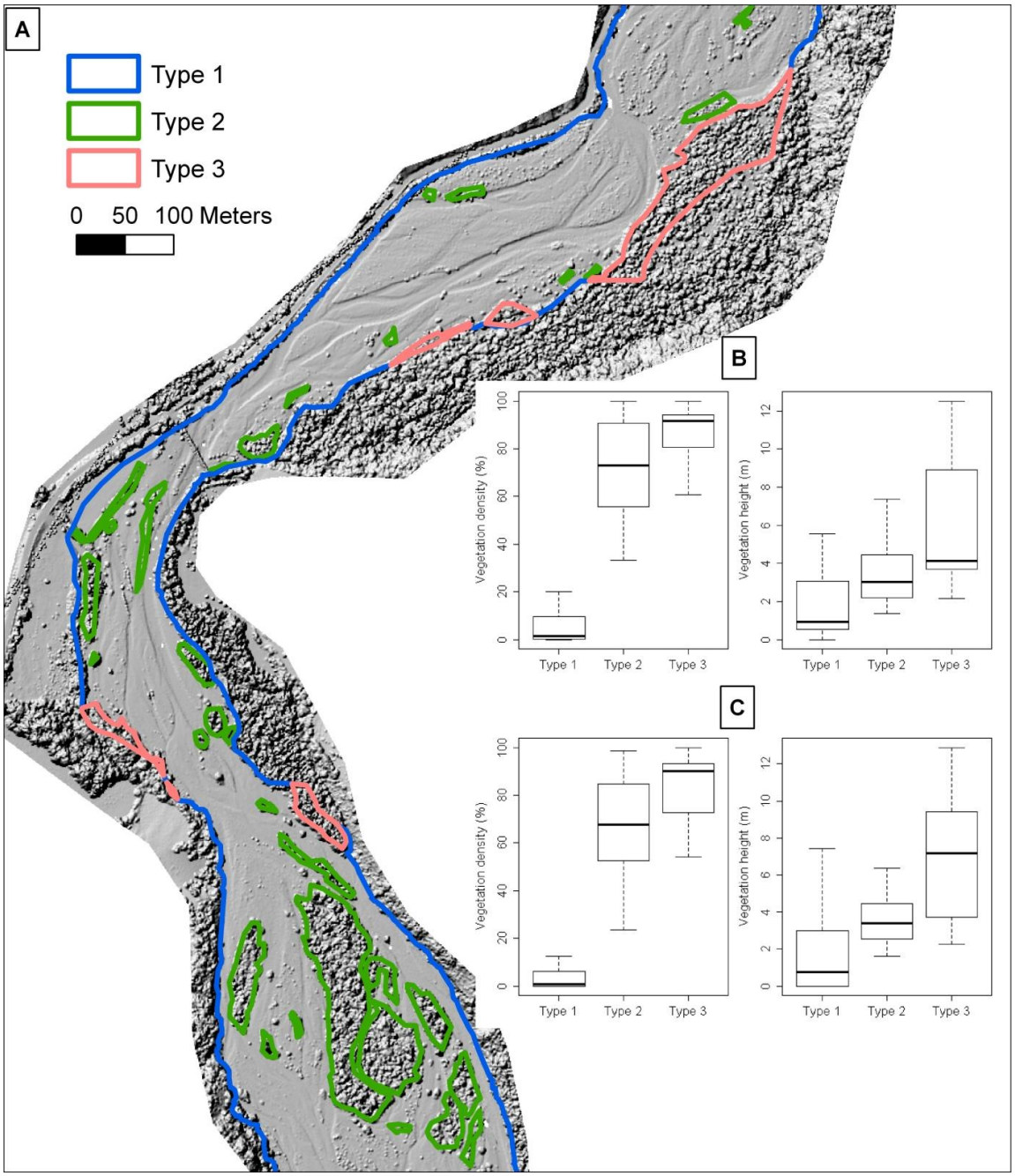

Fig. 19. Segmentation of the floodplain into homogeneous morphological units: (A) example of morphological unit mapping on DSM; boxplots of vegetation cover density and height derived from LiDAR data of 2008 (B) and 2010 (C) for each type of unit; type 1 corresponds to unvegetated or sparsely vegetated exposed gravel bars; type 2 corresponds to exposed gravel bars with dense pioneer vegetation; type 3 corresponds to alluvial forests; boxes represent inner and outer quartiles; horizontal line in the box represents the median; vertical lines represent inner and outer tenths.

Following Taylor (1997), and assuming a Gaussian distribution of errors, individual errors in the DEMs can then be propagated into the DoD from:

$$U_{crit} = t\sqrt{\left(\sqrt{\sigma_{sur2008}{}^2 + \sigma_{int2008}{}^2}\right)^2 + \left(\sqrt{\sigma_{sur2010}{}^2 + \sigma_{int2010}{}^2}\right)^2} \quad (6)$$

where U_{crit} is the level of detection of significant elevation change, $\sigma_{sur2008}$ and $\sigma_{sur2010}$ are the surveying errors of the 2008 and 2010 surveys, respectively, $\sigma_{int2008}$ and $\sigma_{int2008}$ are the interpolation errors of the 2008 and 2010 DEMs, respectively, and t is the critical t value at a chosen confidence interval. We used the 95% confidence interval, which corresponds to t > 1.96. For each DoD pixel, a critical threshold error is calculated with Eq. (6) to derive a LoD. The LoD is subtracted from all DoD cells for determining maps of significant elevation change and sediment budget computation, following the recommendation from Carley et al. (2012).

For sediment budget computation, the uncertainty of volume computation can be calculated following the method described by Lane et al. (2003). All elevation changes are taken into account in the volume change estimation and an uncertainty is calculated following

$$\sigma_v = d^2 \left(\sum_{i=1}^{I}\sum_{j=1}^{J}\left[(\sigma_{2008ij})^2 + (\sigma_{2010ij})^2\right]\right)^{0.5} \quad (7)$$

where σ_v is the uncertainty of volume change, d is the cell size of DEM, σ_{2008} and σ_{2010} are the individual errors in the 2008 DEM and the 2010 DEM, respectively, for each terrain, and the area of DEM is $I*J$ cells (i,j).

3.3.2. Water surfaces

Legleiter (2012) showed that water surface elevations (WSEs) could be derived from LiDAR points if a sufficient number of echoes are recorded within the surface of the channel occupied by water. However, in some cases, laser returns from the water surface can be noisy and inconsistent. They strongly depend on the character of water surface, with no returns from flat water surfaces (e.g., pools) and good returns from areas with high water surface roughness such as broken standing waves (Milan et al., 2010). LiDAR returns may also be provided from particles in suspension in the water column. In our case, mean point density of water surfaces is relatively high with 3.75 points m^{-2} in 2008 and 4.20 points m^{-2} in 2010. Moreover, cross sections of laser returns in wet areas of the channel showed that echoes are aligned around a flat level and are not

associated with suspended particles below the water level (Fig. 20). This observation confirms that they provide a good estimate of the water surface, as already shown by Hicks et al. (2009) on the Waitaki River.

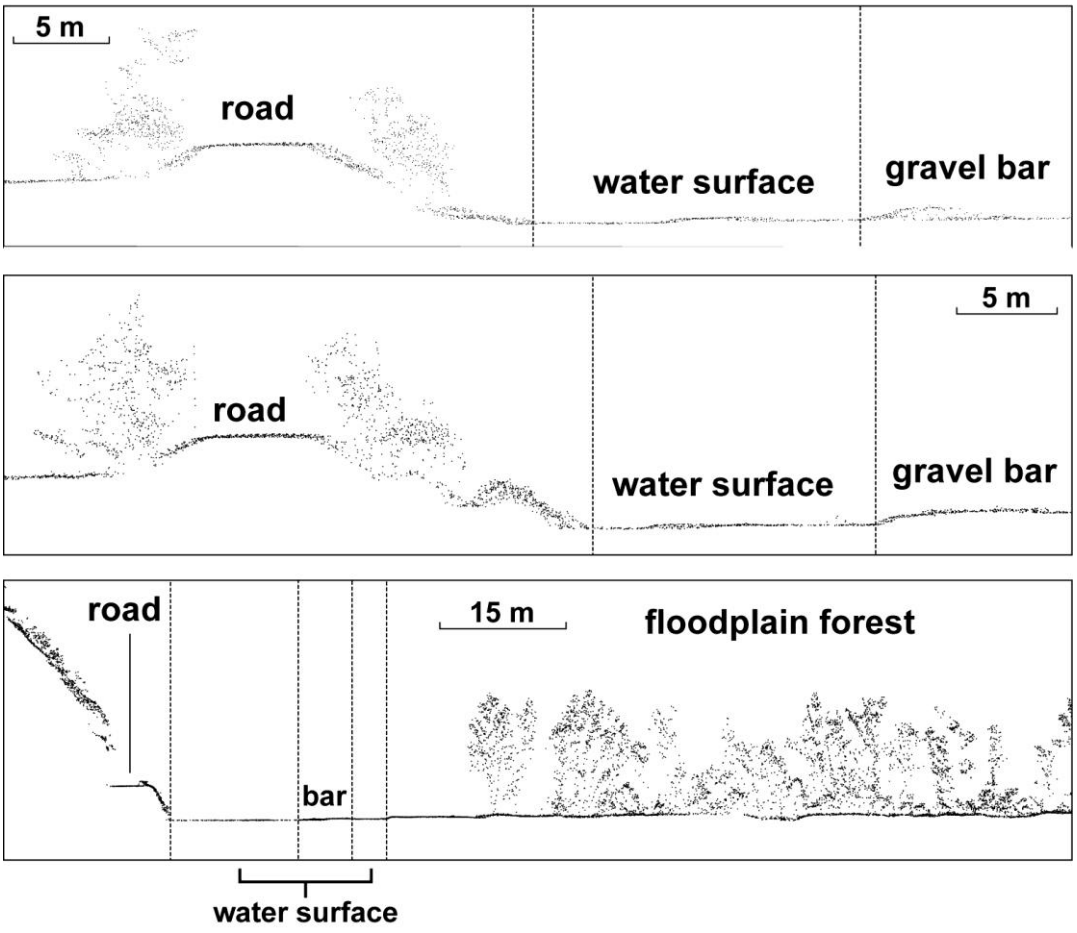

Fig. 20. Some examples of cross section views of unclassified LiDAR point clouds using a 5-m wide-transverse band, illustrating the presence of LiDAR echoes on water surfaces.

Water surfaces were manually delineated on point density maps following the approach of Legleiter (2012) based on the low point density of water surfaces (Fig. 21). Water surface boundaries were next corrected using the DEM-derived slope grid, which allows controlling the position of the water surface boundaries in respect to the position of the banks and to correct some local discrepancies (e.g., water surface boundaries on the top of channel banks). Intensity of the LiDAR returns can be used for the automatic detection of water surfaces (Höfle et al., 2009), but this information was not available in the raw data.

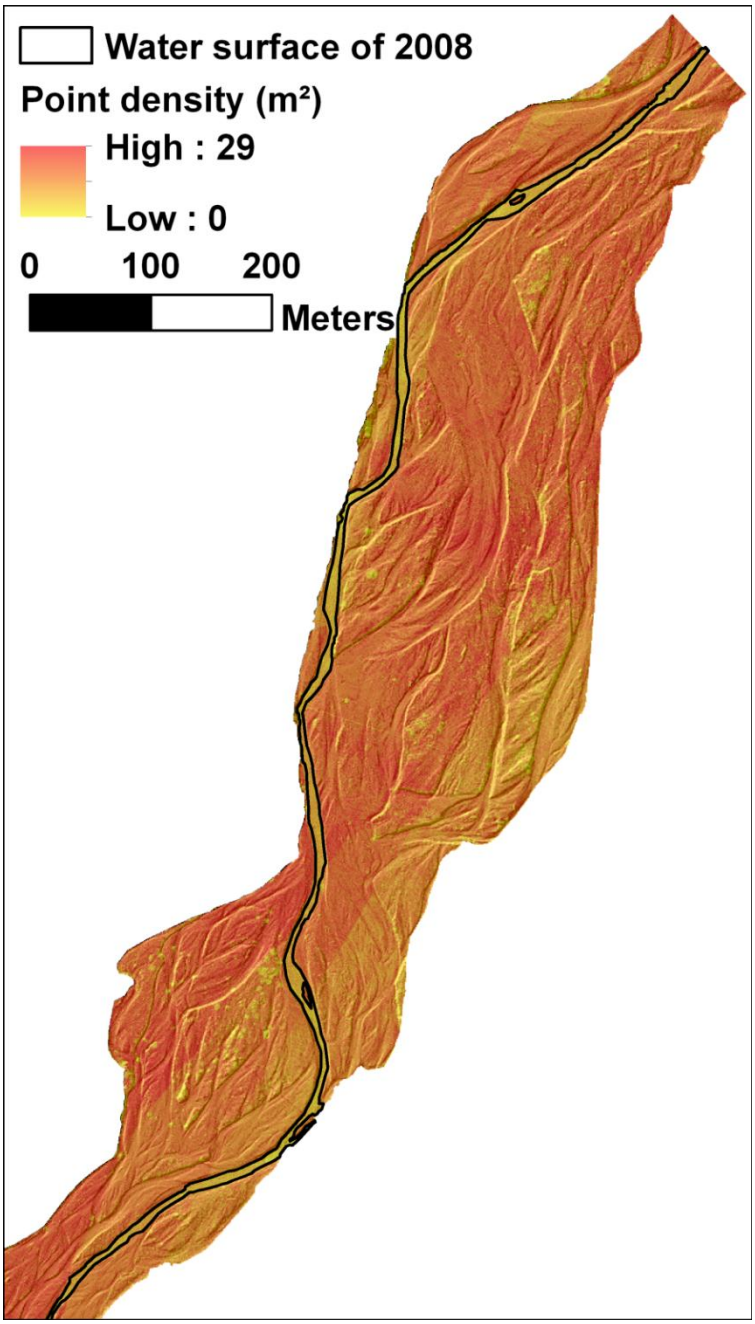

Fig. 21. Example of water surface delineation based on ground point density map of the 2008 LiDAR survey.

For water surfaces, it is important to determine whether elevation change is only caused by water level fluctuation or to real topographic change. In fact, the mean daily discharge was five times higher for the 2010 survey (3.64 m^3 s^{-1}) than for the 2008 survey (0.75 m^3 s^{-1}), corresponding to wet areas representing 5% and 7% of active channel in 2008 and 2010, respectively. For example, for wet surfaces on the two dates, positive elevation changes may be only caused by higher water depths in 2010, and the pixels corresponding to such conditions can be discarded in the sediment budget analysis. Conversely, negative elevation changes indicate that a substantial erosion of the low-flow channel occurred and that the pixel can be conserved. A

simple key based on surface conditions in 2008 and 2010 combined with the direction of elevation change allows discarding surfaces where the observed elevation change cannot be clearly linked to any realistic topographic change. Figure 6 shows which combinations are preserved and which are discarded for sediment budget computation. The scour and fill values for conserved surfaces are an underestimation of true elevation changes because the water depth is not considered. For these water surfaces, uncertainty was defined as the same as gravel bar terrains (we assumed that the roughness of the water surface was similar to one of the gravel bars) and propagated into the DoD following the method described in the previous section.

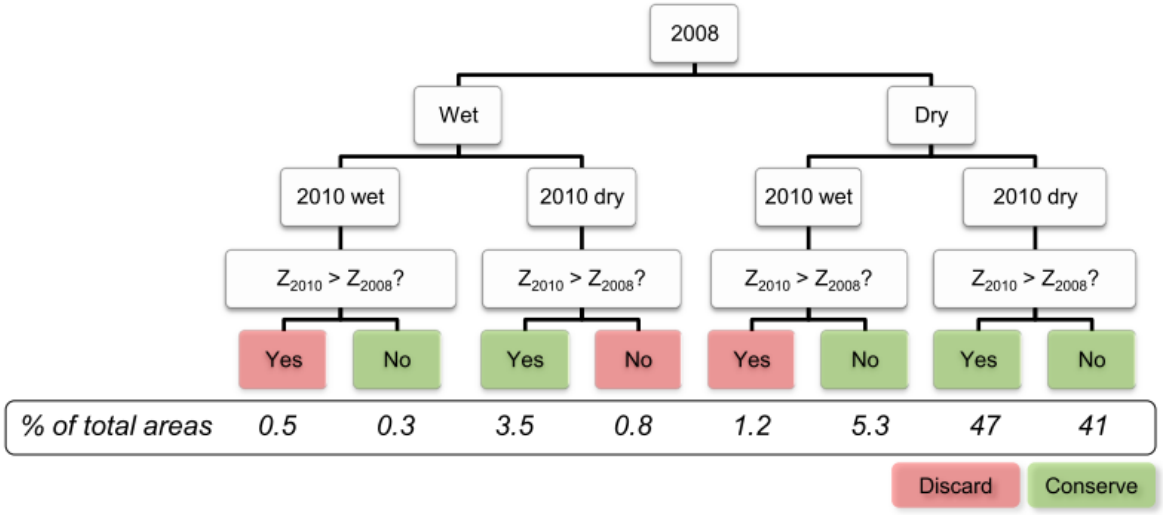

Fig. 22. Synoptic of computation rules for channel surface conditions showing which combinations are preserved and which are discarded for sediment budget computation; Z_{2008} and Z_{2010} correspond to elevation of the LiDAR-derived DEM for 2008 and 2010 respectively; percentage of total surface: percentage of each combination in the total surface of both LiDAR surveys.

3.4. Water depth subtraction

Water depth was measured in the field to compute the mean depth for the mean daily discharges of the Bès River observed during the two LiDAR surveys. Data were collected in the upper part of the study reach. Water supply from tributaries along the 7-km reach is negligible (i.e., the mean annual discharge of the Galabre Torrent is 0.20 $m^3 s^{-1}$). Our sampling strategy was designed to provide a random sampling in proportion to the abundance of morphological units found in the field (riffles, pools, and runs). For the sample of water depths corresponding to the 2008 LiDAR survey discharge, 100 water depth measurements were acquired in the field for an equivalent discharge. Field measurements were taken on 9 October 2012, when the mean daily discharge was 0.495 $m^3 s^{-1}$, a value slightly lower than the mean daily discharge during the 2008 survey. For the sample of water depths corresponding to the 2010 LiDAR survey discharge, 200

field measures of bed topography were sampled with a Leica 1200 differential GPS in RTK mode in May 2011. Water depths were then computed by differencing GPS elevations of bed topography with the closest water surface echo of 2010, taking a maximum search radius of 50 cm. In this case, we assumed that bed topography had undergone few changes since the 2010 LiDAR survey, as confirmed by the hydrological record from the gauging station.

For each water pixel of the DEMs, mean water depth was subtracted from the water surface elevations to evaluate the effect of submerged areas in the sediment budget computation. Uncertainty of the bathymetric reconstruction was defined by the standard error of the mean water depths, and the error was propagated with the same method as described in the previous section.

4. Results

The sediment budget computation was estimated step by step to assess the respective impact of each data processing operation.

4.1. Sediment budget following alignment operation

The raw data showed that the mean elevation difference between 2008 and 2010 laser echoes of the road has a value of −2.6 cm with a standard deviation of 6.3 cm, meaning that 2008 ground points were systematically lower than the 2010 ground points (Fig. 23A). In addition, the longitudinal distribution of Δ_{Zr} along the road highlights high variation (Fig. 23B). On the upper 1.5 km, Δ_{Zr} varies around 0 m, and it increases downstream with negative values. A systematic error was then detected by this procedure, although the independent quality control checkpoints used by the private company for both surveys showed that the LiDAR data points have been correctly georeferenced (the distributions of *xyz* errors are Gaussian, with mean values equal to zero, according to the data quality control report). The presence of systematic error in LiDAR data can be explained by a multitude of factors, amongst which the most important are generally those controlling the position accuracy: GPS hardware, GPS post-processing, GPS satellite constellation during the flight, boresight alignment, IMU hardware, time offset between sensors, and transformation of data in local coordinate systems. This makes quite difficult the identification of the systematic error origin. The most effective ways to reduce the systematic error are to check the calibration of the system (boresight) during the flight and to implement a strip adjustment using overlapping areas. Our discussions with Sintegra allowed us to make sure that these procedures have been done using the most advanced available protocols. Our own analysis of data quality

showed that the systematic error was not totally eliminated by strip adjustment and that surface matching of multidate point clouds is absolutely necessary before DEM differencing.

After the alignment operation, mean Δ_{Zr} is 0.56 cm with a standard deviation of 6 cm (Fig. 23A), and the spatial variability of Δ_{Zr} was strongly reduced by the merging operation (Fig. 23B). Although it was not possible to demonstrate statistically that the mean error after merging is nonsignificantly different from zero and that the systematic error was totally removed by the co-registration, we considered that the offset was sufficiently reduced for computing a reliable sediment budget. With this alignment, the sediment budget considerably decreased from +48,913 m^3 to –4575 m^3, i.e., a reduction of 109% (Table 3). The impact of the merging operation was also clearly observable on erosion and deposition patterns. Before matching the two data sets, the downstream part of the study reach showed a substantial deposition, the result of the offset between the two LiDAR coverages.

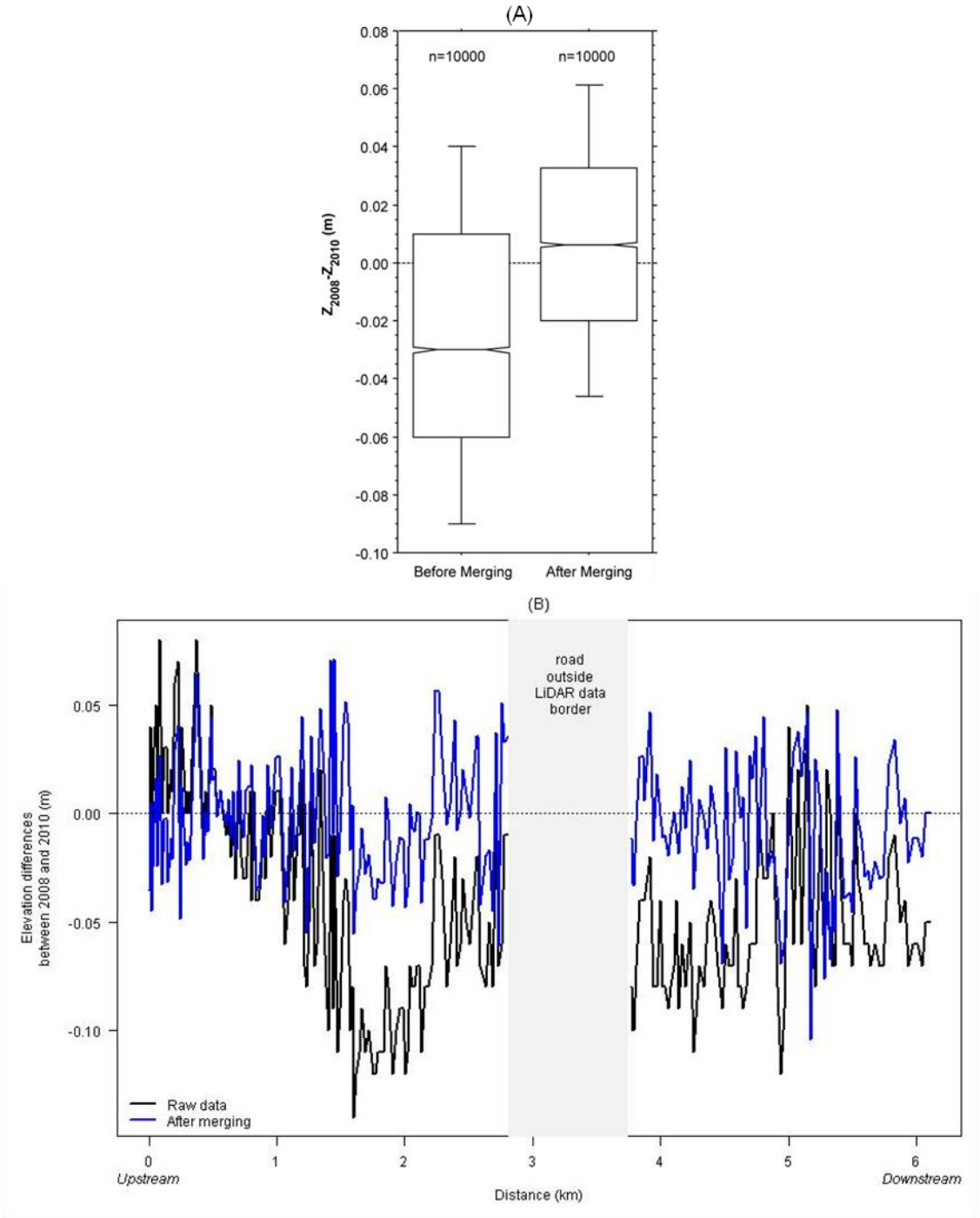

Fig. 23. Elevation differences between 2008 and 2010 ground points situated on the road, before and after the merging of the two sequential point clouds: (A) statistical distributions based on a random sampling of 10,000 points, and (B) longitudinal variation; in (A) n refers to the number of points; boxes represent inner and outer quartiles; horizontal line in the box represents the median; vertical lines represent inner and outer tenths.

Table 3. Volumetric and surficial changes computed from the 2008 and 2010 LiDAR-derived DEMs of the 7-km reach of the Bès River after the different post-processing operations.

			Scour			**Fill**			**Net change**
			Area (m^2)	Volume (m^3)	Mean depth (m)	Area (m^2)	Volume (m^3)	Mean depth (m)	Volume (m^3)
Raw DoD			399 567	123 381	0.31	638 482	172 294	0.27	48 913
After merging operation		Dry surfaces	427 558	118 558	0.28	489 828	120 435	0.25	1 877
		Wet surfaces	67 370	27 473	0.41	53 166	21 021	0.40	−6 452
		Total	**494 928**	**146 031**	**0.30**	**542 994**	**141 456**	**0.26**	**−4 575**
With uncertainty accounting in elevation	Without water depth subtraction	Dry surfaces	191 634	58 256	0.30	220 361	53 432	0.24	−4 824
		Wet surfaces	43 534	15 260	0.35	30 034	11 445	038	−3 815
		Total	**235 168**	**73 516**	**0.31**	**250 395**	**64 877**	**0.26**	**−8 639**
	With water depth subtraction	Dry surfaces	191 634	58 256	0.30	220 361	53 432	0.24	−4 824
		Wet surfaces	69 386	38 215	0.55	40 913	20 994	0.51	−17 221
		Total	**261 020**	**96 471**	**0.37**	**261 274**	**74 426**	**0.28**	**−22 045**

4.2. Sediment budget following uncertainty analysis

The comparison between RTK-GPS and LiDAR points shows a systematic offset of 7 cm on the road and 9 cm on fine-grained exposed gravel bars, showing a systematic under-estimation of altimetry by LiDAR (Fig. 24A). This systematic error increases with the presence of pioneer shrub vegetation but decreases for alluvial forests and river banks. After systematic error correction, statistical distributions of the random error reveal lower values for road and unvegetated or sparsely vegetated exposed gravel bars with a standard deviation of error around 3 cm (Fig. 24B). This precision decreases with more complex terrain (high vegetation density and/or steep slope), with a maximum of 10 cm for river banks (Fig. 24B). The effect of slope on elevation precision is well known, as well as the averaging effect of LiDAR footprint that can explain a stronger deviation with GPS data for rough surfaces. Table 4 summarizes the results of LiDAR data quality control for the different types of terrain.

Table 4. Comparison of airborne LiDAR and ground-based RTK-GPS elevations for different types of terrain; the comparison is based on the April 2010 airborne LiDAR survey and the May 2011 terrestrial survey; N: number of points; SDE: standard deviation of the error; RMSE: root mean square error.

Terrains	N	SDE (cm)	RMSE (cm)
Road	70	2.5	3.1
Fine-grained exposed gravel bars	200	3.3	3.4
Coarse-grained exposed gravel bars	199	3.0	3.6
Exposed gravel bars[a]	399	3.2	3.5
Exposed gravel bars with sparse pioneer vegetation[b]	200	3.1	5.3
Exposed gravel bars with dense pioneer vegetation[c]	198	4.6	6.8
Exposed vegetated gravel bars[d]	398	4.0	6.1
Alluvial forest	189	5.9	6.0
River banks	117	9.9	10.2

[a]Pooling of fine- and coarse-grained gravel bars.
[b]Exposed gravel bars with < 60% of the surface occupied by pioneer shrub vegetation.
[c]Exposed gravel bars with > 60% of the surface occupied by pioneer shrub vegetation.
[d]Pooling of exposed gravel bars with sparse and dense pioneer vegetation.

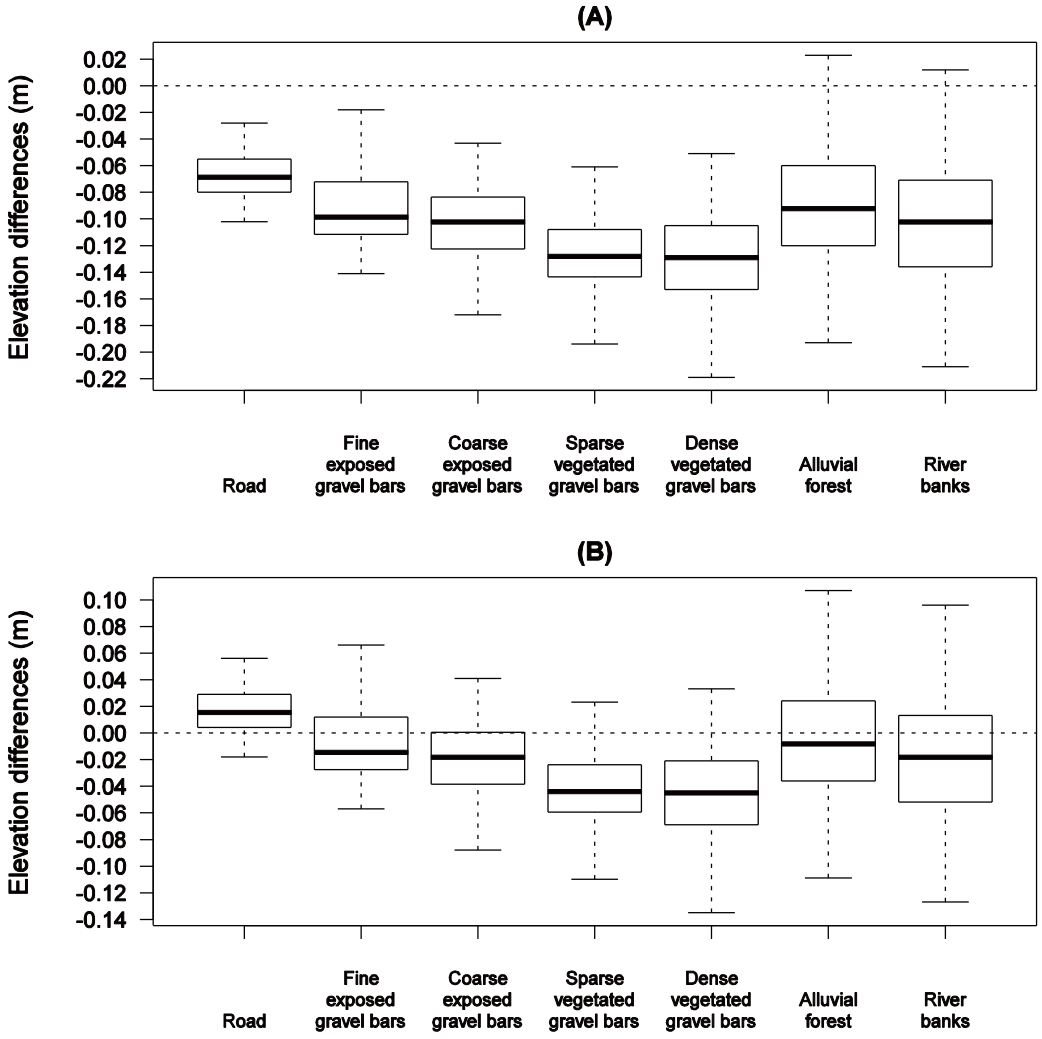

Fig. 24. Elevation differences between LiDAR points and RTK-GPS checkpoints on surfaces with different characteristics, (A) before and (B) after correction of systematic error; n refers to the number of ground points in each bin; boxes represent inner and outer quartiles; horizontal line in the box represents the median; vertical lines represent inner and outer tenths.

As already shown by Heritage et al. (2009) and Milan et al. (2011), the interpolation error calculated as the altimetric difference between LiDAR points and DEM elevations increases with the local topographic variability, and linear regressions can be derived from our data for both the 2008 and 2010 DEMs (Fig. 25). These equations were used to produce a distributed interpolation error as a function of topographic roughness. The median 95% confidence intervals LoD integrating surveying and interpolation errors using Eq. (6) range from 0.17 to 0.30 m depending on surface conditions during both surveys (Table 5). These values are based on the assumption that the surveying error of the 2008 survey is twice as high as for 2010, as attested by the data quality assessment from Sintegra (Table 2).

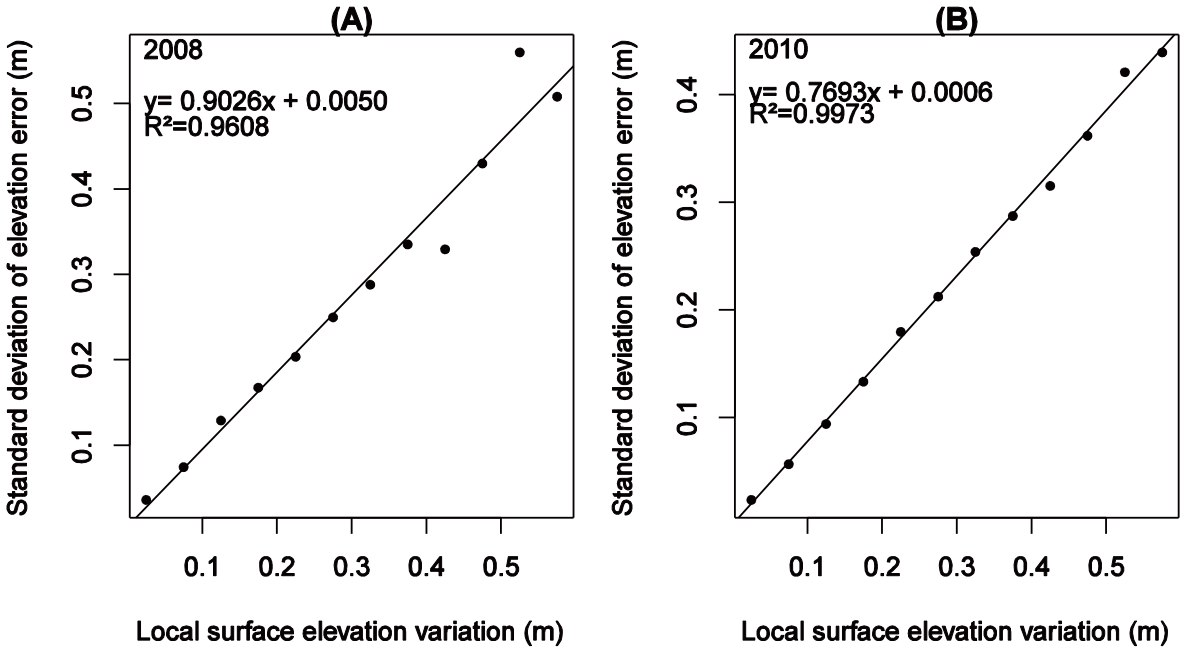

Fig. 25. Standard deviation of interpolation error as a function of local topographic roughness for LiDAR-derived DEMs of 2008 (A) and 2010 (B); standard deviations were averaged using 0.05-m bin of local topographic roughness.

The net sediment budget calculated with DoD thresholding and computation rules for water surfaces shows a considerable difference compared to the budget based only on surface matching, i.e. ,−8,639 m^3 versus –4575 m^3, respectively, corresponding to an 89% increase in absolute value (Table 3). Discarded water surfaces account for 40% of this increase (by removing 1,609 m^3 from the total volume of deposition), and DoD thresholding accounts for 60% (by adding 2,455m^3 to the total volume of erosion). The DoD thresholding has a considerable impact on the net sediment budget of dry surfaces: the 1,877 m^3 positive budget shifted to a 4,824 m^3 negative budget. This is explained by the greater removal of fill surfaces of the exposed channel, those characterized by smaller elevation changes than scour surfaces (Fig. 26A). In fact, total discarded volumes of erosion and deposition for the exposed channel represent 60,302 and 67,003 m^3, respectively. The application of Eq. (7) for the computation of the volume uncertainty for the whole channel gives a value of 58 m^3. This means that the negative net budget of the study reach during the period (− 6,185 m^3) is much higher than the uncertainty level (± 58 m^3).

Table 5. Median value of LoD (cm) for each combination of terrain; (-) corresponds to absence of this combination in data

			2010			
			Exposed gravel bars			
			Unvegetated or with sparse pioneer vegetation	With dense pioneer vegetation	**Alluvial forest**	**Wet surfaces[a]**
2008	**Exposed gravel bars**	Unvegetated or with sparse pioneer vegetation	19	20	-	18
		With dense pioneer vegetation	23	23	-	22
	Alluvial forest		27	30	28	26
	Wet surfaces[a]		17	-	-	17

[a]Only surfaces that respect conditions explained in Fig. 22.

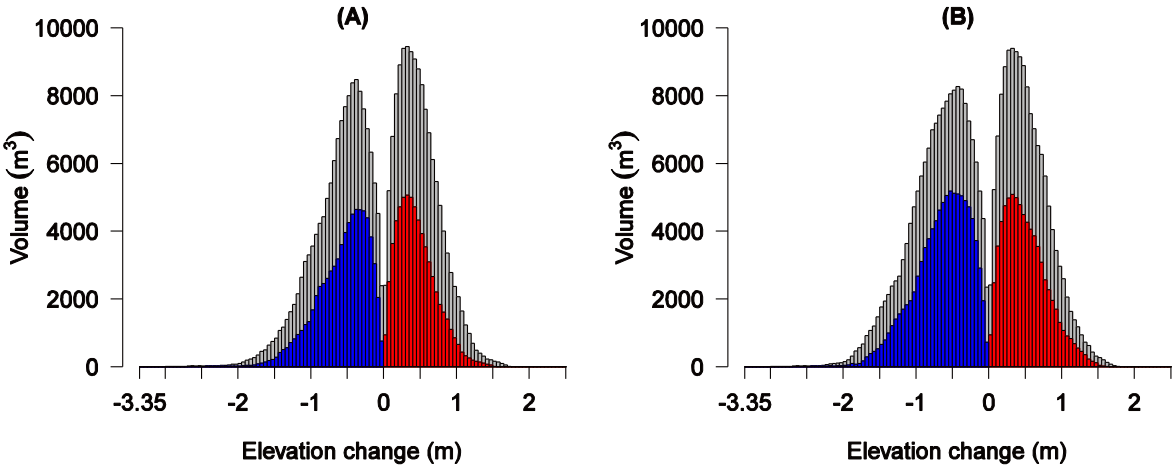

Fig. 26. Distribution of volumetric DoD elevation changes with and without spatially distributed LoD application before (A) and after (B) water depth extraction; unthresholded DoD in grey, and thresholded distribution in red and blue for the erosional and depositional fractions, respectively.

In addition, DoD thresholding also has a substantial effect on the identification of active surfaces of the braided channel. A 53% decrease of the total surface with significant erosion or deposition was obtained after DoD thresholding (Table 3), with a similar decrease for erosion (52%) and deposition (54%). This corresponds to a 50 and 54% decrease for total scour and fill volumes, respectively.

4.3. Sediment budget following water depth subtraction

Water surfaces cover only a few percent of the braided channel surfaces, i.e., 5% in 2008 and 7% in 2010. The lower coverage of submerged surfaces in 2008 is coherent with the lower daily discharge for this period. The normal distribution fits the two distributions of water depths well (Kolmogorov-Smirnov test; $p < 0.01$) (Fig. 27). Mean water depths corresponding to 2008 and 2010 discharges are 20 and 39 cm, respectively. Standard deviations are 9 and 13 cm for 2008 and 2010, respectively.

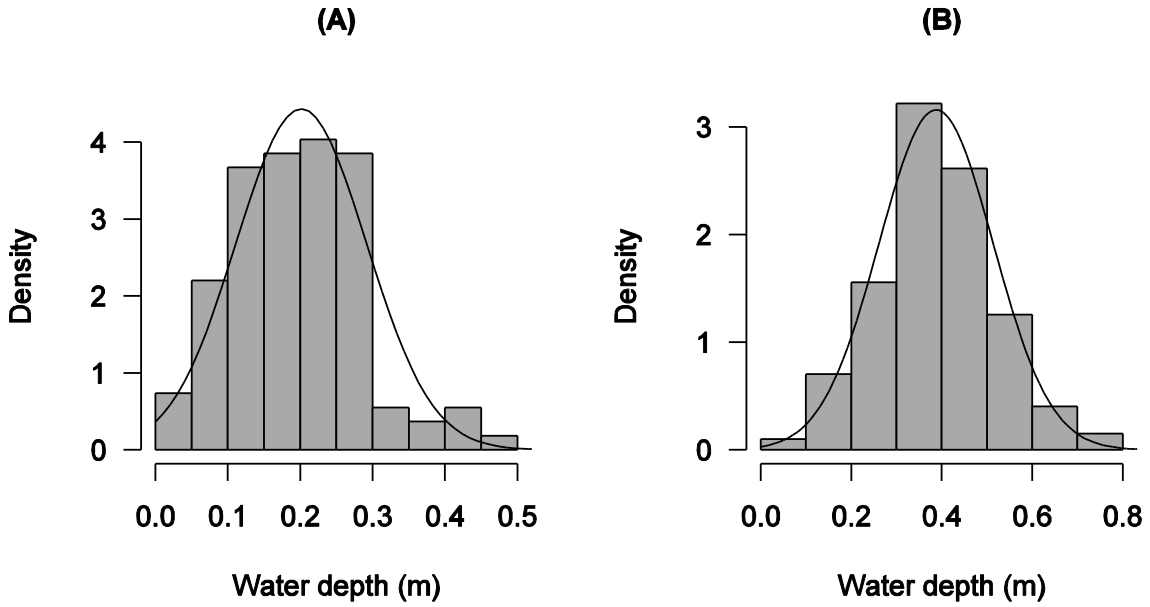

Fig. 27. Distribution of water depths measured in the field and associated normal distribution fits for 2008 (A) and 2010 (B) hydrological conditions.

Fig. 28A shows the distribution of elevation changes between the two DEMs for water surfaces without taking into account water depth. The distribution is normal with a dominance of low negative elevation changes (between 0 and 20 cm). The distribution of elevation changes between the two DEMs is strongly modified when water depth is subtracted from water elevation (Fig. 28B). It becomes bi-modal with a dominance of scour values ranging from 60 to 80 cm. As a consequence, the total scour volume dramatically increases with a total net sediment budget for submerged topography of −17,221 m^3 (Table 3). So submerged topography has a significant impact on the total net sediment budget (−22,045 m^3), corresponding to a 155% decrease in absolute value. Mean depths of erosion and deposition are higher for submerged topography. The mean scour depths are 55 and 30 cm for wet and dry surfaces, respectively. The mean fill depths are lower, with 51 and 24 cm for wet and dry surfaces, respectively.

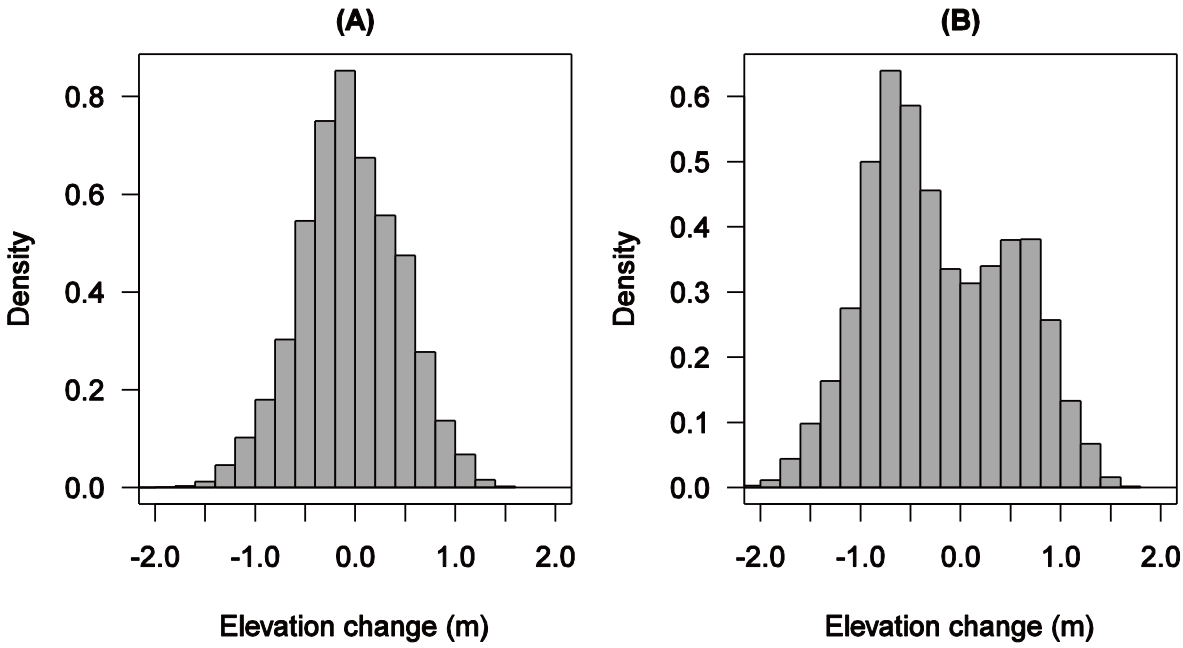

Fig. 28. Distribution of elevation changes between 2008 and 2010 for water surfaces before (A) and after (B) water depth extraction.

Final distribution of volumetric elevation change is bimodal with a mode of [0.30, 0.35 m] for depositional fraction and [-0.55, -0.50 m] for erosional fraction (Fig. 26B). The erosional fraction is slightly larger than the depositional fraction. Depositional fraction is characterized by higher volumes for low elevation changes than erosion fraction. On the contrary, erosion volumes are higher than deposition volumes for high elevation changes. Maximum depths of scour and fill are 2.9 and 1.7 m, respectively. In term of area, both deposition and erosion covered 50% of the total area considered for the sediment budget computation.

4.4. Effect of the 14-year flood on channel forms

The final DoD map including all the successive post-processing steps is shown in Fig. 29. Significant morphological changes are observed. A substantial fraction of the active channel has been reworked, besides some vegetated islands that stayed unchanged. The total active surface finally accounts for 54 and 55% of the 2008 and 2010 active channel surfaces, respectively. Only 18% of vegetated islands have been reworked. Lateral channel shifting is clearly observable with erosion of vegetated terraces or vegetated islands, corresponding to 11 and 5% of total scour volume, respectively. We observed some deposition in secondary channels situated within vegetated island areas. Substantial erosion is related to the formation of new channels via avulsion, and widespread deposition is observed in areas corresponding to low-flow channels in 2008. A 5% increase of the active channel surface was induced by the flood.

A comparison between elevation changes and relative elevations of each DEM shows that deposition occurred preferentially on surfaces characterized by low relative elevations in 2008 (Fig. 30A-C). On the contrary, erosion surfaces are linked with low relative elevations in 2010 (Fig. 30B-D). These two results underline two morphological processes: firstly, an overall filling of low-flow channels associated with bar development; and secondly, bar sculpting with creation of new channels (channel carving).

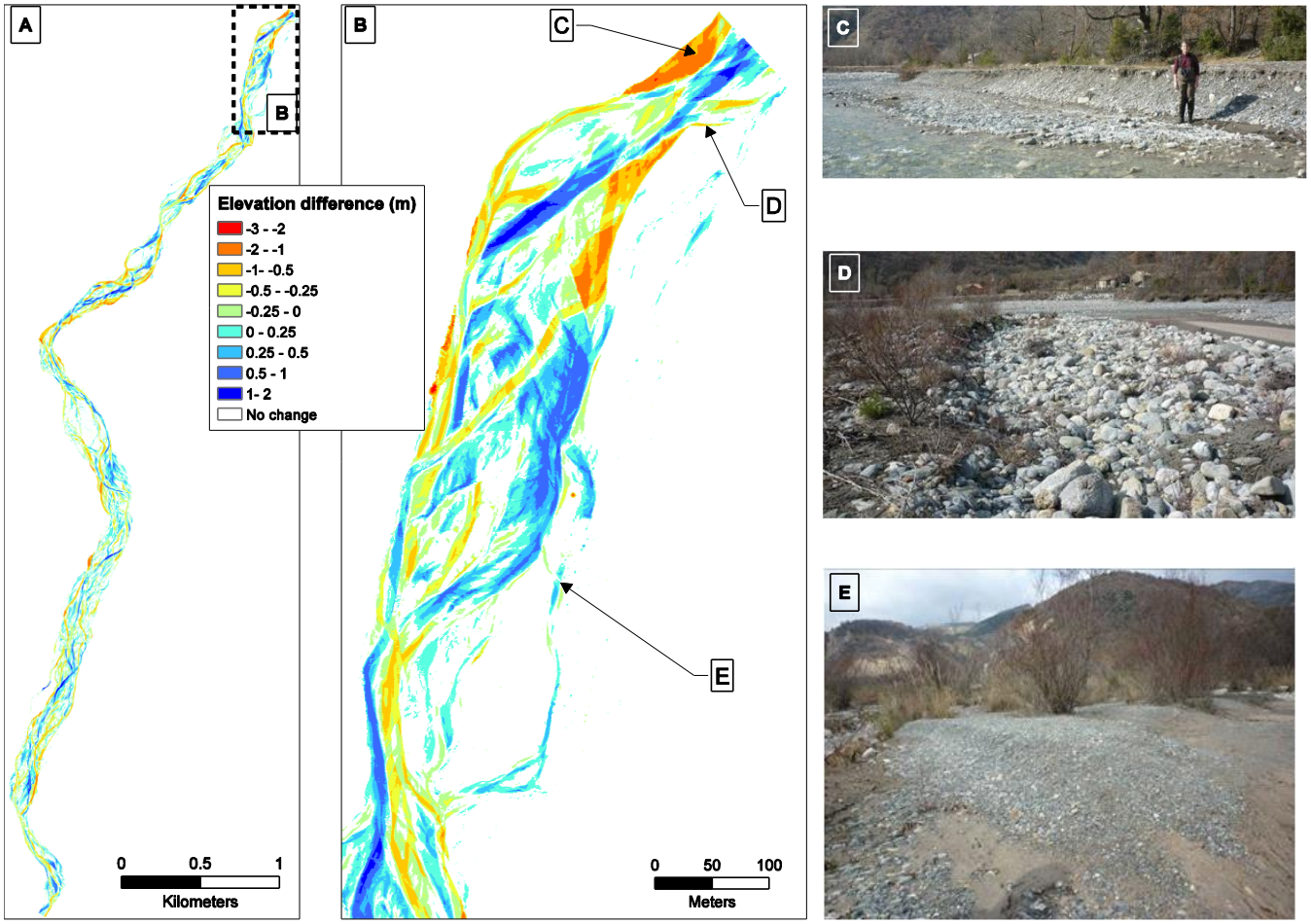

Fig. 29. (A) DEM of difference between 2008 and 2010 after LoD application and depth subtraction; white areas represent areas where elevation changes are lower than the 95% LoD; (B) zoom on the upper part of the study reach, showing typical morphological responses such as lateral shift of the main channel (C) or secondary channel (D), and the formation of a prograding gravel deposits with an avalanche-face in a secondary channel (E).

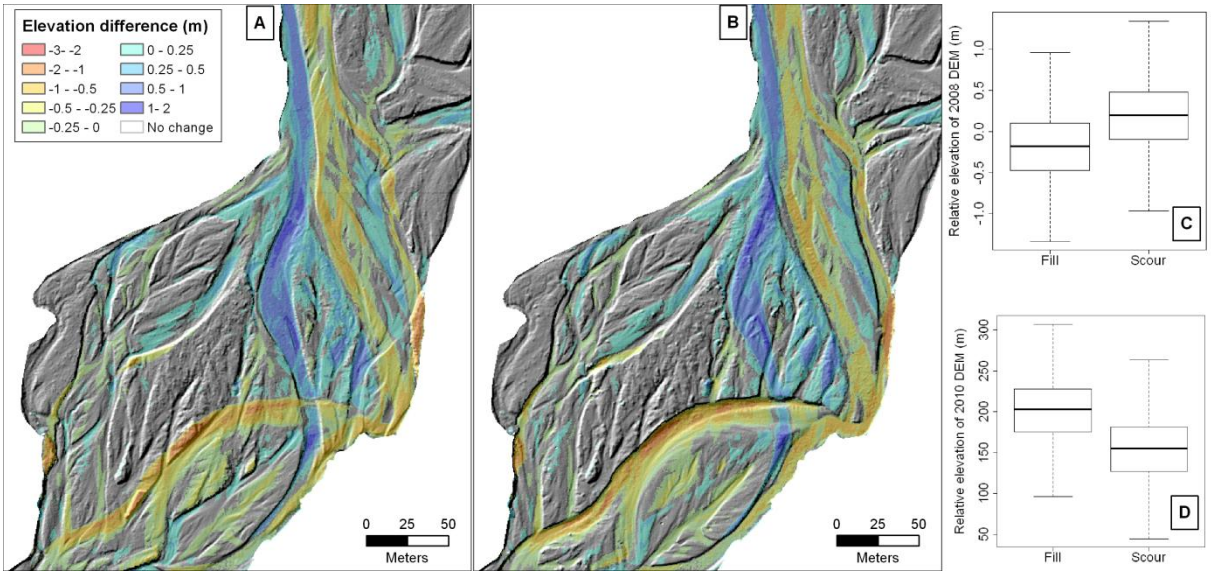

Fig. 30.DoD draped on hillshade views of (A) 2008 and (B) 2010 DEMs ; boxplots of (C) 2008 and (D) 2010 relative elevations for scour and fill pixels.

5. Discussion

This study confirmed that airborne LiDAR data are sufficiently accurate, precise, and reliable to capture the morphological response of a 7-km-long braided river reach with a low relative relief (~ 2 m), provided that great care is taken in the different post-processing steps of the DEMs. The most critical steps for the net budget quantitative extraction are the merging of the sequential ground point clouds and the subtraction of water depths from the submerged parts of the channel. The discarding of nonsignificant elevation changes from uncertainty propagation analysis had a lower effect on the total budget, but it is also a crucial post-processing operation for the comprehensive identification of the spatial patterns of erosion and deposition.

The importance of point cloud merging in diachronic comparisons was already underlined by several studies using airborne LiDAR data in high relief environments (Streutker et al., 2011; DeLong et al., 2012). It is actually evidence that in steep terrains a small planimetric offset will produce a high elevation error. This study confirms that merging is also absolutely necessary in relatively flat river channels, as the propagation of a small systematic error over a large surface has a considerable effect on the volumetric computation of erosion and deposition, and can provide a net budget that is very far from the truth (+48,913 vs. –4575 m^3 in our case, respectively). This point was not explicitly stated in previous studies using sequential airborne LiDAR data in river corridors. This is not a simple problem of georeferencing but rather a problem of alignment of two data sets that have been correctly georeferenced (according to quality

control report) using the same coordinate system. This problem is generally overcome in studies using terrestrial laser scanning by referencing multidate surveys using a set of permanent reflectors deployed in the field before the survey (Milan et al., 2007; Williams et al., 2011). In airborne LiDAR surveys, a direct georeferencing of the laser echoes is provided by the onboard IMU and RTK-GPS and the absolute planimetric accuracy is mainly determined by the performance of these two instruments. In this study, the use of different IMUs during the two surveys, and the changing of satellite constellation during the flight may be the main factors explaining the offset between the two point clouds (Table 2). Moreover, this systematic error was not uniform in space, and therefore, the merging operation needs to be implemented separately for subareas of the braided channel. This processing step can be easily performed with existing surface matching tools, as long as some stable surfaces can be identified in the area of interest.

This study also confirmed the importance of taking into account the submerged topography in the sediment budget computation. A twofold increase of the negative net budget was obtained after subtracting water depths from the two DEMs (the net budget shifted from –8639 to –22,045 m^3 after water depth subtraction). Williams et al. (2011) obtained a similar result for the Rees River where volumes of erosion and deposition derived from wet surfaces were highly significant (46 and 42% of the total volume of erosion and deposition, respectively), even if wet conditions accounted for relatively small areas of the braided channel (25 and 23% of the total surface of erosion and deposition, respectively). Reported values for the Waimakariri River were much more critical, with 66 and 57% of the volumes of erosion and deposition derived from wet surfaces, respectively (Lane et al., 2003). In the case of the Bès River, the relative areas of wet conditions represented 27 and 16% of erosion and deposition surfaces, but accounted for 40 and 28% of erosion and deposition volumes, respectively. In the previously reported study cases, change detection was characterized for regular and small flow events, close to the mean annual flood discharge. For this kind of flow, most of the active channel deformations are probably related to erosion and deposition along and close to the main low-flow channels, which can explain the major contribution of wet areas to the total sediment budget. Results from the Bès show that, even for larger floods prone to rework larger surfaces of the braided channel, the budget error associated with wet area exclusion from DEMs differencing can be significant.

The topography of the submerged channel is notoriously difficult to measure with a high level of precision and accuracy over large coverages. Infrared airborne LiDAR cannot penetrate water, and field measurement is unrealistic over braided rivers at the kilometre scale. This issue is generally overcome using digital bathymetric mapping from synchronous RGB imagery and terrestrial survey of water depths, with a typical range of precision between 20 and 30 cm. In this study, we proposed another approach to estimate channel bathymetry when imagery is not

available, which is frequent in the operational context and can be done retrospectively. The approach requires collecting random samples of water depths in the field for discharge conditions equivalent to those in the LiDAR surveys. This can be easily obtained during one person-day field work with a simple rod as the samples do not need to be localized. The associated random error of the submerged relief can be estimated with the standard error of the mean water depth. Therefore, the uncertainty of volume computation is comparable to those obtained with imagery, as shown by the compilation of studies using ground survey check points to evaluate the quality of remotely sensed braided river DEMs (Table 7). This is true as long as LiDAR data are collected during low-flow conditions. This approach can be used to integrate the submerged topography in the total net budget but cannot be used to derive a comprehensive distributed pattern of erosion and deposition of the submerged channel, as is possible with optical bathymetric mapping (Lane et al., 2003; Rumsby et al., 2008; Williams et al., 2011; Legleiter, 2012).

Table 6. Compilation of studies using synoptic DEMS of gravel-bed braided rivers controlled by independent ground-survey check points (ALS: aerial laser scanning, or airborne LiDAR, OBM: optical bathymetric mapping, TLS: terrestrial laser scanning, BALS: bathymetric aerial laser scanning, TS: total station, RTK-GPS: real-time kinematic global positioning system, ADP: aerial digital photogrammetry); the performance of each technology is assessed with the standard deviation of the error (SDE) between check point and DEM elevations and/or the root mean square error (RMSE) of altimetry, and derived 95% confidence interval level of detection (LoD); NA: not available.

Reference	Site	Space scale	Data set	SDE/RMSE/LoD (cm) exposed	SDE/RMSE/LoD (cm) submerged
This study	Bès River (France) 234 km²	7 × 0.13 km	ALS 04/2010 RTK-GPS 05/2011 (*n*=1386)	3-12/3-12/8-33	NA
Legleiter 2012	Soda Butte Creek (USA)	0.8 km	ALS+OBM 08/2007 TS 08/2007 (*n*=4190)	NA/21/58	NA
Brasington et al. 2012	River Feshie (Scotland) 80 km²	1 × 0.3 km	TLS 07/2007 RTK-GPS 07/2007 (*n*=34266)	14/NA/39	NA
Bailly et al. 2010	Gardon (France)	1.5 km	BALS 03/2007 RTK-GPS 03/2007 (*n*=5443)	NA	20/NA/55
Hicks et al. 2009	Waitaki River (NZ)	4 × 2 km	ALS+OBM RTK-GPS (*n*=207)	5-8/NA/14-22	23/NA/64
Kinzel et al. 2007	Platte River (USA)	11 km	BALS 03/2002 and 06/2005 RTK-GPS 03/2002 and 06/2005(*n*=85)	NA/11/30	NA/18/50
Westaway et al. 2003	Waimakariri (NZ) 4000 km²	3.3 × 1 km	ADP+OBM 02/1999 TS+RTK-GPS 02/1999 (*n*=14930)	26/NA/72	32/NA/89
Westaway et al. 2000	North Ashburton River (NZ)	0.43 × 0.1 km	ADP+OBM 05/1995 TS 05/1995 (*n*=3500)	12/NA/33	25/NA/69

Finally, this study provided a new data set for characterizing the quality of the airborne LiDAR altimetry in the context of braided river channels. The results showed a very high level of precision for dry surfaces (3.5-cm standard deviation of error (SDE) for exposed unvegetated or sparsely vegetated gravel bars). A similar vertical precision was obtained for the Waitaki River by Hicks et al. (2009) with a 5-cm SDE for exposed points that were co-located with a laser shot and 8 cm for exposed points interpolated from nearby laser shots. Other studies using airborne LiDAR altimetry reported much higher SDEs for dry areas: 10 cm for the Waimakariri River (Lane et al., 2003), 21 cm for the Soda Butte Creek (Leigleiter, 2012), and between 11 and 25 cm for the Brenta River (Moretto et al., 2012). A factor that may explain these differences of precision is the density of ground points, which was systematically lower than 3 points m^{-2} in the latter data set versus 7.0 points m^{-2} for the 2010 survey of the Bès River. When compared to other survey techniques, our study shows that airborne LiDAR surveys with a high density of ground points can provide precision for exposed terrains equivalent to terrestrial laser scanning. Standard deviations of error reported from field experiments conducted in braided rivers range between 2 and 14 cm (Milan et al., 2007; Williams et al., 2011; Brasington et al., 2012). The comparison with airborne digital photogrammetry is also meaningful, as the SDE expected from this technique ranges from 12 to 26 cm (Westaway et al., 2000, 2003; Brasington et al., 2003; Lane et al., 2003). However, our study revealed that the precision is highly affected by the presence of a dense vegetation cover (twofold decrease of precision, with a 6-cm SDE for alluvial forest), and the degradation of precision is much higher for river banks (SDE, 10 cm). This increase of precision for vegetated area is caused by the decrease of point density for this area and by the difficulty of vegetation filtration algorithm (Axelsson filter) to completely remove shrub and brush. In fact, this filter is based on a progressive TIN densification where a point is added, if the point meets certain criteria (angle between point and the triangle, distance of the points of the nearest triangle node).

The quality assessment of the LiDAR altimetry from an independent field data set allowed propagating uncertainty for the detection of significant elevation changes. The 95% confidence interval LoD obtained for the Bès River ranged from 19 to 30 cm for the different combinations of exposed surface conditions. This range of values can be compared to reported critical thresholds for braided rivers, obtained for different combinations of techniques (Table 7). This compilation of results clearly shows that high density airborne LiDAR can provide a very high level of detection, as high as some of the reported values for terrestrial laser scanning and significantly higher than the reported values for sequential airborne LiDAR (Hicks et al., 2008; Moretto et al., 2012). As previously shown, this may be related to the ground point density, which is known to have a considerable effect on elevation precision (Wheaton et al., 2010; Milan et al., 2011). Although we can't propose a formal analysis of the effect of point density on elevation precision in

this study, we can, however, show that ground point densities between 5 and 8 points m^{-2} provide a very high level of elevation precision for exposed braided channels.

This study showed that a 14-year return period flood induced significant morphological changes for 54% of the active channel, with erosion of vegetated terraces or vegetated islands. Channel network has been completely reset with very frequent channel avulsions. This result confirmed the observations on the Tagliamento River (Bertoldi et al., 2010), which showed that floods with a return period higher than 2 years, defined as flood pulses, induce a complete rearrangement of the channel network: 60% of the active width underwent changes for a 3-year return period flood. On the Waimakariri River, Hicks et al. (2008) measured significant erosion and deposition on 60-65% of the riverbed for subannual frequency events. This new study confirmed the high level of disturbance in braided river environment for larger floods with a significant reorganisation of terrestrial and aquatic patches.

Table 7. Compilation of studies using sequential DEMs in gravel-bed braided rivers for morphological change detection (ALS: aerial laser scanning, or airborne LiDAR, OBM: optical bathymetric mapping, TLS: terrestrial laser scanning, TS: total station, RTK-GPS: real-time kinematic global positioning system, ADP: aerial digital photogrammetry, ODP: oblique ground-based digital photogrammetry, OAP: oblique ground-based analytical photogrammetry); the performance of each approach is indicated with the 95% confidence interval level of detection (LoD) used to distinguish channel deformation from noise; NA: not available.

Reference	Site	Space scale	Data set	LoD dry-dry (cm)	LoD wet-wet (cm)
This study	Bès River (France) 234 km²	7 × 0.13 km	ALS 10/2008 ALS 04/2010	19-30	NA
Moretto et al. 2012	Brenta River (Italy) 1567 km²	4.5 × 0.8 km	ALS+OBM 08/2010 ALS+OBM 04/2011	36–54	75–86
Williams et al. 2011	Rees River (NZ) 405 km²	2.5 × 0.7 km	TLS+OBM 10/2009 TLS+OBM 04/2010	25	25
Milan et al. 2011	River Nent (UK) 30 km²	0.4 km	TS 07/1998 TS 10/1998 TS 07/1999	22 19	
Rumsby et al. 2008	River Feshie (Scotland) 80 km²	0.8 × 0.18 km	ADP+OBM 08/2000 RTK-GPS 08/2002	6-35	14-66
Hicks et al. 2008	Waimakariri River (NZ) 4000 km²	3 × 1.5 km	ADP+OBM 02/2000 ALS+OBM 05/2000 ALS+OBM 07/2003	32 28	65 69
Milan et al. 2007	Glacier du Ferpècle (Switzerland)	0.12 × 0.06 km	TLS 06/2004 (×9)	6	13
Lane et al. 2003	Waimakariri River (NZ) 4000 km²	3.3 × 1 km	ADP+OBM 02/1999 ADP+OBM 03/1999 ADP+OBM 02/2000 ALS+OBM 05/2000	72 56 32	80 66 65
Fuller et al. 2003	River Coquet (UK) 255 km²	1 × 0.05 km	TS 03/1999 TS 03/2000	24	
Brasington et al., 2003	River Feshie (Scotland) 80 km²	0.3 × 0.08 km	RTK-GPS 07/2000 ADP+OBM 07/2000	6 41	14 80
Chandler et al. 2002	Sunwapta River (Canada) 30 km²	0.125 × 0.08 km	ODP+TS 07-08/1999 (x13)	13	
Brasington et al. 2000	River Feshie (Scotland) 80 km²	0.2 × 0.08 km	RTK-GPS 07/1998 RTK-GPS 07/1999	7	

6. Conclusion

Sequential airborne LiDAR surveys were used to reconstruct the morphological response of a 7-km-long braided river channel to a 14-year flood that occurred in December 2009. The different post-processing steps of the raw data included (i) surface matching of the sequential ground point clouds, (ii) spatially distributed propagation of uncertainty in absolute elevations based on an independent ground-based data set, and (iii) integration of submerged topographic changes based on mean water depths obtained for discharge conditions of the two LiDAR surveys. Data analysis revealed that the merging of the sequential ground point clouds and the water depth subtraction both have a considerable effect on the total net sediment budget of the study reach. A simple method for the subtraction of water depths without using classical optical bathymetric mapping is proposed. This method can be used to integrate the submerged topography in the sediment budget computation, but it cannot provide a comprehensive spatial pattern of channel deformations for the submerged parts of the river corridor. The data quality assessment based on a comparison with independent checkpoints measured in the field revealed that a very high level of detection of elevation changes can be achieved with high density airborne LiDAR data for the exposed part of the braided channel.

CHAPITRE 3

SIGNATURES LONGITUDINALES DE LA MORPHOLOGIE DES RIVIERES EN TRESSES

A. Résumé

La morphologie des rivières en tresses est caractérisée par une juxtaposition de différentes unités définies par des échelles spatiales et temporelles différentes. Des levés LiDAR aéroportés ont été désagrégés en multiples profils en travers, régulièrement espacés de 10 m pour étudier la variation longitudinale de la morphologie en travers à l'échelle de plusieurs kilomètres (1 à 7 km). L'analyse a porté sur un linéaire de plus de 25 km réparti sur 9 sites, dans les bassins versants de la Drôme, du Drac et de la Bléone (Alpes françaises). Un site d'étude a été levé deux fois pour étudier les changements temporels de la morphologie en travers causés par une crue de période de retour 14 ans. Différents indicateurs morphologiques ont été calculés pour chaque section en travers; notamment la largeur de la bande active (*W*) et un indice de la variabilité altimétrique du profil en travers (Bed Relief Index, *BRI*). Les signaux de la largeur de la bande active montrent des fluctuations avec une alternance de séquence d'expansion et contraction de la bande active à différentes échelles. Les changements majeurs du signal de la bande active sont expliqués par des effets de confinement et d'obstruction de la tresse par le fond de vallée. La signature du signal du *BRI* est plus contrôlée par l'histoire récente du chenal et notamment par l'effet de la dernière crue significative. Deux périodes caractéristiques ont été mises en évidence à partir de ces signaux : autour de 3-4 et de 9-10 fois à la largeur de la bande active. La période à 3-4 serait liée à la dynamique des macroformes (bancs élémentaires). La période à 10 pourrait être liée à la dynamique de transfert à long terme des sédiments et pourrait correspondre aux successions longitudinales des mégaformes sédimentaires. Des investigations supplémentaires permettraient de confirmer ces hypothèses.

Mots clés : rivières en tresses, LiDAR aérien, morphologie en travers, signature longitudinale, longueur d'onde.

B. Longitudinal signatures of braided river morphology

Abstract

Morphology of braided rivers is characterised by a juxtaposition of different units that act on a wide range of spatial and temporal scales. Airborne LiDAR surveys of 9 study reaches distributed on five braided rivers in French Alps were disaggregated into 10 m-regularly space cross-section to look at longitudinal variation of cross-sectional morphology at the scale of several kilometers (from 1 to 7 km). One study reach was survey twice to look at the temporal change of cross-sectional morphology due to a 14-yr return period flood. Different indicators of cross-sectional morphology have been calculated on each cross-section: notably active channel width (*W*) and bed relief index (*BRI*). Active channel width signals show fluctuating pattern with multi-scale alternating sequences of expanded and contracted active channels. Major shifts in the active width pattern are explained by the confinement and obstruction effects of the valley floor. *BRI* signatures are more controlled by the recent history of the channel and notably by the effect of the last significant flood. From these signals, two characteristic wavelengths have been identified: 3-4 and 10 times the active channel width. The first could be link to the dynamics of macroforms and the second to the dynamics of megaforms, but more investigations are needed to confirm this hypothesis.

Keywords: braided gravel-bed rivers, airborne LiDAR, cross-sectional morphology, longitudinal signature, wavelength.

1. Introduction

Braided rivers are characterised by a complex network of several low-flow channels, which diverge and converge, interspersed with gravel bars with or without sparse vegetation. Morphology of braided channel is also characterised by a juxtaposition of gravel bars that act on a wide range of spatial and temporal scales. Unit bars are composed of one or several gravel sheets. Unit bars can coexist into complex bars. These complex or compound bars reflect development by a succession of depositional and erosional events that are partially recorded in bar morphology and sedimentology (Rice et al., 2009).

Different indicators were used to describe braided river morphology both in flume and in the field. There are indicators of planform morphology with the braiding index and active channel width. Braiding index measure the degree of braiding and are more or less sensitive to river stage, depending of type of braiding index (channel count, total sinuosity or bar indices, cf. review of Egozi and Ashmore, 2008). In the field, a complex link between braided geometry (braiding index and active width), flood periodicity, sediment regime, and groundwater have been shown by Piégay et al. (2009) and Belletti et al. (2013b). In flume experiments, effects of changing sediment supply conditions on planform morphology have been well studied (Ashmore, 1991a; Hoey and Sutherland, 1991; Germanoski and Schumm, 1993). During aggradation, an increase of bar number, braiding intensity and active channel width are observed, while inverse trends occurred during degradation. Field studies also showed that active channel width normalized by catchment size (W^*) is correlated with the time since the last 10-yrs flood occurred and it is a good proxy of the sediment supply to the braided channel (Piégay et al., 2009; Belletti et al., 2013b). This was confirmed by a recent study showing that, for a given catchment area, aggraded braided reaches have a wider active channel than degraded braided reaches (Liébault et al., 2013a).

There are indicators of cross-sectional morphology like the bed relied index (*BRI*). Bed relief index (*BRI*) can be used to study the morphological signatures of aggraded and degraded braided channels, with the statement that transport-limited systems tend to generate flat beds with low roughness, where energy dissipation is low since all the available energy must be used to transport the imposed sediment load. Conversely, supply-limited systems tend to produce channels with higher roughness to dissipate the energy in excess related to lower sediment supply. Flume experiments of Hoey and Sutherland (1991) and Leduc (2013) demonstrated low value of bed relief index in aggradation and high value in degradation due to the incision of main channel into bars. Contradictory observations were reported by Germanoski and Schumm (1993), who observed an increase of bed relief index during aggradation over the entire braided channel due to

new bars formation, or a decrease when aggradation took place only in active anabranches. These contradictory observations can be linked to the difference in bed relief computation. Field works of Liébault et al. (2013a) on a set of French alpine braided rivers showed better agreement with the results of Hoey and Sutherland (1991) and Leduc (2013).

Recently, Liébault et al. (2013a) used channel entrenchment of active channel in recent wooded terraces (*T*) as an index of bed-level adjustment since the 1950s. They observed a relation between *BRI* and *T* with an increasing bed relief with an increase of *T*. However certain reaches showed low *BRI* for high value of *T*. Their channels are highly incised in wooded terraces but their present-day channel morphology seems to show signs of recovery with the cessation of gravel mining.

Channel morphology of braided rivers has been recently studied to identify characteristic lengths of braided pattern, as it was already done a long time ago for single-thread channels, which have a definable morphological wavelength that scales linearly with channel width defined by the channel spacing of pool-bar units or the wavelength of quasi-regular meanders. From physical models and full-scale rivers, Hundey and Ashmore (2009) highlighted a scale for confluence-bifurcation length, which correspond to 4–5 times the channel width. Zanoni et al. (2008) observed two different scales with Fourier and wavelet analysis of braided river longitudinal topography from physical models. A large scale is related to the planform configuration with a wavelength equal to about three times the active channel width. This scale is observed on the width, the total braiding index and the mean bed elevation data. A shorter scale is revealed from active part of the network with a wavelength equal to about 1.5 times the channel width. This scale is highlighted from active braiding index and the cross-section variability.

The development of airborne LiDAR (light detection and ranging) provides the opportunity to gather fully 3D topography over reaches of several km. It is therefore possible to calculate the previous index, notably W and *BRI* in generalizing cross-sections and exploring longitudinal patterns of indicators. In calculating *BRI* all along a given cross-section, it is possible to explore in real conditions topographic signal and verify if a periodicity exist.

The goals of this paper are to improve understanding of longitudinal signature of braided channels from LiDAR-derived cross-sections of braided rivers by comparing spatial and temporal geomorphic patterns. Can we highlight characteristics wavelength from cross-sectional indicators? To accomplish this, we used high-resolution digital elevation models derived from airborne LiDAR data of a set of braided rivers, and two multitemporal airborne LiDAR surrounding a 14-year return period flood on the Bès River.

2. Study sites

Study sites are situated on five braided rivers of the Southern French Prealps: the upper Drac River, the Bléone River and its main tributary the Bès River, the Drôme River and its tributary the Bez River (Fig. 31). These rivers have been already studied by Piégay et al. (2009), Belletti et al. (2013a, b, 2014) and Liébault et al. (2013a) in a regional context. These study reaches were selected by the availability of LiDAR surveys. General characteristics of study sites are presented in Table 8.

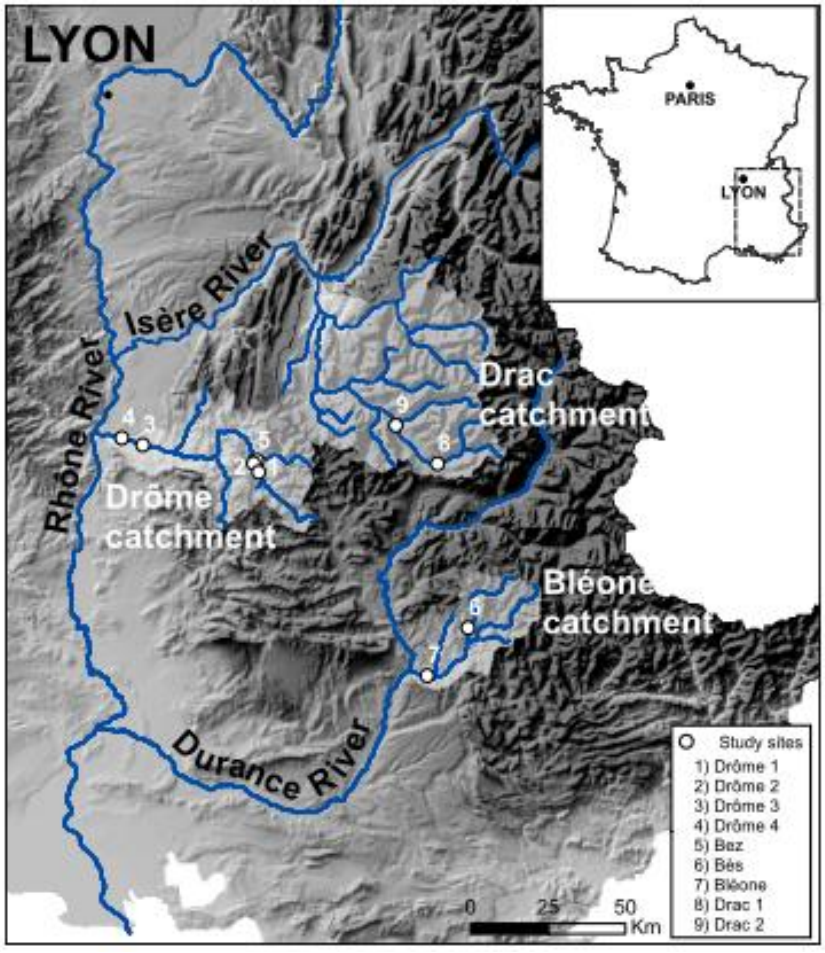

Fig. 31. Location of study sites in SE France.

Table 8. Characteristics of the study sites at the time of LiDAR surveys; NA: not available. Bès 08 and Bès 10 correspond to the Bès study reach surveying in 2008 and 2010, respectively.

Catchment	Drôme					Upper Drac		Bléone		
Geology	Limestones and marls					Marls, limestones and sandstones and metamorphic and intrusive rocks		Limestones, marls, sandstones and molassic rocks		
Hydrology	Snowmelt and Mediterranean conditions					Mountainous and Mediterranean influences		Mountainous and Mediterranean influences		
Altitude (min-max asl)	86-2 000					765-3 400		405-2 961		
River	Drôme				Bez	Drac		Bléone	Bès	
Study sites	Drôme 1	Drôme 2	Drôme 3	Drôme 4	Bez	Drac 1	Drac 2	Bléone	Bès 08	Bès 10
Drainage area (km²)	253	261	1529	1633	269	265	766	890	234	
Main stream length (km)	1.04	1.45	3.65	2.32	2.42	2.22	4.66	3.19	7.20	7.21
Channel slope	0.008	0.007	0.005	0.004	0.011	0.010	0.011	0.007	0.012	
Date of LiDAR survey	13-14/09/2010					08/02/2011		14/04/2011	27/10/2008	19/04/2010
Hydrometric station	Luc-en-Diois		Saillans		Châtillon-en-Diois	Chabottes	St-Jean-St-Nicolas	-	Pérouré	
Mean daily discharge frequency during LiDAR survey	0.08-0.09		0.14-0.13		0.14-0.12	0.33	0.3	NA	0.14	0.78
Number of months since the last Q_{10} flood	81 (Q>50 years)					NA	NA	NA	182	4
Number of months since the last Q_2 flood	-				9	NA	NA	NA	60	-

The Drôme River underwent intensive gravel mining and embankment and few braided reaches have persisted. Two study sites (Fig. 32B-C), Drôme 1 (midpoint at 44°38'38.34" N., 5°25'33.18" E.) and Drôme 2 (midpoint at 44°39'57.16" N., 5°24'42.69" E.) are situated on the upper Drôme between Luc-en-Diois and the confluence with the Bez. Here, the river is characterised by alternating straight single-thread and braided sections. Two other sites (Fig. 32E-F), Drôme 3 (midpoint at 44°44'1.83" N., 4°57'41.71" E.) and Drôme 4 (midpoint at 44°45'33.32" N., 4°52'32.69" E.), are situated on the lower part of the Drôme River, upstream of the town of Livron. They correspond to preserved braided reaches of the lower Drôme valley, which has been embanked along most of its course. These two braided reaches are part of the "Ramières du Val de Drôme" Natural Reserve. Another site (midpoint at 44°40'42.20" N., 5°25'30.05"E.) is situated on a right bank tributary of the upper Drôme, the Bez River, with a drainage area of 227 km² (Fig. 32D).

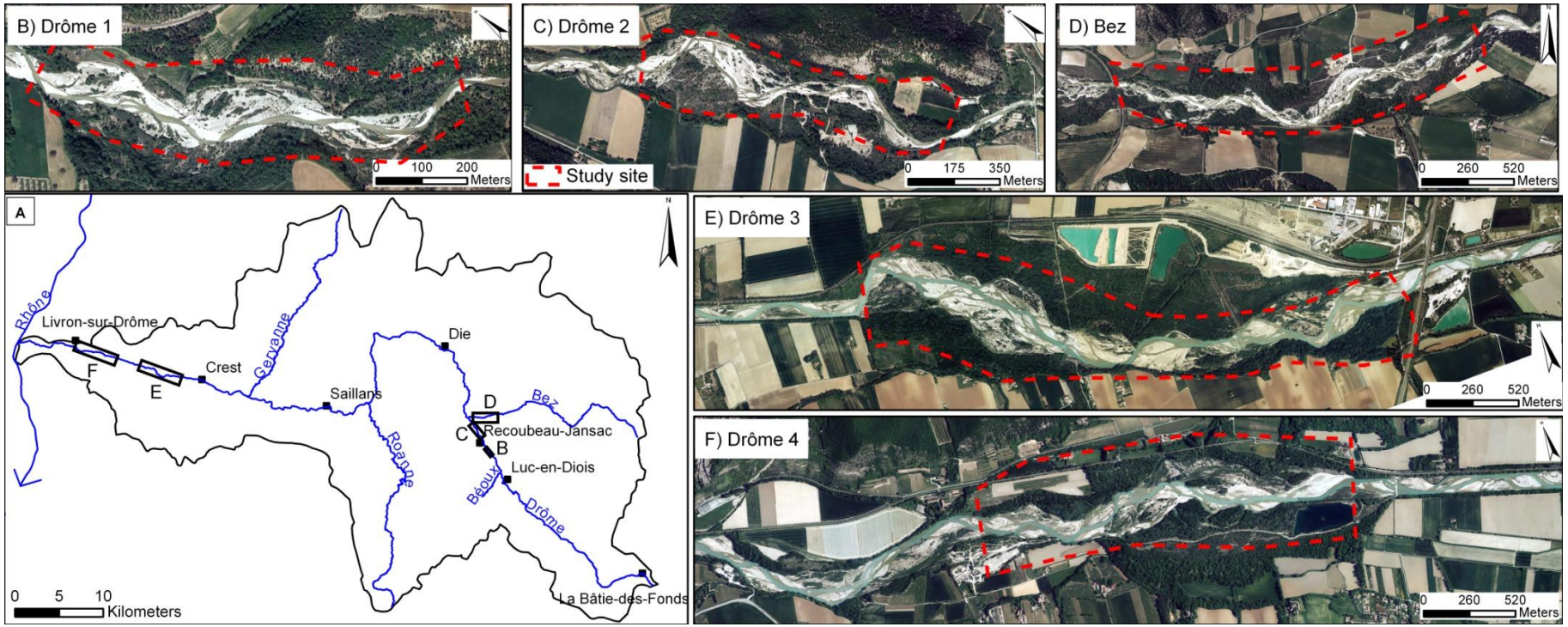

Fig. 32. (A) Drôme catchment with location of aerial photography zooms (B to F) showing study site limits; source: Orthophotos 2010 IGN.

The two study sites on the Drac River are situated on the upper catchment, upstream of the Sautet reservoir. Gravel mining was intensive during the 1980s and 1990s, with ~20 mining sites along the river. It gradually stopped between 2008 and 2012, except for a site at the entrance of the Sautet reservoir. The Drac 1 site (midpoint at 44°38'57.10" N., 6° 9'14.00" E.; Fig. 33B) is situated in the downstream part of the Chabotte plain, and the Drac 2 site (midpoint at 44°45'36.62" N., 5°59'39.53" E.; Fig. 33C) corresponds to a braided section confined in a steep valley upstream to the Sautet reservoir. These two sites are situated just upstream to a gravel mining site, closed for the Drac 1 reach.

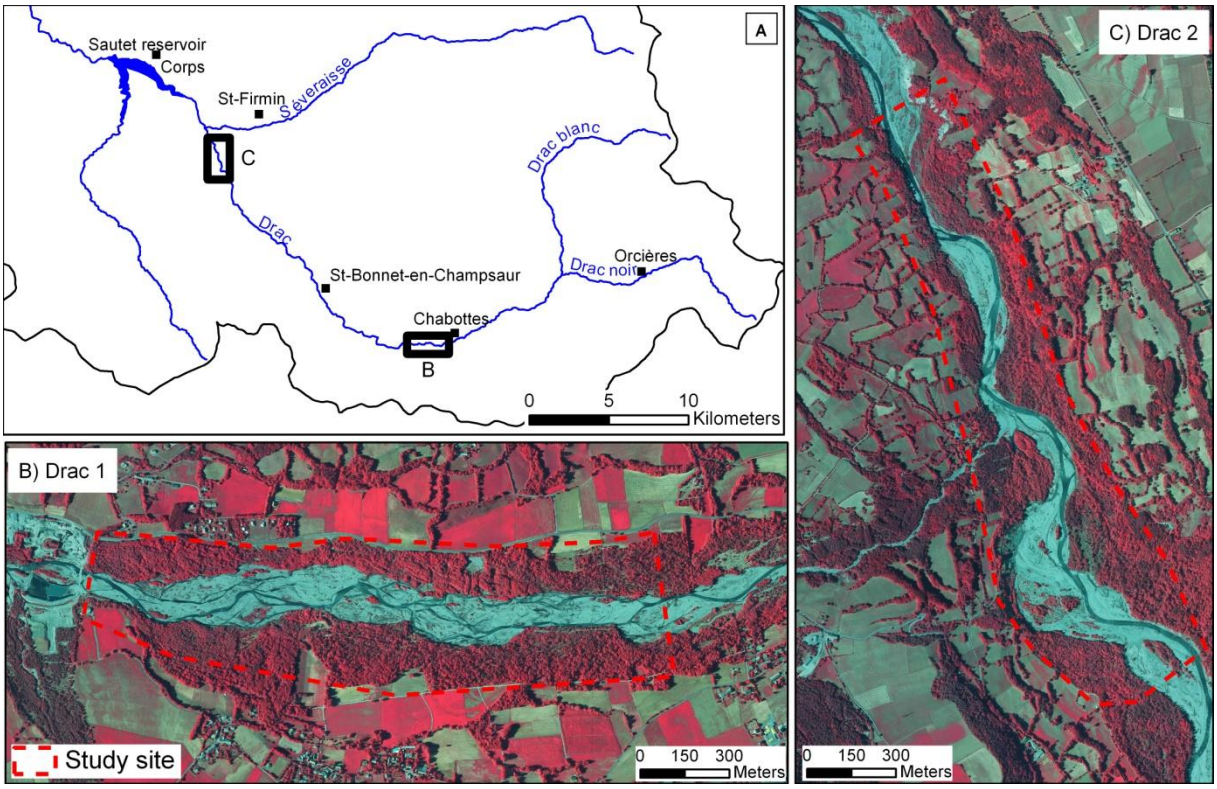

Fig. 33. (A) Upper Drac catchment with location of aerial photography zooms (B-C) showing study site limits; source: Infrared orthophotos 2009 IGN.

A study site was selected on the lower Bléone River upstream to Malijai reservoir, in the unconstrained part of this intensively embanked valley (Bléone, midpoint at 44° 2'9.09" N., 6° 4'12.68" E.; Fig. 34C). Two sites of gravel extraction are located upstream and downstream of the study site (stopped in 2002). Another site (Bès, midpoint at 44°09’32.89’’ N., 6°14’36.49’’ E.; Fig. 34B) covers the last 7 km of the Bès River, the main tributary to the Bléone River, with a drainage area of 234 km².

On the Bès River, temporal pattern of braided morphology was studied with the comparison of two topographic surveys (27 October 2008, 19 April 2010). Hydrology between the two surveys is

characterized by a main flood composed of two successive peaks between the 22 and 24 December 2009, with a return period of 10- and 14-yr, respectively. The instantaneous peak discharge was estimated at 171 m^3 s^{-1}. This multi-peak flood was generated by a rapid air temperature warming associated with a wet Mediterranean southwestern depression, when the catchment was covered by a substantial snow layer (Navratil et al., 2012). For the rest of the period, discharges were low with high spring flows of moderate intensity.

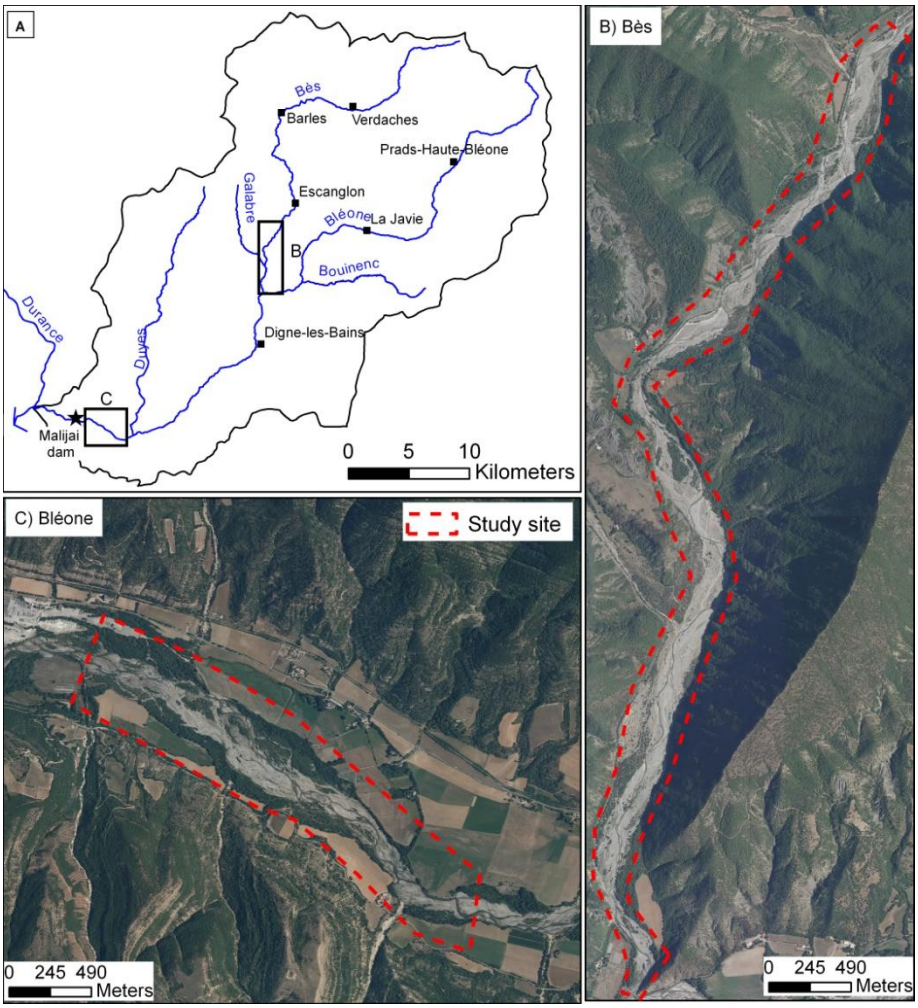

Fig. 34. (A) Bléone catchment with location of aerial photography zooms (B and C) showing study site limits; source: Orthophotos 2009 IGN.

3. Methodology

3.1. LiDAR specifications

Two private companies were in charge of the LiDAR surveys: Sintegra for the Drac and Bléone sites and Helimap for the Drôme sites. Technical specifications of airborne LiDAR surveys are described in Table 9. DEMs of 0.5 or 1 m resolution were derived from ground point clouds by triangulation and linear interpolation, which provide good interpolation method for river channel morphology (Heritage et al., 2009).

Table 9. Technical specifications of airborne LiDAR surveys; the altimetric and planimetric errors were provided by the private company from RTK-GPS ground control points locally measured on a road; SDE: standard deviation of error; NA: not available.

	Bléone sites			Drôme sites	Drac
	Bès		Bléone		
Date	27/10/2008	19/04/2010	14/04/2011	13-14/09/2010	08/02/2011
Company	Sintegra	Sintegra	Sintegra	Helimap	Sintegra
Laser scan	Riegl LMS Q560	Leica ALS60	Riegl LMS Q560	Riegl VQ 480	Riegl LMS Q560
Elevation precision of laser points (SDE in cm)	10	5	10	5.2	1.5
Planimetric precision of laser points (SDE in cm)	15	15	25	NA	25
Ground point density (points m^{-2})	7.6	6.4	4.1	3.5	4
DEM resolution (m)	0.5	0.5	1	0.5	0.5

3.2. Geomatic procedure to extract geomorphic indicators

3.2.1. Cross-sectional morphometry

Cross-sectional geometry was extracted from LIDAR-derived DEMs on regularly-spaced cross-sections. Cross-sections were automatically extracted in ArcGIS from the centerline of the active channel, with a spacing of 10 m (Fig. 35). Cross-section lines were systematically

perpendicular to the active channel centerline. Cross-section lines were converted in point spacing every 0.5 or 1 m depending on the DEM resolution and DEM pixel elevation were extracted to each point. Indicators were then automatically calculated with a specifically designed R script, from these point databases. Cross-sectional geometry corresponds to topography of dry areas and water surface. In fact, infrared airborne LiDAR cannot penetrate water, but recent studies shows that water surface elevations could be derived from LiDAR points (Legleiter, 2012; Lallias-Tacon et al., 2014).

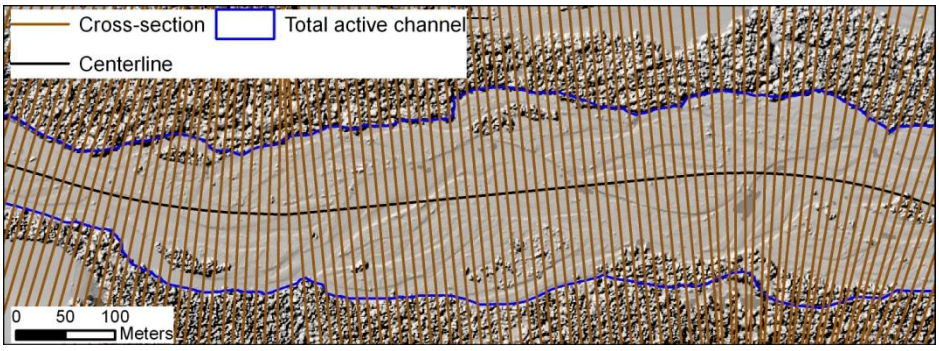

Fig. 35. Example of 10 m-regularly spaced cross-sections, derived from a centerline.

Active channel width and bed relief index (*BRI*) were used to characterize cross-sectional geometry. *BRI* is calculated as the standard deviation of elevation on the entire active channel width, and it gives an index of the channel macro-roughness (Liébault et al., 2013a). As LiDAR-derived cross-sections do not include topography of submerged surface because infrared airborne LiDAR cannot penetrate water, LiDAR data were collected during low-flow conditions (Table 2) to minimise effects of water flow level on *BRI* computation. In cross-sections where vegetated islands are presents, a *BRI* is calculated for each section on either side of the island and a composite *BRI* is calculated as the weighted average of *BRI* of each section according to their length.

On the Bès River, for each cross-section, the number of wetted channels was also extracted from delineation achieved on LiDAR-derived point density maps following the approach of Legleiter (2012) based on the low point density of water surfaces (Fully details in 3.3.2 of chapter 2 and Fig. 21).

Change in inter-data morphological signatures was studied on the Bès River using two sequential LIDAR derived-DEMs, surrounding a 14-yr flood. In this case, we also extracted these indicators to explore their significance in term of changes through time.

3.2.2. Channel entrenchment into recent alluvial terraces

We measured channel entrenchment into recent alluvial terraces. In fact, in the French alpine rivers, wooded terraces in the margins of active channels generally correspond to an old braided channel that has been abandoned during the second half of the 20th century following channel narrowing and incision (Liébault and Piégay, 2002). Therefore, their elevation is a good approximation of the active channel elevation during the first half of the 20th century. These terraces were identified by the combination between the channel extent in 1950s mapped on photographs of this period (1948-1969) and the terrace observed on the DEM (Fig. 36). For each cross-section concerned by the presence of 1950s terrace, elevation differences between mean elevation of these terraces for each banks and mean elevation of active channel (named *T*) were calculated to have a value of channel entrenchment into recent alluvial terraces. Higher *T* was conserved between both banks.

3.2.1. Sediment budget

The method used to generate DEM of Difference (DoD) between the two LiDAR-derived DEM and the sediment budget computation is fully detailed in Lallias-Tacon et al., 2014. Sediment budget is segregated at the sub-reach scale of 10 m to explore spatial fluctuation.

3.3. Longitudinal variation of indicators

Longitudinal variations of indicators are analysed to explore any change in longitudinal signal. Wavelet transform analysis was performed with Morlet function as "mother wavelet" for characterizing the fluctuations. Wavelet transform is more suitable than fourier Transform to detect specific non-stationary processes embedded in space series occurring at multiple scales with space-varying amplitude and frequency. Morlet wavelets have already been used by for characterizing fluctuations of morphological parameters in a flume experiment of braided pattern (Zanoni, 2008). Global wavelet spectrums were computed for each indicator, which allows examining energy fluctuations in function of period. Major peaks of energy were identified and corresponding periods have been scaled with active channel width (characteristics wavelength). Only peaks out of cone of influence limits were conserved. Morlet function of "dplR" package has been used in R software.

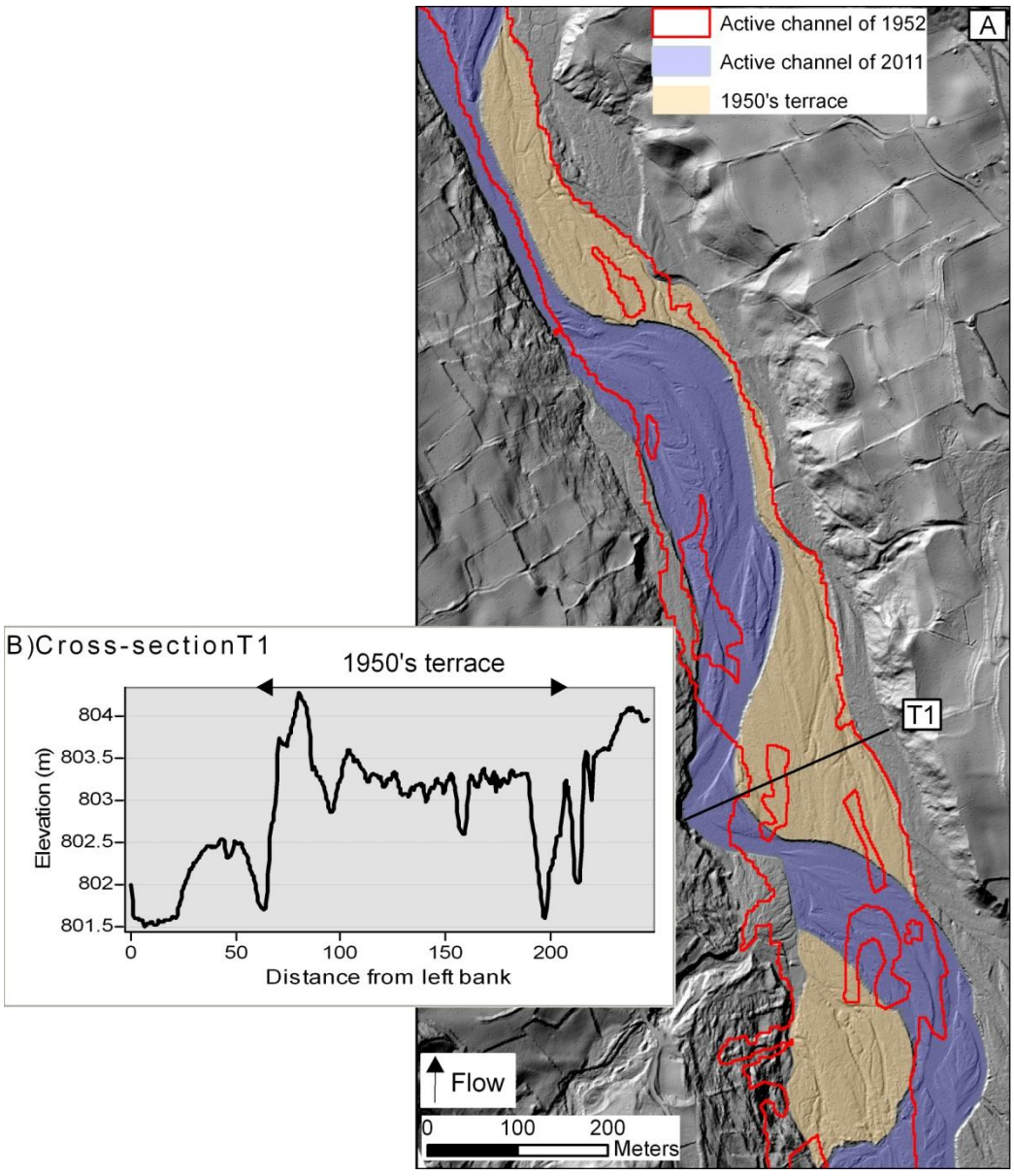

Fig. 36. (A) Map showing the active channel extent in 1950s on hillshaded DEM of the Drac 2 study site; (B) Topography of cross-section of T1, located on A, showing elevation difference between actual active channel and 1950's terrace.

4. Results

In a first step, the longitudinal variability of the Bès morphological signatures was studied because this 7-km reach is the longest and we have two surveys so it is possible to fully explore the potentiality of the proposed methodology and identify geomorphic indicators before exploring inter-river comparisons.

4.1. The Bès River

4.1.1. Longitudinal variability of morphological signatures

Both 2008 and 2010 LiDAR surveys of the Bès River revealed a high longitudinal variability of active channel width within a range from 43 to 218 m, with a mean value of 127.5 m in 2010 (Fig. 37A). The 7-km-long reach can be divided in four parts, from the visual interpretation of the active width longitudinal pattern. In the upper section of the reach (0-2.5 km, part 1A), the channel is characterized by a fluctuating active width around a mean value of 113 m in 2010. At 2.5 km, a major channel constriction zone is observed from which a regular increase of active width takes place (part 2A), and after 3.3 km, several zones of active channel expansion are again observed around a higher mean active width (163 m in 2010) than for the first zone (part 3A). This zone of higher active channel width stops at around 6 km and a last zone of channel constriction is observed (part 4A).

The number of wetted channels, used as an index of braiding intensity, was extracted along the 7-km reach. This index shows almost the same longitudinal pattern as for active width with a first part (0-2.5 km, part 1C) showing alternation of single-thread and multi-thread channels (Fig. 37C). The dominant braiding index is 2, and it never exceeds 4. Between 2.5 and 4 km, in the channel constriction zone, a single-thread morphology takes place (part 2C). From 4 km, the reach is characterised by the persistence of a high number of wetted channels during 2 km, with a significantly higher braiding intensity than in the upstream braided reach (part 3C). Here, the dominant braiding intensity is equal to 3, and up to 5 wetted channels are observed locally. Downstream from this lower braided reach, another channel constriction zone appears with a dominant single-thread morphology (part 4C).

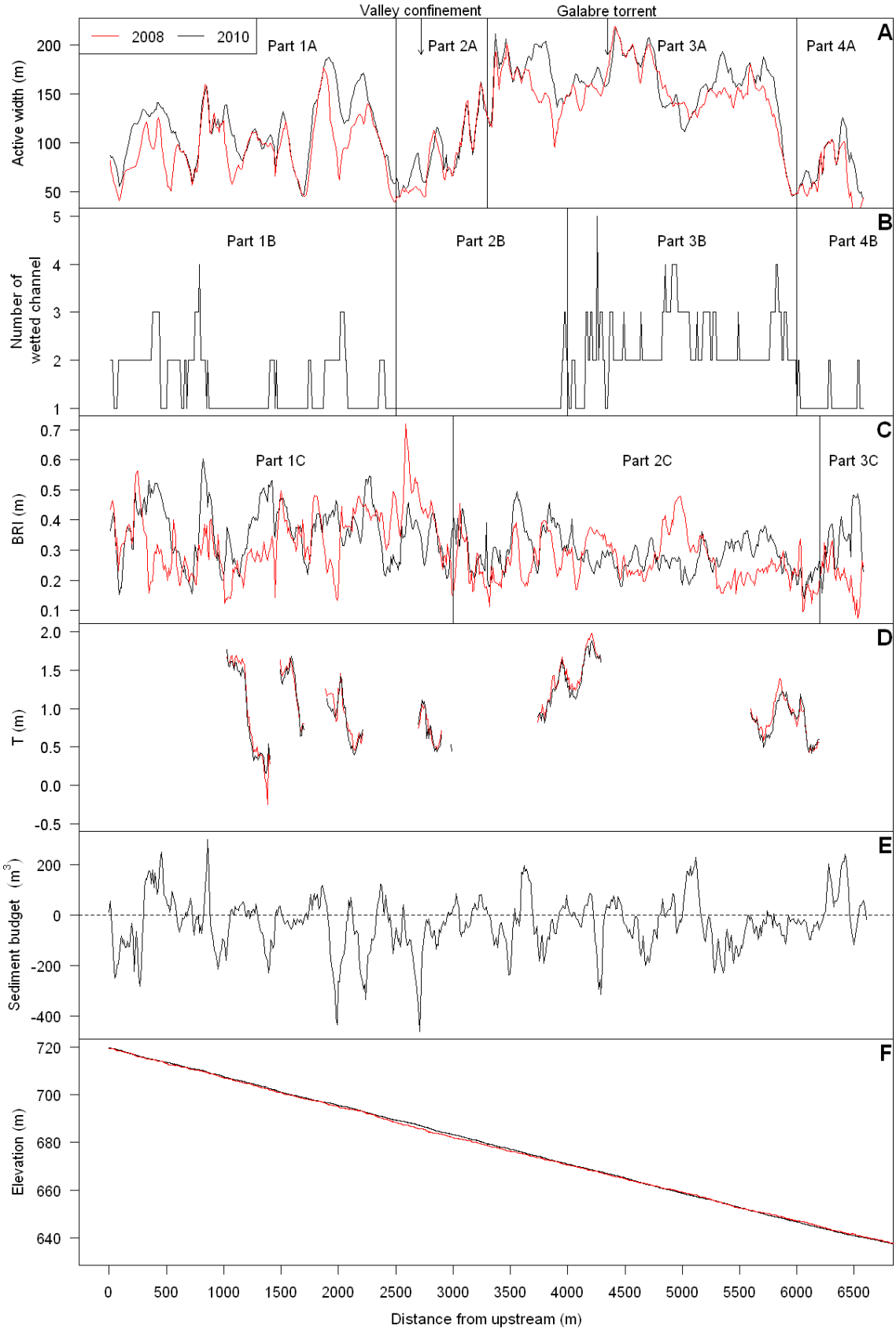

Fig. 37. A) Longitudinal variation of (A) active channel width; (B) number of wetted channel; (C) *BRI* ; (D) *T*; (E) sediment budget; and (F) channel slope on the Bès River in 2008 (in red) and in 2010 (in black).

Both 2008 and 2010 *BRI* signals also show a high longitudinal variability, with an upper reach where *BRI* fluctuates around a mean of 0.35 (Fig. 37C, part 1C), and a lower reach where *BRI* fluctuates around a lower mean value of 0.26 (part 2C). Although this general structure is conserved after the 2009 flood, it is clear that patterns of high-frequency fluctuations of the *BRI* change after the flood, and this is not observed for active channel width where most of the peaks did not change their position. Autocorrelation analysis of active width and *BRI* did not show any correlation between the two signals.

As a summary of these first observations, it is possible to identify two distinct braided reaches for the study site: (i) an upper narrow braided reach with a low braiding index and a rough bed (high *BRI*), and (ii) a lower wide braided reach with a high braiding index, and a flatbed (low *BRI*). These two braided reaches are limited downstream by major channel constriction zones where single-thread morphology appears. It is interesting to see that these distinct channel morphologies appear without any change of the channel slope. The long profile of the 7-km reach shows a fairly regular slope of 1.2 %, without any break along the way (Fig. 37F). The only detectable changes in the valley which may have a morphological effect on the braided pattern are the downstream decrease of valley confinement before and after the constriction zone at 2.5 km, and an important tributary input (Galabre Torrent, 35 km²) in the upper section of the lower braided reach. The potential effect of these two controlling factors is discussed in the next section of the chapter.

Two other longitudinal signals have been extracted along the 7-km reach for helping the interpretation of morphological signatures. The first is the channel entrenchment (*T*) in the 1950s terrace, which was expected to provide instructive information about the spatial variability of the long-term sediment regime of the reach. It finally appears that *T* signal is too much discontinuous, because the 1950s terrace has not been sufficiently conserved along the reach (Fig. 37D). Cumulative frequencies of *T* values extracted along the reach show that the 1950s terrace stands between 0.4 and 1.7 m above the active channel, without any clustering of values in this range (Fig. 38).

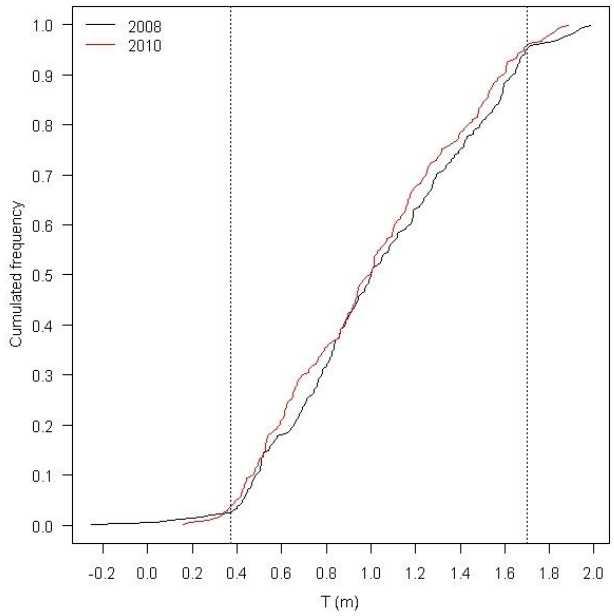

Fig. 38. Cumulative frequency of *T* values for the Bès reach in (A) 2008; and (B) 2010.

The last longitudinal signal was provided by the net sediment budget of the December 2009 flood, which was derived from change detection of multitemporal LiDAR scenes (see chapter 2). This signal is presented in Fig. 37E. Relatively regular alternating sequences of net deposition and net erosion zones emerge from this signal, as a result of the discontinuous nature of bedload transport. The upper and lower braided reaches did not present any specific behaviour. However, a concentration of major net erosion peaks appears in the vicinity of the channel constriction zone at 2.5 km. This transition zone between the two braided plains emerges as a very active sediment transfer cell where the most important channel deformations occurred. Another singularity of the signal is detected near the confluence with the Bléone, where a 1-km-long and continuous net erosion cell is observed. This kind of pattern is unique among the 7-km reach, and it is again in the upstream vicinity of a major constriction zone that this singularity appears.

4.1.1. Periodicity of morphological signatures

Periodicity of morphological signatures was investigated using wavelet transform analysis. Wavelet spectrums of active channel width revealed one dominant peak at 1200 m (10 times the mean active width, *W*), and one secondary peak at 500 m (4*W*) (Fig. 39B). The 2009 flood did not have any effect on the periodicity of active channel width, since the 2008 and 2010 wavelet spectrums do not show any significant change. This is not the case for the *BRI*, where a substantial change of the periodicity is observed between 2008 and 2010 (Fig. 39A). The 2008 signal show a single dominant peak at 1150 m, which confirm results from the active channel width. In 2010,

this peak has been lost, and two smaller peaks are observed at 470 and 900 m. For the net sediment budget of the 2009 flood, a period of 660 m (5W) was detected (Fig. 39C). The same period is clearly observed for fill volumes but not for scour volumes, which presents a peak around 1100 m.

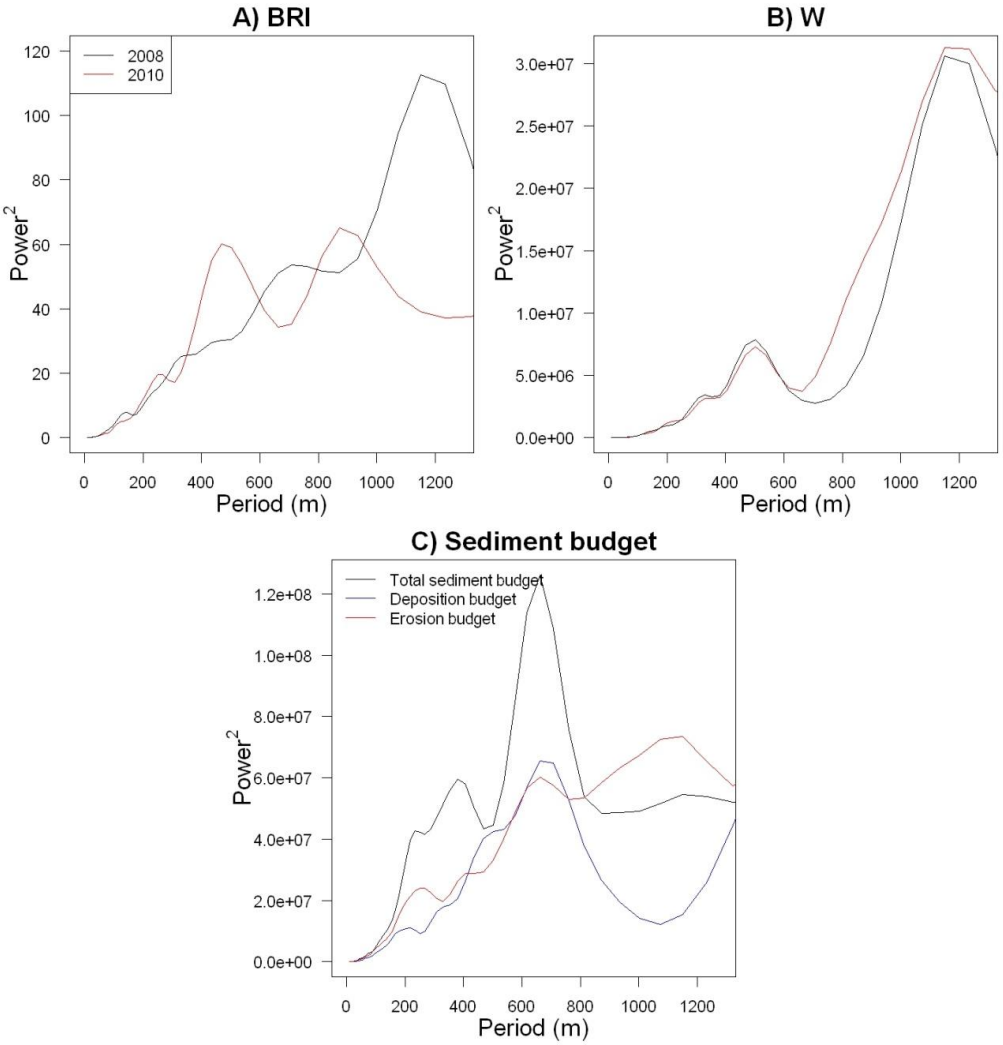

Fig. 39. Global wavelet spectrum of longitudinal signals of (A) *BRI*; (B) active channel width; and (C) sediment budget on Bès reach in 2008 and in 2010.

Longitudinal wavelet power spectrums were investigated to get information about the space domain of each period (Fig. 40). This analysis revealed that the low frequency period around 1 km is representative of the entire 7-km reach (Fig. 40A, C and D), whereas the high-frequency period around 500 m is mainly supported by the upper 2.5-km of the reach. This reach corresponds to the upper confined braided plain. These results also confirm an effect of the 2009 flood on the *BRI* signal (Fig. 40A and B), whereas the space domain of the active width signal has not been affected by the flood (Fig. 40C and D).

In the next part of the chapter, results from the Bès River are compared to morphological signatures of other braided reaches using the same signal processing method to see if some generalization can emerge from the dataset.

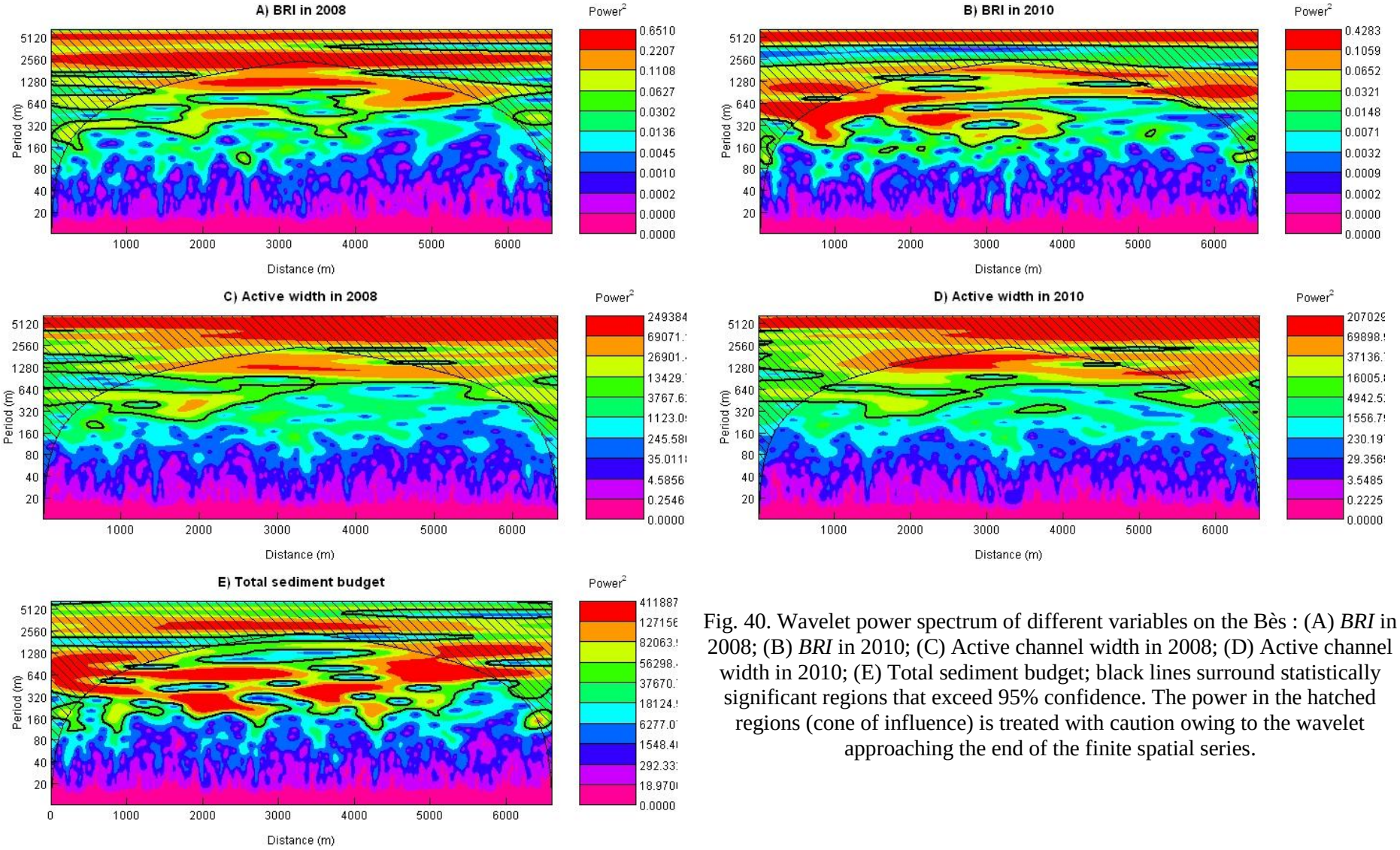

Fig. 40. Wavelet power spectrum of different variables on the Bès : (A) *BRI* in 2008; (B) *BRI* in 2010; (C) Active channel width in 2008; (D) Active channel width in 2010; (E) Total sediment budget; black lines surround statistically significant regions that exceed 95% confidence. The power in the hatched regions (cone of influence) is treated with caution owing to the wavelet approaching the end of the finite spatial series.

4.2. Comparison with morphological signatures of other braided channels

4.2.1. Longitudinal variability of signatures

Longitudinal signals of active channel width and *BRI* were extracted along the 8 braided reaches where airborne LiDAR data were available (Fig. 41). These data confirm the fluctuating pattern of active width already seen on the Bès, with multi-scale alternating sequences of expanded and contracted active channels. These apparently regular oscillations are locally disturbed by more irregular patterns. For several sites, some major peaks of active width can be detected. The peak of Drôme 2 at 0.9 km is located just upstream from a major contact of the channel with the hillslope on the right bank. The peak at 0.9 km on the Bez site is also associated with a similar context: a downstream control from a major constraint on the left bank, where the river hits obliquely a 10-m high Quaternary terrace. A similar contact with a high terrace produces the same effect on Drôme 3, at 1.6 km. The active width expansion on this site at its downstream limit can also be associated with a confinement from the artificial embankment of the channel. On the Drac 2, a strong active channel expansion is observed at 1 km, under the obstruction effect of a large alluvial fan on the left bank. On the Drôme 1, it is the whole braided system which seems to be controlled by a constriction zone at its downstream end, confined between a Quaternary terrace on the left side and the marly hillslope on the right side. Finally, for the Drac 1, the whole braided system is also controlled in its downstream end by two large alluvial fans on each side of the valley.

BRI signatures extracted from LiDAR data also show apparent regular oscillations with major peaks. Although for some sites, it is possible to detect a correlation with the active width signal (Drac 2 and Bez, which shows a positive correlation between W and *BRI*), it is not possible to conclude about a general spatial concordance between the two signals. The *BRI* seems to follow its own trajectory, with a succession of high and low roughness reaches which are very difficult to interpret. It is not really possible to detect any clear association with some potential predictors, and the *BRI* signature seems to be more controlled by the recent history of the channel, and notably by the effect of the last significant flood, as demonstrated for the Bès River in the previous section.

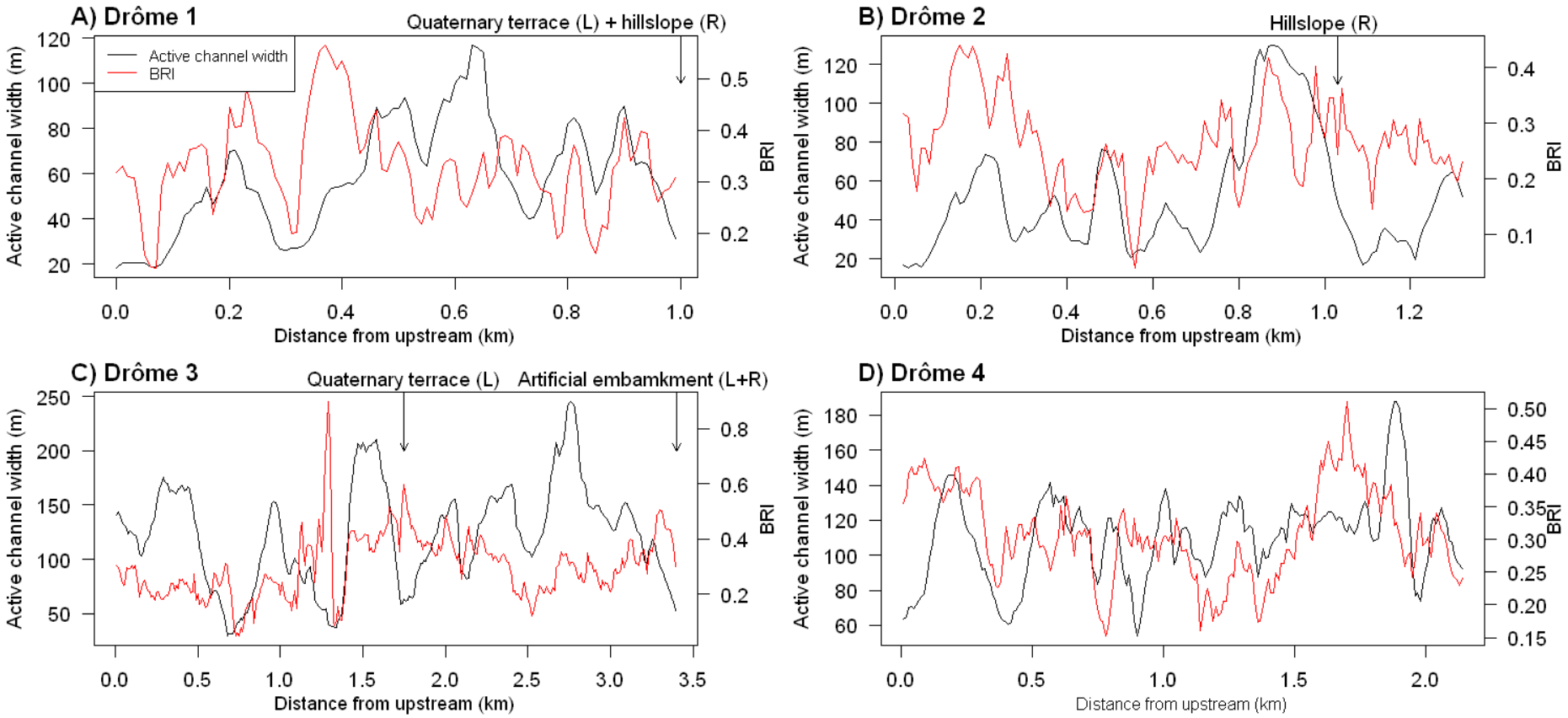

Fig. 41. Longitudinal variation of active channel width in black and *BRI* in red for (A) Drôme 1; (B) Drôme 2; (C) Drôme 3; (D) Drôme 4; (E) Bez; (F) Bléone; (G) Drac 1: (H) Drac 2; arrows on the top of plots indicated valley floor obstruction zones located on left (L) or right (R) banks.

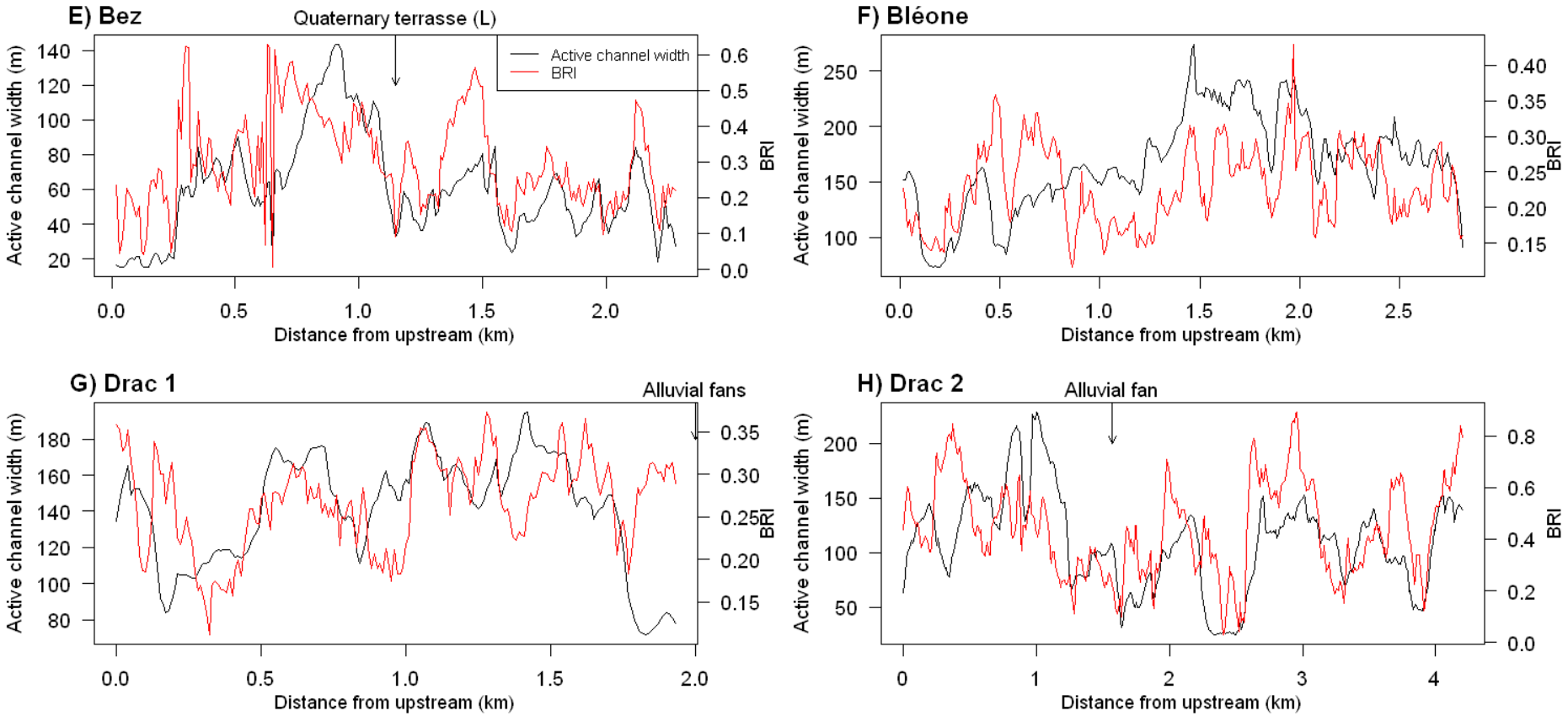

Fig. 41 (Continued).

4.2.2.Periodicity of longitudinal signatures

Wavelet power spectrums were produced for each site to objectively detect periodicity in active width and *BRI* signals, as it was previously done for the Bès River (Fig. 42). Periods were systematically normalized by the mean active channel width along the reach to get comparable data between sites. This normalized variable is referred as the relative wavelength. Most of the power spectrums revealed single or multiple peaks, and a synthetic table reporting the characteristic wavelengths for each site helps to find some emerging periods for active width and *BRI* (Table 10). For each site, detected wavelengths can be ordered in short, medium, and large wavelengths according to their magnitude.

Periodicity analysis of active width signals successfully detected a relative wavelength close to 10W for the Bès, the Bez and the Drac 2 sites. Reported values range from 8.8 to 9.8. It was not possible to detect this long period on the other sites because reaches are too short to see such periods. Another group of periods in the range between 3 and 4.7 emerges. This medium-scale period is detected almost everywhere, except for Drôme 2 and Bez. For 4 sites, a short period around 2W is detected, but cannot be generalized. *BRI* periodicity analysis gave similar results, with a 10W period on 3 sites, a 3-4W period almost everywhere, and a 2W period detected on 6 sites.

Analysis of wavelet power spectrums on the space domain gave some information about the spatial continuity/discontinuity of these periods (Fig. 43). It is generally observed a much better spatial continuity for active width periods than *BRI* periods, which are often detected only for specific sub-reaches and are not always representative of the entire reach. This is in agreement with results obtained for the Bès, which showed that *BRI* signal is more variable in time and space.

Table 10. Summary of characteristic wavelengths for each reach; short characteristic wavelengths are lower than 3, medium characteristic wavelengths are comprised between 3 and 5 and long characteristic wavelengths are higher than 5; NA indicated that the length of reach is too short to have this scale of characteristic wavelength.

	Characteristic wavelengths					
	W			*BRI*		
	Short	Medium	Long	Short	Medium	Long
Drôme 1	2.5	3.9	NA	2.1	4.3	NA
Drôme 2	2.6	-	NA	2.5	-	NA
Drôme 3	-	4.7	NA	2.2	4.5	NA
Drôme 4	-	3.7	NA	1.8	3.5	NA
Bez	-	-	8.8	-	4	9-6
Bès 2008	-	3.9	9.4	-	-	9.4-5.6
Bès 2010	-	3.9	9.4	-	3.7	7
Bléone	1.5	3.1	NA	2-1	-	NA
Drac 1	2.3	3.6	NA	1.5	3.8	NA
Drac 2	-	3	9.8-6	-	3	8

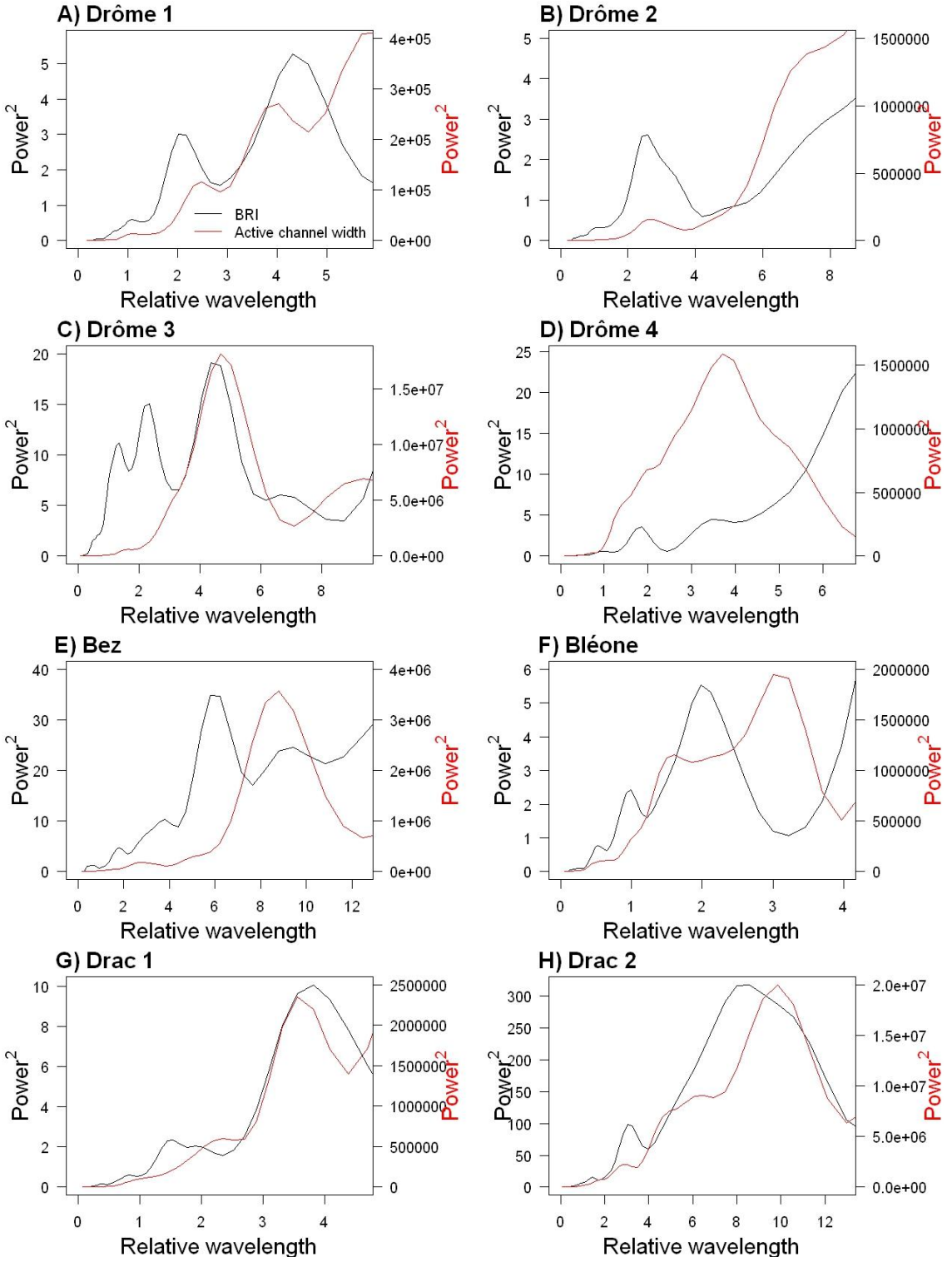

Fig. 42. Global wavelet spectrum of active width in red and *BRI* in black for (A) Drôme 1; (B) Drôme 2; (C) Drôme 3; (D) Drôme 4; (E) Bez; (F) Bléone; (G) Drac 1: (H) Drac 2; x axis is expressed in relative wavelength, corresponding to period divided by active channel width.

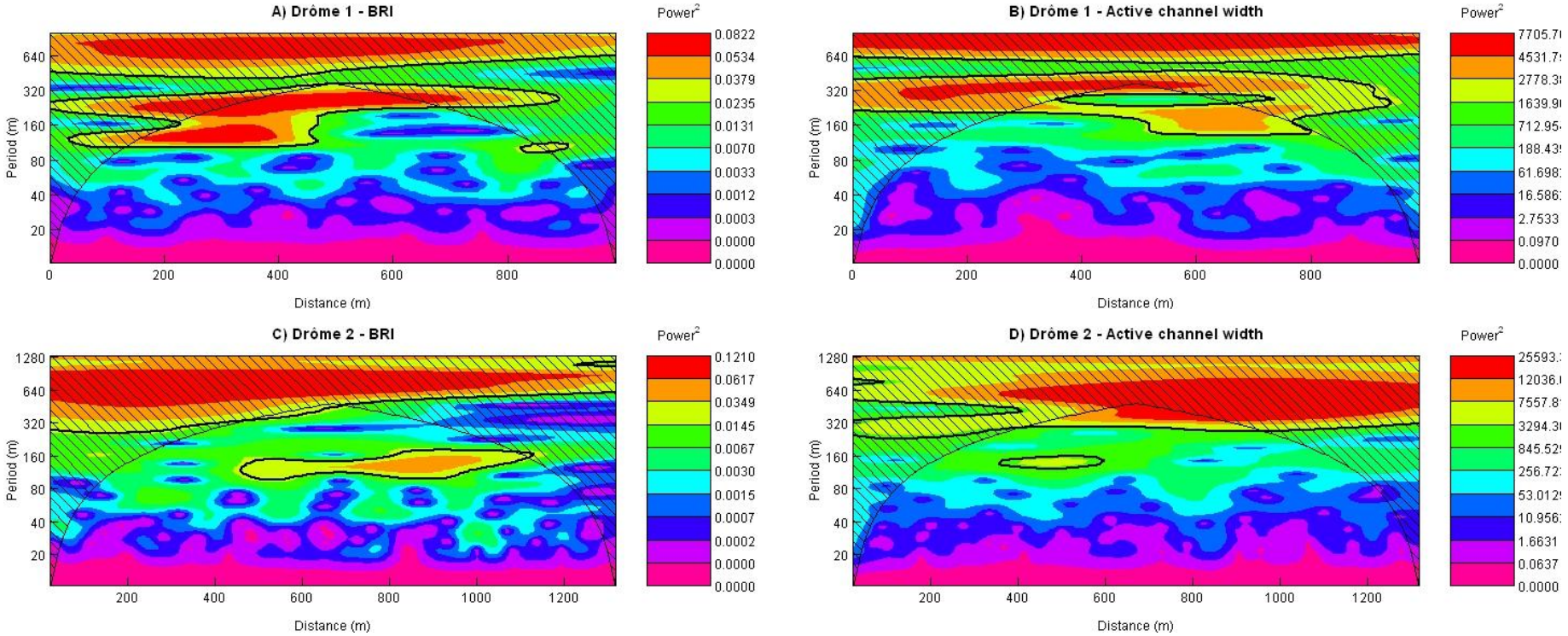

Fig. 43. Wavelet power spectrum of *BRI* and active channel width for each reach.

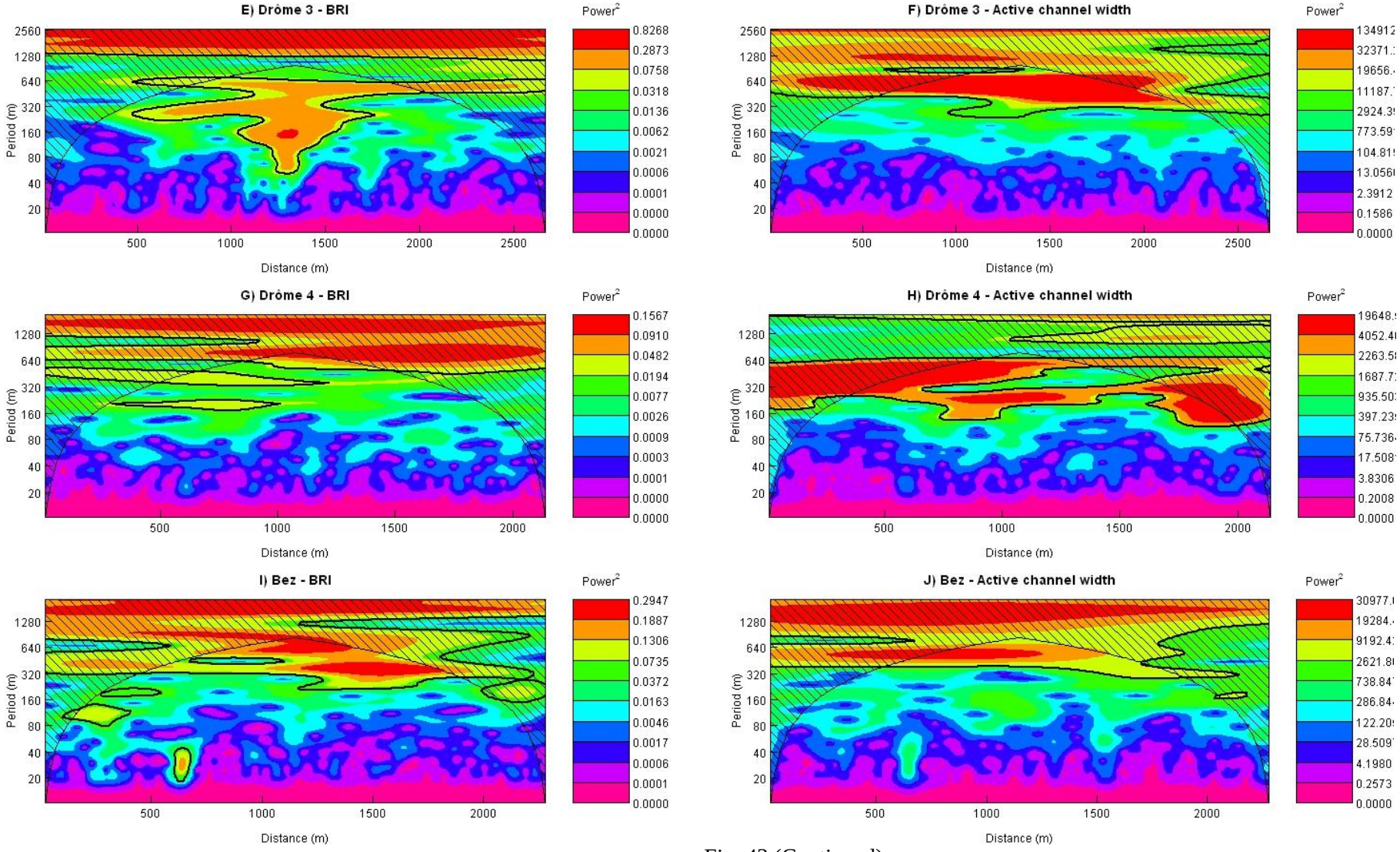

Fig. 43 (Continued).

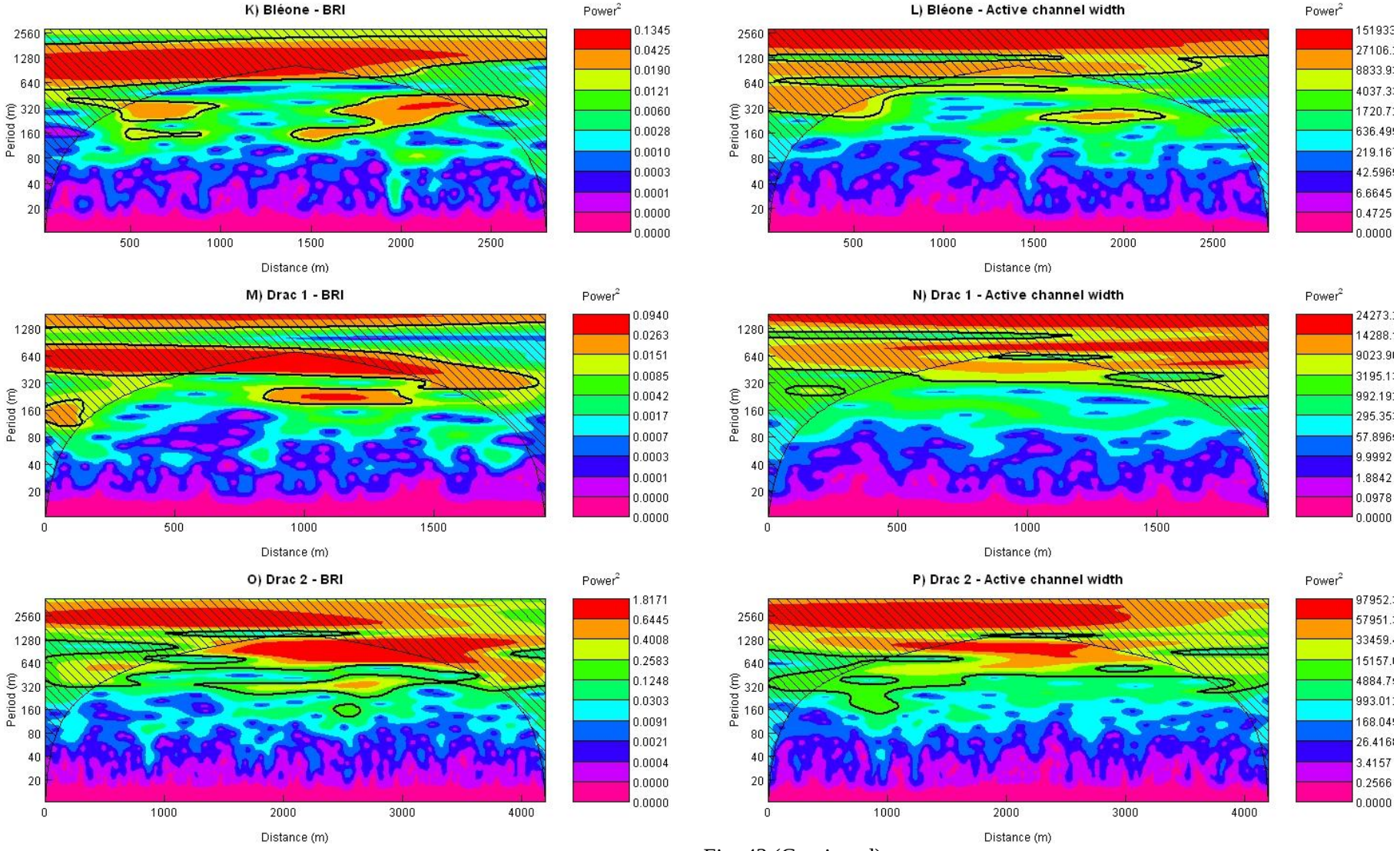

Fig. 43 (Continued).

5. Discussion

5.1. Longitudinal discontinuity in morphological signatures

The description of morphological signatures along the 7-km reach of the Bès River revealed, along a uniform slope, the formation of two distinct braided systems separated by a major valley constriction zone. Morphological properties of the downstream braided system converge towards transport-limited conditions, with an increase of active width and braiding intensity, and a decrease of channel roughness. The main physical fact that can be used for explaining the shift in braided system properties occurring at 2.5 km is the presence of a major bend corresponding to a valley constriction zone separating two braided plains. These two braided plains are confined in a relatively narrow valley floor. The mean unconstrained valley floor width measured between the road on the right bank and hillslopes on the left bank is 220 m, but the upstream plain is more confined than the downstream one. The mean unconstrained valley floor width shifted from 190 m to 250 m before and after the bend, respectively. This 25% decrease of valley confinement along the reach is likely to have an effect on the pattern of active width, and subsequently on the macro-roughness of the channel. Another possible explanation of the contrasting morphological signature between the two braided plains is the presence of an important tributary input downstream from the bend. The Galabre Torrent (drainage area: 35 km²) joins the Bès River 1.6 km downstream from the bend. Several observations do not support a strong tributary effect on morphological signatures: (i) the shift of morphological signals occurs right after the bend, and so far upstream from the confluence; (ii) the graded slope of the Bès is uniform along the reach, and the tributary input does not have any effect on the slope, suggesting that its sediment supply to the Bès is largely compensated by the increase in water supply and is not high enough to induce a shift in the mainstream sediment regime; (iii) according to the scaling law of active channel width for braided rivers in SE France (Equation 1), the increase in drainage area after the Galabre confluence (+ 35 km²) cannot explain the observed increase in active channel width after the bend (50% increase, whereas equation 1 predicts a 7% increase).

Following these observations, it is likely that valley confinement is the major control explaining the contrasting braided signature along the Bès River. The higher confinement of the upstream braided system contributes to reduce the active channel width, and subsequently to decrease the braiding intensity and increase the channel roughness. The downstream braided system is still confined, but to a lesser degree, and its morphological signature is likely more

representative of the conditions imposed by water and sediment fluxes from the catchment. But even here, channel morphology cannot be seen as totally unconstrained, and one can likely expect a wider active channel and a lower *BRI* if the braided system were forming in a wider alluvial plain.

Data collected for more than 25 km of uncontrolled braided channels, in complement to the analysis of the Bès River, revealed that the longitudinal signatures are the results of both the inherent morphodynamics of braided channels, and the confinement and obstruction effects of the valley floor, which can explain major shifts in the active width pattern. These effects produce some random disturbances on channel morphology, which can affect our ability to read and detect significant periodicity in morphological signatures. Major active channel expansion zones are not always associated with autogenic megaforms of sediment transfer (Church and Jones, 1982; Rice et al., 2009), but can be often explained by valley floor controls on sediment continuity and its morphological expression. This confinement or obstruction effect on braided signatures is omnipresent on the synoptic dataset. It is also present on the diachronic set, with the singular channel deformations observed near constriction zones after the 2009 flood on the Bès. These study cases highlight the importance of taking into account local conditions in which the braided system evolves if one seeks to explore the links between morphological signature and sediment regime. Minor changes of valley confinement can have a substantial effect on morphological signatures.

5.2. Periodicity of morphological signatures

A period corresponding to 10 times the mean active channel width emerges from the Bès data. This period is representative of the entire 7-km reach, and it was not disturbed by the 2009 flood. It can be interpreted as a persistent scale of the braided channel, which does not depend on the last medium flood, and which likely reflects more the long-term sediment transfer pattern and morphodynamics of the braided channel. This is not the case of the *BRI*, whose periodicity has been modified by the occurrence of a 14-yr flood, likely under the effect of sediment redistribution along the reach. This 10W period was not confirmed by every investigated site, because most of them are too short to detect such a long period, but on the two sites which are theoretically long-enough to see this periodicity, the 10W period was effectively detected by the wavelet analysis.

Another period at 3-4W was also detected for most of the investigated sites. This medium-scale period is in good agreement with experimental results of longitudinal oscillations of braided river morphology reported by Zanoni (2008), who found a consistent normalized period equal to 3

times the mean active channel, which did not depend on the hydraulic parameters of the runs. This constant period was attributed to the inherent morphodynamics of the whole braided channel network, since space domain analysis revealed that this period is persistent along the whole experimental reach. It was not the case of the shorter periods detected by signal processing, which were characterized by intermittent behaviour in the longitudinal direction, and which were mostly attributed to the activity of the main branch of the braided channel. Our field-based observations are in good agreement with this interpretation, since the shorter periods detected by wavelet analysis (1-2W) were also the most intermittent ones in the space domain diagrams.

Although our field-based analysis of braided channel signatures confirmed some of the experimental findings reported by Zanoni (2008), it also revealed the existence of a characteristic relative wavelength of 10 times the active width, which was not seen in laboratory, likely because the length of the flume was too short to permit the full longitudinal development of the braided channel dynamics. It is also difficult to detect this wavelength in the field, because it is generally hard to find a long-enough unconstrained braided system with a constant mean active width. The most favourable situations for such conditions are the piedmont zones, where the braided systems are not constrained by hillslopes and are not influenced by large tributary inputs. However, in the French alpine context, piedmont braided rivers are often severely disturbed by engineering works, or past gravel mining activities, and it is difficult to find extended linear of preserved braided systems.

How can we physically explain the superimposed periods of 3-4W and 10W emerging from the investigated braided signatures? It is only possible to propose speculative explanations here, because this question needs much more empirical, experimental and numerical evidences for a comprehensive analysis. One possible way to follow is to investigate the link of the spatial periodicity with the spatial arrangement and dynamics of macroforms (unit bars) and megaforms (compound bars, or bar complexes, in the terminology proposed by Rice et al., 2009) constitutive of braided channels. It is likely that the medium-scale wavelength (3-4W) is closely linked with processes of unit bar construction and destruction, and more related to the short-term (e.g. annual) sediment transfer patterns of the braided channel. This is supported by the Bès observations, which show that the 14-yr flood erosion-deposition characteristic period (5W) is close to the medium-scale period of morphological signatures obtained for both active width and *BRI*. One can reasonably expect that this sediment-transfer period scales with the intensity of the flood, and that the characteristic wavelength of the annual flood would be closer to 3-4W. Some authors already explored the characteristic length scales of braided morphology (e.g. length of confluence-bifurcation units) and established a link with the initial unit bar morphology from which the braided system evolves (Ashmore, 2009; Hundey and Ashmore, 2009). These studies generally

scale their metrics with the width of the branch where the unit bar develops, and not the active channel of the braided system, so it is difficult to establish a comparison with our observations. Nevertheless, some characteristic lengths emerge from these works, in relation with the dynamics of elementary bars.

On the other hand, the 10W period should be more related to the construction of bar complexes, or what was referred as sedimentation zones by Church and Jones (1982), for which very little information is available in the literature. In the investigated braided systems, these megaforms look like a longitudinal succession of large alluvial fans, with a distal front transverse to the active channel, along which the main channel flows (Fig. 44). These megaforms are also detectable on the longitudinal variation of elevation residuals from a linear fit of the long profile obtained along a reach with uniform slope on the Bès (calculated from mean cross-section elevation). Six different parts are observed on this diagram (Fig. 45). Wavelet analysis of this signal underlines a characteristic wavelength around 10W. Positive residuals can be interpreted as preferential sediment deposition zones, whereas negative residuals may be seen as preferential erosional reaches. Some questions still remain about their origin and dynamics. Are they a heritage from the last extreme flood and so controlled by the sediment transfer pattern during catastrophic events, or are they more the result of an autogenic process related to the long-term pattern of sediment transfer in braided systems? This sediment transfer over long time as low-amplitude waves have already been discussed by Griffiths (1979, 1993) and longer-term alternations of bed elevation and braiding intensity observed by Ashmore (1991a) and Bertoldi et al., 2006 in experimental flume may be tied to such pulses (Ashmore, 2013). These open questions would need much more investigation to find some answers.

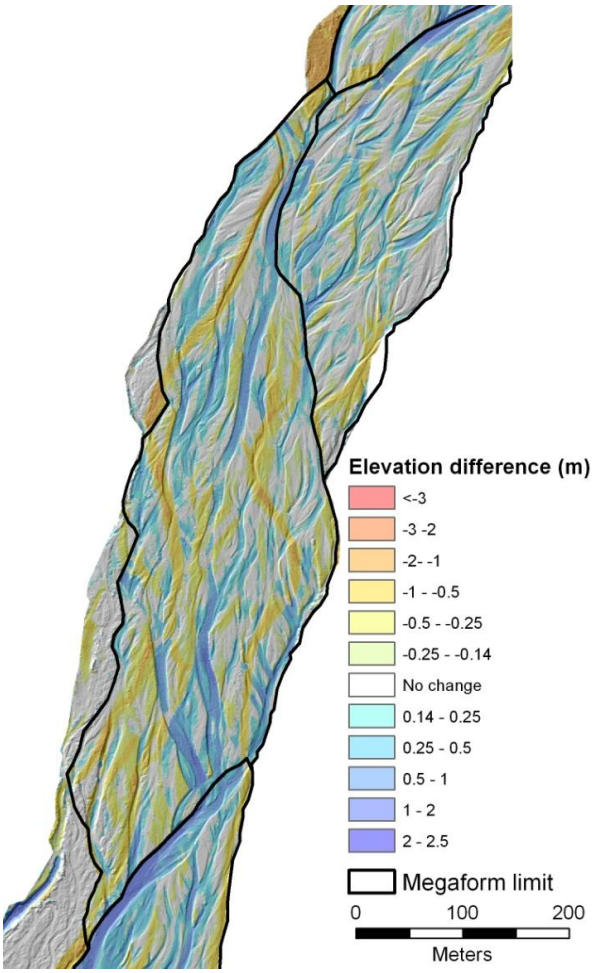

Fig. 44. Example of delineation of megaform on the Bès River; the DoD draped on the hillshade view of the DEM of 2008.

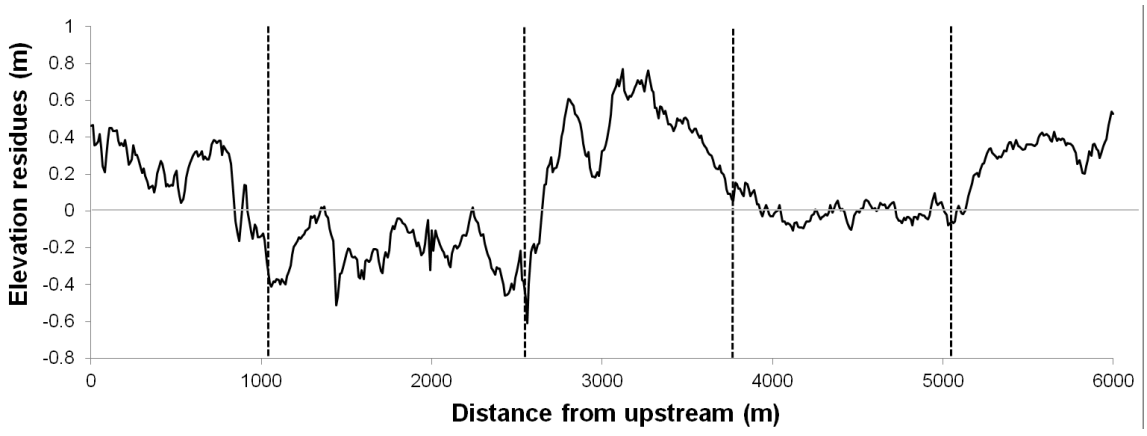

Fig. 45. Longitudinal variation of elevation residuals on the Bès reach, calculated from a linear fit of the long profile along the reach with uniform slope.

6. Conclusion

This paper is based on a disaggregation process of airborne LiDAR data into 10 m-regular spaced cross-sections. This methodology allows us to study longitudinal pattern of cross-sectional braided river morphology: the active channel width and the *BRI* over a kilometer-scale. Active channel width signals show fluctuating pattern with multi-scale alternating sequences of expanded and contracted active channels. Major shifts in the active width pattern are explained by the confinement and obstruction effects of the valley floor. *BRI* signatures show high fluctuations too along reaches but they are more controlled by the recent history of the channel and notably by the effect of the last significant flood. From these signals, two major characteristic wavelengths have been identified: 3-4 and 10 times the active channel width. The first could be linked to short term sediment transfer and to unit bar processes. In fact, sediment budget of a 14 year return period showed closer wavelength of 5 times the active channel width. The larger scale seems to be a persistent scale of the braided river and was not disturbed by a Q_{10} flood. It could be linked to the long term sediment transfer pattern and more related to bar complex construction. These observations have to be reinforced with empirical, experimental and numerical analysis.

CHAPITRE 4

CARACTERISATION DE L'HISTOIRE DE LA FORMATION DE LA PLAINE D'INONDATION ET DE LA REPONSE DE LA VEGETATION DE RIVIERES EN TRESSES PAR LIDAR AEROPORTE ET PHOTOGRAPHIES AERIENNES

A. Résumé

Ce chapitre combine des données de LiDAR aérien avec une étude diachronique de photographies aériennes pour reconstruire l'historique de formation des différentes unités spatiales composant la plaine d'inondation et relier cette structure avec les caractéristiques des unités de végétation. 3 rivières en tresses ont été étudiées dans les Alpes françaises avec un degré croissant d'activité : le Bouinenc, la Drôme et le Bès. Les données LiDAR ont été analysées pour extraire la topographie à partir d'un modèle numérique de terrain (MNT) de résolution 1 m et les caractéristiques de la végétation à partir d'un modèle numérique de canopée (MNC) de résolution 1 m. Les photographies aériennes séquentielles ont été utilisées pour dater la formation des unités spatiales de la plaine d'inondation. Les unités de végétation ont été cartographiées par photointerprétation à partir des données LiDAR et des photographies aériennes (végétation pionnière clairsemée et dense, végétation post-pionnière et lande arbustive). Nous avons mis en évidence les différentes phases d'incision associées aux phases de rétraction/élargissement de la bande active et les effets des crues fortes sur la morphologie du lit. Deux périodes d'incision ont été identifiées, une commençant avant 1948 et une autre dans la seconde partie du 20ème siècle. Ces phases d'incision sont associées principalement à des déficits en apport sédimentaire. Le caractère brutal des phases d'incision est contrôlé par l'intensité des crues avec une incision forte pour les crues de période de retour 50 ans. Les crues moyennes et fortes induisent des élargissements de la bande active avec des impacts plus faibles en cas d'apport sédimentaire déficitaire. Les changements à long terme jouent un rôle significatif pour expliquer la mosaïque de la végétation de la plaine d'inondation avec une végétation bien développée et composée majoritairement d'unités matures dans le cas d'une rétraction et d'une incision sur le long terme. Les rivières plus actives présentent une diversité d'unité de végétation plus équilibrée. La présence de lande arbustive semble être un bon indicateur des périodes d'incision. Enfin, la classification des unités de végétation par photointerprétation est bien validée par une analyse discriminante avec les informations dérivées du LiDAR et l'âge des unités établi par la juxtaposition des positions des chenaux observées sur les photographies aériennes depuis les années 1950. Cette approche permet aussi d'identifier des erreurs de classification et de les interpréter.

Ce travail a fait l'objet d'une publication soumis à la revue *Catena* qui est présentée dans les pages suivantes.

Mots clés: LiDAR aérien; photographies aériennes anciennes; rivières en tresses; végétation de la plaine d'inondation; incision du chenal; crues.

B. Use of airborne LiDAR and historical aerial photos for characterising the history of floodplain morphology and vegetation responses of braided rivers

Lallias-Tacon, S., Liébault F., Piégay H., submitted, Use of airborne LiDAR and historical aerial photos for characterising the history of floodplain morphology and vegetation responses of braided rivers, Catena.

Abstract

This paper combines airborne light detection and ranging (LiDAR) data with historical aerial photos to reconstruct floodplain formation and relate this geomorphic organisation with vegetation patch characteristics. This is achieved on three different braided rivers in the French Alps with an increasing degree of activity: the Bouinenc Torrent, the Drôme and Bès Rivers. LiDAR data were analysed to extract both understorey topography from 1-m resolution digital elevation models (DEMs) and the characteristics of vegetation from 1-m resolution canopy height models (CHMs). Sequential aerial photographs were used to date floodplain formation. Vegetation units were mapped from both LiDAR and aerial photos (sparse and dense pioneer vegetation, post-pioneer vegetation and shrubland). We established the channel incision timing associated with active channel narrowing or widening and identified the effects of large floods on channel morphology. Two major incision periods were identified: one which started before 1948 and another one in the second half of the 20^{th} century. These incision phases were mainly related to a decrease in sediment supply. Flood intensity controlled smooth or abrupt channel incisions, with a high incision for a Q_{50} flood in the context of a deficit in sediment supply. The geomorphic effect of large and medium floods in terms of active channel widening was clearly modulated by sediment supply conditions. Long-term geomorphic changes play a significant role in explaining vegetation mosaics with a well-developed vegetated floodplain mainly composed of mature units following long-term narrowing and incision. Rivers with greater activity show an equi-diversity of floodplain vegetation units. The presence of shrub patches seems to be a good indicator of incision periods. Photointerpretation classes of physiognomic vegetation units were satisfactorily validated by LiDAR information and age patches established from overlays of the different channel

positions observed on the historical aerial series using discriminant analysis. This approach also provides insights into identifying misclassifications and their interpretation.

Keywords: airborne LiDAR; historical aerial photos; braided rivers; floodplain vegetation; channel incision; flood.

1. Introduction

The high morphological activity of braided rivers forms floodplains composed of a mosaic of sedimentary deposits with different development stages, spatial extents, thicknesses and spatial coverage of overbank fine sediment, vegetation units, flooding frequency, and ages (Reinfelds and Nanson, 1993; Haschenburger and Cowie, 2009; Datry et al., 2014). This complex floodplain mosaic is the result of hydrological and sediment supply forcing within a specific valley configuration that imposes the space available for the river to build its channel (Haschenburger and Cowie, 2009). Mechanisms of floodplain formation and destruction include lateral shifting of the braided channels, sediment deposition during high-magnitude flood events, and reactivation of abandoned channels (Reinfelds and Nanson, 1993; Warburton et al., 1993). These elementary processes take place in a general regime which can lead to river channel aggradation, degradation, or equilibrium. It is well known, for example, that braided channel incision and narrowing can occur as a response to a sediment supply decrease. In this context, the valley bottom is characterised by a series of successive topographic levels, lower and lower from the valley side to the river bank (Reinfelds and Nanson, 1993). Studies conducted in the French alpine valleys have highlighted that grazing abandonment in valley floors and the sediment supply decrease throughout the 20th century have been efficient drivers of floodplain construction during this time period (Liébault and Piégay, 2002; Kondolf et al., 2007; Piégay et al., 2009).

The complexity of floodplain vegetation patches is related to (i) the capacity of the braided river to renew its floodplain and (ii) the valley bottom size. Braided rivers are sometimes so shifting and the floodplain so narrow that the active channel occupies the entire valley bottom and annually scours emerging vegetation, whereas in less active braided systems, vegetation can more easily establish and survive over a few decades so that the annual turnover rate only partly renews the vegetation mosaic, thus preserving an alluvial forest (Piégay et al., 2006). This vegetation dynamics was formalised by Paola (2001), who introduced the term T* corresponding to the time required for vegetation to grow to a sufficiently mature state that it can resist scouring in relation with bed mobility frequency. This normalised time was successfully used in the field (Hicks et al., 2008) and in laboratory experiments (Tal and Paola, 2010) to explain vegetation dynamics in braided channels. As the floodplain vegetation structure and extent are strongly linked to channel shifting during critical floods, the time since the last critical flood (e.g., Q10) is also a useful indicator for vegetation dynamics, as shown by Belletti et al. (2013a, 2014) in a historical analysis of channel changes on a set of braided rivers in southeastern France. The effect of flooding on braided river floodplains was also highlighted by Comiti et al. (2011), who showed that the fluctuations in the relative area of islands are controlled by the flood history.

Braided river floodplains support vegetation mosaics frequently rejuvenated by floods and channel shifting and are thus dominated by pioneer vegetation units to middle stages of succession. Less active areas are commonly colonised by pioneer vegetation, typically dominated by species that are well adapted to intermittent flood disturbances, most of which belong to the Salicaceae family (willows and poplars) (Karrenberg et al., 2002). The vegetation succession model is classically described as a progressive shift from a bare substrate to pioneer herbaceous structures, to pioneer shrublands, to post-pioneer forests, and finally to mature forests (Marston et al., 1995), which can take a few decades to a few centuries. Floods can induce total destruction of vegetation followed by rejuvenation of the succession, whereas partial destruction induces regressions or bifurcations in succession (Corenblit et al., 2007).

Development of riparian vegetation depends to a large extent on flooding frequency and scouring, overbank fine sedimentation and water table availability defined by floodplain surface and gravel layer elevations (Stella et al., 2013; Singer et al., 2014). Stella et al. (2013) showed that channel bed incision and associated groundwater table decline contributed to overall forest decline on the Drôme River. Vegetation patterns are therefore closely related to the history of the braided channel, creating complex physical settings in terms of water stress and complex age mosaics.

Floodplain vegetation characteristics are commonly studied by photointerpretation from aerial photographs and field measurements including dendrochronology (Stella et al., 2013) and plant inventory (Pautou and Girel, 1986; Gurnell et al., 2001; Kondolf et al., 2007; Dufour and Piégay, 2010). The physical drivers such as the relative elevation of patches in relation to the water surface are usually collected during field campaigns (Dufour et al., 2007). Amongst the physical drivers of the vegetation patches, channel shifting and floodplain renewal have been most widely studied using geographical information systems (GISs) and sequential aerial photos following the pioneering work of Marston et al. (1995). GISs, sequential aerial photos and historical maps have also been used to explore forest evolution over time, showing the fairly recent establishment of such ecosystems due to complex geomorphic changes (Kondolf et al., 2007).

Today, airborne light detection and ranging (LiDAR) provides access to both the understorey topography and the characteristics of vegetation along a river reach at a scale of a few tenths of a kilometre and with a high altimetric precision. Recent studies have explored airborne LiDAR data to describe riparian forests (Hall et al., 2009; Johansen et al., 2010; Michez et al., 2013; Picco et al., 2014). These studies characterised vegetation patches (e.g. extent, longitudinal continuity, height, density, and overhanging characteristics) based on the Canopy Height Model (CHM). On braided rivers, most of the previous studies using LiDAR data focused on braided dynamics. On the Tagliamento River (Italy), Bertoldi et al. (2011, 2013) explored combined data from airborne LiDAR, color air photographs and ground measurements to (1) study the colonisation pattern of

exposed river sediments by riparian trees and its impact on channel topography (Bertoldi et al., 2011) and (2) investigate wood recruitment and deposition dynamics (Bertoldi et al., 2013). No studies have yet explored the capacity of LiDAR technology to inform on floodplain changes and the associated floodplain vegetation pattern, an important factor in regions where sediment delivery has decreased over the last century, providing sequential floodplain topographic levels and informing on the coevolution patterns between vegetation patches and channel forms.

This paper aims to reconstruct floodplain formation and relate this geomorphic organisation to vegetation patch characteristics. This is achieved by combining information from sequential aerial photographs and airborne LiDAR data. LiDAR data provide both information on vegetation patches (density and height) and their ground elevation over entire floodplain reaches. Three study reaches, which differ in floodplain history and the contemporary riparian forest mosaic, are compared to provide a range of conditions at the regional scale.

In the context of 20th century narrowing and incision in the French Alps, we wish to test (1) whether these floodplains are characterised by a series of well-developed topographic levels over the reaches; (2) whether floods have an impact on this floodplain organisation with alternating narrowing and widening periods according to flood intensity; (3) whether the vegetation mosaic reflects long-term incision and associated changes in water availability; and (4) whether the difference in braided river activity with increasing channel shifting impacts vegetation mosaics with a predominance of fairly young patches.

2. Study site

This study investigated three different sites in Southeastern France: the upper Drôme River between the Luc-en-Diois and Recoubeau-Jansac bridges, and the downstream parts of the Bès River and the Bouinenc Torrent, two tributaries of the Bléone River (Fig. 46A).

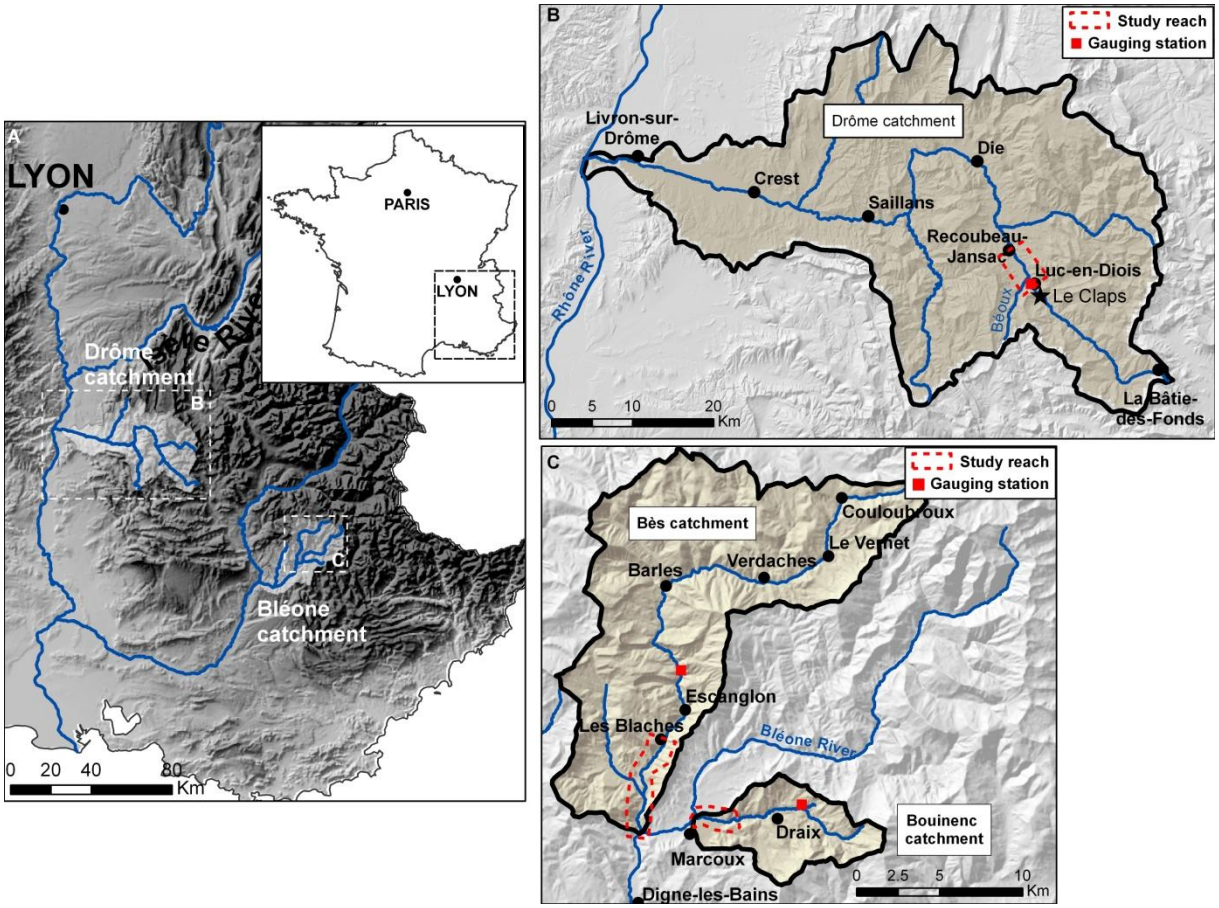

Fig. 46. Study sites: (A) location in SE France; (B) general map of the Drôme catchment with the position of the study reach; (C) general map of the Bès and the Bouinenc catchments with the position of the study reaches.

The Drôme River is a left bank tributary of the mid-Rhône River (Fig. 46B). Its main channel is 106 km long. The 1640-km² catchment is located primarily within the Vercors and Diois massifs, a mountainous area underlain by Mesozoic limestones and marls, with a maximum elevation of ca. 2000 m. The Drôme River was severely impacted by intensive gravel mining in the 1970s and 1980s, and subsequently has incised along its entire length (Landon et al., 1998; Kondolf et al., 2002; Toone et al., 2014). As a result, few braided reaches have persisted.

The 5-km study reach (midpoint at 44°38′17.15″ N, 5°25′59.85″ E) is characterised by alternating straight single-thread and braided sections. This reach drains a 225-km2 catchment,

presents a mean channel slope of 0.01, an active width between 10 and 200 m, and no significant bank protections (Toone et al., 2014). It is mainly supplied in coarse sediment by the Béoux Torrent, which joins the Drôme 200 m upstream of the study reach. The coarse sediment load of the Drôme River upstream from Luc-en-Diois is trapped behind the Claps rockslide, which occurred in 1442 (Piégay et al., 2004).

The floodplain supports an extensive riparian forest that has developed since the 1950s. It is dominated by poplars (*Populus nigra*), willows (*Salix alba*), ash (*Fraxinus excelsior*), and alders (*Alnus glutinosa*) (Piégay and Landon, 1997; Gagnage, 2008). Poplars currently display local evidence of severe crown dieback (Gagnage, 2008; Dunford et al., 2009; Stella et al., 2013). Significant poplar growth declines coincided with the beginning of intensive gravel mining activity in the early 1970s (Stella et al., 2013). These declines were most severe in sectors where a thin alluvial substrate lies above shallow bedrock, and for many trees they were triggered during drought years (Stella et al., 2013).

Discharge has been recorded at the Luc-en-Diois gauging station since 1907. This station is located approximately 800 m upstream of the study reach. The hydrological regime reflects the influence of both snowmelt and the Mediterranean conditions (dry summer and autumn storms), with floods occurring in spring and fall. Between 1948 and 2010, two major floods occurred in January 1994 and December 2003, with 100- and 45-year return periods, respectively, and several medium floods (Q10>Q<Q50) occurred with the largest in 1951 and 1978 with 16- and 17-year return periods, respectively (Toone et al., 2014) (Fig. 47A). Major droughts during vegetation growing seasons, with multiple years of lower-than-average stream flows, occurred in 1964–1965, 1989–1991 and 2003–2006 (Stella et al., 2013). Flood activity has shown a long-term, overall decrease since 1850, with an abrupt, rapid reduction in the number of flood days per decade between approximately 1950 and 2002 (Landon et al., 1998; Liébault, 2003).

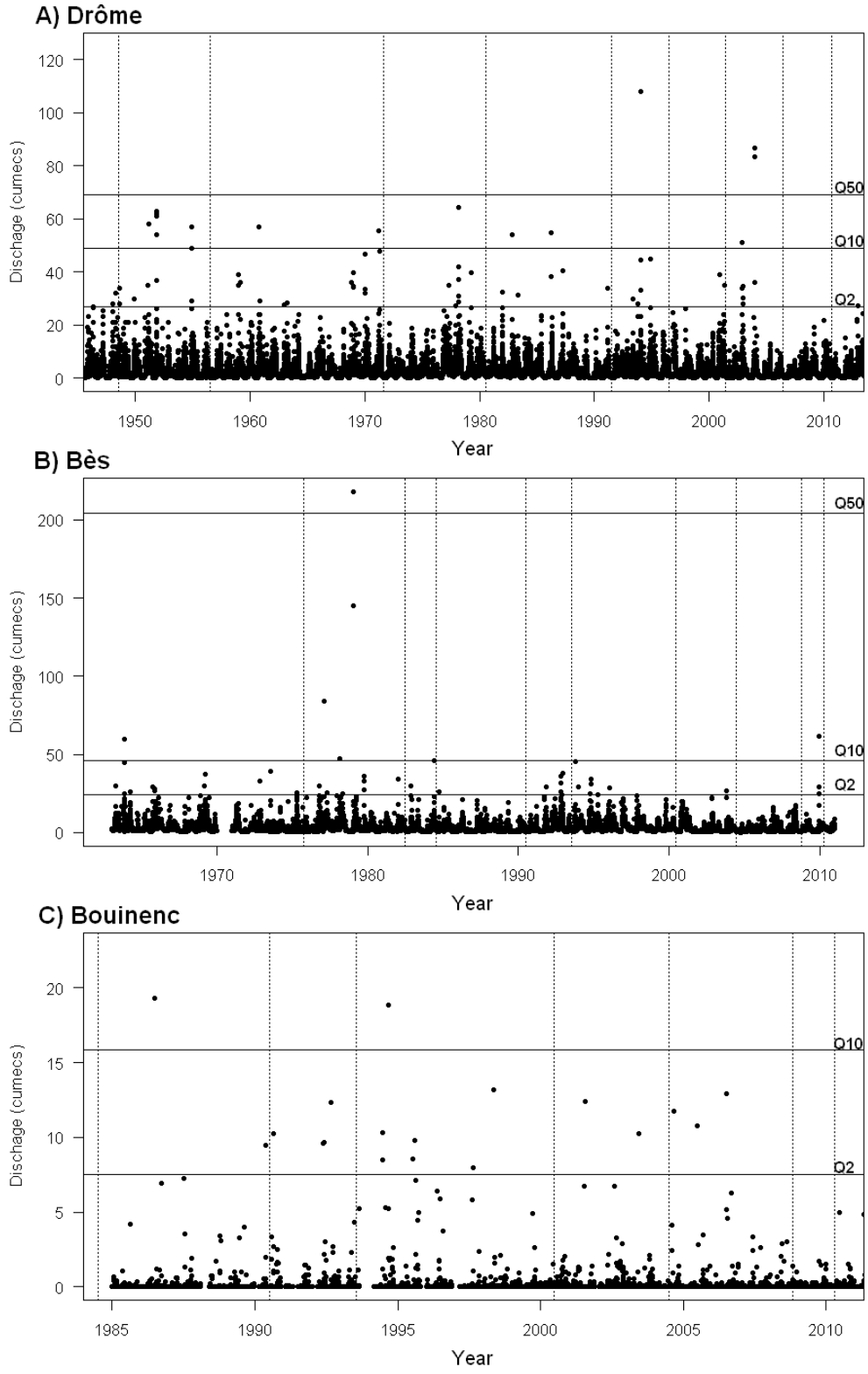

Fig. 47. (A) Mean daily discharge series of the Drôme River between 1948 and 2010 at Luc-en-Diois; data from the Luc-en-Diois gauging station (DREAL Rhône-Alpes); (B) the Bès River between 1963 and 2010 at Pérouré; data from the Pérouré gauging station (DREAL PACA); (C) maximum daily discharge series of the Laval Torrent (tributary of the upper Bouinenc Torrent) between 1983 and 2010; data from the ORE Draix-Bléone gauging station; dotted vertical lines correspond to the date of aerial photographs; solid horizontal lines correspond to the discharge of 2-, 10- and 50-year return period floods.

The Bès River is the main tributary to the Bléone River located near Digne-les-Bains, with a 234-km² drainage area and a 39-km-long main channel (Fig. 46C). The geology of the catchment consists of sedimentary rocks, mainly Mesozoic and Cenozoic limestones, marls and marly limestones. Elevations range from 640 to 2700 m.

The study reach covers the last 7 km of the Bès River (midpoint at 44°09′32.89″ N, 6°14′36.49″ E). Here, the Bès is braided with a channel slope of 0.014, a surface median grain size (D50) of 40–50 mm (derived from gravel surface photographs processed with Digital Gravelometer software) and a mean active channel width of 130 m. A recent study showed aggradation conditions upstream from the study reach (Liébault et al., 2013a). Vegetated patches located in the river channel are mainly composed of poplars (*Populus spp*.), alders (*Alnus glutinosa*), ash (*Fraxinus excelsior*), willows (*Salix herbacea*), elms (*Ulmus glabra*) and shrubs (*Rubus spp., Juncus spp.*) (Navratil et al., 2010).

The flow record has been available since 1963 at the Pérouré gauging station approximately 1.5 km upstream of the study reach. The hydrological regime is characterised by spring snowmelt high flows, summer low flows, and rainfall autumn high flows. The mean annual discharge is 2.78 m3 s−1. Between 1963 and 2010, two major floods (Q>Q50) occurred in February 1977 and January 1979 (two successive days), and two medium floods (Q10>Q<Q50) occurred in 1963 and 2009 (Fig. 47B).

The Bouinenc Torrent is a tributary to the Bléone River, near Digne-les-Bains (Fig. 46C). It drains a 38.9-km² steep catchment cut into interbedded Jurassic marls and limestones of the Digne Prealps. Elevation ranges from 680 to 2270 m (Liébault et al., 2012). Substantial reforestation is observed on the Bouinenc catchment due to both torrent-control works and decreasing demographic pressure since the 1850s (rural depopulation and land abandonment) (Vallauri and Vincent, 1999). Most of the hillslopes are affected by dramatic gullying in black marls, which forms a typical badland morphology and erodes marly terrains at a rate of ~1 cm yr –1 (Mathys et al., 2003). Gullies mostly produce fine sediments transported as suspension and have not contributed to the river's gravel recharge.

The study reach corresponds to the last 3 km of the torrent, where the Bouinenc develops a wandering pattern in a 200-m-wide floodplain. The overall channel slope is 0.016 and the mean active channel width is 24 m (range: 10–45 m). Two short bedrock reaches with marl outcrops are observed along the reach, 0.95 and 1.78 km upstream from the confluence with the Bléone (Liébault et al., 2012). The floodplain supports an extensive riparian forest.

The climatic setting is Mediterranean, with a mean annual rainfall of ~900 mm. Most precipitation falls during spring and autumn, but severe convective storms also occur during

summer (Liébault et al., 2012). The discharge of the Bouinenc has only been recorded since 2008 by Irstea, but a gauging station of the ORE Draix-Bléone observatory has been present on the Laval (0.86 km²), a tributary of the upper Bouinenc, since 1983. Two medium floods (Q10>Q<Q50) occurred in 1986 and in 1994 in the Laval (Fig. 47C). A historical database recording natural hazard events (BD-RTM) reports damaging floods for the Bouinenc Torrent in September 1962 and 1986.

3. Methodology

The general approach used to characterise the history of the floodplain morphology and vegetation responses is based on the combination of airborne LiDAR data and historical aerial photographs.

3.1. Data acquisition and pre-processing

3.1.1. Airborne LiDAR data

LiDAR surveys were collected by private companies, Helimap on the Drôme River and Sintegra on the Bès River and Bouinenc Torrent. Technical specifications of airborne LiDAR surveys are described in Table 11. The LiDAR returns were classified as ground and no ground points by data providers. Digital Terrain Models (DTMs) of 1-m resolution were derived from ground point clouds by triangulation and linear interpolation.

Table 11. Technical specifications of airborne LiDAR surveys; the altimetric and planimetric errors were provided by private companies from RTK-GPS ground control points locally measured on a road. SDE: standard deviation of error; NA: not available.

	Bès \ Bouinenc	Drôme
Device	Riegl LMS Q560	Riegl VQ-480
Date	19/04/2010	13-14/09/2010
Elevation precision of laser points (SDE in cm)	5.0	5.2
Planimetric precision of laser points (SDE in cm)	15	NA
Ground point density (points m^{-2})	6.4	3.5

Digital Surface Models (DSMs) were extracted from the highest return point in 1-m pixel. For the Drôme River, the DSM presents many holes that were corrected using a 3×3-m median filter and by selection of the maximum value between the DSM and the filtered DSM. Canopy Height Model (CHM) rasters (pixel size, 1 m) were produced by subtracting the DTM from the DSM (Fig. 48A).

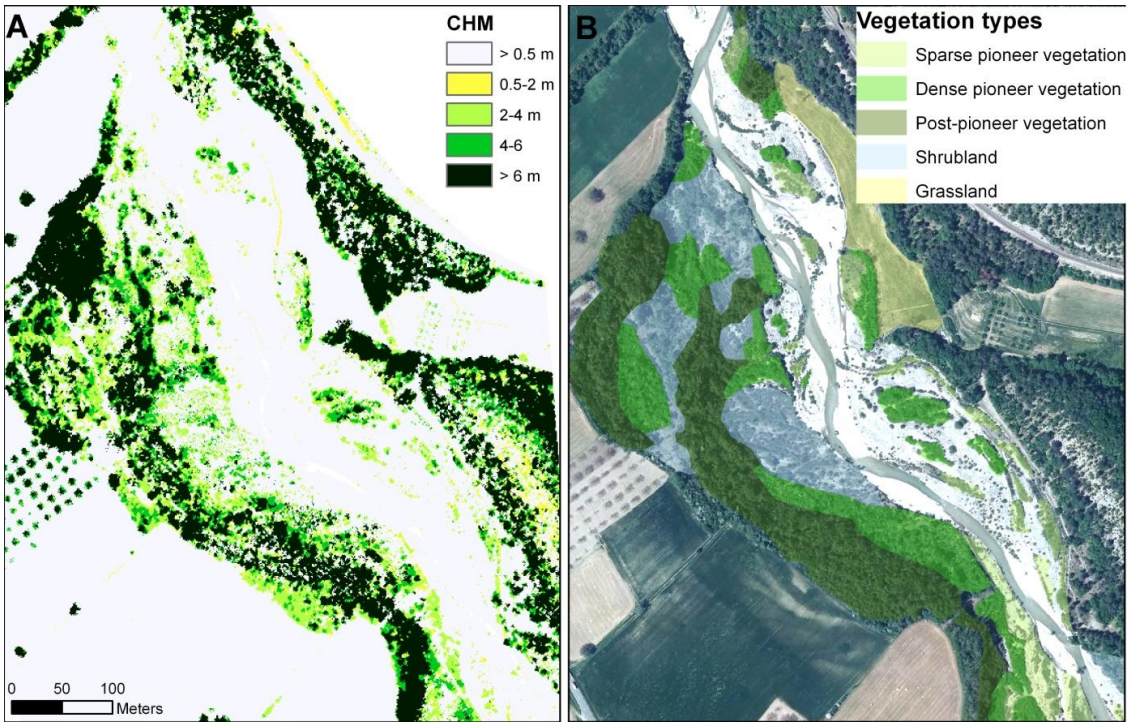

Fig. 48. (A) Extract of the Canopy Height Model (CHM) raster on the Drôme River; (B) example of vegetation type mapping on the 2010 orthophotos; source: IGN.

Detrended DEMs were constructed by removing the valley slope with a MATLAB script specifically developed for this purpose. First, the valley floor mean elevation is extracted for 1-m reaches, perpendicular to the river centerline. Then a long profile is derived and high frequencies

are filtered. Finally, the mean elevation derived from the long profile is subtracted for each DEM pixel of the valley floor (Fig. 49).

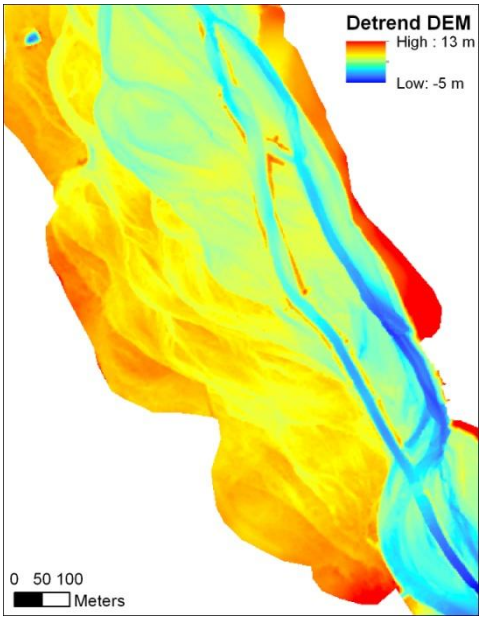

Fig. 49. Extract of detrended DEM on the Drôme River.

3.1.2.Historical and recent aerial photographs

For the Bouinenc Torrent and the Bès River, a set of historical air photos were selected to reconstruct channel changes over a period of 62 years (1948, 1956, 1975, 1982, 1984, 1990, 1993, 2000 and 2004) (Table 12). This was completed with two recent dates (2008 and 2010) for which channel morphology was extracted from two LiDAR surveys. Each historical aerial photograph was georectified based on 2004 orthophotos. Control points were chosen only in the proximity of the river corridor, to avoid distortions due to the relief. The georectification quality was measured with the root-mean-square error (RMSE) and visual control. After this pre-processing, the active channel (water and unvegetated gravel bars) and vegetated islands (pioneer and mature vegetation combined) were manually delineated by the same operator for each date.

Table 12. Data used to reconstruct long-term channel changes of the Bès and Bouinenc study sites.

Year	Type	Scale/Resolution	Source
1948	Black and white photographs	1:30000	IGN
1956		1:25000	
1975		1:30000	
1982		1:17000	
1984		1:30000	
1990		1:30000	
1993	RGB photographs	1:20000	
2000		1:25000	
2004	Orthophotos	0.5 m	
2008	Airborne LiDAR survey	0.5 m	Irstea
2010		0.5 m	

For the Drôme River, active channel and vegetated islands were mapped by Toone et al. (2014) using eight series of aerial photographs (1948, 1956, 1971, 1980, 1991, 1996, 2001 and 2006) (Table 13). This work was completed with the 2010 delineation of the active channel and vegetated islands, mapped on the LiDAR-derived DSM.

Table 13. Data used to reconstruct the long-term lateral evolution of the Drôme study site.

Year	Type	Scale/Resolution	Source
1948	Black and white photographs	1:30000	IGN
1956		1:25000	
1971		1:25000	
1980		1:25000	
1991	Colour photographs	1:17000	
1996	Black and white photographs	1:25000	
2001	Colour photographs	1:25000	
2006	Ortho-photographs	0.5 m	
2010	Airborne LiDAR survey	0.5 m	Irstea

3.2. Long-term evolution and present-day floodplain morphology

From active channel polygons, active channel widths were extracted every 10 m along the study reaches to reconstruct narrowing/widening trends over time. Between each pair of observations, the mosaic of the landscape turnover (overlay) was built according to Belletti et al.

(2014) and four types of landscape changes were obtained: (1) floodplain construction (active channel becoming perennial vegetation in the floodplain), (2) island formation (active channel becoming a vegetated island), (3) floodplain erosion (perennial vegetation in the floodplain becoming an active channel) and (4) island erosion (vegetated island becoming an active channel).

The approximate age of floodplain patches was deduced from the diachronic analysis of historical air photos over the last 60 years. This age corresponds to the date of definitive abandonment of a surface by the active channel, which means the area becomes vegetated by perennial vegetation. Mean relative elevations of dated floodplain patches (relative elevation above the mean active channel elevation) were measured using LiDAR data.

3.3. Attributes of riparian vegetation patches

Vegetation patches were photointerpreted using 2009 orthophotos and CHMs (Fig. 48B). Vegetation types were defined following Dufour's classification (2005), which is based on the pioneering studies conducted by Pautou and Girel (1986) and Marston et al. (1995) on the Ain River. Six generic types were retained: (1) sparse pioneer vegetation, (2) dense pioneer vegetation, (3) post-pioneer vegetation, (4) shrubland, (5) grassland, (6) grassland with shrub colonisation and (7) man-made vegetation (Table 14.).

Table 14. Description of vegetation units (from Dufour, 2005).

Vegetation units	Characteristics
Sparse pioneer vegetation	Sand, gravel, and cobble deposits colonized by low willow shrubs <2-4 m high.
Dense pioneer vegetation	Sand, gravel, and cobble deposits with dense willows or poplars >3-4 m high/
Post-pioneer vegetation	Mixed hardwood-softwood forest, trees > 6 m high; Populus nigra, Fraxinus excelsior, Alnus glutinosa, Quercus robur, Acer spp., Ulmus minor
Shrubland	Dense, diverse, mesophytic shrubs (Crataegus monogyna, Lonicera xylosteum, Ligustrum lantana, Ligustrum vulgare, Prunus spinosa, Viburnum lantana) with some softwood trees (Populus nigra)
Grassland	Dry grassland without willows
Grassland with shrub colonization	Dry grassland with some willows and spiny shrubs (Bromus erectus with Salix eleagnos, Prunus spinosa, Crataegus monogyna)
Man-made vegetation	Planting trees, gravel edges…

Some variables were extracted for each vegetation patch. Vegetation height and cover were derived from the CHM raster. Vegetation height corresponds to the mean value of pixels greater than 0.5 m, and vegetation cover corresponds to the proportion of pixels greater than 0.5 m. Each vegetation patch was also characterised in terms of relative elevation, area, distance to the main wetted channel and age.

We performed a factorial discriminant analysis (FDA) based on the following vegetation patch variables: vegetation height, vegetation cover, floodplain age, relative elevation and distance from main channel. The median and relative interquartile range of these variables were used, the discriminant factor being the vegetation type.

4. Results

4.1. Floodplain history at a pluri-decadal scale

4.1.1. Active channel width changes

Study reaches showed different patterns of active channel changes over the last few decades. The Drôme River showed a relatively stable active width between 1948 and 2010, with a mean value of 36 m in 1948 and 40 m in 2010 (Fig. 50 and Fig. 51A). Some periods underwent slight active channel narrowing, mainly 1956–1970, 1996–2001 and 2006–2010, whereas widening was observed for the following periods: 1948–1956 (+ 60 m), 1991–1996 (+ 49 m) and 2001–2006 (+ 47 m). The 1956 planform presented the highest active width and the most highly developed braided pattern. Compared to the 1956 planform, the 2010 planform showed a 33% decrease in active width and a decline of braided sections with significant reach-scale straightening in some parts (Fig. 50).

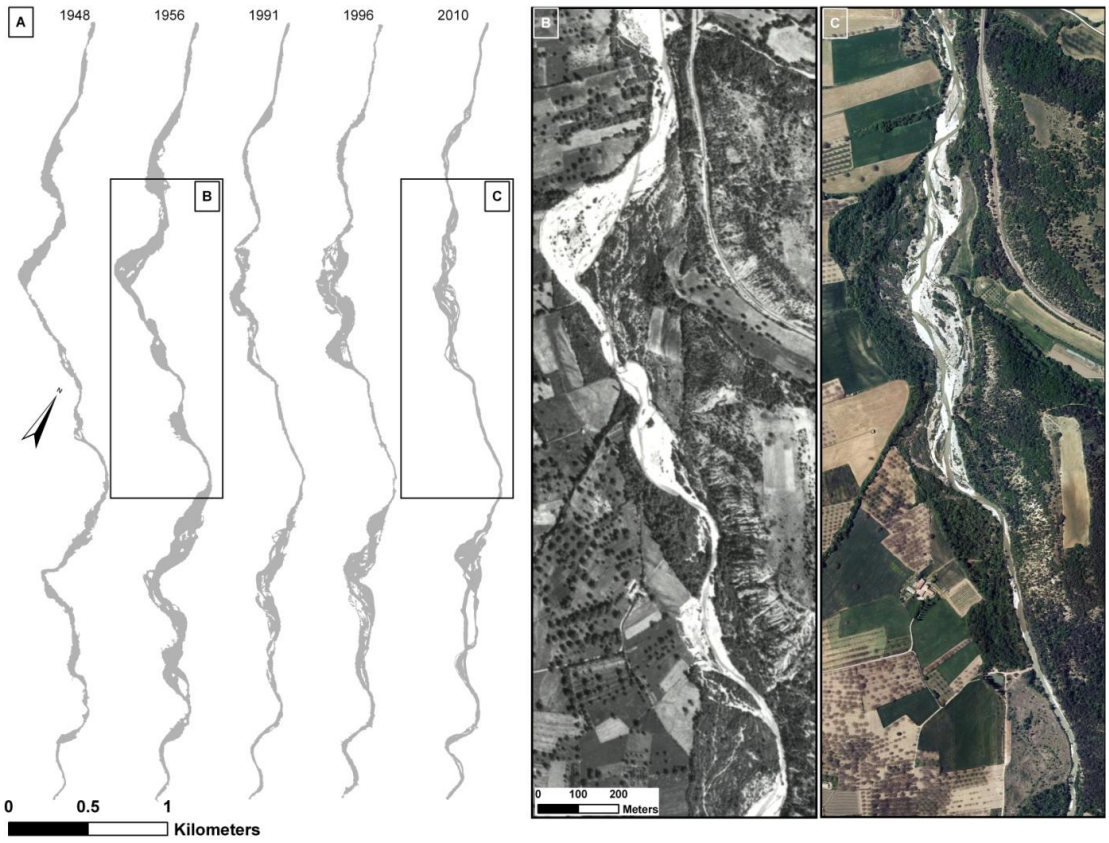

Fig. 50. Active channels of the Drôme River between 1948 and 2010: (A) active channel extent; (B) 1956 aerial photograph (IGN); (C) 2010 orthophotograph (IGN).

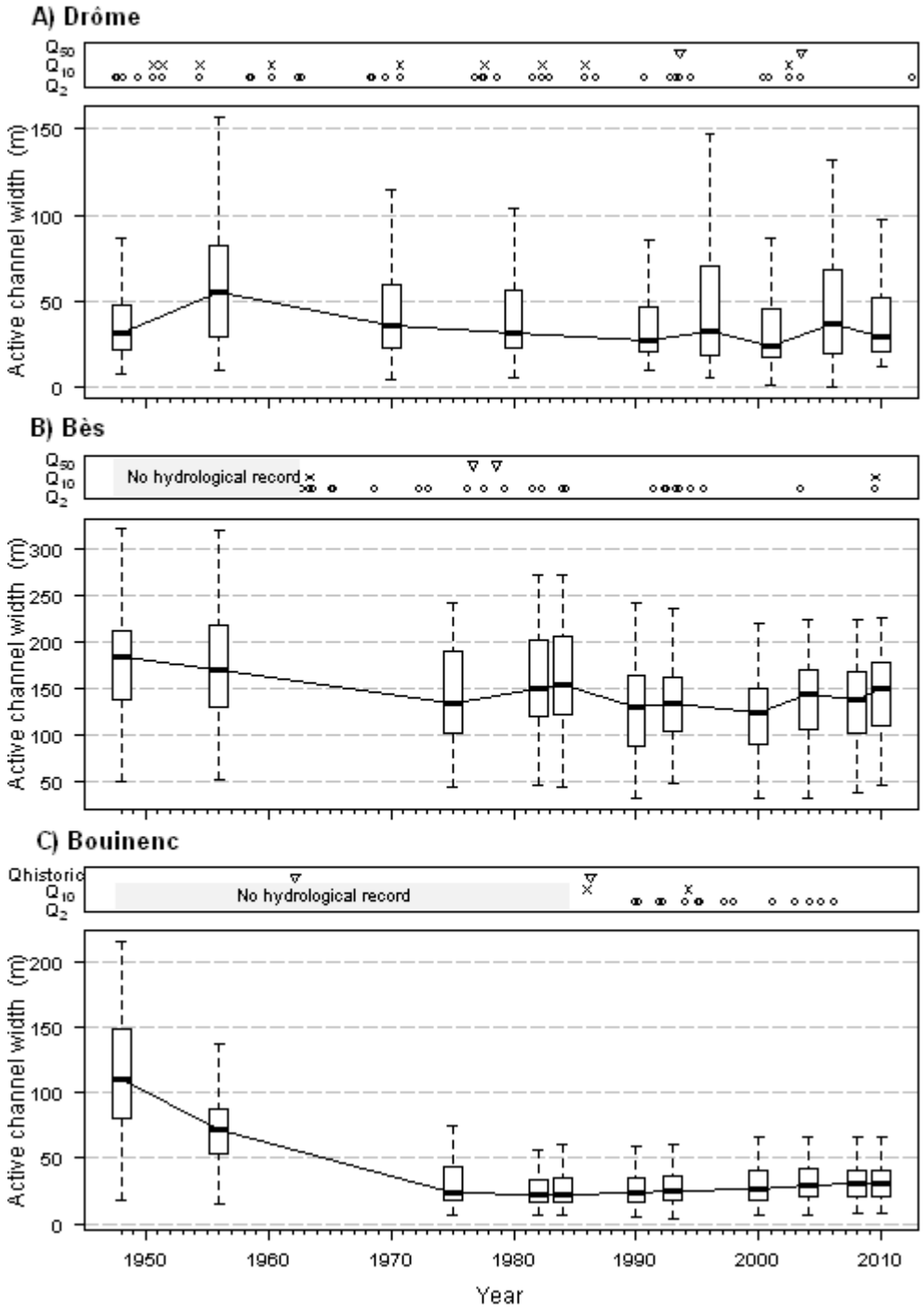

Fig. 51. Active channel widths between 1948 and 2010 of (A) the Drôme River; (B) the Bès River; and (C) the Bouinenc Torrent, Occurrence of small (Q2<Q<Q10), medium (Q10>Q>Q50) and large (Q>Q50) floods are indicated at the top of the graph. The length of the hydrological series for each of the three sites are 1907–2014, 1963–2014 and 1983–2013, respectively. Historic floods (Qhistoric) correspond to floods recorded on BD-RTM on the Bouinenc Torrent.

Like the Drôme, the Bès River showed a relatively stable active channel over the last 60 years, with a slight decrease in the mean active width between 1948 and 2010, 180 m and 143 m, respectively, i.e. 21% narrowing (Fig. 51B). The narrowing period was mainly between 1948 and

1975 and between 1984 and 1990. Significant active width increases were observed for the following periods: 1975–1984 (+12 m), 2000–2004 (+17 m) and 2008–2010 (+8 m) (Fig. 51B).

Active channel changes of the Bouinenc Torrent displayed a very different pattern from the two other sites. A dramatic active width decrease was observed during the period, mainly between 1948 and 1975, during which the torrent lost 73% of its active channel (Fig. 51C, Fig. 52). This resulted in a shifting pattern from braided to wandering. Since 1975, the active channel width has only very slightly increased.

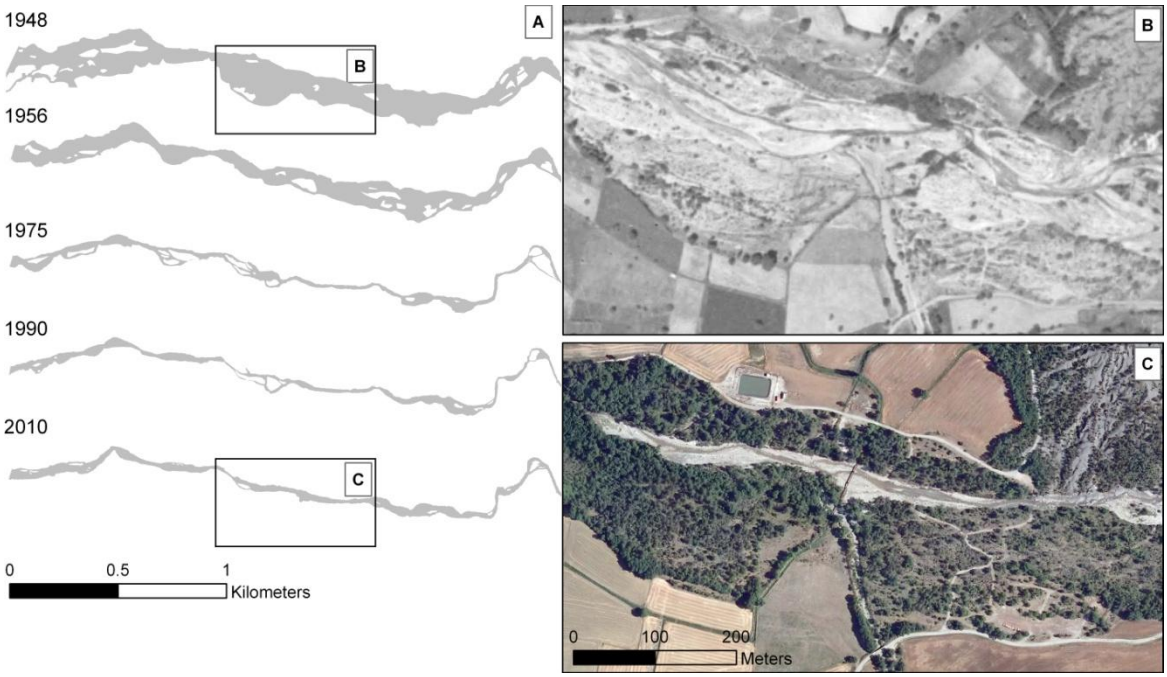

Fig. 52. Active channels of the Bouinenc Torrent between 1948 and 2010: (A) active channel extent; (B) 1948 aerial photograph (IGN); (C) 2009 orthophotograph (IGN). Extent of vegetated floodplain observed on 2009 photograph corresponds to the extent of active channel in1948.

4.1.2.Floodplain erosion and construction linked to channel shifting

On the Drôme River, three periods were characterised by net floodplain destruction, during which active channel shifting and subsequent riparian vegetation rejuvenation occurred: 1948–1956, 1991–1996 and 2001–2006 (Fig. 53A). The 1971–1980 period showed a net equilibrium between floodplain erosion and construction, demonstrating considerable lateral shifting of the active channel. Other periods showed net floodplain construction with substantial vegetation encroachment. Two periods showed an increase in island formation: 1991–1996 and 2006–2010.

On the Bès River, five periods showed net floodplain construction: 1948–1956, 1956–1975, 1984–1990, 1993–2000 and 2004–2008 (Fig. 53B). This is particularly true between 1984 and 1990, where floodplain erosion represented only 12% of floodplain construction. Some periods were characterised by significant net floodplain erosion: 1975–1982, 2000–2004 and 2008–2010 (Fig. 53B). Trends affecting island surface areas did not differ from floodplain surface areas. It is nevertheless interesting to see that the absolute values of changes are equivalent for islands and floodplains, which is not the case for the Drôme where island surface areas are much lower than floodplain surface areas.

On the Bouinenc Torrent, three periods of net floodplain formation were observed (Fig. 53C). This was particularly observed between 1948 and 1975 (0.47 m² km-1 yr-1 between 1948 and 1956, and 0.18 m² km-1 yr-1 between 1956 and 1975). Periods between 1984 and 1993 show equivalent floodplain erosion and formation surface areas, demonstrating active channel shifting. The following periods were characterised by very low values of floodplain turnover, with a slight trend towards net floodplain erosion.

Floodplain turnover rates were calculated from the ratio between the mean annual floodplain erosion rate over the last 60 years and the total floodplain surface areas in 2010. The Bès River showed the highest value with a yearly floodplain turnover of 5.3%, versus 0.9% for the Drôme River and 0.6% for the Bouinenc Torrent.

.

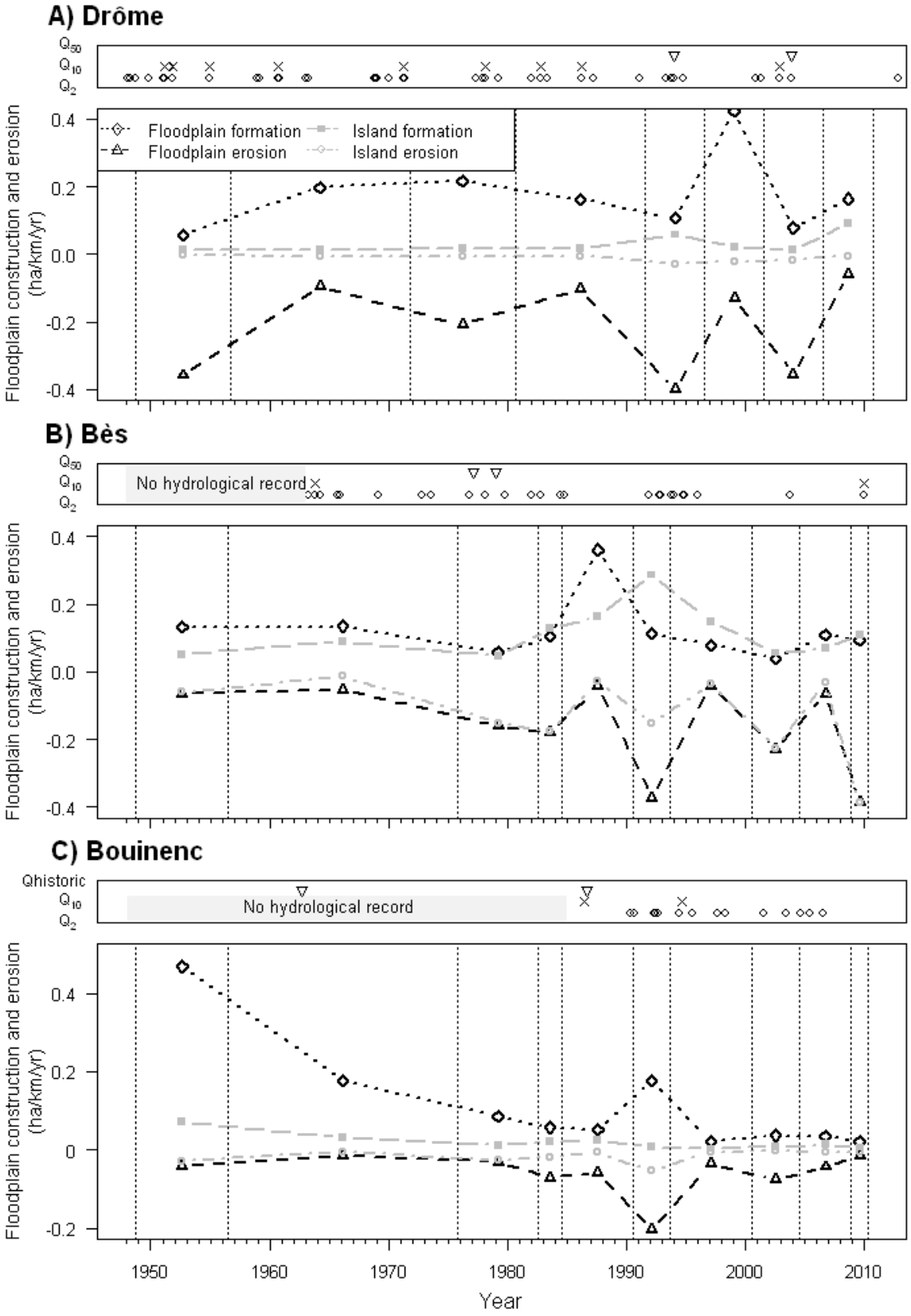

Fig. 53. Floodplain construction and erosion for each study reach over time: (A) Drôme River; (B) Bès River; (C) Bouinenc Torrent. Occurrence of small (Q2<Q<Q10), medium (Q10>Q>Q50) and large (Q>Q50) floods are indicated at the top of the graph. Historic floods (Qhistoric) correspond to floods recorded on BD-RTM on the Bouinenc Torrent. Dotted vertical lines correspond to the date of aerial photographs.

4.1.3.Relative elevation of dated floodplain surfaces

Time variations of active channel elevation reconstructed from terrace remnants are presented in Fig. 54. On the Drôme River (Fig. 54A), the first period of incision occurred before 1948, as attested by the difference in elevation between the 1948 terrace and the floodplain surfaces already vegetated in 1948. The 1948 terrace stands 0.5 m below these surfaces. Between 1948 and 1956, the bed level was stable, and a slow incision was detected between 1956 and 1971. A rapid incision was observed between 1971 and 1996, with acceleration between 1991 and 1996 when a major flood occurred (January 1994). The 2001 remnant surfaces indicate that aggradation occurred between 1996 and 2001, but caution should be exercised for this period, since the 2001 remnant surfaces were not well preserved along the reach and are likely not representative of the bed level changes. Even if the 2001 surfaces are discarded, the 2006 surfaces indicate channel stability between 1996 and 2006, and therefore a specific signature of channel recovery during this decade, when a major flood occurred in December 2003. Finally, another rapid incision was detected between 2006 and 2010, with a rate that had not been observed before.

On the Bès River, the first period of stability or slight aggradation was observed until 1975 with a higher aggradation for the 1975 remnant surfaces. This period was followed by an abrupt incision period between 1975 and 1982, when two major floods occurred in 1977 and 1979 (Fig. 54B). A difference of 0.7 m was observed between the two surface levels. The new bed level only showed a few changes over the two decades that followed with, however, a slight incision trend. This period was interrupted by a period of aggradation between 2000 and 2004.

On the Bouinenc, the first period of incision occurred before 1948, as attested by the difference in elevation between the 1948 terrace and the floodplain surfaces already vegetated in 1948 (Fig. 54C). The 1948 terrace stands 0.4 m below these surfaces. A second progressive incision was detected beginning in 1956 with an increased incision after 1990. This period was interrupted by two aggradation periods: the first period between 1984 and 1990 and the second between 2000 and 2008. After 1975, caution should be used because the remnant surface areas are very low.

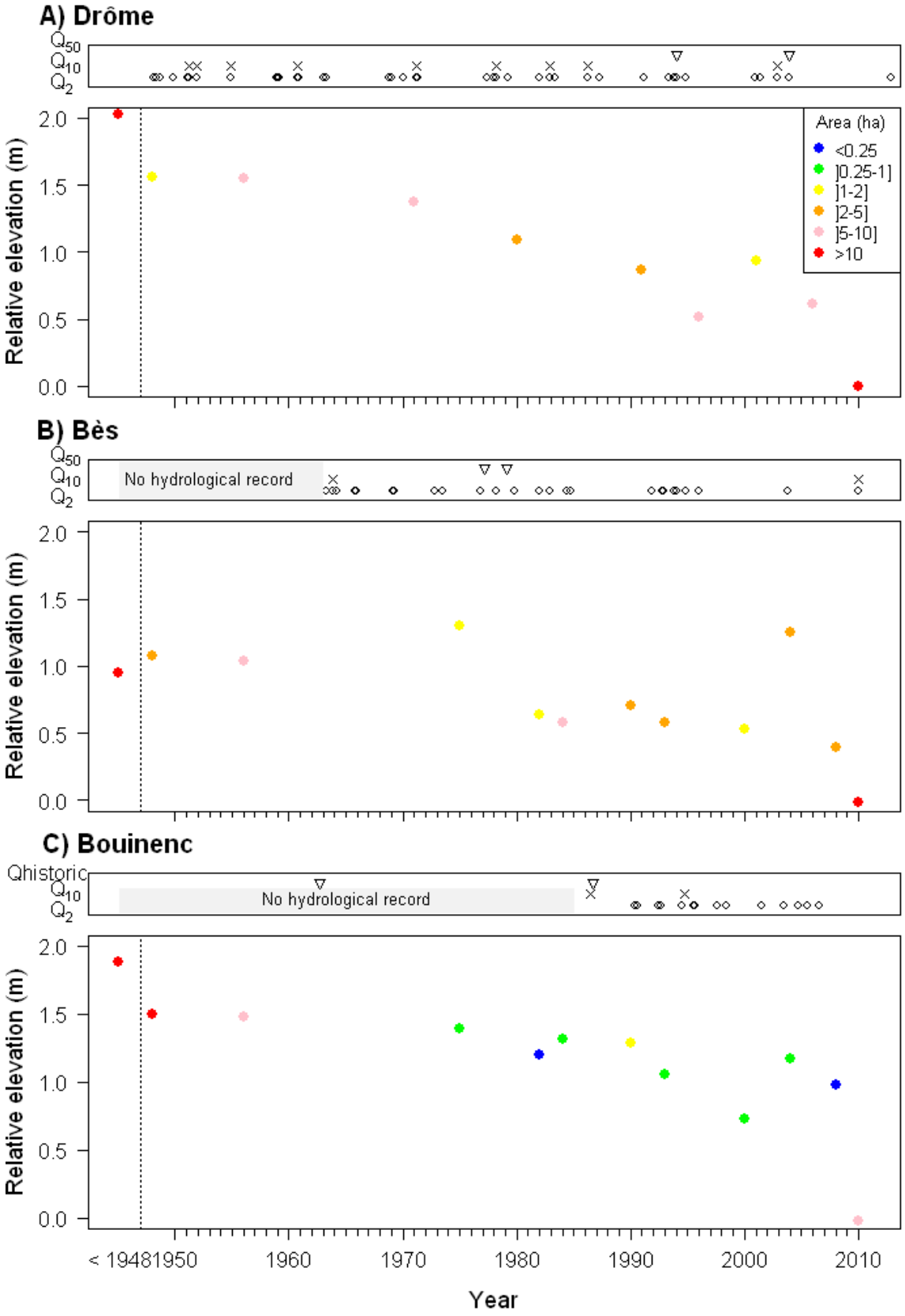

Fig. 54. Relative elevation of remnant surface over time of (A) the Drôme River; (B) the Bès River; and (C) the Bouinenc Torrent; Standard errors are lower than the size of the symbol. Colours indicate the area interval of the remnant surface. Occurrence of small (Q2<Q<Q10), medium (Q10>Q>Q50) and large (Q>Q50) floods are indicated at the top of the graph. Historic floods (Qhistoric) correspond to floods recorded on BD-RTM on the Bouinenc Torrent.

4.2. Contemporary responses of riparian vegetation

4.2.1. Validation of vegetation patch types from LiDAR data

Factor discriminant analysis (FDA) by vegetation types showed that sparse pioneer, dense pioneer and post-pioneer vegetation are clearly distinguished by vegetation height, cover percentage and age (Fig. 55). These three units showed typical changes in vegetation characteristics following the classic ecological succession. Sparse pioneer vegetation patches had the lowest heights and cover percentages. Dense pioneer vegetation patches were slightly taller but much denser than sparse-pioneer vegetation patches. Post-pioneer vegetation patches presented the highest heights and cover percentages. Shrubland vegetation had intermediate height and cover percentage and differed from the other types in its higher relative elevation and the high variability in vegetation height. This may be related to different local conditions, possibly drier, limiting recruitment and growth to a dense riparian unit.

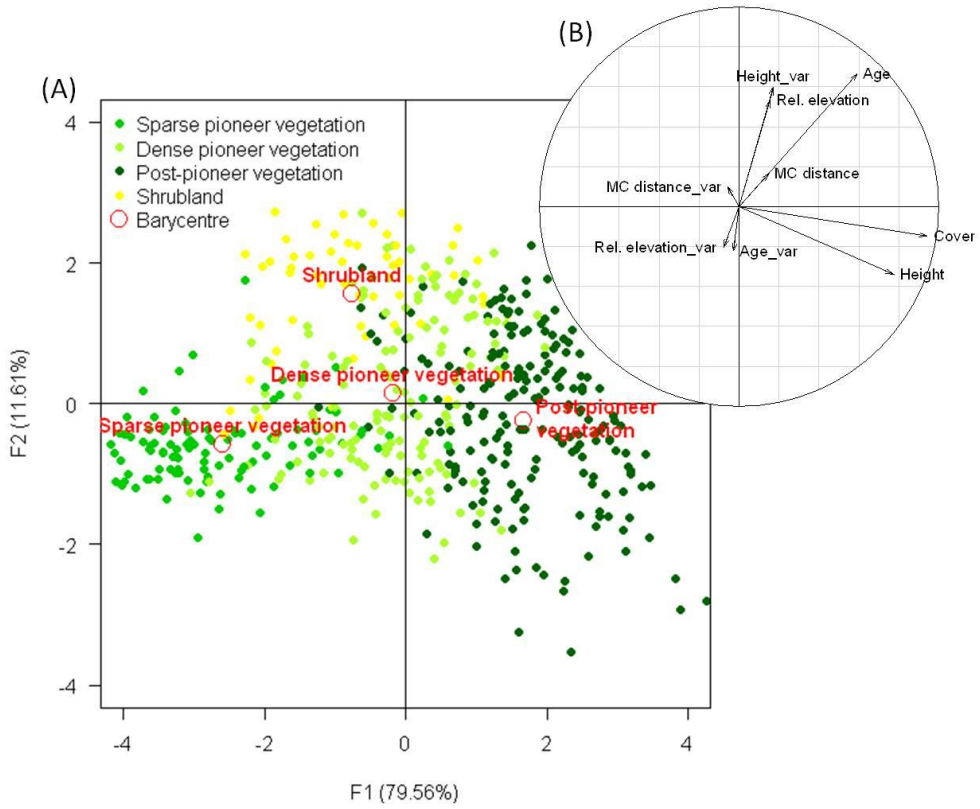

Fig. 55. Results of the FDA discriminated by vegetation type: (A) the F1 × F2 factor map displaying vegetation patches in vegetation type; (B) the correlation circle of variables corresponding to statistical characteristics of vegetation patches (median and relative interquartile range:"_var"). Height: vegetation height, Age: floodplain age; Rel. elevation: Relative elevation; MC distance: distance from main channel median; Cover: vegetated cover percentage.

4.2.1. Inter-site comparison of vegetation patch types

The vegetation mosaic between the three reaches was fairly contrasted, as confirmed by the chi-square test (Table 15). The Bès River is characterised by a high proportion of sparse pioneer vegetation, the Bouinenc River by a high proportion of shrubland. The Drôme River is characterised by a more equi-distribution of vegetation types (Fig. 56).

Table 15. Result of the chi-square test.

Residuals (Adjusted) :

	Drôme	Bès	Bouinenc
Sparse pioneer vegetation	**106.4**	**166.2**	**-278.4**
Dense pioneer vegetation	**198.4**	**-136.0**	**-76.3**
Post-pioneer vegetation	**-176.0**	**144.7**	**43.7**
Shrubland	**-53.8**	**-190.8**	**246.8**

The values in bold are significant at alpha level = 0.05

.

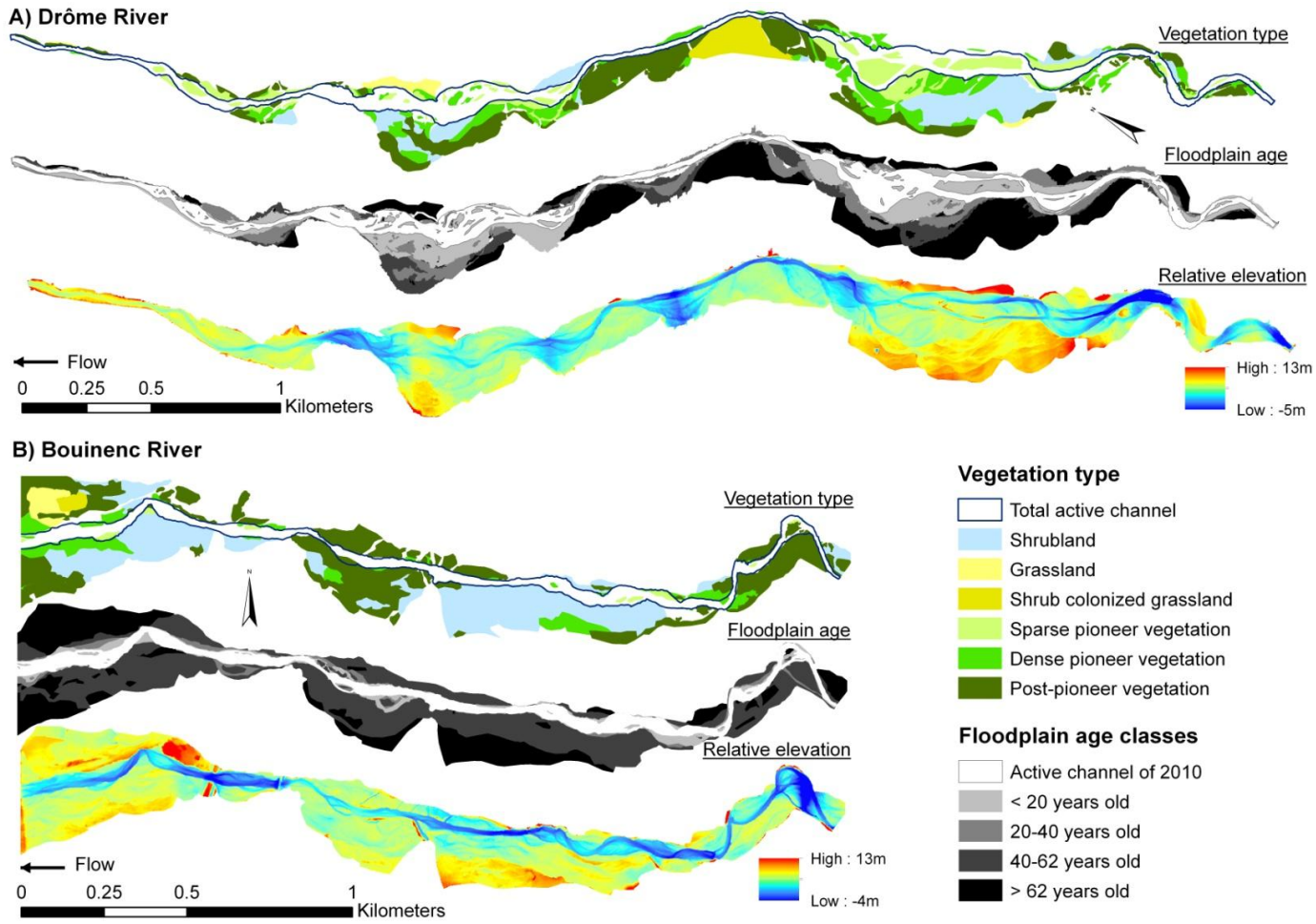

Fig. 56. Map of vegetation units, floodplain age classes and relative elevation for the Drôme River (A); the Bouinenc Torrent (B); and the Bès River (C); (D) boxplot of patch area for each study reach; (E) corresponding area of each type of vegetation (except grassland). Percent in each box corresponds to the percent of each type for each study reach.

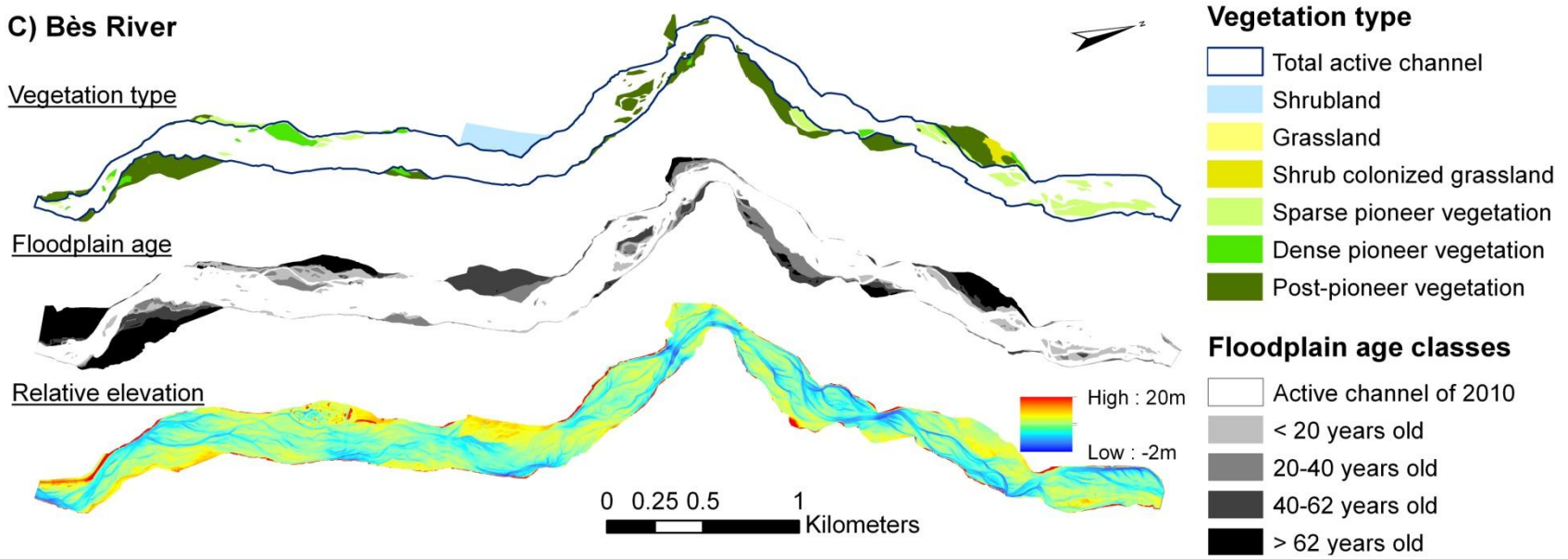

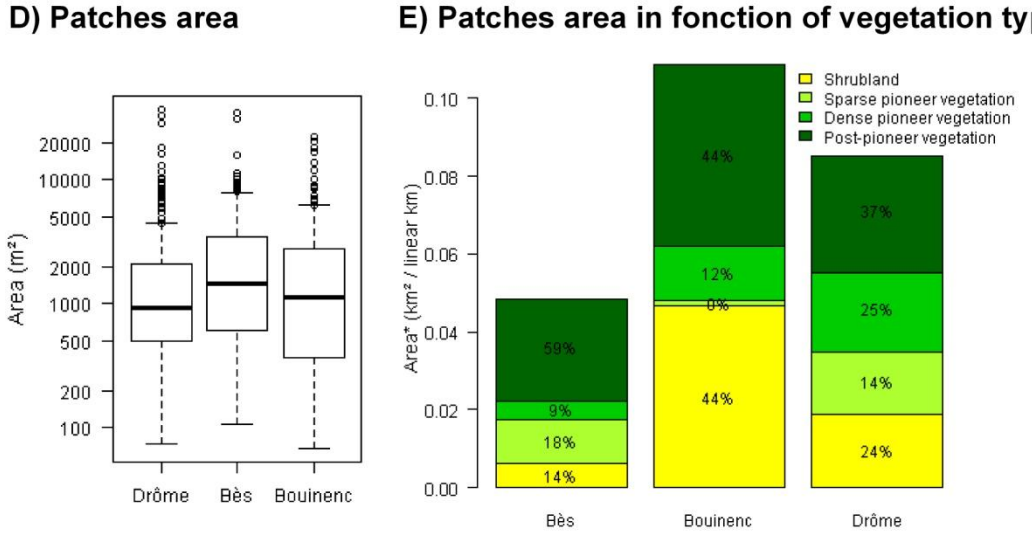

Fig. 58 (continued).

4.2.2. Type and characteristics of vegetation patches over time

On the Drôme, shrublands established at different periods (Fig. 57A). Post-pioneer and dense-pioneer patches also occurred over the whole period. Sparse pioneer vegetation was observed between 1980 and 1991. Some of these patches did not evolve to post-pioneer vegetation, which can be surprising because the successional trend is not as clear here. Younger surfaces were dominated by sparse vegetation.

On the Bès, the succession organisation is much clearer, with sparse vegetation dominant on the younger surfaces and then replaced by dense-pioneer and post-pioneer vegetation (Fig. 57B). Post-pioneer vegetation was then dominant before the 1980s with a small patch of shrubland established during the 1956–1975 period. Sparse and dense-pioneer patches also occurred in the 1990s.

On the Bouinenc Torrent, vegetation established prior to 1975 was predominantly both mature forest and shrubland (Fig. 57C). In the recent period, shrubland almost disappeared, the mature vegetation decreased in frequency where the dense-pioneer and the sparse-pioneer vegetation became dominant. The age gradient was again well established. A surprising peak of dense pioneer patches was observed between 1990 and 1993 and also to a lesser extent for sparse pioneer vegetation.

Consequently, shrubland units and mature riparian units are approximately the same age but regarding the relative elevation, it can be observed that shrubland units had clearly higher relative elevation than post-pioneer vegetation on the Drôme and the Bès (Fig. 58). The elevation difference was lower for the Bouinenc Torrent.

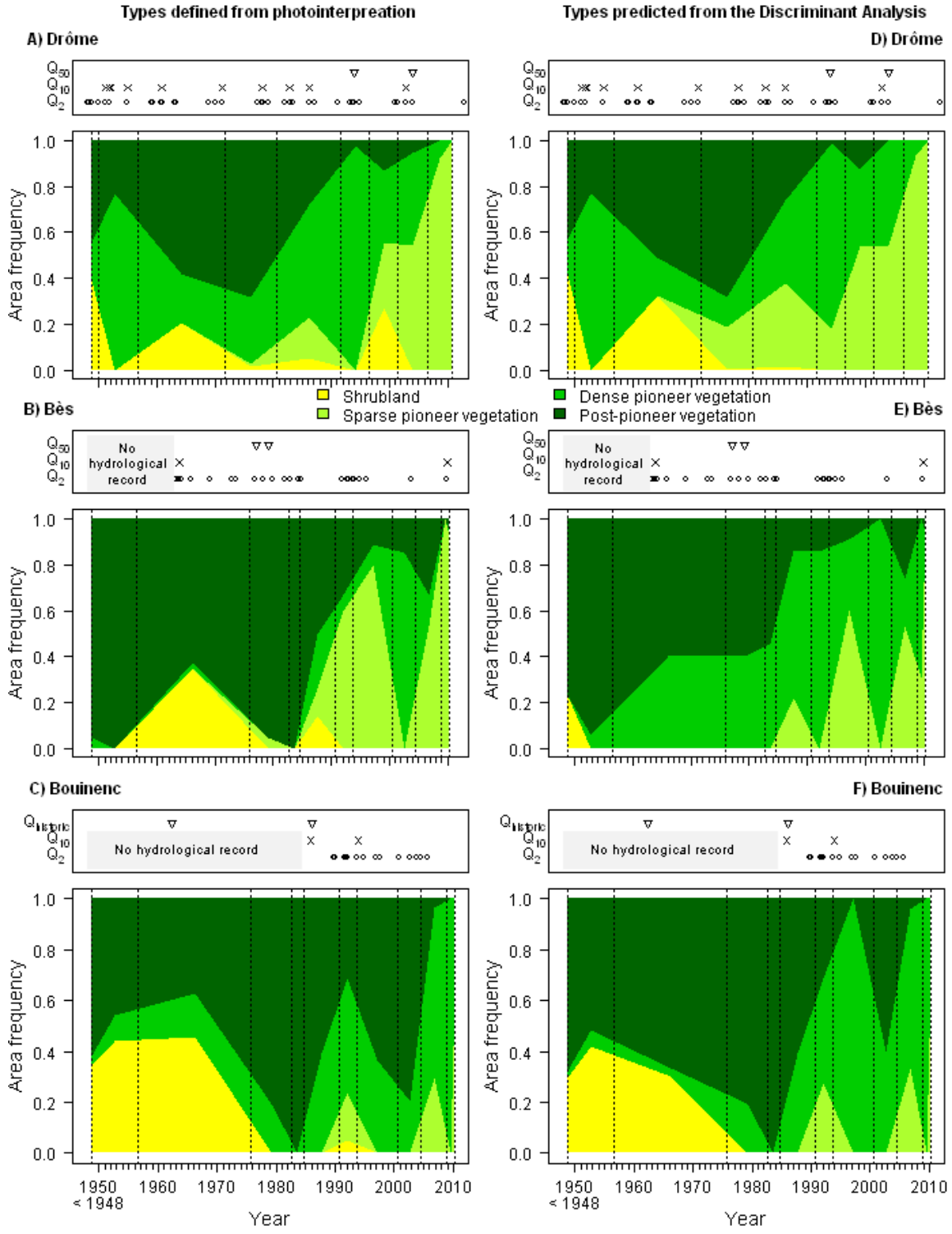

Fig. 57. Frequency of vegetation types per period of floodplain construction following photointerpretation protocol proposed by Dufour (2005) for (A) the Drôme River; (B) the Bès River; (C) the Bouinenc River and frequency of vegetation types per period of floodplain construction predicted from the FDA for (D) the Drôme River; (E) the Bès River; (F) the Bouinenc River. Occurrence of small (Q2<Q<Q10), medium (Q10>Q>Q50) and large (Q>Q50) floods are indicated on the top of the graph. Historic floods (Qhistoric) correspond to floods recorded on BD-RTM on the Bouinenc Torrent; Dotted vertical lines correspond to the date of aerial photographs.

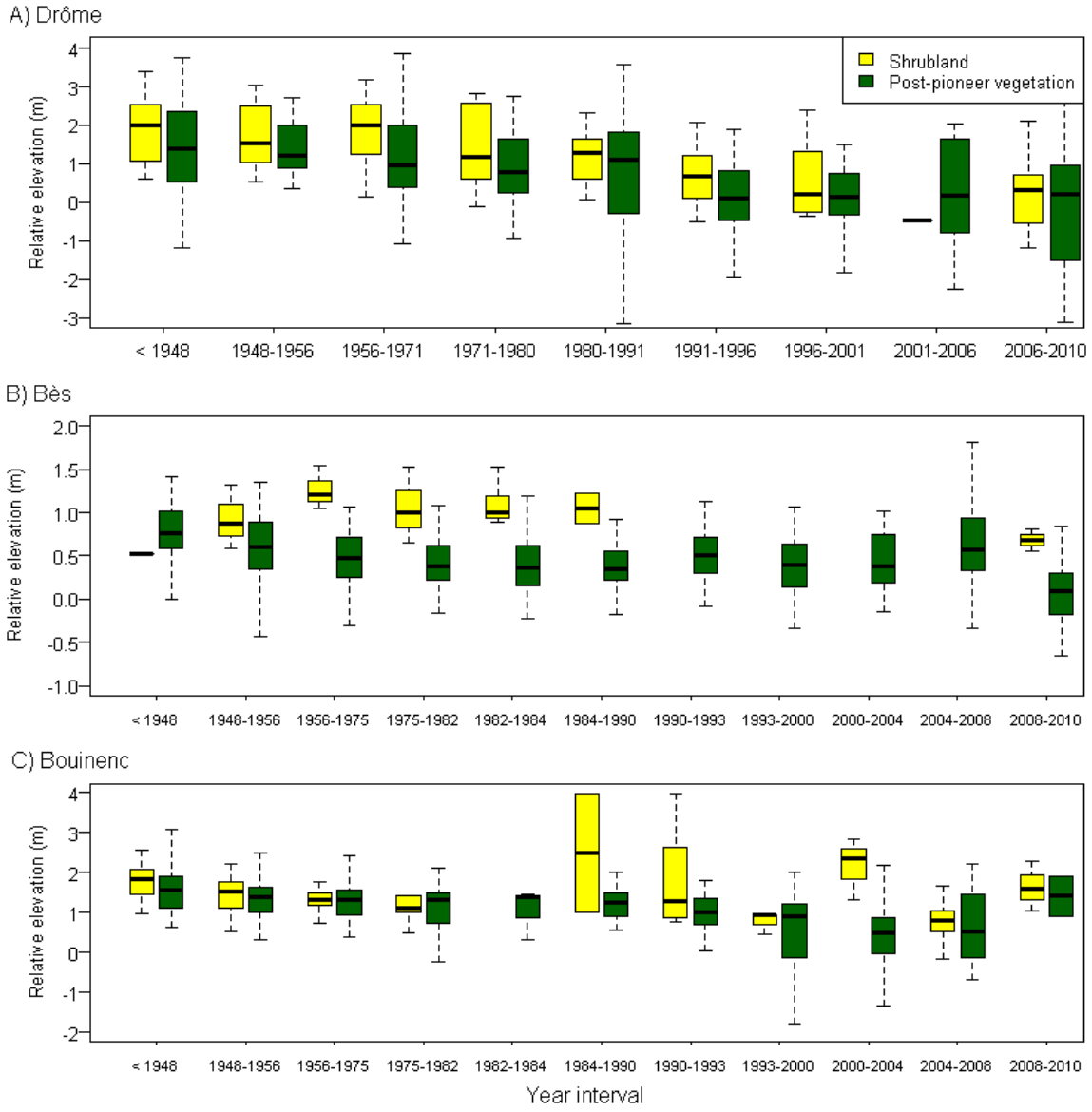

Fig. 58. Relative elevation of shrubland and post-pioneer vegetation units per period of floodplain construction of (A) the Drôme River; (B) the Bès River; (C) the Bouinenc River.

5. Discussion

Fig. 59 summarises changes over time in terms of lateral and altimetric channel changes as well as vegetation units.

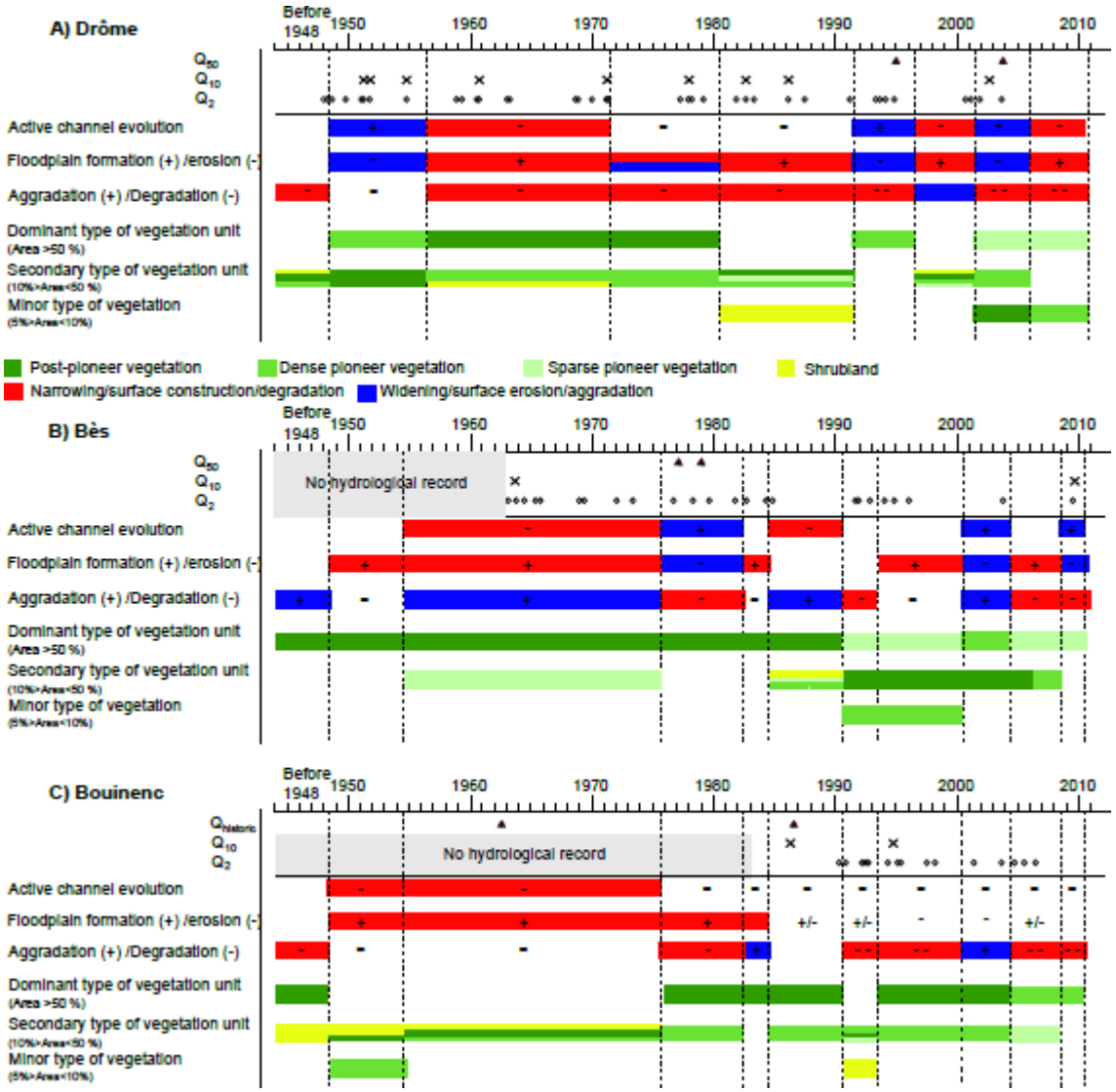

Fig. 59. Summary diagram of lateral and vertical evolution of active channel and vegetation characteristics over time for (A) the Drôme River; (B) the Bès River; (C) the Bouinenc River. Occurrence of small (Q2<Q<Q10), medium (Q10>Q>Q50) and large (Q>Q50) floods are indicated at the top of the graphs. Historic floods (Qhistoric) correspond to floods recorded on BD-RTM on the Bouinenc Torrent.

5.1. History of floodplain topographic levels

Fusion of information delivered by historical aerial photos and LiDAR data revealed an early period of channel incision starting before 1948 for the Drôme River and Bouinenc Torrent. This

early incision was not detected on the Bès River. Previous field investigations along tributaries to the Drôme River have already shown the existence of a terrace level occupied by trees established in the 1920s, which was attributed to the cumulative effect of the climate change following the end of the Little Ice Age and torrent control works of the 1860–1914 period (Liébault and Piégay, 2002; Liébault et al., 2008). These early studies were based on a few cross-sections levelled in the field, the generalisation of which can be challenged. With the systematic analysis of floodplain relief using high-resolution LiDAR-derived DEMs, this study confirmed that the active channels in the 1950s were already entrenched in a vegetated floodplain which formed during the first half of the 20th century. This old floodplain is also visible locally in the Bès on the 1948 aerial photos, but at that time, the active channel occupied almost the entire valley floor, and this channel stands at the same elevation as the few isolated vegetated patches. One possible explanation for this peculiar situation could be the relative position of this reach in the catchment-scale sediment cascade. Compared to the Drôme and the Bouinenc, the Bès is more distally situated in relation to its active sediment sources, which could explain a longer response time to changing sediment supply associated with climate change and the torrent control works carried out in the late 19th century. Even if the drainage area of the Bès is equivalent to the Drôme at Recoubeau, a major sediment discontinuity related to the Claps rockslide is present in the Drôme, and its main sediment source is the Béoux Torrent, located just upstream from the study reach.

Bed level evolution during the second half of the 20th century shows contrasting responses between sites. On the Bouinenc Torrent, the analysis revealed a slow progressive channel incision forming since the 1950s that can be associated with the effect of spontaneous reforestation after the Second World War, already demonstrated in the Southern Prealps and associated with rural depopulation (Taillefumier and Piégay, 2003). This is in good agreement with reconstructed active channel changes, which show the same pattern already seen on tributaries to the Drôme, where it has been associated with a downstream progressing incision induced by a sediment supply decrease (Liébault et al., 2005). The second incision phase, which started in the 1990s, is more difficult to explain. One possibility is that it corresponds to the recovery of a possible aggradation following the large 1986 and 1994 floods (attested by the comparison of 1984 and 1990 remnant surfaces).

On the Drôme River, it appears that channel incision started in the 1970s, and this corresponds to the onset of an active period of gravel mining in this valley (Stella et al., 2003), which stopped in the early 1990s with the prohibition of gravel mining in active channels (passed in 1994 by the Ministry of the Environment). It is remarkable to observe an acceleration of channel incision between 1991 and 1996, a period when a major flood occurred in January 1994. Another major flood occurred in 2003 but did not induce a significant incision. This contrasting response can be

linked with the cessation of gravel mining, which has likely contributed to channel recovery by preventing any further sediment deficit. The onset of another accelerated incision from 2006 onward is more difficult to explain, but the real existence of this late incision phase must be questioned since the 2006 remnant surfaces are highly localised and may not be representative of the whole reach. This has not been confirmed by recent long profile surveys in this reach, in which no incision was detected.

On the Bès, the major incision is observed after the occurrence of two major floods in 1977 and 1979; this incision is abrupt, occurring between 1975 and 1982. A slight incision was observed from 1982, which probably resulted from a reduction in sediment delivery as observed on the head-catchment torrent but in a smaller proportion due to its distal situation in relation to active sediment sources. An aggradation was observed, however, between 2000 and 2004. This aggradation is probably related to a flood occurring in November 2000. In fact, hydrological data on the Bès River have not recorded significant floods at the Pérouré gauging station during this period. However, BD-RTM recorded a flood in November 2000 that caused a great deal of damage upstream from the study reach such as bed scouring inducing the destruction of a bridge and bank erosion.

Finally, it seems that relative elevation between the channel and the different floodplain levels is not only linked to channel incision, but also to gravel progradation on the lowest floodplain levels that were still very connected to the overflows during high floods. This is particularly true for some of the lower floodplain levels observed on the Drôme prior to the 2003 flood or on the Bès prior to the 1977 and 1979 Q50 floods.

5.2. Impacts of floods on lateral morphological changes

On the Drôme River, lateral morphological changes are clearly related to large and medium floods. Positive fluctuations of the active channel and floodplain erosion are related to the occurrence of large floods in 1994 and 2003 with Q>Q50, which widened and reactivated the braided pattern. This type of flood did not occur between 1948 and 1956, but three consecutive medium floods (Q>Q10) were observed during this period. We can also note that after 1956, several equivalent medium floods occurred with no widening response of the channel. No widening pattern was then observed between 1971 and 1980, whereas a 17-year return period flood occurred in 1978. However, this period is characterised by substantial lateral shifting of the active channel. Toone et al. (2014) argued that the impacts of this flood (avulsion, reach-scale straightening and incision) were facilitated by a context of sediment deficit, the presence of an

impoverished, heterogeneous alluvial cover, a post-flood period of decline in flood frequency and anthropogenic routing of the channel by artificial gravel embankments.

On the Bès River, two large floods in 1977 and 1979 can easily explain the widening between 1975 and 1982, and a medium flood in 2009 can explain the widening between 2008 and 2010. The increase of the active channel width between 2000 and 2004 probably stems from a flood occurring in November 2000 that was not recorded at the Pérouré gauging station but was recorded on the BD-RTM.

On the Bouinenc torrent, a long-term pattern of narrowing was observed and medium floods, which occurred in 1962, 1986 and 1994, had no significant effect on the active channel width.

On the Drôme and Bès Rivers, no long-term pattern of widening or narrowing was observed but lateral fluctuations are significantly associated with large and medium floods, although this link is complex. On the Drôme, medium floods had greater effects in the 1950s than today. This could be the consequence of a decreasing sediment supply from the Béoux, where active channel narrowing is observed (Liébault, 2003). Moreover, shifting is also exacerbated in aggrading systems and slightly decreased when the channel is incising, as shown by Toone et al. (2014). This is not the case of the Bès, where strong responses to medium floods are still observed today, because of the high sediment supply from the catchment. The impact of the flood pulse (with a return period greater than 2 years) and in particular a 10-year flood return period on braided river morphology has already been shown by previous authors (Bertoldi et al., 2010; Belletti et al., 2014) and is confirmed in this case. The lower impact of floods on channel width in the context of sediment deficit has also been highlighted by Belletti et al. (2014).

On the Bouinenc torrent, long-term active channel narrowing was observed with a critical period between 1948 and 1975, in accordance with the model description for the small torrents in the Drôme, Eygues and Roubion catchments (Liébault and Piégay, 2002; Liébault et al., 2005). This can be interpreted as an effect of a sediment supply decrease due to catchment reforestation. Similar to the most recent period on the Drôme reach, recent floods (1962, 1986 and 1993) had no effect on the channel because there was no sediment available to promote flow divergence in the channel and maximise shear stress on banks and widen the active channel to the1948 level. As shown by Constantine et al. (2010), Alber (2012) and Toone et al. (2014), it seems that channel shifting is exacerbated in active bedload transport conditions and slows down when sediment supply and bar dynamics are reduced.

5.3. Impacts of long-term changes on contemporary vegetation mosaic

Long-term geomorphic changes play a significant role in explaining vegetation mosaics. Long-term narrowing of the Bouinenc Torrent until 1975 resulted in a well-developed vegetated floodplain for the most part composed of mature units (shrubland and post-pioneer units).

A high relative proportion of shrubland area on the Bouinenc and the Bès until 1975 compared to other types of unit can result from the incision starting between 1975 and 1982. This phenomenon was more pronounced on the Bouinenc because of high surface production before 1975 caused by substantial narrowing.

On the Drôme River, the shrubland area is related to a long period of channel narrowing because of no flood activity and bed level incision. Therefore, shrubland patches seem to be a good indicator of the incision period. Vegetation development is strongly affected by high floodplain surface elevation compared to the water table level (Stella et al., 2013; Singer et al., 2014). So incision impacts vegetation by disconnecting it from the water level and preventing vegetation recruitment and seed colonisation by hydrochory. For example, Stella et al. (2013) showed on the Drôme that the riparian forest decline stems from bed incision associated with drought years.

Shrubland units have approximately the same age of mature riparian units but different physionomic characteristics. LiDAR data confirmed that these units are more frequent on fairly higher elevation units than post-pioneer units, giving greater value to the interpretation that this difference in physiognomy is related to drier conditions, explaining lower tree density and height. These units clearly describe the long-term floodplain changes and can be a proxy of terrace development in the sense they are less and less effectively connected to the present functioning of the river channel.

5.4. Impacts of the difference in braided river activity on contemporary vegetation mosaics

Vegetation mosaics differ greatly from one river to another depending on both differences in local conditions related to water accessibility and frequency of pioneer units related to the turnover rate due to active braiding. Higher turnover results in less vegetated area, notably for old patches (shrubland and mature riparian forest).

Still active, the Bès River shows a lower vegetated floodplain but a much better equi-distribution of different vegetation units related mainly to a higher turnover rate. This is also true for the Drôme, where all vegetation units are equi-represented. However, the presence of denser pioneer vegetation than on the Bès River shows a river that is less active than the Bès, as attested by the turnover rate, and therefore has much more homogeneous vegetation mosaics. The Bouinenc Torrent is the least active with a well-developed vegetated floodplain of mature riparian forest which has undergone very little turnover.

Both the Bès and the Drôme Rivers show greater habitat diversity than the Bouinenc River, but the Drôme River, less active than the Bès River, shows a higher vegetated floodplain than the Bès River. Consequently, as shown on the Magra, the progressive evolution from a bar-braided pattern to a single-thread system generates a decrease in channel and bar habitats as well as the expansion of woodland units (Dufour et al., 2015). In terms of landscape diversity, Dufour et al. (2004) showed that higher active rivers present lower landscape diversity due the domination of bar units with fewer vegetation units. However, as confirmed in this present study, they showed that these rivers exhibit advantageous ecological habitats such as pioneer units, maintaining a diversity of ages and species within riparian forests.

5.5. Validation of vegetation succession model

The combination of vegetation characteristics derived from LiDAR data and age determination from sequenced aerial photos gives good results in terms of vegetation unit classification. The three classes (sparse, dense pioneer and post-pioneer vegetation) show typical changes in vegetation characteristics following the classical ecological succession in terms of height and density. However, several misclassifications in the vegetation succession model are observed. This is particularly true on the Drôme River, where dense pioneer vegetation patches were observed for all ages. This was also observed on the Bouinenc River. Possible explanations may be related to human interventions on vegetation, disturbing vegetation succession, which may explain a contradiction between the physical setting (relative elevation, unit age) and vegetation characteristics (height and density) or photointerpretation misclassifications. Twenty-two per cent of the units are misclassified according to the FDA confusion matrix (Table 16). Notably, shrublands are only well classified 63% of the time and can be misclassified 18% of the time as dense pioneer vegetation, and also significantly misclassified with sparse pioneer and post-pioneer units. Fig. 57C, D and E redraws the frequency of vegetation types per period of floodplain construction for which the vegetation types are predicted from the FDA. In this figure, many of the misclassifications in succession models are no longer observed. Classification of vegetation

patches from combined LiDAR information (tree density and height, relative surface elevation) and sequential aerial photo information (surface age) should allow more objective vegetation classification: the present study provides the discriminant functions for this task.

Table 16. FDA confusion matrix discriminated by vegetation type.

From \ to	Sparse pioneer	Dense pioneer	Post-pioneer	Shrubland	Total	% correct
Sparse pioneer	84	17	0	2	103	82%
Dense pioneer	14	106	9	14	143	74%
Post-pioneer	1	26	168	7	202	83%
Shrubland	6	10	5	36	57	63%
Total	105	159	182	59	505	78%

6. Conclusion

Five main conclusions can be drawn from this study:

(1) The combination of LiDAR data with historical aerial photos allows for reconstruction of the timing of channel incision associated with channel narrowing or widening, and for the identification of the effect of large floods on channel morphology. This study underlines two major periods of incision, one starting before 1948 and a second in the second half of the 20th century.

(2) Flood intensity controls smooth or abrupt channel incision, with high incision for Q50 floods in the context of a sediment supply deficit.

(3) Large and medium floods induce channel widening with decreasing impacts in limited sediment supply conditions.

(4) Long-term changes play a significant role in explaining vegetation mosaics with a well-developed vegetated floodplain composed mostly of mature units with long-term narrowing. Rivers with higher activity show an equi-diversity of floodplain vegetation units. Presence of shrub patches seems to be a good indicator of incision periods.

(5) Photointerpretation classes of physiognomic vegetation units are fully validated by LiDAR data and age patches established from overlays of the different channel positions observed on the

historical aerial series using FDA. This approach also provides insights into identifying misclassifications and their interpretation.

CHAPITRE 5

CONCLUSION GENERALE ET PERSPECTIVES

L'étude de la morphologie fluviale a connu de récentes avancées avec le développement de nouvelles technologies pour la mesure topographique. Cette thèse s'inscrit dans ce contexte, l'objectif étant de tester de nouvelles méthodologies s'appuyant sur les données LiDAR, combinées à des mesures de terrain ou des informations tirées de photographies aériennes, afin d'améliorer la connaissance des structures et des dynamiques morphologiques des rivières en tresses. Ce chapitre synthétise les principales avancées méthodologiques et thématiques de cette thèse, ainsi que les pistes de recherche qui n'ont pas pu aboutir à des résultats consolidés. Pour finir, quelques perspectives sont développées.

1. Apports méthodologiques des données LiDAR pour l'étude des rivières en tresses

Pour répondre aux 3 grands questionnements scientifiques de cette thèse, qui sont (i) la détection des changements morphologiques à l'échelle d'une crue, (ii) l'analyse des signatures morphologiques longitudinales, et (iii) l'analyse de changements morphologiques pluri-décennaux en lien avec les unités végétales de la mosaïque fluviale, différentes approches méthodologiques ont été développées. Il s'agit de (i) la différenciation de données LiDAR séquentielles pour le calcul d'un bilan sédimentaire (Chapitre 2); (ii) l'extraction automatique de la signature morphologique des tresses à partir de profils en travers dérivés du LiDAR (Chapitre 3); (iii) le couplage du LiDAR avec les photographies aériennes historiques pour accéder à la topographie, aux caractéristiques de la végétation mais aussi à la datation des surfaces constitutives de la mosaïque fluviale (Chapitre 4).

1.1. Détection des changements morphologiques suite à une crue

Cette thèse montre dans un premier temps que l'utilisation de données LiDAR séquentielles à forte densité de points (7-9 points/m²) a permis de détecter de manière fiable et robuste les changements morphologiques d'un lit en tresses suite à une crue d'une période de retour de 14 ans. Des étapes de traitement sont cependant essentielles pour élaborer un bilan sédimentaire et pour caractériser la variabilité spatiale des changements morphologiques. Le réalignement des données LiDAR est une étape primordiale même si les données fournies par le prestataire sont déclarées exemptes d'erreur systématique de positionnement, après vérification sur des points de contrôle au sol. L'exemple du Bès montre d'une part que même si cette erreur systématique est faible (3 cm), sa propagation sur un tronçon de plusieurs kilomètres engendre une erreur

considérable sur le calcul du bilan sédimentaire, et que d'autre part cette erreur n'est pas uniforme spatialement et qu'un réalignement par sous-tronçons est nécessaire. L'exemple du Bès a aussi montré que même si les surfaces en eau lors des acquisitions LiDAR représentent moins de 5-7 % de la surface de la bande active, l'estimation grossière de leur contribution au bilan sédimentaire (à partir des hauteurs d'eau moyennes associées aux débits mesurés lors des acquisitions LiDAR) révèle qu'elles doivent impérativement être prises en compte. Elles représentent en effet 40% du volume en érosion et 28% du volume déposé. Enfin, la caractérisation de la variabilité spatiale de l'incertitude en fonction des états de surface (et notamment de la rugosité altimétrique du lit) est aussi nécessaire pour élaborer une cartographie fiable des changements altimétriques. La propagation des incertitudes en fonction des états de surface a permis d'établir les seuils critiques de détection des changements d'altitudes qui sont compris entre 19 et 30 cm (avec un intervalle de confiance à 95%). Cette méthodologie a été mise en œuvre sous ArcGIS et *R* pour le calcul du bilan sédimentaire et les calculs d'incertitudes (Cf. scripts R en annexe A).

1.2. Extraction d'indicateurs de la morphologie en tresses

Les données LiDAR ont été utilisées pour caractériser la signature morphologique des lits en tresses à l'échelle plurikilométrique. L'avancée méthodologique de cette thèse est l'extraction automatique d'indicateurs morphologiques sur des profils en travers de la bande de tressage espacés de 10 m. Ceci a permis d'étudier les variations longitudinales de plusieurs métriques morphologiques (largeur de bande active, *BRI*, nombre de chenaux) et d'établir des longueurs d'onde caractéristiques de ces signaux. Cette méthodologie a été mise en œuvre sous ArcGIS pour l'extraction systématique des profils en travers et sous *R* pour calculer les indicateurs de façon automatisée et traiter le signal (ondelettes). Les scripts réalisés sous *R* sont présentés en annexe B.

1.3. Reconstruire l'évolution contemporaine des plaines alluviales et caractériser les peuplements riverains

Les données LiDAR permettent aussi d'accéder facilement à la topographie sous couvert végétal et donc d'étudier la topographie de la plaine alluviale. Couplé à une étude diachronique de photographies aériennes, le LiDAR a permis de reconstruire la chronologie de l'incision des lits en tresses à partir de l'extraction et de la datation des surfaces végétalisées de la plaine alluviale entre les années 1950 et aujourd'hui.

Les données LiDAR permettent enfin d'accéder aux caractéristiques de la végétation riveraine (hauteur, densité de la végétation, altitude des unités forestières par rapport à la rivière). Couplé à une étude diachronique de photographies aériennes, le LiDAR a permis de croiser les caractéristiques de la végétation avec les conditions topographiques locales et l'historique de construction de la plaine alluviale. Cette méthodologie a mis en évidence que les unités de végétation déterminées par photo-interprétation sont bien validées par les informations extraites du LiDAR (hauteur, densité) et l'âge des peuplements calculé à partir de la superposition des différentes positions de la bande active observées sur les photographies aériennes historiques. Cette approche a montré qu'une classification des unités de végétation à partir des informations LiDAR et de la datation des surfaces à partir des archives photographiques permet d'éliminer des erreurs de classification par photo-interprétation et fournit ainsi une classification plus objective de la végétation.

2. Apports thématiques des données LiDAR pour l'étude des rivières en tresses

Cette thèse a permis de valoriser des résultats concluants pour l'étude de la dynamique des rivières en tresses sous la forme de 3 articles (un publié, un soumis et un à soumettre). Ces principaux résultats sont synthétisés ci-après. Cependant, certaines pistes de recherche explorées n'ont pas permis d'aboutir à des résultats consolidés et donc à un article scientifique. Ceux-ci sont présentés dans le paragraphe 2.4. Ils concernent principalement le lien entre la morphologie en travers et le régime sédimentaire.

2.1. Impact des crues

La thèse a permis d'apporter des éclairages sur l'effet géomorphologique des crues dans les lits en tresses à partir (i) de l'analyse fine de la crue de décembre 2009 sur le Bès, et (ii) de l'analyse de la variabilité interannuelle de la largeur de bande active sur les autres sites. Cette thèse confirme l'impact des crues de périodes de retour 10 ans et plus sur la morphologie des tresses. Sur le Bès, la crue de 2009 a été suffisamment puissante pour initier de nombreuses avulsions et remanier 54% de la bande active. Ce chiffre doit être vu comme une estimation basse, compte tenu de la non prise en compte des zones où l'érosion et le dépôt se sont compensés et où le bilan altimétrique est nul malgré la remobilisation du lit. Le patron longitudinal du *BRI* a été complètement modifié par la crue, contrairement au patron longitudinal de la largeur de bande

active. A l'échelle pluri-décennale, cette thèse montre aussi que l'effet morphologique des crues sur la largeur de bande active est fortement modulé par les conditions de recharge sédimentaire du tronçon. A période de retour équivalente, on observe en effet des réponses morphologiques beaucoup plus fortes dans les années 1950 que dans les années 1990 sur la Haute Drôme, vraisemblablement sous l'effet d'apports sédimentaires qui étaient plus importants. Le torrent de la Béoux, qui constitue la source sédimentaire principale de la Drôme en amont de Recoubeau, s'est en effet fortement rétracté depuis les années 1950 (Liébault et al., 2013b), ce qui traduit une tendance à la diminution des apports sédimentaires. Il est également montré que les crues de forte intensité accélèrent l'incision du lit lorsque les apports sédimentaires sont faibles.

Ces résultats sont en adéquation avec les observations de Bertoldi et al. (2010), Comiti et al. (2011) et Belletti et al. (2014). Les processus d'avulsion avec réarrangement du réseau de chenaux observés largement sur le Bès pour une crue de période de retour 14 ans avaient déjà été mis en évidence sur le Tagliamento par Bertoldi et al. (2010) qui attribuaient ces processus aux crues de période de retour supérieure à 2 ans ("flood pulse"). Les conditions hydrologiques associées à ces phénomènes d'avulsion sont importantes à déterminer, car ces processus contrôlent la destruction et la construction des bancs, et in fine, la dynamique de colonisation végétale du lit. Cette thèse ne permet pas de confirmer ce seuil hydrologique car un seul événement de crue a été observé sur le Bès. Comme sur le Tagliamento, cette thèse a montré que le transport solide ne concernait pas toute la bande active, même pour une crue de période de retour 14 ans (54% de la bande active remanié sur le Bès, et ~60% sur le Tagliamento pour des crues de plein bord).

L'impact des crues décennales sur la largeur de la bande active et sur la surface des îles végétalisées avaient déjà été mis en évidence par différents auteurs. Belletti et al. (2014) ont aussi observé qu'en contexte de déficit sédimentaire, l'impact des crues sur la dynamique latérale était plus faible. Sur la rivière Piave (Alpes italiennes), fortement impactée par les extractions de graviers, Comiti et al. (2011) ont aussi observé une expansion de la bande active à partir des années 1990 sous l'effet cumulé de l'occurrence rapprochée de 2 crues décennales, de l'arrêt des extractions de graviers, et de conditions encore favorables de recharge sédimentaire par les affluents.

2.2. Longueur d'onde

L'analyse a porté sur un linéaire de tressage de plus de 25 km réparti sur 9 sites, dans les bassins versants de la Drôme, du Drac et de la Bléone. Ces données mettent clairement en évidence l'effet du confinement de la tresse sur ses propriétés morphologiques. Sur le site du Bès où se développe une tresse confinée dans une vallée intramontagnarde relativement étroite, des

signatures morphologiques très contrastées sont observées de part et d'autre d'un verrou en aval duquel le fond de vallée s'élargit de 25%, alors que la pente du lit reste uniforme. La réduction du confinement se traduit ici par un élargissement de la bande active, une amplification du taux de tressage, et une réduction de la rugosité altitudinale du lit. Sur les autres sites étudiés, on voit aussi très nettement apparaître l'influence des obstructions et du confinement (cônes de déjections, terrasses quaternaires, versants) sur la variabilité longitudinale de la largeur de bande active. Ces irrégularités ponctuelles liées au contexte local engendrent des ruptures dans les signaux morphologiques, ce qui peut parfois perturber la lecture des périodicités morphologiques longitudinales régies par les écoulements au sein d'un environnement alluvial non contraint.

Malgré ces effets locaux, des longueurs d'ondes caractéristiques ont pu être mises en évidence pour la largeur de la bande active et le *BRI*, à partir de la méthode des ondelettes. Ces périodes ont été normalisées par la largeur moyenne de bande active (*W*) pour pouvoir établir des comparaisons entre les sites. Deux périodes caractéristiques émergent de cette analyse, avec une première période normalisée de 3-4 * *W* et une deuxième égale à 9-10 * *W*. La période à 3-4 * *W* serait liée à la dynamique des macroformes (bancs élémentaires) et se rapproche de celle déjà observée en canal expérimental (Zanoni et al., 2008). Elle est également proche de la période caractéristique des déformations morphologiques obtenue sur le Bès à partir de l'analyse du bilan sédimentaire net de la crue de décembre 2009, de période de retour 14 ans. En revanche, la période à 10 * *W* n'a jamais été observée ni en canal, ni en conditions naturelles. Elle pourrait être liée à la dynamique de transfert à long terme des sédiments et correspondre ainsi aux successions longitudinales des mégaformes sédimentaires (Church, 1983; Griffiths, 1993). Cette longueur d'onde n'est pas toujours visible sur le terrain car le tronçon alluvial doit être suffisamment long et uniforme pour que celle-ci puisse s'exprimer. Le signal du *BRI* met aussi en évidence des longueurs d'ondes caractéristiques, parfois en accord avec celle de la largeur, mais ces longueurs d'onde semblent plus liées à une morphologie plus dynamique régie par les derniers épisodes de crues.

2.3. Morphologie, changement à long terme et mosaïque de la végétation

Le couplage des données LiDAR avec une étude diachronique de photographies aériennes pour dater l'âge des niveaux du lit majeur a permis de mettre en lumière différentes phases d'incision sur les 3 sites étudiés (Drôme amont, Bès et Bouinenc). Cette étude confirme que la bande de tressage observée dans les années 1950 est déjà bien enfoncée dans une "terrasse" contemporaine végétalisée sur la Drôme et le Bouinenc. Celle-ci date probablement du début du siècle et pourrait être liée à la fin du petit âge glaciaire et sur la Drôme aux travaux de correction des torrents

(Liébault and Piégay, 2002; Liébault et al., 2008). Cet enfoncement n'est pas observé sur le Bès, probablement en raison d'apports sédimentaires encore actifs sur le bassin versant, mais sur les photographies aériennes de 1948 des terrasses boisées sont cependant observées.

Une deuxième période d'incision est observée dans la deuxième moitié du 20ème siècle sur les trois rivières. Cette période a sans doute différentes causes et différentes modalités. L'incision observée sur le Bouinenc à partir des années 1950 est probablement liée à la reforestation spontanée due à la déprise rurale, diminuant ainsi les apports sédimentaires à la rivière. Ceci a été observé sur les affluents de la Drôme (Liébault et al., 2005), où la datation des terrasses récentes a permis de montrer que l'incision s'est propagée depuis l'amont sous l'effet du tarissement des sources sédimentaires. Sur la Drôme, une phase d'incision démarre dans les années 1970 sous l'effet des extractions de graviers stoppées dans les années 1990. Sur le Bès, l'incision est brutale mais de faible durée, entre 1975 et 1982. Elle serait liée ici à l'occurrence de deux crues de forte intensité. En effet, plusieurs auteurs ont déjà souligné que de tels événements pouvaient favoriser l'incision du lit dans des contextes de déficit sédimentaire (Belletti et al., 2014; Toone et al., 2014). Cependant sur le Bès, les surfaces conservées étant limitées, l'interprétation de ces résultats reste délicate. Certaines crues de plus faible intensité peuvent également provoquer des exhaussements du lit mais ceux-ci ne contrecarrent pas le processus d'incision à long terme.

La mosaïque de la végétation des lits en tresses est fortement liée au changement morphologique à long terme. Une rétraction et une incision de la bande active à long terme conduit à une prédominance d'unités de végétation matures (végétation post-pionnière et lande arbustive). Les rivières plus actives présentent une forêt alluviale moins développée et les différentes unités de végétation sont représentées de façon équilibrée.

Les unités de landes arbustives sont caractéristiques des périodes d'incision. Ces unités caractérisées par une densité d'arbres et des hauteurs plus faibles que les unités de végétation post-pionnière résultent de conditions de sécheresse plus élevées provoquées par une déconnection de ces surfaces par rapport à la nappe alluviale.

2.4. Lien entre la morphologie en travers et le régime sédimentaire

Les signatures morphologiques des tresses extraites sur les sites de la Drôme, du Drac et de la Bléone ont été étudiées afin d'inférer un lien avec le régime sédimentaire. Différents indicateurs ont été utilisés pour évaluer le régime sédimentaire des sites d'études: la largeur de la bande active normalisée par la taille du bassin versant (W^*) et la différence d'altitude entre les "terrasses" arborées récentes (post 1948) et la bande active (T). Le *BRI* a été utilisé comme un indicateur de la

morphologie en travers qui renseigne sur la rugosité induite par les macroformes. Il est aussi considéré comme étant potentiellement un indicateur du régime sédimentaire (Liébault et al., 2013a).

*W** correspond au ratio entre la largeur mesurée de la bande active et une largeur prédite de bande active, calculée à partir d'une loi puissance ajustée entre la largeur de la bande active et la surface du bassin versant sur un échantillon de 49 tronçons en tresses des Alpes françaises (Equation 1, Piégay et al., 2009).

$$W_{pred} = 8.05\, A^{0.44} \quad (1)$$

$$W^{*} = W/W_{pred} \quad (2)$$

Avec W_{pred}, la largeur de la bande active prédite, A la surface du bassin versant et W la largeur de la bande active mesurée.

Ce calcul de *W** diffère un peu de celui proposé par Belletti et al. (2013a) qui correspond au ratio $W/A^{0.4}$, mais notre *W** permet de caractériser simplement les tronçons en surlargeur (W*> 1) qui indiquent plutôt des conditions limitées en capacité de transport et ceux en sous-largeur (W*<1), qui indiquent plutôt des conditions limitées en fourniture sédimentaire. Ainsi une diminution du *BRI* est attendu quand *W**>1, car les systèmes en condition de transport limité vont générer des lits plats avec un faible relief, où la dissipation d'énergie est faible car toute l'énergie disponible est utilisée pour le transport de la charge sédimentaire (Montgomery and Buffington, 1997).

Un autre indicateur du régime sédimentaire est la différence d'altitude entre les "terrasses" arborées et la bande active (*T*). On admet ici que l'encaissement est induit par un régime sédimentaire déficitaire qui se produit sur une période de temps plus ou moins longue, et que l'enfoncement est proportionnel à la durée de cette période et au caractère plus ou moins marqué du déficit sédimentaire, qui module la vitesse à laquelle le lit s'incise. Les encaissements les plus marqués devraient donc être associés à des *BRI* plus élevés, si on admet une dynamique d'incision ininterrompue depuis les années 1950.

Les résultats ont montré un lien complexe entre le *BRI* et la largeur de la bande active (Fig. 60A). En effet, une corrélation négative entre *BRI* et *W* peut être observée pour les sites ayant une largeur de bande active supérieure à 100 m montrant une diminution de la rugosité altitudinale du lit avec l'augmentation de la largeur de la bande active. Cette tendance s'inverse pour les largeurs de bande active inférieures à 100 m, où le *BRI* est faible. Ainsi, ces rivières sont caractérisées par un lit avec une largeur et une rugosité altitudinale faibles. L'analyse des photographies aériennes

montre que ces sites présentent plutôt un lit de style divaguant et ne sont plus véritablement des lits en tresses au sens strict du terme, ce qui pourrait expliquer qu'ils ne suivent pas la tendance mise en évidence pour les lits larges.

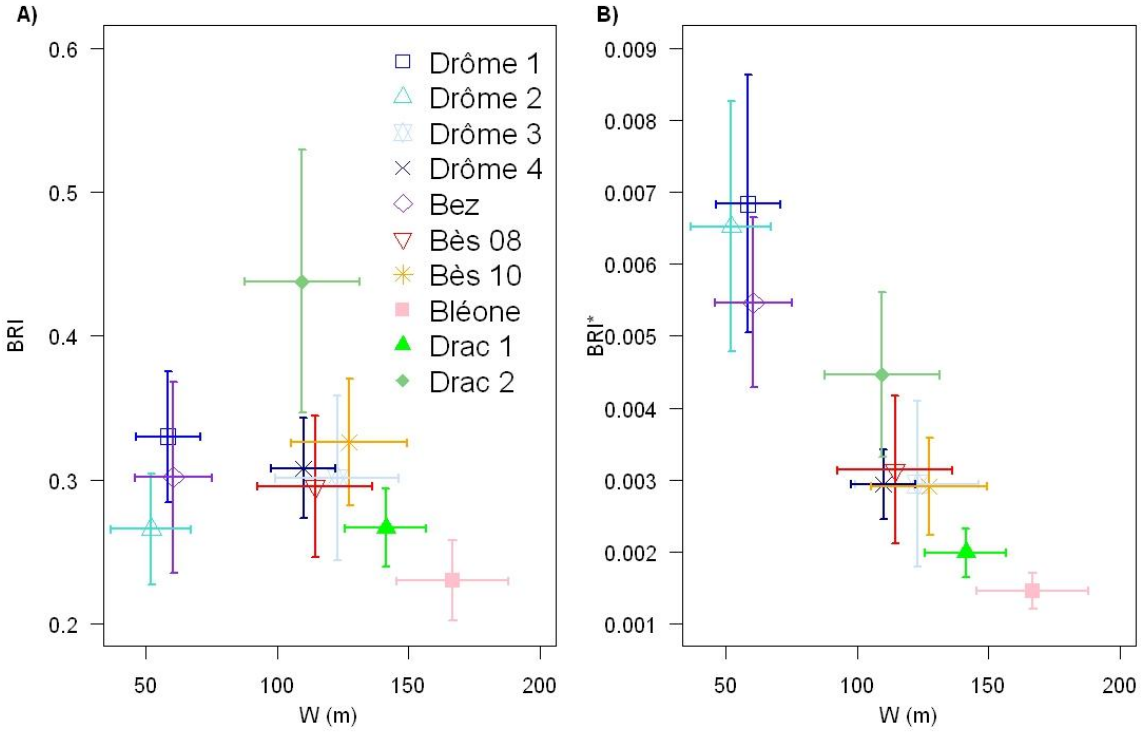

Fig. 60. *BRI* (A) et *BRI**(B) en fonction de la largeur de la bande active (*W*), la longueur des barres correspond à l'écart type.

Afin d'établir un indicateur de rugosité altimétrique qui s'affranchit de l'effet de taille et qui puisse être étudié sur une large gamme d'échelles spatiales, en partant du principe que les fluctuations altimétriques du lit sont d'autant plus fortes que la rivière est grande, il a été proposé de normaliser le *BRI* par la largeur de la bande active (Liébault et al., 2013a). Cet indicateur appelé *BRI** a été tracé en fonction de la largeur de bande active (Fig. 60B). Les résultats montrent une autocorrélation (*spurious correlation*) forte, qui s'explique par le poids de la largeur sur le calcul du *BRI**. Cet effet était moins marqué avec les données de Liébault et al. (2013a) (Fig. 61) où une loi puissance peut être ajustée entre le *BRI** et la largeur de la bande active, mais ici la largeur de bande active n'explique que 55% de la variabilité du *BRI**. Ces données ont été produites à partir de profils en travers mesurés sur le terrain par nivellement. La plus forte influence de la largeur sur le *BRI** calculé à partir des données LiDAR s'explique vraisemblablement par la sous-estimation du *BRI* réel sous l'effet de la non prise en compte de la topographie immergée, l'onde LiDAR n'arrivant pas à traverser la colonne d'eau.

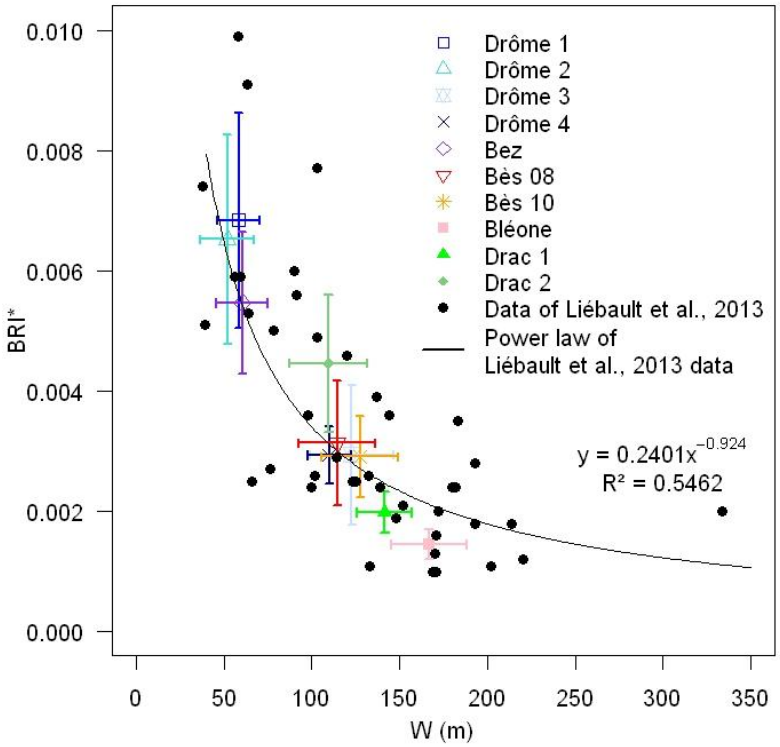

Fig. 61. *BRI** en fonction de *W*, les données de cette thèse sont combinées avec les données de Liébault et al. (2013a). L'ajustement selon une loi puissance ne prend en compte que les données collectées sur le terrain (Liébault et al., 2013a).

La variabilité des données autour de la loi puissance pourrait-elle être liée aux différences de régime sédimentaire ? Le Drac 2 s'écarte beaucoup de la loi. Ce site semble avoir une rugosité altimétrique très élevée pour la largeur observée. L'observation des photographies aériennes montre que ce site présente plutôt un lit de style divaguant, qui pourrait expliquer cette observation. Le Drac 1 et la Bléone présentent quant-à-eux des valeurs faibles de *BRI** par rapport à leur largeur active. Ces observations peuvent refléter une recharge sédimentaire soutenue par rapport aux autres sites. Ces deux sites ont été marqués par l'occurrence d'une crue récente à l'issue desquelles les bandes actives se sont élargies (Fig. 62). Il serait intéressant de continuer à suivre ces deux sites pour savoir si cette évolution est ponctuelle dans le temps ou reflète une restauration à plus long terme des conditions de transport. Les autres sites ne s'éloignent que très peu de la loi proposée en 2013.

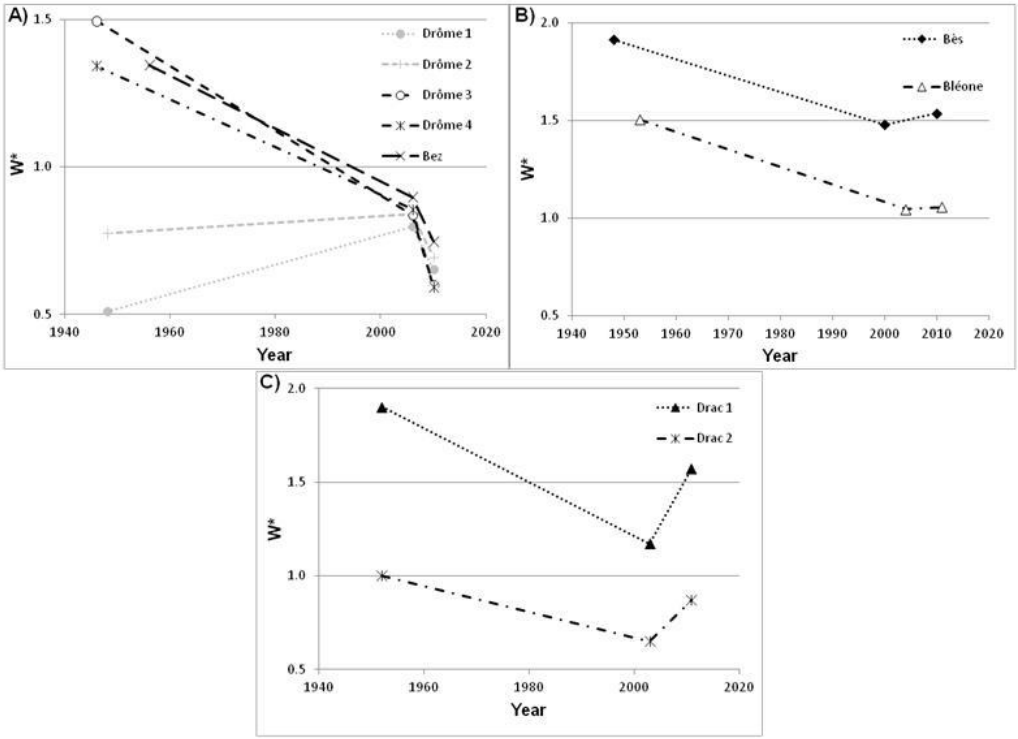

Fig. 62. Evolution de la largeur relative de la bande (W*) entre 1950 et 2010 pour chaque site d'étude pour (A) le bassin versant de la Drôme; (B) le bassin versant de la Bléone; et (C) le bassin versant du Drac.

La rugosité altimétrique du lit a enfin été croisée avec les indicateurs de régime sédimentaire, tout d'abord à partir du lien entre le *BRI* et la largeur normalisée (*W**) pour l'ensemble des sites étudiés (n=3226 sections en travers). Les données ne révèlent aucune relation claire entre les deux variables (Fig. 63A). De plus, les relations observées ne sont le résultat que de la relation entre le *BRI* et le *W* observée plus haut. Par exemple, pour un *W** supérieur à un 1 une relation positive pourrait être observée mais celle-ci est seulement due au fait que la Bléone à une plus grande largeur que les autres rivières et donc un *BRI* plus faible.

Quand *BRI** est considéré, se pose le problème de l'autocorrélation entre les variables (Fig. 63B). Ce diagramme montre néanmoins deux groupes distincts. Un premier groupe présente des valeurs de *BRI** élevées en condition de sous-largeur (*W**<1, Drôme amont et Drac 2) et des valeurs faibles de *BRI** en condition de surlargeur (*W**>1, Bès, Drac 1). Un deuxième groupe (Drôme aval et Bléone) montre les mêmes tendances mais avec des valeurs de *BRI** plus faibles. Ces sites correspondent aux basses vallées et possèdent des puissances plus élevées, ce qui pourrait expliquer les plus faibles valeurs de *BRI**. D'après ce graphique, le Bès, le Drac 1 et la Bléone sont les tronçons qui présentent les tresses les plus actives (surlargeur marquée et très faible rugosité altimétrique).

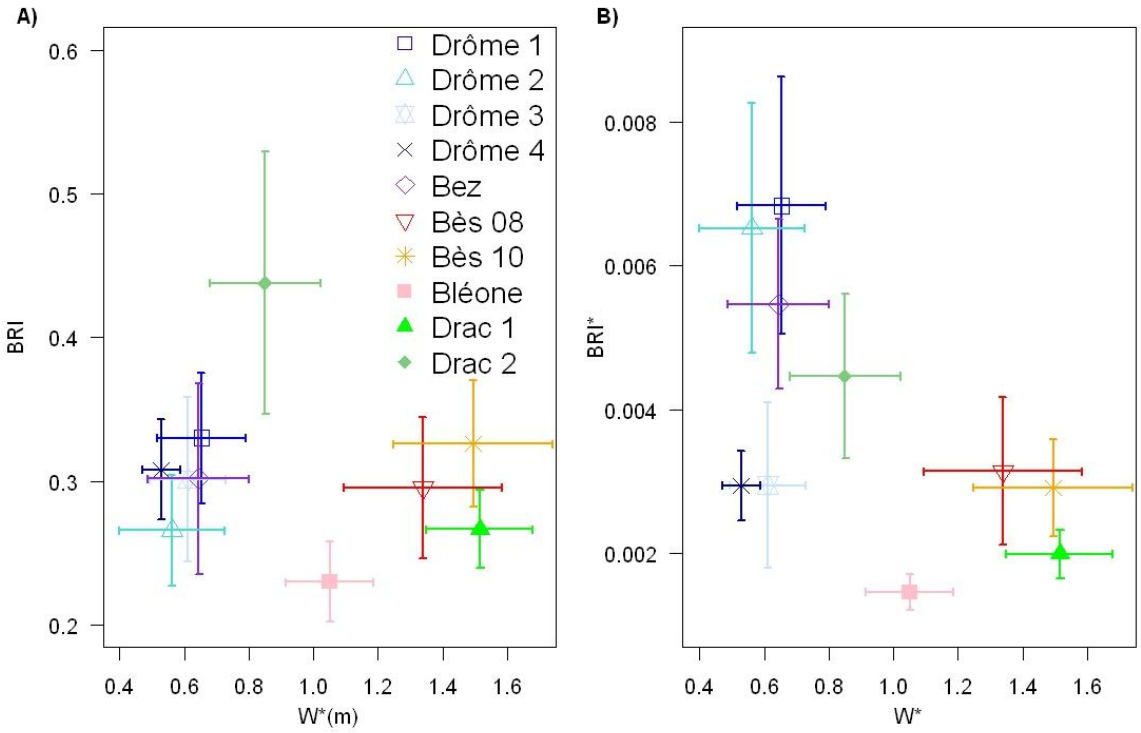

Fig. 63. *BRI* (A) et *BRI**(B) en fonction de *W**, la longueur des barres correspond à l'écart-type.

Enfin, le *BRI** a été tracé en fonction de *T*, comme précédemment effectué par Liébault et al. (2013a) (Fig. 64). Bien que les données de cette thèse soient limitées par la faible étendue des valeurs de *BRI**, il est intéressant d'observer que les données concordent bien avec la boucle d'ajustement précédemment publiée. Ainsi, la Bléone, le Drac 1 et la Drôme 4 se situeraient dans un contexte de recharge sédimentaire à l'origine d'un faible *BRI** mais d'un enfoncement du lit toujours élevé dans les "terrasses". La faible valeur de *BRI** observée sur le tronçon 4 de la Drôme, pourrait aussi être liée au fait que ce site est très à l'aval comparativement aux autres et pourrait être lié seulement à la différence observée entre les sites amont et aval (Cf. § précédent).

En conclusion, *BRI* et *BRI** semblent avoir un lien complexe avec la largeur du lit avec des différences entre les tresses amont et aval. L'échantillon étudié pendant cette thèse ne permet ainsi pas d'approfondir la relation entre la rugosité du lit et le régime sédimentaire. Il est sans doute nécessaire d'étoffer le nombre de tronçons étudiés et de mieux caractériser le régime sédimentaire de chacun d'eux.

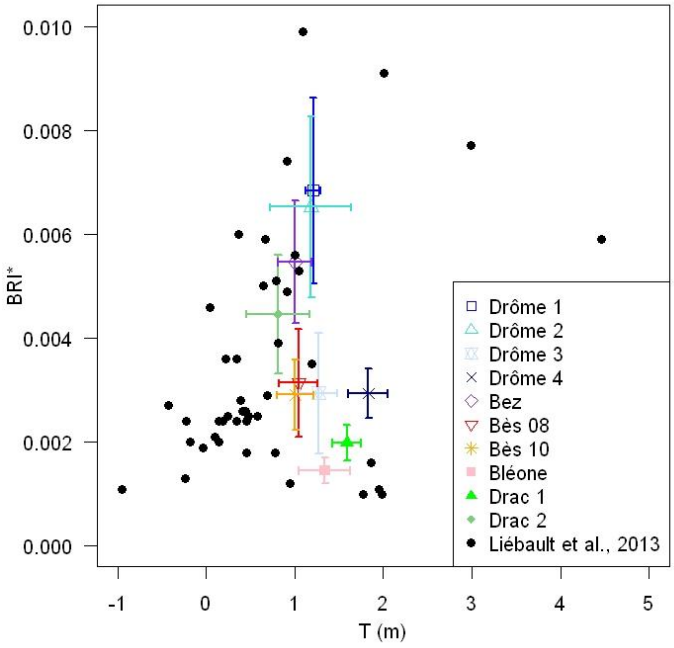

Fig. 64. *BRI** en fonction de *T*, les données de cette thèse sont combinées avec les données de Liébault et al. (2013a).

3. Perspectives

3.1. Perspectives méthodologiques

Cette thèse a montré que le LiDAR aéroporté présente un intérêt indéniable pour l'étude de la morphodynamique des tresses. Cependant depuis quelques années, la photogrammétrie par corrélation dense (fondée sur la technique SfM, *Structure from Motion*, développée dans le domaine de la vision par ordinateur) émerge comme une méthode concurrente. Celle-ci présente l'avantage d'être plus facile à mettre en œuvre que la photogrammétrie classique grâce notamment à la disponibilité de logiciels libres et performants spécialement dédiés au traitement d'images non géolocalisées présentant des angles de vue et des échelles variables d'un même objet. D'autre part, les résultats en termes de précision et de densité de points sont assez semblables à ceux du LiDAR aérien (Javernick et al., 2014; Woodget et al., 2015). On peut même envisager aujourd'hui que cette technique relativement bon marché favorise des acquisitions plus fréquentes à partir de drones, permettant d'obtenir une meilleure caractérisation de la dynamique temporelle des lits en tresses. C'est ainsi que sur le tronçon de la Drôme entre Luc-en-Diois et Recoubeau-Jansac des photographies aériennes haute-résolution sont acquises annuellement depuis 2005 par drone,

paramoteur ou ULM (Table 17). Ces données archivées sont en cours de traitement pour la création de MNS permettant de suivre les changements morphologiques à l'échelle annuelle.

Table 17. Tableau récapitulatif des campagnes de levés par photographies aériennes sur la Drôme entre Luc-en-Diois et Recoubeau-Jansac.

Date	Producteur	Type	Gamme spectrale	Appareil photographique	Hauteur de vol (m)	Nombre de clichés
23-27/05/2005	UMR 5600	Drone pixy	RVB	Canon G5	-	579
15-19/05/2006	UMR 5600	Drone pixy	RVB	Canon G5	-	674
21-25/05/2007	UMR 5600	Drone pixy	RVB	Canon EOS Canon G5	-	933 > 400
19-22/05/2008	UMR 5600	Drone pixy	RVB	Canon G9	-	-
30/09/2008	Paracom	Parapente motorisé	RVB	Canon G9	200 350	442
17/06/2009	Paracom	Parapente motorisé	RVB	Canon G9	200 350 500	365
26/05/2010	Paracom	Parapente motorisé	RVB	Sony DSLR-A350	350 700	272
25/05/2011	Paracom	Parapente motorisé	RVB	Sony DSLR-A350	200 700	157
10/07/2012	Paracom	Parapente motorisé	RVB	Sony DSLR-A350	200 350 700	541
02/07/2013	Paracom	Parapente motorisé	RVB	Sony DSLR-A350	200 700	382
02/06/2014	UMR 5600 Franck Toussaint	ULM pendulaire Air Création	RVB	Nikon D700	300 600	381

Par contre, contrairement au LiDAR, la photogrammétrie SfM ne permet pas de déterminer les altitudes sous la végétation et c'est donc seulement la topographie de la bande active exempte de végétation qui est accessible rétrospectivement.

Concernant la bathymétrie qui ne peut pas être capturée avec un LiDAR classique, une étude récente a montré que la photogrammétrie SfM permettait d'obtenir de fortes densités de point sous l'eau, à condition de travailler en eau claire et peu profonde et d'appliquer un facteur de correction de la réfraction par l'eau (Woodget et al., 2015). De manière plus classique, l'utilisation d'orthophotos prises conjointement avec les données LiDAR permet aussi de mesurer la topographie immergée par l'application d'une calibration empirique entre la radiométrie du pixel et la hauteur d'eau mesurée sur le terrain le jour du levé. Cette technique dite bathymétrie optique est

souvent associée au levé LiDAR pour accéder à la topographie immergée (Lane et al., 2003; Bertoldi et al., 2011; Legleiter, 2012; Moretto et al., 2012a).

Pour la mesure de la bathymétrie, le LiDAR vert (ou LiDAR bathymétrique) est aussi une solution en cours de développement, mais elle est encore très exploratoire et les capteurs sont encore peu disponibles en France (Allouis et al., 2010; Bailly et al., 2010; Kinzel et al., 2013). Actuellement, le LiDAR vert ne permet pas de mesurer la topographie des surfaces immergées en conditions de faible hauteurs d'eau < 30–40 cm (Kinzel et al., 2007; Bailly et al., 2010). Des cas d'applications du LiDAR vert et de la photogrammétrie SfM à la détection des changements dans les lits en tresses permettraient d'apporter un éclairage sur leur plus-value par rapport au LiDAR classique.

3.2. Perspectives thématiques

Les résultats de cette thèse soulignent l'intérêt du LiDAR pour l'étude de l'impact des crues sur la morphologie des rivières en tresses en étudiant les changements morphologiques du lit et en calculant le bilan sédimentaire. La généralisation de MNT après chaque événement de crues, qui semble possible avec l'utilisation des drones, permettrait de mieux comprendre les mécanismes de déplacement des sédiments à l'échelle des bancs et de se rapprocher des observations réalisées en laboratoire. Un suivi sur le long-terme de la dynamique des tresses permettrait de réaliser des observations très riches sur les fluctuations altimétriques du lit en lien avec la variabilité hydrologique et la dynamique de progradation de la charge sédimentaire. Elle permettrait aussi de mieux comprendre les dynamiques sédimentaires à l'origine des structures complexes des lits en tresses, constitués d'une mosaïque de bancs unitaires et composites, dont l'interprétation fonctionnelle reste encore aujourd'hui difficile.

La thèse a produit des résultats d'analyse des signatures morphologiques des tresses qui incitent à s'interroger à la fois sur le caractère généralisable de ces résultats, et sur les processus physiques sous-jacents. Les acquisitions LiDAR devenant de plus en plus attractives en termes de coût, elles se sont multipliées ces dernières années dans le domaine de la gestion des rivières, et il serait intéressant de pouvoir étendre l'analyse des signatures longitudinales proposée ici à d'autres linéaires en tresses. Ce travail permettrait de consolider les résultats obtenus et d'explorer les liens statistiques avec les longueurs caractéristiques des macroformes et mégaformes qui composent les bandes de tressage. Bien que les zones de piémont apparaissent comme des environnements privilégiés pour l'étude des signatures longitudinales, dans la mesure où on trouve ici des linéaires importants où les perturbations liées aux affluents ou au confinement sont généralement absentes, il apparaît que dans le contexte alpin, ces secteurs ont souvent subi de fortes pressions

(endiguements, extractions de graviers) et les tresses se retrouvent souvent dans un état dégradé. Il serait donc intéressant d'explorer d'autres systèmes en tresses moins impactés, comme le Tagliamento en Italie, ou les rivières en tresses de Nouvelle Zélande. L'analyse des processus physiques sous-jacents, très difficile sur le terrain faute de moyens d'observation des phénomènes pendant les crues, peut s'appuyer sur des expériences en laboratoire ou sur des modèles numériques.

De plus, l'intégration au jeu de données de la thèse de nouvelles données décrivant des systèmes présentant des régimes sédimentaires bien caractérisés permettrait de mieux explorer le lien entre la morphologie d'un lit et le régime sédimentaire. L'intégration de systèmes diversifiés se situant le long du continuum fluvial permettrait de confirmer les différences entre les tresses amont et aval mises en évidence dans cette thèse.

Cette thèse a enfin mis en évidence l'intérêt de lier les caractéristiques géomorphologiques du lit avec les caractéristiques de la végétation. Le travail a été conduit à l'échelle pluri-décennale afin de mettre en lumière la construction progressive de la bande alluviale et la réponse de la végétation. La réalisation de MNT à pas de temps plus courts (e.g., interannuels ou plus fins encore) permettrait de mieux caractériser l'établissement et la croissance de la végétation et les changements morphologiques associés. Ce travail est d'ailleurs en cours de réalisation sur la Drôme avec les MNS dérivés des photographies haute résolution et des levés terrain de la végétation (Master de Bianca Räpple, travail de recherche de Kristell Michel, UMR 5600-CNRS).

Plus largement, les données issues du LiDAR aérien utilisées dans cette thèse, et les méthodologies qui ont été testées et développées, offrent de vraies potentialités pour déterminer des indicateurs de l'état hydromorphologique des cours d'eau. A partir d'un LiDAR, il est ainsi possible d'identifier et de caractériser des digues ou d'autres aménagements anthropiques parfois non visibles sur les photographies aériennes car enfouis sous la végétation mais clairement visibles sur les MNT. D'autres indicateurs peuvent être également calculés sur un linéaire de plusieurs dizaines voire centaines de km comme l'altitude relative des berges par rapport au chenal en eau. Explorer ces questions à l'échelle des réseaux est ainsi un challenge sur lequel mon équipe se penche maintenant, en partenariat avec les collègues italiens d'Ispra et les collègues belges de Gembloux qui disposent de MNT à l'échelle d'ensembles régionaux (régions du Piémont et de Wallonie). Elles s'appuient pour partie sur les réflexions qui ont émergé dans le cadre de mon travail de thèse.

REFERENCES BIBLIOGRAPHIQUES

Alber, A., 2012. Etude multi-scalaire de la dynamique latérale des tronçons fluviaux. PhD thesis, Université Lumière Lyon 2, Lyon, 262 pp.

Allouis, T., Bailly, J.S., Pastol, Y., Le Roux, C., 2010. Utilisation conjointe de trains d'ondes LiDAR vert et infrarouge pour la bathymétrie des eaux de très faible profondeurs. Revue Française de Photogrammétrie et de Télédétection 191, 52-61.

Ashmore, P., 1991a. Channel morphology and bed load pulses in braided, gravel-bed streams. Geografiska Annaler. Series A, Physical Geography 73(1), 37-52.

Ashmore, P., 1991b. How do gravel-bed rivers braid? Canadian Journal of Earth Sciences 28(3), 326-341.

Ashmore, P., 2009. Intensity and characteristic length of braided channel patterns. Canadian Journal of Civil Engineering 36(10), 1656-1666.

Ashmore, P., Bertoldi, W., Gardner, J.T., 2011. Active width of gravel-bed braided rivers. Earth Surface Processes and Landforms 36(11), 1510-1521.

Ashmore, P., 2013. Morphology and dynamics of braided rivers. In: Shroder, J.F. (Ed.), Treatise on Geomorphology. Academic Press, San Diego, pp. 289-312.

Ashmore, P.E., 2001. Braiding phenomena: statics and kinematics. Gravel Bed Rivers V. New Zealand Hydrological Society, Christchurch, New Zealand, pp. 95-120.

Ashworth, P.J., Ferguson, R.I., 1986. Interrelationships of channel processes, changes and sediments in a proglacial braided river. Geografiska Annaler Series A-Physical Geography 68(4), 361-371.

Ashworth, P.J., 1996. Mid-channel bar growth and its relationship to local flow strength and direction. Earth Surface Processes and Landforms 21(2), 103-123.

Ashworth, P.J., Best, J.L., Jones, M., 2004. Relationship between sediment supply and avulsion frequency in braided rivers. Geology 32(1), 21-24.

Axelsson, P., 2000. DEM generation from laser scanner data using adaptive TIN models. International Archives of the Photogrammetry, Remote Sensing and Spatial Information Sciences XXXIII (Part B4), 110-117.

Bailly, J.S., Le Coarer, Y., Languille, P., Stigermark, C.J., Allouis, T., 2010. Geostatistical estimations of bathymetric LiDAR errors on rivers. Earth Surface Processes and Landforms 35(10), 1199-1210.

Belletti, B., 2012. Analyse régionale de la structure et de la dynamique biogéomorphologiques des rivières en tresses du bassin du rhône. PhD thesis, Université Jean Moulin, Lyon 3, Lyon, 246 pp.

Belletti, B., Dufour, S., Piégay, H., 2013a. Regional variability of aquatic pattern in braided reaches (example of the French Rhône basin). Hydrobiologia 712(1), 25-41.

Belletti, B., Dufour, S., Piégay, H., 2013b. What is the relative effect of space and time to explain the braided river width and island patterns at a regional scale? River Research and Applications, doi: 10.1002/rra.2714.

Belletti, B., Dufour, S., Piégay, H., 2014. Regional assessment of the multi-decadal changes in braided riverscapes following large floods (Example of 12 reaches in South East of France). Adv. Geosci. 37, 57-71.

Bertoldi, W., Tubino, M., 2005. Bed and bank evolution of bifurcating channels. Water Resources Research 41(7), W07001.

Bertoldi, W., Amplatz, T., Miori, S., Zanoni, L., Tubino, M., 2006. Bed load fluctuations and channel processes in a braided network laboratory model. River Flow 2006, Vols 1 and 2, 937-945.

Bertoldi, W., Tubino, M., 2007. River bifurcations: experimental observations on equilibrium configurations. Water Resources Research 43(10), W10437.

Bertoldi, W., Gurnell, A., Surian, N., Tockner, K., Zanoni, L., Ziliani, L., Zolezzi, G., 2009a. Understanding reference processes: linkages between river flows, sediment dynamics and vegetated landforms along the Tagliamento River, Italy. River Research and Applications 25(5), 501-516.

Bertoldi, W., Zanoni, L., Tubino, M., 2009b. Planform dynamics of braided streams. Earth Surface Processes and Landforms 34(4), 547-557.

Bertoldi, W., Zanoni, L., Tubino, M., 2010. Assessment of morphological changes induced by flow and flood pulses in a gravel bed braided river: the Tagliamento River (Italy). Geomorphology 114(3), 348-360.

Bertoldi, W., Gurnell, A.M., Drake, N.A., 2011. The topographic signature of vegetation development along a braided river: results of a combined analysis of airborne lidar, color air photographs, and ground measurements. Water Resources Research 47, W06525.

Bertoldi, W., Gurnell, A.M., Welber, M., 2013. Wood recruitment and retention: the fate of eroded trees on a braided river explored using a combination of field and remotely-sensed data sources. Geomorphology 180, 146-155.

Bollati, I.M., Pellegrini, L., Rinaldi, M., Duci, G., Pelfini, M., 2014. Reach-scale morphological adjustments and stages of channel evolution: the case of the Trebbia River (northern Italy). Geomorphology 221(0), 176-186.

Bowen, Z.H., Waltermire, R.G., 2002. Evaluation of light detection and ranging (LIDAR) for measuring river corridor topography. Journal of the American Water Resources Association 38(1), 33-41.

Brasington, J., Rumsby, B.T., Mac Vey, R.A., 2000a. Monitoring and modelling morphological change in a braided gravel-bed river using high resolution GPS-based survey. Earth Processes and Landforms 25, 973-990.

Brasington, J., Rumsby, B.T., Mcvey, R.A., 2000b. Monitoring and modelling morphological change in a braided gravel-bed river using high resolution GPS-based survey. Earth Surface Processes and Landforms 25(9), 973-990.

Brasington, J., Vericat, D., Rychkov, I., 2012. Modeling river bed morphology, roughness, and surface sedimentology using high resolution terrestrial laser scanning. Water Resources Research 48, W11519.

Bravard, J.-P., 1989. La métamorphose des rivières des Alpes françaises à la fin du Moyen-Age et à l'époque Moderne. Bulletin de la Société Géographique de Liège 25, 145-157.

Bravard, J.-P., Peiry, J.-L., 1993. La disparition du tressage fluvial dans les Alpes françaises sous l'effet de l'aménagement des cours d'eau (19-20ème siècles). Zeitschrift für Geomorphologie, Supplement Band 88, 67-79.

Bravard, J.-P., 2000. Le comportement hydromorphologique des cours d'eau au Petit Age Glaciaire dans les Alpes françaises et sur leur piedmont. 25èmes Journées Scientifiques de GFHN, Meudon, pp. 105-110.

Brice, J.C., 1964. Channel patterns and terraces of the Loup Rivers in Nebraska. Geological Survey Professional Paper 422-D.

Brice, J.C., 1978. Countermeasures for hydraulic problems at bridges / J. C. Brice , J. C. Blodgett, and others. Federal Highway Administration. Report ; no. FHWA-RD-78-162. Dept. of Transportation, Federal Highway Administration, Offices of Research and Development : for sale the National Technical Information Service, Washington : Springfield, Va.

Bridge, J.S., 1993. The interaction between channel geometry, water flow, sediment transport and deposition in braided rivers. Geological Society, London, Special Publications 75(1), 13-71.

Bristow, C.S., 1987. Brahmaputra River: channel migration and deposition. In: Ethridge, E.G., Flores, R.M., Harvey, M.D. (Eds.), Recent Developments in Fluvial Sedimentology. SEPM Special Publication, Oxford, pp. 63-74.

Buffington, J.M., Montgomery, D.R., 2013. Geomorphic classification of rivers. In: Shroder, J.F. (Ed.), Treatise on Geomorphology. Academic Press, San Diego, pp. 730-767.

Carley, J.K., Pasternack, G.B., Wyrick, J.R., Barker, J.R., Bratovich, P.M., Massa, D.A., Reedy, G.D., Johnson, T.R., 2012. Significant decadal channel change 58-67 years post-dam accounting for uncertainty in topographic change detection between contour maps and point cloud models. Geomorphology 179, 71-88.

Carson, M.A., 1984a. Observations on the meandering-braided river transition, The Canterbury Plains, New Zealand: part two. New Zealand Geographer 40(2), 89-99.

Carson, M.A., 1984b. Observations on the meandering-braided river transition, the Canterbury Plains, New Zealand: part one. New Zealand Geographer 40(1), 12-19.

Carson, M.A., Griffiths, G.A., 1989. Gravel transport in the braided Waimakariri River - mechanisms, measurements and predictions. Journal of Hydrology 109(3-4), 201-220.

Cavalli, M., Tarolli, P., 2011. Application of LiDAR technology for rivers analysis. Italian Journal of Engineering Geology and Environment Special Issue 1, 33-44.

Chandler, J., Ashmore, P., Paola, C., Gooch, M., Varkaris, F., 2002. Monitoring river-channel change using terrestrial oblique digital imagery and automated digital photogrammetry. Annals of the Association of American Geographers 92(4), 631-644.

Charlton, M.E., Large, A.R.G., Fuller, I.C., 2003. Application of airborne LiDAR in river environments: the River Coquet, Northumberland, UK. Earth Surface Processes and Landforms 28(3), 299-306.

Church, M., Jones, D., 1982. Channel bars in gravel-bed rivers. In: Hey, R.D., Bathurst, J.C., Thorne, C.R. (Eds.), Gravel-bed Rivers. John Wiley and Sons, Chichester, pp. 291-338.

Church, M., 1983. Pattern of instability in a wandering gravel bed channel. In: Collinson, J.D., Lewin, J. (Eds.), Modern and ancient fluvial systems. Blackwell, Oxford, pp. 169-180.

Comiti, F., Da Canal, M., Surian, N., Mao, L., Picco, L., Lenzi, M.A., 2011. Channel adjustments and vegetation cover dynamics in a large gravel bed river over the last 200 years. Geomorphology 125(1), 147-159.

Constantine, J.A., Dunne, T., Piégay, H., Kondolf, G.M., 2010. Controls on the alluviation of oxbow lakes by bed-material load along the Sacramento River, California. Sedimentology 57(2), 389-407.

Corenblit, D., Tabacchi, E., Steiger, J., Gurnell, A.M., 2007. Reciprocal interactions and adjustments between fluvial landforms and vegetation dynamics in river corridors: a review of complementary approaches. Earth-Science Reviews 84(1-2), 56-86.

Datry, T., Corti, R., Belletti, B., Piégay, H., 2014. Ground-dwelling arthropod communities across braided river landscape mosaics: a Mediterranean perspective. Freshwater Biology 59(6), 1308-1322.

DeLong, S.B., Prentice, C.S., Hilley, G.E., Ebert, Y., 2012. Multitemporal ALSM change detection, sediment delivery, and process mapping at an active earthflow. Earth Surface Processes and Landforms 37(3), 262-272.

Dufour, S., 2005. Contrôles naturels et anthropiques de la structure et de la dynamique des forêts riveraines des cours d'eau du bassin rhodanien (Ain, Arve, Drôme et Rhône). PhD thesis, Université Jean Moulin Lyon 3, France, 244 pp.

Dufour, S., Barsoum, N., Muller, E., Piégay, H., 2007. Effects of channel confinement on pioneer woody vegetation structure, composition and diversity along the River Drôme (SE France). Earth Surface Processes and Landforms 32(8), 1244-1256.

Dufour, S., Piégay, H., 2010. Channel vertical mobility, hydro-geomorphic disturbances and understory vegetation in floodplain forests of the Ain River (France). Geomorphologie-Relief Processus Environnement(4), 371-386.

Dufour, S., Rinaldi, M., Piégay, H., Michalon, A., 2015. How do river dynamics and human influences affect the landscape pattern of fluvial corridors? Lessons from the Magra River, Central–Northern Italy. Landscape and Urban Planning 134(0), 107-118.

Dunford, R., Michel, K., Gagnage, M., Piégay, H., Tremelo, M.L., 2009. Potential and constraints of unmanned aerial vehicle technology for the characterization of Mediterranean riparian forest. International Journal of Remote Sensing 30(19), 4915-4935.

Edwards, P.J., Kollmann, J., Gurnell, A.M., Petts, G.E., Tockner, K., Ward, J.V., 1999. A conceptual model of vegetation dynamics on gravel bars of a large Alpine river. Wetlands Ecology and Management 7(3), 141-153.

Egozi, R., Ashmore, P., 2008. Defining and measuring braiding intensity. Earth Surface Processes and Landforms 33(14), 2121-2138.

Erwin, S.O., Schmidt, J.C., Wheaton, J.M., Wilcock, P.R., 2012. Closing a sediment budget for a reconfigured reach of the Provo River, Utah, United States. Water Resources Research 48, W10512.

Ferguson, R.I., Werrity, A., 1983. Bar development and channel change in the gravelly River Feshie, Scotland. In: Collinson, J., Lewin, J. (Eds.), Modern and Ancient Fluvial Systems. Blackwell Scientific Publications, Oxford, pp. 182-194.

Ferguson, R.I., 1987. Hydraulic and sedimentary controls of channel pattern. River channels: environment and process. Blackwell, pp. 129-158.

Ferguson, R.I., Ashworth, P.J., 1992. Spatial patterns of bedload transport and channel change in braided and near-braided rivers. In: Billi, P., Hey, R.D., Thorne, C.R., Tacconi, P. (Eds.), Dynamics of Gravel-bed Rivers. John Wiley and Sons, Chichester, UK, pp. 477-496.

Fuller, I.C., Large, A.R.G., Charlton, M.E., Heritage, G.L., Milan, D.J., 2003. Reach-scale sediment transfers: an evaluation of two morphological budgeting approaches. Earth Surface Processes and Landforms 28(8), 889-903.

Gagnage, M., 2008. Evaluation des effets des changements morphologiques fluviaux sur la santé des peupliers. Master's thesis, Université Lumière Lyon 2, France, 101 pp.

Germanoski, D., Schumm, S.A., 1993. Changes in braided river morphology resulting from aggradation and degradation. Journal of Geology 101(4), 451-466.

Goff, J.R., Ashmore, P., 1994. Gravel transport and morphological change in braided Sunwapta River, Alberta, Canada. Earth Surface Processes and Landforms 19(3), 195-212.

Gran, K.B., Montgomery, D.R., 2005. Spatial and temporal patterns in fluvial recovery following volcanic eruptions: Channel response to basin-wide sediment loading at Mount Pinatubo, Philippines. Geological Society of America Bulletin 117(1-2), 195-211.

Griffiths, G.A., 1979. Recent sedimentation history of the Waimakariri River, New Zealand. Journal of Hydrology New Zealand 18, 6-28.

Griffiths, G.A., 1993. Sediment translation waves in braided gravel-bed rivers. Journal of Hydraulic Engineering-Asce 119(8), 924-935.

Gurnell, A., Tockner, K., Edwards, P., Petts, G., 2005. Effects of deposited wood on biocomplexity of river corridors. Frontiers in Ecology and the Environment 3(7), 377-382.

Gurnell, A., Surian, N., Zanoni, L., 2009. Multi-thread river channels: a perspective on changing European alpine river systems. Aquatic Sciences 71(3), 253-265.

Gurnell, A.M., Petts, G.E., Hannah, D.M., Smith, B.P.G., Edwards, P.J., Kollmann, J., Ward, J.V., Tockner, K., 2001. Riparian vegetation and island formation along the gravel-bed Fiume Tagliamento, Italy. Earth Surface Processes and Landforms 26(1), 31-62.

Gurnell, A.M., Petts, G.E., 2002. Island-dominated landscapes of large floodplain rivers, a European perspective. Freshwater Biology 47(4), 581-600.

Hall, R.K., Watkins, R.L., Heggem, D.T., Jones, K.B., Kaufmann, P.R., Moore, S.B., Gregory, S.J., 2009. Quantifying structural physical habitat attributes using LIDAR and hyperspectral imagery. Environmental Monitoring and Assessment 159(1-4), 63-83.

Ham, D., Church, M., 2012. Morphodynamics of an extended bar complex, Fraser River, British Columbia. Earth Surface Processes and Landforms 37(10), 1074-1089.

Haschenburger, J.K., Cowie, M., 2009. Floodplain stages in the braided Ngaruroro River, New Zealand. Geomorphology 103(3), 466-475.

Heritage, G., Hetherington, D., 2007. Towards a protocol for laser scanning in fluvial geomorphology. Earth Surface Processes and Landforms 32(1), 66-74.

Heritage, G.L., Milan, D.J., Large, A.R.G., Fuller, I.C., 2009. Influence of survey strategy and interpolation model on DEM quality. Geomorphology 112(3-4), 334-344.

Hervouet, A., Dunford, R., Piégay, H., Belletti, B., Trémélo, M.L., 2011. Analysis of post-flood recruitment patterns in braided-channel rivers at multiple scales based on an image series collected by unmanned aerial vehicles, ultra-light aerial vehicles, and satellites. Giscience & Remote Sensing 48(1), 50-73.

Hicks, D.M., Duncan, M.J., Lane, S.N., Tal, M., Westaway, R., 2008. Contemporary morphological change in braided gravel-bed rivers: new developments from field and laboratory studies, with particular reference to the influence of riparian vegetation. In: Habersack, H., Piégay, H., Rinaldi, M. (Eds.), Gravel-bed Rivers VI: From Process Understanding to River Restoration. Elsevier, Amsterdam, pp. 557-584.

Hicks, D.M., Shankar, U., Duncan, M.J., Rebuffé, M., Aberle, J., 2009. Use of remote-sensing with two-dimensional hydrodynamic models to assess impacts of hydro-operations on a large, braided, gravel-bed river: Waitaki River, New Zealand. In: Sambrook Smith, G.H., Best, J.L., Bristow, C.S., Petts, G.E. (Eds.), Braided Rivers: Process, Deposits, Ecology and Management. Blackwell Publishing Ltd., Oxford, UK, pp. 311-326.

Hicks, D.M., 2012. Remotely sensed topographic change in gravel riverbeds with flowing channels, Gravel-Bed Rivers. John Wiley & Sons, Ltd, pp. 303-314.

Hodgson, M.E., Bresnahan, P., 2004. Accuracy of airborne LiDAR-derived elevation: empirical assessment and error budget. Photogrammetric Engineering and Remote Sensing 70(3), 331-339.

Hoey, T.B., Sutherland, A.J., 1991. Channel morphology and bedload pulses in braided rivers - a laboratory study. Earth Surface Processes and Landforms 16(5), 447-462.

Höfle, B., Vetter, M., Pfeifer, N., Mandlburger, G., Stotter, J., 2009. Water surface mapping from airborne laser scanning using signal intensity and elevation data. Earth Surface Processes and Landforms 34(12), 1635-1649.

Hong, L.B., Davies, T.R.H., 1979. A study of stream braiding. Geological Society of America Bulletin 90(12 Part II), 1839-1859.

Howard, A.D., Keetch, M.E., Vincent, C.L., 1970. Topological and geometrical properties of braided streams. Water Resources Research 6(6), 1674-1688.

Hundey, E.J., Ashmore, P.E., 2009. Length scale of braided river morphology. Water Resources Research 45, W08409.

Iavarone, A., Vagners, D., 2003. Sensor fusion: generating 3D by combining airborne and tripod mounted LIDAR data. Proceeding of ISPRS workshop on "Visualization and Animation of Reality-based 3D Models". International Archives of Photogrammetry, Remote Sensing and Spatial Information Sciences XXXIV (5/W10), pp. 7.

Jackson, R., Jr, 1978. Preliminary evaluation of lithofacies models for meandering alluvial streams, Fluvial Sedimentology, Calgary, Canada, pp. 543-576.

Jackson, R.G., 1975. Hierarchical attributes and a unifying model of bed forms composed of cohesionless material and produced by shearing flow. Geological Society of America Bulletin 86(11), 1523-1533.

Javernick, L., Brasington, J., Caruso, B., 2014. Modeling the topography of shallow braided rivers using Structure-from-Motion photogrammetry. Geomorphology 213(0), 166-182.

Johansen, K., Arroyo, L.A., Armston, J., Phinn, S., Witte, C., 2010. Mapping riparian condition indicators in a sub-tropical savanna environment from discrete return LiDAR data using object-based image analysis. Ecological Indicators 10(4), 796-807.

Junk, W.J., Bayley, P.B., Sparks, R.E., 1989. The flood pulse concept in river-floodplain systems. Canadian special publication of fisheries and aquatic sciences 106(1), 110-127.

Karrenberg, S., Edwards, P.J., Kollmann, J., 2002. The life history of Salicaceae living in the active zone of floodplains. Freshwater Biology 47(4), 733-748.

Kinzel, P.J., Wright, C.W., Nelson, J.M., Burman, A.R., 2007. Evaluation of an experimental LiDAR for surveying a shallow, braided, sand-bedded river. Journal of Hydraulic Engineering-ASCE 133(7), 838-842.

Kinzel, P.J., Legleiter, C.J., Nelson, J.M., 2013. Mapping river bathymetry with a small footprint green LiDAR: applications and challenges. JAWRA Journal of the American Water Resources Association 49(1), 183-204.

Kleinhans, M.G., Ferguson, R.I., Lane, S.N., Hardy, R.J., 2013. Splitting rivers at their seams: bifurcations and avulsion. Earth Surface Processes and Landforms 38(1), 47-61.

Knighton, D., 1998. Fluvial forms and processes, a new perspective. Arnold, London, 383 pp.

Kondolf, G.M., Piégay, H., Landon, N., 2002. Channel response to increased and decreased bedload supply from land use change: contrasts between two catchments. Geomorphology 45(1-2), 35-51.

Kondolf, G.M., Piégay, H., Landon, N., 2007. Changes in the riparian zone of the lower Eygues River, France, since 1830. Landscape Ecology 22(3), 367-384.

Krigström, A., 1962. Geomorphological studies of sandur plains and their braided rivers in Iceland. Geografiska Annaler 44(3/4), 328-346.

Lallias-Tacon, S., Liébault, F., Piégay, H., 2014. Step by step error assessment in braided river sediment budget using airborne LiDAR data. Geomorphology 214, 307-323.

Landon, N., Piégay, H., Bravard, J.P., 1998. The Drôme river incision (France): from assessment to management. Landscape and Urban Planning 43(1-3), 119-131.

Lane, S.N., Chandler, J.H., Richards, K.S., 1994. Developments in monitoring and modeling small-scale river bed topography. Earth Surface Processes and Landforms 19(4), 349-368.

Lane, S.N., Richards, K.S., Chandler, J.H., 1995. Morphological estimation of the time-integrated bed load transport rate. Water Resources Research 31(3), 761-772.

Lane, S.N., Westaway, R.M., Hicks, D.M., 2003. Estimation of erosion and deposition volumes in a large, gravel-bed, braided river using synoptic remote sensing. Earth Surface Processes and Landforms 28(3), 249-271.

Leduc, P., 2013. Étude expérimentale de la dynamique sédimentaire des rivières en tresses. PhD thesis, Université de Grenoble, Grenoble, 257 pp.

Legleiter, C.J., 2012. Remote measurement of river morphology via fusion of LiDAR topography and spectrally based bathymetry. Earth Surface Processes and Landforms 37(5), 499-518.

Leopold, L.B., Wolman, M.G., 1957. River channel patterns: braided, meandering and straight. United States Geological Survey Professional Paper 282 B, 39-85.

Liébault, F., Piégay, H., 2002. Causes of 20th century channel narrowing in mountain and piedmont rivers of southeastern France. Earth Surface Processes and Landforms 27(4), 425-444.

Liébault, F., 2003. Les rivières torrentielles des montagnes drômoises : évolution contemporaine et fonctionnement géomorphologique actuel (massif du Diois et de Baronnies). PhD thesis, Université Lumière Lyon II, France, 358 pp.

Liébault, F., Gomez, B., Page, M., Marden, M., Peacock, D., Richard, D., Trotter, C.M., 2005. Land-use change, sediment production and channel response in upland regions. River Research and Applications 21(7), 739-756.

Liébault, F., Piégay, H., Frey, P., Landon, N., 2008. Tributaries and the management of main-stem geomorphology, River Confluences, Tributaries and the Fluvial Network. John Wiley & Sons, Ltd, pp. 243-270.

Liébault, F., Bellot, H., Chapuis, M., Klotz, S., Deschatres, M., 2012. Bedload tracing in a high-sediment-load mountain stream. Earth Surface Processes and Landforms 37(4), 385-399.

Liébault, F., Lallias-Tacon, S., Cassel, M., Talaska, N., 2013a. Long profile responses of alpine braided rivers in SE France. River Research and Applications 29(10), 1253-1266.

Liébault, F., Remaître, A., Peteuil, C., 2013b. Géomorphologie des rivières de montagne. In: Recking, A., Richard, D., Degoutte, G. (Eds.), Torrents et rivières de montagne: Dynamique et aménagement. Quae, Versailles, pp. 15-89.

Luchi, R., Bertoldi, W., Zolezzi, G., Tubino, M., 2007. Monitoring and predicting channel change in a free-evolving, small Alpine river: Ridanna Creek (North East Italy). Earth Surface Processes and Landforms 32(14), 2104-2119.

Marston, R.A., Girel, J., Pautou, G., Piégay, H., Bravard, J.P., Arneson, C., 1995. Channel metamorphosis, floodplain disturbance, and vegetation development - Ain River, France. Geomorphology 13(1-4), 121-131.

Mathys, N., Brochot, S., Meunier, M., Richard, D., 2003. Erosion quantification in the small marly experimental catchments of Draix (Alpes de Haute Provence, France). Calibration of the ETC rainfall-runoff-erosion model. Catena 50(2-4), 527-548.

Michez, A., Piégay, H., Toromanoff, F., Brogna, D., Bonnet, S., Lejeune, P., Claessens, H., 2013. LiDAR derived ecological integrity indicators for riparian zones: application to the Houille river in Southern Belgium/Northern France. Ecological Indicators 34, 627-640.

Milan, D.J., Heritage, G.L., Hetherington, D., 2007. Application of a 3D laser scanner in the assessment of erosion and deposition volumes and channel change in a proglacial river. Earth Surface Processes and Landforms 32(11), 1657-1674.

Milan, D.J., Heritage, G.L., Large, A.R.G., Entwistle, N.S., 2010. Mapping hydraulic biotopes using terrestrial laser scan data of water surface properties. Earth Surface Processes and Landforms 35(8), 918-931.

Milan, D.J., Heritage, G.L., Large, A.R.G., Fuller, I.C., 2011. Filtering spatial error from DEMs: implications for morphological change estimation. Geomorphology 125(1), 160-171.

Milan, D.J., Heritage, G.L., 2012. LiDAR and ADCP use in gravel-bed rivers: advances since GBR6. In: Church, M., Biron, P.M., Roy, A.G. (Eds.), Gravel-bed Rivers: Processes, Tools, Environments. John Wiley & Sons, Ltd, Chichester, UK, pp. 286-302.

Montgomery, D.R., Buffington, J.M., 1997. Channel-reach morphology in mountain drainage basins. Geological Society of America Bulletin 109(5), 596-611.

Moretto, J., Delai, F., Rigon, E., Picco, L., Mao, L., Lenzi, M.A., 2012a. Assessing short term erosion-deposition processes of the Brenta River using LiDAR surveys. WIT Transactions on Engineering Sciences 73, 149-160.

Moretto, J., Rigon, E., Mao, L., Delai, F., Picco, L., Lenzi, M.A., 2012b. Assessing morphological changes in gravel-bed rivers using LiDAR data and colour bathymetry. Erosion and Sediment Yields in the Changing Environment 356, 419-427.

Mosley, M.P., 1981. Semi-determinate hydraulic geometry of river channels, South Island, New-Zealand. Earth Surface Processes and Landforms 6(2), 127-137.

Nanson, G.C., Knighton, A.D., 1996. Anabranching rivers: their cause, character and classification. Earth Surface Processes and Landforms 21(3), 217-239.

Navratil, O., Legout, C., Gateuille, D., Esteves, M., Liébault, F., 2010. Assessment of intermediate fine sediment storage in a braided river reach (southern French Prealps). Hydrological Processes 24(10), 1318-1332.

Navratil, O., Evrard, O., Esteves, M., Legout, C., Ayrault, S., Nemery, J., Mate-Marin, A., Ahmadi, M., Lefevre, I., Poirel, A., Bonte, P., 2012. Temporal variability of suspended sediment sources in an alpine catchment combining river/rainfall monitoring and sediment fingerprinting. Earth Surface Processes and Landforms 37(8), 828-846.

Notebaert, B., Verstraeten, G., Govers, G., Poesen, J., 2009. Qualitative and quantitative applications of LiDAR imagery in fluvial geomorphology. Earth Surface Processes and Landforms 34(2), 217-231.

Paola, C., 2001. Modelling stream braiding over a range of scales. In: Mosley, M.P. (Ed.), Gravel Bed Rivers V. New Zealand Hydrological Society, New Zealand, pp. 11–46.

Pautou, G., Girel, J., 1986. La végétation de la basse vallée de l'Ain : organisation et évolution. Document de Cartographie Ecologique 29, 75-96.

Picco, L., Mao, L., Rainato, R., Lenzi, M.A., 2014. Medium-term fluvial island evolution in a disturbed gravel-bed river (Piave River, Northeastern Italian Alps). Geografiska Annaler Series a-Physical Geography 96(1), 83-97.

Pickup, G., Higgins, R.J., 1979. Estimating sediment transport in a braided gravel channel - Kawerong River, Bougainville, Papua-New-Guinea. Journal of Hydrology 40(3-4), 283-297.

Piégay, H., Landon, N., 1997. Promoting ecological management of riparian forests on the Drôme River, France. Aquatic Conservation-Marine and Freshwater Ecosystems 7(4), 287-304.

Piégay, H., Walling, D.E., Landon, N., He, Q.P., Liébault, F., Petiot, R., 2004. Contemporary changes in sediment yield in an alpine mountain basin due to afforestation (the upper Drôme in France). Catena 55(2), 183-212.

Piégay, H., Grant, G., Nakamura, F., Trustrum, N., 2006. Braided river management: from assessment of river behaviour to improved sustainable development, Braided Rivers : Process, Deposits, Ecology and Management. Blackwell Publishing Ltd., pp. 257-275.

Piégay, H., Alber, A., Slater, L., Bourdin, L., 2009. Census and typology of braided rivers in the French Alps. Aquatic Sciences 71(3), 371-388.

Pierson, T.C., Scott, W.E., Vallance, J.W., Pringle, P.T., 2009. Eruption-related lahars and sedimentation response downstream of Mount Hood: field guide to volcaniclastic deposits along the Sandy River, Oregon. Field Guides 15, 221-236.

Rabatel, A., Deline, P., Jaillet, S., Ravanel, L., 2008. Rock falls in high-alpine rock walls quantified by terrestrial LiDAR measurements: a case study in the Mont Blanc area. Geophysical Research Letters 35(10), L10502.

Reinfelds, I., Nanson, G., 1993. Formation of braided river floodplains, Waimakariri River, New-Zealand. Sedimentology 40(6), 1113-1127.

Reusser, L., Bierman, P., 2007. Accuracy assessment of LiDAR-derived DEMs of bedrock river channels: Holtwood Gorge, Susquehanna River. Geophysical Research Letters 34(23), L23s06.

Rice, S.P., Church, M., Wooldridge, C.L., Hickin, E.J., 2009. Morphology and evolution of bars in a wandering gravel-bed river; lower Fraser river, British Columbia, Canada. Sedimentology 56(3), 709-736.

Rinaldi, M., 2003. Recent channel adjustments in alluvial rivers of Tuscany, central Italy. Earth Surface Processes and Landforms 28(6), 587-608.

Rumsby, B.T., Brasington, J., Langham, J.A., McLelland, S.J., Middleton, R., Rollinson, G., 2008. Monitoring and modelling particle and reach-scale morphological change in gravel-bed rivers: applications and challenges. Geomorphology 93(1-2), 40-54.

Rundle, A.S., 1985a. The mechanism of braiding. Z GEOMORPHOLOGIE S 55, 1.

Rundle, A.S., 1985b. Braid morphology and the formation of multiple channels. The Rakaia, New Zealand. Zeits. Geomorph. N.F 55, 15-37.

Schumm, S.A., 1985. Patterns of alluvial rivers. Annual Review of Earth and Planetary Sciences 13, 5-27.

Singer, M.B., Sargeant, C.I., Piégay, H., Riquier, J., Wilson, R.J.S., Evans, C.M., 2014. Floodplain ecohydrology: climatic, anthropogenic, and local physical controls on partitioning of water sources to riparian trees. Water Resources Research 50(5), 4490-4513.

Smith, N.D., 1970. The braided stream depositional environment: comparison of the Platte River with some silurian clastic rocks, North-Central Appalachians. Geological Society of America Bulletin 81(10), 2993-3014.

Smith, N.D., 1974. Sedimentology and bar formation in the Upper Kicking Horse River, a braided outwash stream. The Journal of Geology 82(2), 205-223.

Smith, N.D., 1978. Some comments on terminology for bars in shallow rivers. Fluvial Sedimentology 5, 85-88.

Stella, J.C., Riddle, J., Piégay, H., Gagnage, M., Tremelo, M.L., 2013. Climate and local geomorphic interactions drive patterns of riparian forest decline along a Mediterranean Basin river. Geomorphology 202, 101-114.

Streutker, D.R., Glenn, N.F., Shrestha, R., 2011. A slope-based method for matching elevation surfaces. Photogrammetric Engineering and Remote Sensing 77(7), 743-750.

Surian, N., Rinaldi, M., 2003. Morphological response to river engineering and management in alluvial channels in Italy. Geomorphology 50(4), 307-326.

Surian, N., Rinaldi, M., 2004. Channel adjustments in response alteration of sediment fluxes: examples from Italian rivers. Sediment Transfer through the Fluvial System(288), 276-282.

Surian, N., Cisotto, A., 2007. Channel adjustments, bedload transport and sediment sources in a gravel-bed river, Brenta River, Italy. Earth Surface Processes and Landforms 32(11), 1641-1656.

Surian, N., 2009. Effects of Human Impact on Braided River Morphology: Examples from Northern Italy, Braided Rivers. Blackwell Publishing Ltd., pp. 327-338.

Surian, N., Mao, L., Giacomin, M., Ziliani, L., 2009a. Morphological effects of different channel-forming discharges in a gravel-bed river. Earth Surface Processes and Landforms 34(8), 1093-1107.

Surian, N., Rinaldi, M., Pellegrini, L., Audisio, C., Maraga, F., Teruggi, L., Turitto, O., Ziliani, L., 2009b. Channel adjustments in northern and central Italy over the last 200 years. Management and Restoration of Fluvial Systems with Broad Historical Changes and Human Impacts 451, 83-95.

Taillefumier, F., Piégay, H., 2003. Contemporary land use changes in prealpine Mediterranean mountains: a multivariate GIS-based approach applied to two municipalities in the Southern French Prealps. Catena 51(3–4), 267-296.

Tal, M., Gran, K., Murray, A.B., Paola, C., Hicks, D.M., 2004. Riparian vegetation as a primary control on channel characteristics in multi-thread rivers. Riparian Vegetation and Fluvial Geomorphology 8, 43-58.

Tal, M., Paola, C., 2010. Effects of vegetation on channel morphodynamics: results and insights from laboratory experiments. Earth Surface Processes and Landforms 35(9), 1014-1028.

Taylor, J., 1997. An introduction to error analysis: the study of uncertainties in physical measurements. University Science Books, Sausalito, California.

Theule, J.I., Liébault, F., Loye, A., Laigle, D., Jaboyedoff, M., 2012. Sediment budget monitoring of debris-flow and bedload transport in the Manival Torrent, SE France. Natural Hazards and Earth System Sciences 12(3), 731-749.

Tockner, K., Malard, F., Ward, J.V., 2000. An extension of the flood pulse concept. Hydrological Processes 14(16-17), 2861-2883.

Toone, J., Rice, S.P., Piégay, H., 2014. Spatial discontinuity and temporal evolution of channel morphology along a mixed bedrock-alluvial river, upper Drôme River, southeast France: contingent responses to external and internal controls. Geomorphology 205, 5-16.

Turitto, O., Baldo, M., Audisio, C., Lollino, G., 2010. A LiDAR application to assess long-term bed-level changes in a cobble-bed river: the case of the Orco River (north-western Italy). Geografia Fisica e Dinamica Quaternaria 33(1), 61-76.

Vallauri, D., Vincent, P., 1999. Histoire de l'occupation de l'espace au XIXème siècle dans les bassins expérimentaux du Saignon, du Brusquet et du Laval (Alpes-de-Haute-Provence). In: Mathys, N. (Ed.), Les bassin versants expérimentaux de Draix, laboratoire d'étude de l'érosion en montagne - actes du colloque "Draix, Le Brusquet, Digne", 22-24 octobre 1997. Cemagref éditions, Antony, pp. 263-277.

Warburton, J., Davies, T.R.H., Mandl, M.G., 1993. A meso-scale field investigation of channel change and floodplain characteristics in an upland braided gravel-bed river, New Zealand. Geological Society, London, Special Publications 75(1), 241-255.

Wehr, A., Lohr, U., 1999. Airborne laser scanning - an introduction and overview. Journal of Photogrammetry and Remote Sensing 54(2-3), 68-82.

Welber, M., Bertoldi, W., Tubino, M., 2012. The response of braided planform configuration to flow variations, bed reworking and vegetation: the case of the Tagliamento River, Italy. Earth Surface Processes and Landforms 37(5), 572-582.

Westaway, R.M., Lane, S.N., Hicks, D.M., 2000. The development of an automated correction procedure for digital photogrammetry for the study of wide, shallow, gravel-bed rivers. Earth Surface Processes and Landforms 25(2), 209-226.

Westaway, R.M., Lane, S.N., Hicks, D.M., 2003. Remote survey of large-scale braided, gravel-bed rivers using digital photogrammetry and image analysis. International Journal of Remote Sensing 24(4), 795-815.

Wheaton, J.M., Brasington, J., Darby, S.E., Sear, D.A., 2010. Accounting for uncertainty in DEMs from repeat topographic surveys: improved sediment budgets. Earth Surface Processes and Landforms 35(2), 136-156.

Wheaton, J.M., Brasington, J., Darby, S.E., Kasprak, A., Sear, D., Vericat, D., 2013. Morphodynamic signatures of braiding mechanisms as expressed through change in sediment storage in a gravel-bed river. Journal of Geophysical Research: Earth Surface 118(2), 759-779.

Whiting, P.J., Dietrich, W.E., Leopold, L.B., Drake, T.G., Shreve, R.L., 1988. Bedload sheets in heterogeneous sediment. Geology 16(2), 105-108.

Williams, P.F., Rust, B.R., 1969. The sedimentology of a braided river. Journal of Sedimentary Research 39(2), 649-679.

Williams, R.D., Brasington, J., Vericat, D., Hicks, D.M., Labrosse, F., Neal, M.N., 2011. Monitoring braided river change using terrestrial laser scanning and optical bathymetric mapping. In: Smith, M., Paron, P., Griffiths, J. (Eds.), Geomorphological Mapping: Methods and Applications. Elsevier, Amsterdam, pp. 508-529.

Woodget, A.S., Carbonneau, P.E., Visser, F., Maddock, I.P., 2015. Quantifying submerged fluvial topography using hyperspatial resolution UAS imagery and structure from motion photogrammetry. Earth Surface Processes and Landforms 40(1), 47-64.

Zanoni, L., 2008. Field and laboratory evidence of large scale dynamics in braided rivers. PhD thesis, Universit`a degli Studi di Trento, Trento, 151 pp.

Zanoni, L., Bertoldi, W., Tubino, M., 2008. Spatial scales in braided networks: experimental observations. River, Coastal and Estuarine Morphodynamics: Rcem 2007, Vols 1 and 2, 201-207.

Ziliani, L., Surian, N., 2012. Evolutionary trajectory of channel morphology and controlling factors in a large gravel-bed river. Geomorphology 173, 104-117.

LISTE DES FIGURES

LISTE DES TABLES

ANNEXES

A. Calcul du bilan sédimentaire – Code R

```
################################################################################
######## 1) Bilan sédimentaire avec calcul de l'incertitude sans soustraction de la hauteur d'eau
################################################################################

######1.A Bilan sédimentaire des surfaces émergées et des surfaces en eau ######

# dataset2: base de donnée avec en colonne : numéro du pixel (Num), altitude du pixel en 2008 #
# (Z08), altitude du pixel en 2010 (Z10), #
# type de surface en 2008 et 2010 (Etat), rugosité en 2008 (RUGO08), rugosité en 2010 #
(RUGO10), densité des points en 2008 (DENS08), #
# densité des points en 2010 (DENS08). Toutes ces données ont été calculées sur ARCGIS#

dataset2$GRID_CODE <- dataset2$Z10 -  dataset2$Z08    ## différence d'altitude entre 2010 et
#2008 pour chaque pixel

## Exclusion des pixels en eau selon les règles d'exclusion définies en fig. 26
dataset2$Commentaire <- rep("Inclu",length(dataset2$Num))

ind=which(dataset2$Etat == "WetWet" & dataset2$GRID_CODE > 0)  # Etat: "Année1,Année2",
Wet: Surface en eau
dataset2$Commentaire[ind]= "Exclu"

ind=which(dataset2$Etat == "WetExposed" & dataset2$GRID_CODE < 0 )  # Exposed: bancs de
graviers
dataset2$Commentaire[ind]= "Exclu"

ind=which(dataset2$Etat == "ExposedWet" & dataset2$GRID_CODE > 0 )
dataset2$Commentaire[ind]= "Exclu"

ind=which(dataset2$Etat == "VegWet" & dataset2$GRID_CODE > 0 ) # Veg : Bancs végétalisés
dataset2$Commentaire[ind]= "Exclu"

ind=which(dataset2$Etat == "FaWet" & dataset2$GRID_CODE > 0 )  # Fa: forêt alluvial
dataset2$Commentaire[ind]= "Exclu"

dataset3 <- dataset2[dataset2$Commentaire=="Inclu",]

## Calcul de la limite de détection (LoD)
## association de l'écart type de l'erreur pour chaque type de surface (mesuré par échantillon de
#points dGPS)
# multiplié par deux en 2008 suivant l'erreur deux fois plus élevée mesurée par Sintegra an 2008
#par rapport à 2010
dataset3$ECsurface08 <- 0
ind=which(dataset3$Etat == "ExposedExposed" | dataset3$Etat == "ExposedVeg" |
dataset3$Etat == "WetWet" | dataset3$Etat == "WetExposed" | dataset3$Etat == "ExposedWet" )
```

```
dataset3$ECsurface08 [ind] <- 0.035*2
ind =which(dataset3$Etat == "FaExposed" | dataset3$Etat == "FaFa" | dataset3$Etat == "FaVeg" |
dataset3$Etat == "FaWet")
dataset3$ECsurface08 [ind] <- 0.059*2
ind =which(dataset3$Etat == "VegExposed"| dataset3$Etat == "VegVeg" | dataset3$Etat
=="VegWet" )
dataset3$ECsurface08 [ind] <- 0.046*2

dataset3$ECsurface10 <- 0
ind=which(dataset3$Etat == "ExposedExposed" | dataset3$Etat == "VegExposed" | dataset3$Etat
== "FaExposed" |
dataset3$Etat == "WetWet"| dataset3$Etat == "WetExposed" | dataset3$Etat == "ExposedWet"
| dataset3$Etat == "VegWet" | dataset3$Etat == "FaWet" )
dataset3$ECsurface10 [ind] <- 0.035
ind =which(dataset3$Etat == "FaFa" )
dataset3$ECsurface10 [ind] <- 0.059
ind =which(dataset3$Etat == "ExposedVeg" | dataset3$Etat == "VegVeg"| dataset3$Etat ==
"FaVeg" )
dataset3$ECsurface10 [ind] <- 0.046

## calcul de l'erreur liée à l'interpolation
ind <- which (dataset3$DENS08 < 2.5)
dataset3$RUGO08[ind] <- 0
ind <- which (dataset3$DENS10 < 2.5)
dataset3$RUGO10[ind] <- 0
dataset3$ECrugo08 <- 0.005007 + (0.9025516*dataset3$RUGO08)
dataset3$ECrugo10 <- 0.0005826 + (0.7693884*dataset3$RUGO10)
dataset3$EC08 <- sqrt(dataset3$ECsurface08^2 + dataset3$ECrugo08^2) ## fonction dérivée de
#la fig. 25
dataset3$EC10 <- sqrt(dataset3$ECsurface10^2 + dataset3$ECrugo10^2) ## fonction dérivée de
#la fig. 25

## calcul du niveau de détection pour chaque pixel
dataset3$LoD <- 1.96* sqrt(dataset3$EC08^2 + dataset3$EC10^2 ) ## Cf. équation 6

## Soustraction de la limite de détection à chaque pixel
dataset4 <- dataset3[,c(3,4,9,17)]

dataset4$DodLod95wcond=rep(0,length(dataset4$GRID_CODE))
ind=which(dataset4$GRID_CODE > dataset4$LoD | dataset4$GRID_CODE < (-dataset4$LoD) )
dataset4$DodLod95wcond[ind]=dataset4$GRID_CODE[ind]

dataset4$DodLod95wcond_2=rep(0,length(dataset4$GRID_CODE))
ind=which(dataset4$DodLod95wcond > 0)
dataset4$DodLod95wcond_2[ind] <- dataset4$DodLod95wcond[ind] - dataset4$LoD[ind]

ind=which(dataset4$DodLod95wcond < 0)
dataset4$DodLod95wcond_2[ind] <- dataset4$DodLod95wcond[ind] + dataset4$LoD[ind]

dataset4$Volume95wcond <- dataset4$DodLod95wcond_2 * 0.250# aire du pixel

# Bilan sédimentaire des surfaces en dépôt
depotLoD95wcond <- dataset4$Volume95wcond[which(dataset4$Volume95wcond > 0 )]
SumdepotLoD95wcond <- sum(depotLoD95wcond)
SumdepotLoD95wcond
```

```
SurfacedepotLoD95wcond<- length(depotLoD95wcond) * 0.250
SurfacedepotLoD95wcond

# Bilan sédimentaire des surfaces en érosion
erosionLoD95wcond<- dataset4$Volume95wcond[which(dataset4$Volume95wcond < 0 )]
SumerosionLoD95wcond <- sum(erosionLoD95wcond)
SumerosionLoD95wcond

SurfaceerosionLoD95wcond <- length(erosionLoD95wcond) * 0.250
SurfaceerosionLoD95wcond

# Bilan sédimentaire total
BSloD95wcond <- SumdepotLoD95wcond + SumerosionLoD95wcond
BSloD95wcond

################################################################################
######1.B Bilan sédimentaire des surfaces en eau ######

dataset4eau <- dataset4[c(dataset4$Etat == "WetWet" | dataset4$Etat == "WetExposed"  |
dataset4$Etat == "ExposedWet"  | dataset4$Etat == "FaWet"  | dataset4$Etat == "VegWet"),]

depotLoD95wcondeau <- dataset4eau$Volume95wcond[which(dataset4eau$Volume95wcond > 0
)]
SumdepotLoD95wcondeau <- sum(depotLoD95wcondeau)
SumdepotLoD95wcondeau

SurfacedepotLoD95wcondeau<- length(depotLoD95wcondeau) * 0.250
SurfacedepotLoD95wcondeau

erosionLoD95wcondeau<-  dataset4eau$Volume95wcond[which(dataset4eau$Volume95wcond  <
0 )]
SumerosionLoD95wcondeau <- sum(erosionLoD95wcondeau)
SumerosionLoD95wcondeau

SurfaceerosionLoD95wcondeau <- length(erosionLoD95wcondeau) * 0.250
SurfaceerosionLoD95wcondeau

BSloD95condeau<- SumdepotLoD95wcondeau + SumerosionLoD95wcondeau
BSloD95condeau

################################################################################
######1.C Bilan sédimentaire des surfaces emmergées ######

dataset4dry <- dataset4[c(dataset4$Etat != "WetWet" & dataset4$Etat != "WetExposed"  &
dataset4$Etat != "ExposedWet"  & dataset4$Etat != "FaWet"  & dataset4$Etat != "VegWet"),]

depotLoD95wconddry <- dataset4dry$Volume95wcond[which(dataset4dry$Volume95wcond > 0
)]
SumdepotLoD95wconddry <- sum(depotLoD95wconddry)
SumdepotLoD95wconddry

SurfacedepotLoD95wconddry<- length(depotLoD95wconddry) * 0.250
SurfacedepotLoD95wconddry
```

```
erosionLoD95wconddry<-  dataset4dry$Volume95wcond[which(dataset4dry$Volume95wcond  < 0 )]
SumerosionLoD95wconddry <- sum(erosionLoD95wconddry)
SumerosionLoD95wconddry

SurfaceerosionLoD95wconddry <- length(erosionLoD95wconddry) * 0.250
SurfaceerosionLoD95wconddry

BSloD95conddry<- SumdepotLoD95wconddry + SumerosionLoD95wconddry
BSloD95conddry

#############################################################################
######1.D Bilan sédimentaire des surfaces exclues ######

datasetexclu <- dataset2[dataset2$Commentaire=="Exclu",]
datasetexclu$Volume <-  datasetexclu$GRID_CODE* 0.250

depotexclu <- datasetexclu$Volume[which(datasetexclu$Volume > 0 )]
Sumdepotexclu <- sum(depotexclu)
Sumdepotexclu

Surfacedepotexclu<- length(depotexclu) * 0.250
Surfacedepotexclu

erosionexclu<- datasetexclu$Volume[which(datasetexclu$Volume < 0 )]
Sumerosionexclu <- sum(erosionexclu)
Sumerosionexclu

Surfaceerosionexclu <- length(erosionexclu) * 0.250
Surfaceerosionexclu

BSexclu <- Sumdepotexclu + Sumerosionexclu
BSexclu

#############################################################################
######1.E Bilan sédimentaire selon la formule de Lane et al. (2003) (Cf. Eq. 7)  ######

dataset3$VolumeLane <- dataset3$GRID_CODE  * 0.250

depotVolumeLane <- dataset3$VolumeLane[which(dataset3$VolumeLane > 0 )]
SumdepotVolumeLane <- sum(depotVolumeLane)
SurfacedepotVolumeLane <- length(depotVolumeLane) * 0.250

erosionVolumeLane <- dataset3$VolumeLane [which(dataset3$VolumeLane< 0 )]
SumerosionVolumeLane <- sum(erosionVolumeLane)
SumerosionVolumeLane

SurfaceerosionVolumeLane<- length(erosionVolumeLane) * 0.250
SurfaceerosionVolumeLane

BSVolumeLane <- SumdepotVolumeLane + SumerosionVolumeLane

# Incertitude
dataset3$IncertVolLane <- 0
dataset3$IncertVolLane <- ((dataset3$EC08)^2+(dataset3$EC10)^2)
```

```
IncertVol <- ((0.5)^2)*((sum(dataset3$IncertVolLane))^(0.5))

################################################################################
######## 2) Bilan sédimentaire avec calcul de l'incertitude et soustraction de la hauteur d'eau
################################################################################

######2.A Bilan sédimentaire des surfaces émergées et des surfaces en eau ######

## Soustraction de la hauteur d'eau moyenne mesurée sur le terrain à chaque pixel en eau en
#fonction de l'année.
dataset2$Z08modif2 <- dataset2$Z08
ind=which(dataset2$Etat == "WetExposed")
dataset2$Z08modif2[ind]= dataset2$Z08[ind] - 0.2

ind=which(dataset2$Etat == "WetWet")
dataset2$Z08modif2[ind]= dataset2$Z08[ind] - 0.2

dataset2$Z10modif2 <- dataset2$Z10
ind=which(dataset2$Etat == "ExposedWet")
dataset2$Z10modif2[ind]= dataset2$Z10[ind] - 0.39

ind=which(dataset2$Etat == "WetWet")
dataset2$Z10modif2[ind]= dataset2$Z10[ind] - 0.39

ind=which(dataset2$Etat == "FaWet")
dataset2$Z10modif2[ind]= dataset2$Z10[ind] - 0.39

ind=which(dataset2$Etat == "VegWet")
dataset2$Z10modif2[ind]= dataset2$Z10[ind] - 0.39

dataset2$GRID_CODEmodif <- dataset2$Z10modif2- dataset2$Z08modif2

## Calcul de la limite de détection (LoD)
## association de l'écart type de l'erreur pour chaque type de surface (mesuré par échantillon de
#points dGPS)
# multiplié par deux en 2008 suivant l'erreur deux fois plus élevée mesurée par Sintegra an 2008
#par rapport à 2010
dataset2$ECsurface08 <- 0
ind=which(dataset2$Etat == "ExposedExposed" | dataset2$Etat == "ExposedVeg" |
 dataset2$Etat == "ExposedWet" )
dataset2$ECsurface08 [ind] <- 0.035*2
ind =which(dataset2$Etat == "FaExposed" | dataset2$Etat == "FaFa" | dataset2$Etat == "FaVeg" |
dataset2$Etat == "FaWet")
dataset2$ECsurface08 [ind] <- 0.059*2
ind =which(dataset2$Etat == "VegExposed"| dataset2$Etat == "VegVeg" | dataset2$Etat
=="VegWet" )
dataset2$ECsurface08 [ind] <- 0.046*2
ind=which(dataset2$Etat == "WetWet" | dataset2$Etat == "WetExposed" )
dataset2$ECsurface08 [ind] <- 0.017

dataset2$ECsurface10 <- 0
ind=which(dataset2$Etat == "ExposedExposed" | dataset2$Etat == "VegExposed" | dataset2$Etat
== "FaExposed" |
 dataset2$Etat ==  "WetExposed" )
```

```
dataset2$ECsurface10 [ind] <- 0.035
ind =which(dataset2$Etat ==  "FaFa" )
dataset2$ECsurface10 [ind] <- 0.059
ind  =which(dataset2$Etat  ==  "ExposedVeg"  |  dataset2$Etat  ==  "VegVeg"|  dataset2$Etat  ==
"FaVeg" )
dataset2$ECsurface10 [ind] <- 0.046
ind=which(dataset2$Etat == "WetWet"|  dataset2$Etat ==     "ExposedWet" | dataset2$Etat ==
"VegWet"  | dataset2$Etat ==     "FaWet"      )
dataset2$ECsurface10 [ind] <- 0.018

## calcul de l'érreur liée à l'interpoloation
ind <- which(dataset2$DENS08 < 2.5)
dataset2$RUGO08[ind] <- 0
ind <- which(dataset2$DENS10 < 2.5)
dataset2$RUGO10[ind] <- 0

dataset2$ECrugo08 <- 0.005007  + (0.9025516*dataset2$RUGO08)
dataset2$ECrugo10 <- 0.0005826 + (0.7693884*dataset2$RUGO10)
dataset2$EC08 <-  sqrt(dataset2$ECsurface08^2 +  dataset2$ECrugo08^2)
dataset2$EC10 <-  sqrt(dataset2$ECsurface10^2 +  dataset2$ECrugo10^2)

## calcul du niveau de détection pour chaque pixel
dataset2$LoD <- 1.96* sqrt(dataset2$EC08^2 +   dataset2$EC10^2 )

## calcul du bilan sédimentaire
dataset5 <- dataset2[,c(4,3,13,20)]

dataset5$DodLod95heau=rep(0,length(dataset5$GRID_CODEmodif))
ind=which(dataset5$GRID_CODEmodif  >  dataset5$LoD  |  dataset5$GRID_CODEmodif  <  (-
dataset5$LoD) )
dataset5$DodLod95heau[ind]=dataset5$GRID_CODEmodif[ind]

dataset5$DodLod95heau_2=rep(0,length(dataset5$GRID_CODEmodif))
ind=which(dataset5$DodLod95heau > 0)
dataset5$DodLod95heau_2[ind] <- dataset5$DodLod95heau[ind] - dataset5$LoD[ind]

ind=which(dataset5$DodLod95heau < 0)
dataset5$DodLod95heau_2[ind]  <- dataset5$DodLod95heau[ind] + dataset5$LoD[ind]

dataset5$Volume95heau <- dataset5$DodLod95heau_2 * 0.250

depotLoD95heau <- dataset5$Volume95heau[which(dataset5$Volume95heau > 0 )]
SumdepotLoD95heau <- sum(depotLoD95heau)
SumdepotLoD95heau

SurfacedepotLoD95heau<- length(depotLoD95heau) * 0.250
SurfacedepotLoD95heau

erosionLoD95heau<- dataset5$Volume95heau[which(dataset5$Volume95heau < 0 )]
SumerosionLoD95heau <- sum(erosionLoD95heau)
SumerosionLoD95heau

SurfaceerosionLoD95heau <- length(erosionLoD95heau) * 0.250
SurfaceerosionLoD95heau
```

```
BSloD95heau <- SumdepotLoD95heau + SumerosionLoD95heau
BSloD95heau

######2.B Surfaces en eau ##############################################

dataset5eau <- dataset5[c(dataset5$Etat == "WetWet" | dataset5$Etat == "WetExposed"  |
dataset5$Etat == "ExposedWet"  | dataset5$Etat == "FaWet"  | dataset5$Etat == "VegWet"),]

depotLoD95heaueau <- dataset5eau$Volume95heau[which(dataset5eau$Volume95heau > 0 )]
SumdepotLoD95heaueau <- sum(depotLoD95heaueau)
SumdepotLoD95heaueau

SurfacedepotLoD95heaueau<- length(depotLoD95heaueau) * 0.250
SurfacedepotLoD95heaueau

erosionLoD95heaueau<- dataset5eau$Volume95heau[which(dataset5eau$Volume95heau < 0 )]
SumerosionLoD95heaueau <- sum(erosionLoD95heaueau)
SumerosionLoD95heaueau

SurfaceerosionLoD95heaueau <- length(erosionLoD95heaueau) * 0.250
SurfaceerosionLoD95heaueau

BSloD95condeauheau_eau<- SumdepotLoD95heaueau + SumerosionLoD95heaueau
BSloD95condeauheau_eau
```

B. Calcul des indicateurs des profils en travers – Code R

```
##############################################################################
######## 1) Calcul BRI, BRI * selon formule de Liébault et al. 2013a#########
   ############################################################################
#dataset: base de données avec en colonne : numéro du point (Num), nom de la section en #travers
# (Name), altitude du point (Z), type de la surface défini sur ArcGIS (bande active, bancs
#végétalisés, terrasses rive droite, terrasses rive gauche (Type), île vegétalisé cartographiée sur
#ArcGIS (île vegétalisée)

## Préparation du jeu de donnée
# Remplace "Cross Section_1" par "1" de la colonne "Name"
dataset$NOM2<- gsub("[Cross Section_]","",dataset$Name)

dataset2 <- dataset[dataset$Z != - 9999 ,] # on enlève les points sans valeur d'altitude (=en dehors
#du MNT)

dataset2$TYPE[is.na(dataset2$TYPE)]<- "ND" # on remplace NA par ND
dataset2$Ilesveg[is.na(dataset2$Ilesveg)]<- "ND" # on remplace NA par ND

dataset3 <- dataset2[dataset2$TYPE == "BA" | dataset2$TYPE == "BV",] # on sélectionne les
#points compris dans la bande de tressage (bande active + bancs végétalisés)
datasetBT <- dataset3[with(dataset3, order(Num)), ]

ind = which(dataset3$Ilesveg == "Ilesveg") # on enlève les îles végétalisées
dataset4 <- dataset3[-ind,]
dataset4t <- dataset4[with(dataset4, order(Num)), ]

##Numérotation des sous-tronçons correspondants à chaque partie de zone active d'un profil en
travers#########################
dataset4t$NumSsCS <- 1

n <- length(dataset4t$Num)
for(i in 2:n){
  if(dataset4t$Num[i] == ((dataset4t$Num[i-1])+1))   {
     dataset4t$NumSsCS[i] <- dataset4t$NumSsCS[i-1]}
     else{dataset4t$NumSsCS[i] <- (dataset4t$NumSsCS[i-1])+1 }}

# Calcul du BRI par sous-transect (exemple: un transect avec une île végétalisée au milieu = deux
#sous-transects de part et d'autre de l'île)

uNameSsCS=unique(dataset4t$NumSsCS) # avec NumSsCS, numéro des sous-transects

# Calcul de l'altitude moyenne des sous-transect (MoyenneT)
MoyenneT <- numeric(length(uNameSsCS))
for (i in 1:length(uNameSsCS)){
x=dataset4t$Z [which(dataset4t$NumSsCS==uNameSsCS[i])]
                    MoyenneT [i] <- mean(x)}
```

```
RESULTAT_1=data.frame(uNameSsCS,MoyenneT)

dataset_2<-merge(dataset4t,RESULTAT_1,by.x="NumSsCS",by.y="uNameSsCS",sort=FALSE)

###############
# Calcul de la déviation entre l'altitude du point et l'altitude moyenne du sous-transect
dataset_2$DeviaALT <- dataset_2$Z - dataset_2$MoyenneT
###############

# Calcul du BRI par sous-transect
BRI <- numeric(length(uNameSsCS))

for (i in 1:length(uNameSsCS)){
x= dataset_2$DeviaALT [which(dataset_2$NumSsCS==uNameSsCS[i])]
                    BRI [i] <- sd (x)}

nSsCS <-as.data.frame(table(dataset_2$NumSsCS))
head(nSsCS)
names(nSsCS) <- c("uNameSsCS","NombreSsCS")

uName <- unique(dataset_2$NOM2)
nTr <-as.data.frame(table(dataset_2$NOM2))
RESULTAT_2<-merge(BRI,nSsCS,by.x="uNameSsCS",by.y="uNameSsCS",sort = F)
NOMCS <- numeric(length(uNameSsCS))
for (i in 1:length(uNameSsCS)){
x<-dataset_2$NOM2[which(dataset$NumSsCS==uNameSsCS[i])]
NOMCS[i] <- unique(x)
}

List_SsTR=data.frame(uNameSsCS,NOMCS)

RESULTAT_3<-merge(RESULTAT_2,List_SsTR,by.x="uNameSsCS",by.y="uNameSsCS",sort
= F)
BRIbistot <- numeric(length(uName))
for (i in 1:length(uName)){
x=RESULTAT_3$BRIbis[which(RESULTAT_3$NOMCS==uName[i])]
                    BRIbistot [i] <- sum(x)}

RESULTATBRITOT=data.frame(uName,BRIbistot)
RESULTATBRITOT_2<-merge(RESULTATBRITOT,nTr,by.x="uName",by.y="uName",sort =
F)
# BRI par transect
RESULTATBRITOT_2$BRI <- RESULTATBRITOT_2$BRIbistot
/((RESULTATBRITOT_2$NombreTr-1) *0.5)

# BRI*par transect

RESULTATBRITOT_2$BRIbistot_adi <- RESULTATBRITOT_2$BRI
/((RESULTATBRITOT_2$NombreTr-1) *0.5)

RESULTATBRITOT_2$NOM <- as.numeric(as.character(RESULTATBRITOT_2$uName))
RESULTATBRITOT_2 <- RESULTATBRITOT_2 [with(RESULTATBRITOT_2, order(NOM)),
]
```

```
#########################################################################
######## 2) Calcul de la largeur des transects#########
#########################################################################

RESULTATFINAL_BES08$LONGBA <-  (RESULTATFINAL_BES08$NombreTr - 1) * 0.5 #
# si points tous les 50 cm

#########################################################################
######## 3) Calcul l'altitude moyenne des terrasses#########
#########################################################################

###### Altitude terrasse  ######
dataset$NOM2fact <- as.factor(dataset$NOM2)

ALTmoyenne <- as.data.frame(tapply(dataset$Z,list(dataset$NOM2fact,dataset$TYPE),mean))

ALTmoyenne$ALTterrassesRD50 <- ALTmoyenne$TerrRD50 - ALTmoyenne$BT
ALTmoyenne$ALTterrassesRG50 <- ALTmoyenne$TerrRG50 - ALTmoyenne$BT
mean(c(ALTmoyenne$ALTterrassesRG50,ALTmoyenne$ALTterrassesRD50),na.rm=T)
sd(c(ALTmoyenne$ALTterrassesRG50,ALTmoyenne$ALTterrassesRD50),na.rm=T)

#########################################################################
######## 4) Formule ondelette#########
#########################################################################
Fonction Morlet du package dplR

WaveletBRIBES08 <- morlet(y1 = RESULTATFINAL_BES08_2$BRI, x1 =
RESULTATFINAL_BES08_2$DIST, dj = 0.1, siglvl = 0.95)

#########################################################################
########5) Graphique ondelette cf. figure 39#########
#########################################################################
# Graphique wave.plot modifié du package "dplR"
waveletplot4 <- function (wave.list, wavelet.levels = quantile(wave.list$Power,
   probs = seq(from = 0, to = 1, by = 0.1)), add.coi = TRUE,
   add.sig = T, x.lab = gettext("Time"), period.lab = gettext("Period"),main.lab=gettext("SSSS"),
   crn.lab = gettext("RWI"), key.cols = rev(rainbow(length(wavelet.levels) -
      1)), key.lab = parse(text = paste0("\"", gettext("Power"),
      "\"^2")), add.spline = FALSE, f = 0.5, nyrs = NULL, crn.col = "black",
   crn.lwd = 1, coi.col = "black", crn.ylim = range(wave.list$y) *
      1.1, side.by.side = FALSE)
{
   y <- wave.list$y
   x <- wave.list$x
   wave <- wave.list$wave
   period <- wave.list$period
   Signif <- wave.list$Signif
   coi <- wave.list$coi
   coi[coi == 0] <- 1e-12
   Power <- wave.list$Power
   siglvl <- wave.list$siglvl
   if (any(diff(x) <= 0) || any(diff(period) <= 0)) {
      stop("'wave.list$x' and 'wave.list$period' must be strictly ascending")
   }
```

```
  if (period[1] <= 0) {
    stop("'wave.list$period' must be positive")
  }
  Signif <- t(matrix(Signif, dim(wave)[2], dim(wave)[1]))
  Signif <- Power/Signif
  period2 <- log2(period)
  ytick <- unique(trunc(period2))
  ytickv <- (2^(ytick)*10)
  coi2 <- log2(coi)
  coi2[coi2 < 0] <- 0
  coi2.yy <- c(coi2, rep(max(period2, na.rm = TRUE), length(coi2)))
  coi2.yy[is.na(coi2.yy)] <- coi[2]
  yr.vec.xx <- c(x, rev(x))
  par.orig <- par(c("mar", "las", "mfrow"))
  on.exit(par(par.orig))
  nlevels <- length(wavelet.levels)
  seq.level <- seq_len(nlevels - 1)
  key.labs <- formatC(wavelet.levels, digits = 4, format = "f")
  asp <- NA
  xaxs <- "i"
  yaxs <- "i"
  las <- 1
  xlim <- range(x, finite = TRUE)
  ylim <- range(period2, finite = TRUE)
  z <- Power
  if (side.by.side) {
    layout(matrix(c(2, 1), nrow = 1, byrow = TRUE), widths = c(1,0.2))
    mar <- c(3, 1, 3, 3)
    par(mar = mar, tcl = 0.5, mgp = c(3, 0.25, 0), las = 1)
    plot.new()
    plot.window(ylim = c(1, nlevels), xlim = c(0, 1), xaxs = xaxs,
      yaxs = yaxs, asp = asp)
    rect(0, seq.level, 1, 2:nlevels, col = key.cols)
    axis(4, at = seq_along(wavelet.levels), labels = key.labs)
    title(key.lab, cex.main = 1)
    mar <- c(3, 3, 3, 1)
    par(mar = mar, tcl = 0.5, mgp = c(5, 0.25, 0))
    plot.new()
    plot.window(xlim, ylim, "", xaxs = xaxs, yaxs = yaxs,
      asp = asp, las = 1)
    .filled.contour(as.double(x), as.double(period2), z,
      as.double(wavelet.levels), key.cols)
    if (add.sig) {
      contour(x, period2, Signif, levels = 1, labels = siglvl,
        drawlabels = FALSE, axes = FALSE, frame.plot = FALSE,
        add = TRUE, lwd = 2, col = "black")
    }
    if (add.coi) {
      polygon(yr.vec.xx, coi2.yy, density = c(10, 20),
        angle = c(-45, 45), col = coi.col)
    }
    axis(1)

    axis(2, at = ytick, labels = ytickv)
```

```
    title(xlab = x.lab,line=2)
    title(ylab = period.lab,line=2)
    title(main=main.lab)
    box()

  }
  else {
    layout(matrix(c(2, 1), ncol = 1, byrow = TRUE), heights = c(1,0.3))
    mar <- c(3, 3, 0.1, 3)
    par(mar = mar, tcl = 0.5, mgp = c(1.5, 0.25, 0), las = las)
    plot.new()
    plot.window(xlim = c(1, nlevels), ylim = c(0, 1), xaxs = xaxs,
      yaxs = yaxs, asp = asp)
    rect(seq.level, 0, 2:nlevels, 1, col = key.cols)
    axis(1, at = seq_along(wavelet.levels), labels = key.labs)
    title(sub = key.lab, cex.sub = 1, line = 1.5)
    par(mar = mar, tcl = 0.5, mgp = c(1.5, 0.25, 0))
    plot.new()
    plot.window(xlim, ylim, "", xaxs = xaxs, yaxs = yaxs,
      asp = asp, las = las)
    .filled.contour(as.double(x), as.double(period2), z,
      as.double(wavelet.levels), key.cols)
    if (add.sig) {
      contour(x, period2, Signif, levels = 1, labels = siglvl,
        drawlabels = FALSE, axes = FALSE, frame.plot = FALSE,
        add = TRUE, lwd = 2, col = "black")
    }
    if (add.coi) {
      polygon(yr.vec.xx, coi2.yy, density = c(10, 20),
        angle = c(-45, 45), col = coi.col)
    }
    axis(1)
    axis(2, at = ytick, labels = ytickv)
    axis(3, labels = NA)
    axis(4, at = ytick, labels = NA)
   title(xlab = x.lab)
    title(ylab = period.lab,line=2)
    box()

  }
  invisible()
}
```